Research Topics

Cellular and molecular mechanisms of lung regeneration, repair, and fibrosis

Edited by
Chunheng Mo, Xiao Xiao Tang, Shigeyuki Shichino
and Gianluca Bagnato

Published in
Frontiers in Cell and Developmental Biology
Frontiers in Immunology
Frontiers in Genetics
Frontiers in Endocrinology

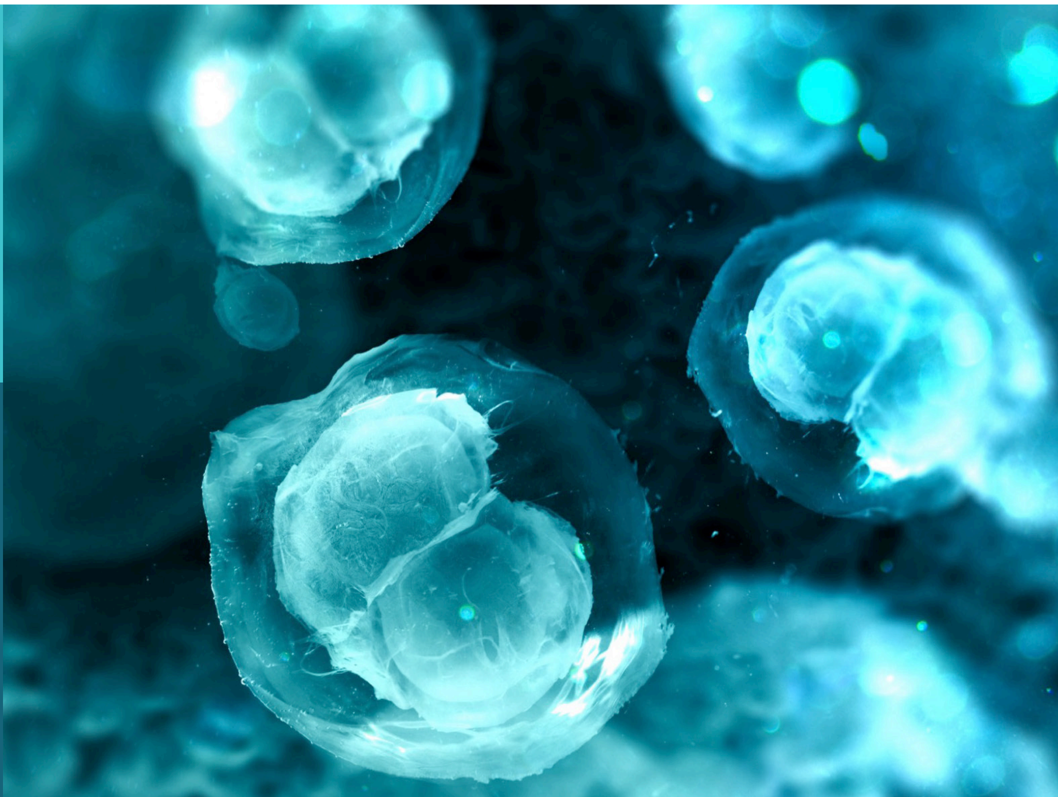

ISSN 1664-8714
ISBN 978-2-8325-4325-2
DOI 10.3389/978-2-8325-4325-2

About Frontiers

Frontiers is more than just an open access publisher of scholarly articles: it is a pioneering approach to the world of academia, radically improving the way scholarly research is managed. The grand vision of Frontiers is a world where all people have an equal opportunity to seek, share and generate knowledge. Frontiers provides immediate and permanent online open access to all its publications, but this alone is not enough to realize our grand goals.

Frontiers journal series

The Frontiers journal series is a multi-tier and interdisciplinary set of open-access, online journals, promising a paradigm shift from the current review, selection and dissemination processes in academic publishing. All Frontiers journals are driven by researchers for researchers; therefore, they constitute a service to the scholarly community. At the same time, the *Frontiers journal series* operates on a revolutionary invention, the tiered publishing system, initially addressing specific communities of scholars, and gradually climbing up to broader public understanding, thus serving the interests of the lay society, too.

Dedication to quality

Each Frontiers article is a landmark of the highest quality, thanks to genuinely collaborative interactions between authors and review editors, who include some of the world's best academicians. Research must be certified by peers before entering a stream of knowledge that may eventually reach the public - and shape society; therefore, Frontiers only applies the most rigorous and unbiased reviews. Frontiers revolutionizes research publishing by freely delivering the most outstanding research, evaluated with no bias from both the academic and social point of view. By applying the most advanced information technologies, Frontiers is catapulting scholarly publishing into a new generation.

What are Frontiers Research Topics?

Frontiers Research Topics are very popular trademarks of the *Frontiers journals series*: they are collections of at least ten articles, all centered on a particular subject. With their unique mix of varied contributions from Original Research to Review Articles, Frontiers Research Topics unify the most influential researchers, the latest key findings and historical advances in a hot research area.

Find out more on how to host your own Frontiers Research Topic or contribute to one as an author by contacting the Frontiers editorial office: frontiersin.org/about/contact

Cellular and molecular mechanisms of lung regeneration, repair, and fibrosis

Topic editors
Chunheng Mo — West China Second University Hospital, Sichuan University, China
Xiao Xiao Tang — First Affiliated Hospital of Guangzhou Medical University, China
Shigeyuki Shichino — Tokyo University of Science, Japan
Gianluca Bagnato — University of Messina, Italy

Citation
Mo, C., Tang, X. X., Shichino, S., Bagnato, G., eds. (2024). *Cellular and molecular mechanisms of lung regeneration, repair, and fibrosis*. Lausanne: Frontiers Media SA.
doi: 10.3389/978-2-8325-4325-2

Table of contents

frontiers | Frontiers in Cell and Developmental Biology

TYPE Editorial
PUBLISHED 08 January 2024
DOI 10.3389/fcell.2023.1346875

OPEN ACCESS

EDITED AND REVIEWED BY
Ramani Ramchandran,
Medical College of Wisconsin, United States

*CORRESPONDENCE
Chunheng Mo,
✉ chunhengmo@gmail.com,
✉ chunhengmo@scu.edu.cn
Xiao Xiao Tang,
✉ tangxiaoxiao@gird.cn
Mengli Yan,
✉ yanmengli2020@163.com

RECEIVED 30 November 2023
ACCEPTED 26 December 2023
PUBLISHED 08 January 2024

CITATION
Mo C, Yan M, Tang XX, Shichino S and Bagnato G (2024), Editorial: Cellular and molecular mechanisms of lung regeneration, repair, and fibrosis.
Front. Cell Dev. Biol. 11:1346875.
doi: 10.3389/fcell.2023.1346875

Editorial: Cellular and molecular mechanisms of lung regeneration, repair, and fibrosis

Chunheng Mo[1]*, Mengli Yan[1,2]*, Xiao Xiao Tang[3,4]*, Shigeyuki Shichino[5] and Gianluca Bagnato[6]

[1]Key Laboratory of Birth Defects and Related Diseases of Women and Children of MOE, State Key Laboratory of Biotherapy, West China Second University Hospital, Sichuan University, Chengdu, China, [2]Institute of Hematology, Henan Key Laboratory of Stem Cell Differentiation and Modification, Henan Provincial People's Hospital, Zhengzhou University People's Hospital, Henan University People's Hospital, Zhengzhou, Henan, China, [3]State Key Laboratory of Respiratory Disease, National Clinical Research Center for Respiratory Disease, National Center for Respiratory Medicine, Guangzhou Institute of Respiratory Health, The First Affiliated Hospital of Guangzhou Medical University, Guangzhou, China, [4]Guangzhou Laboratory, Bio-Island, Guangzhou, China, [5]Division of Molecular Regulation of Inflammatory and Immune Diseases, Research Institute of Biomedical Sciences, Tokyo University of Science, Chiba, Japan, [6]Department of Clinical and Experimental Medicine, University of Messina, Messina, Italy

KEYWORDS

lung fibrosis, lung regeneration, lung repair, cellular and molecular mechanisms, machine learning

Editorial on the Research Topic
Cellular and molecular mechanisms of lung regeneration, repair, and fibrosis

Organ fibrosis poses a significant threat to human health, contributing to over 30% of diseases that result in disability and mortality (Rockey et al., 2015; Zhou et al., 2022; Bhattacharya and Ramachandran, 2023; Yan et al., 2023). Idiopathic pulmonary fibrosis (IPF) is a progressive and often fatal lung disease characterized by fibrosis. Unfortunately, the median survival for IPF patients is only 3–5 years. Currently, the FDA-approved oral agents for pulmonary fibrosis, Pirfenidone and Nintedanib, can only slow down disease progression and do not provide a cure. Therefore, there is an urgent need to develop more effective therapeutic approaches for lung fibrosis and gain a deeper understanding of the cellular and molecular mechanisms underlying this condition (Zhang et al., 2023a; Zhang et al.; Podolanczuk et al., 2023).

Impaired lung regeneration and repair processes can contribute to the development of lung fibrosis after injury (Basil et al., 2020). The lungs function as the primary organs of the respiratory system, taking in over 10,000 L of air daily to facilitate oxygen uptake into the bloodstream and the elimination of carbon dioxide (Neupane et al., 2020; Qiu et al., 2023). As organs in direct contact with the external environment, the lungs are susceptible to injury from various factors such as environmental pollution, smoking, chemical substances, and viral and bacterial infections (Zhang et al.; Deng et al., 2023). Following injury, the lungs possess a regenerative capacity and initiate a repair program by mobilizing various type of stem cells, including type 2 alveolar epithelial (AT2) cells, basal cells, club cells, lineage-negative epithelial progenitors (LNEPs), bronchioalveolar stem cells (BASCs), and respiratory airway secretory cells (RASCs) (Figure 1) (Meng et al., 2023). Effective lung repair and regeneration are crucial biological processes for restoring the normal

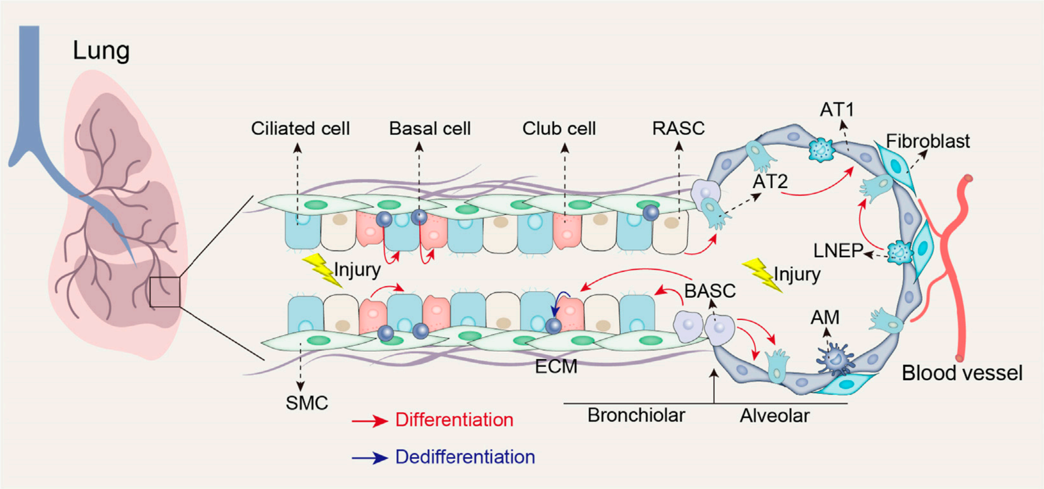

FIGURE 1
Stem cell populations involved in lung repair and regeneration following injury. Following airway injury, basal cells can differentiate into club cells and ciliated cells; club cells can differentiate into ciliated cells and possess the ability to dedifferentiate into basal cells when basal cells are depleted; BASCs can differentiate into both club cells and ciliated cells. Following alveolar injury, BASCs contribute to the replenishment of both AT1 and AT2 cells; LNEPs have the potential to differentiate into AT2 cells; RASCs can differentiate into AT2 cells, while AT2 cells themselves can differentiate into AT1 cells. AT1, Type 1 alveolar epithelial cells; SMC, Smooth muscle cell; ECM, Extracellular matrix; AM, Alveolar macrophages.

physiological function of lungs after injury. However, chronic damage or disease can impede the lung regenerative abilities, resulting in fibrosis and functional impairment (Basil et al., 2020). Understanding of the cellular and molecular mechanisms underlying lung regeneration and repair is essential for comprehending the pathogenesis of lung fibrosis and developing effective therapeutic strategies.

The cellular and molecular mechanisms of lung regeneration, repair, and fibrosis are currently not fully understood. This Research Topic includes eight original articles and one review article that enhance and expand our knowledge regarding theses mechanisms. The findings contribute to our understanding of lung regeneration, repair, fibrosis, and offer potential new prognosis and therapeutic approaches for lung fibrosis and associated disorders.

Lung fibrosis and chronic obstructive pulmonary disease (COPD) occur due to lung injury and inadequate repair processes (Basil et al., 2020). Lung regeneration and repair following injury depends on the interaction between epithelial progenitor cells and fibroblasts in the alveolar stem cell niche. However, distorted Wnt/β-catenin signaling in fibroblasts may disrupt the crucial interactions between epithelial cells and fibroblasts, leading to impaired lung regeneration and repair (El Agha and Thannickal, 2023). In this regard, Khedoe et al. investigated the impact of cigarette smoke (CS) on Wnt/β-catenin signaling in fibroblasts and its effect on lung epithelial organoid formation. They exposed fibroblasts to CS extract (CSE) and an endoplasmic reticulum (ER) stress inducer Thapsigargin (Tg). CSE induced oxidative stress, while Tg stimulated the integrated stress response (ISR) and the unfolded protein response. Both CSE and Tg suppressed Wnt/β-catenin signaling and impaired the ability of fibroblasts to support lung epithelial organoid formation. Moreover, treatment with the Wnt activator reversed this inhibitory effect. These findings demonstrated that CSE exposure induces oxidative stress and hampers lung epithelial organoid formation via inhibiting the Wnt/β-catenin signaling pathway in fibroblasts.

Moreover, airway organoids offer an ideal model for studying the cellular and molecular mechanisms underlying airway epithelium regeneration and repair (van der Vaart and Clevers, 2021). Gentemann et al. employed airway organoids combined with femtosecond laser-based nanosurgery to investigate airway repair at a high spatio-temporal resolution, which is challenging to achieve *in vivo*. They found that the repair of airway organoids after cell ablation involves crucial mechanisms regulating native airway epithelial wound healing. This *in vitro* airway injury model provides a new approach to studying airway repair following localized injury and offers valuable insights into the single-cell level mechanisms driving epithelial repair.

Early intervention plays a crucial role in effectively treating IPF. However, the prognosis for individuals diagnosed with IPF is currently discouraging. To improve outcomes, it is essential to identify precise biomarkers, especially during the early stages of the disease, to enable timely therapeutic interventions (Moss et al., 2022). Zhang et al. integrated expression datasets from bulk tissue and single-cell datasets to analyze gene expression patterns in IPF. They found differentially expressed switch genes that showed correlations with clinical indicators, with the midkine (MDK) gene emerging as a particularly strong marker for the disease. The cellular communication-related genes of MDK were found to be differentially expressed in epithelial cells. A midkine score was calculated using MDK and its related genes, and machine learning models were developed to predict IPF using bulk gene expression datasets. The midkine score showed correlations with clinical indexes, and the machine learning model achieved a high level of accuracy in classifying IPF. These findings not only provide a new biomarker for IPF diagnosis but also offer valuable insights into the pathogenesis of the disease.

Besides MDK, cuproptosis-related genes (CRGs) may also serve as biomarkers for diagnosing IPF. Metal ions, including iron and copper, play crucial roles in cell metabolism, survival, and death. Alongside iron-dependent ferroptosis, cuproptosis has emerged as a recently identified form of programmed cell death. Cuproptosis is characterized by its dependence on copper, the accumulation of fatty acylated proteins, and the reduction of iron-sulfur cluster proteins (Stockwell, 2022; Tang et al., 2022; Xu et al., 2023). Shi et al. investigated the association between cuproptosis and IPF. They identified a positive correlation between activated dendritic cells and CRGs such as lipoyltransferase 1 (*LIPT1*), lipoic acid synthetase (*LIAS*), glutaminase (*GLS*), and dihydrolipoamide branched chain transacylase E2 (*DBT*). They also found correlations between CRGs and immune cell infiltration, emphasizing the significance of immune heterogeneity in IPF patients with distinct cuproptosis clusters. Moreover, an eXtreme Gradient Boosting (XGB) machine-learning model was developed for IPF diagnosis, exhibiting promising performance with lower residuals, a higher area under the curve, and validation using external datasets. These findings offer novel insights into the relationship between cuproptosis and IPF, as well as a potential diagnostic model for IPF patients.

In addition to CRGs, chemokines hold potential as biomarkers for diagnosing IPF. Chemokines, which are small proteins secreted by various cell types, play a crucial role in lung repair and fibrosis (Liu et al., 2021). Zhao et al. investigated the potential of a chemokine-related gene signature as a biomarker for IPF diagnosis. They successfully identified eleven chemokine-related genes that effectively differentiated IPF patients from controls. Additionally, two IPF subtypes were identified based on chemokine-related gene expression, with subtype 1 exhibiting higher pulmonary function parameters and stromal scores compared to subtype 2. Notably, altered expression of chemokine-related genes was observed in both bleomycin-induced mice and transforming growth factor beta-1 (TGFβ-1)-induced fibroblast cells. These findings suggest the potential of the identified chemokine-related genes as biomarkers for IPF and shed light on their involvement in the disease's pathogenesis.

IPF and scleroderma-associated interstitial lung disease (SSc-ILD) are chronic fibrotic diseases that share common fibrosis pathways. SSc-ILD occurs in individuals with scleroderma, an autoimmune disease, and affects the lungs (Fields et al., 2023). It is characterized by inflammation and fibrosis in the lungs, resulting in progressive scarring and impaired lung function. The current treatment options for SSc-ILD involve non-specific immunosuppressive drugs and anti-fibrotic agents. However, these therapies have varying effectiveness, high costs, and potential side effects (Vonk et al., 2021). Woo et al. discussed the potential of targeting the nucleotide-binding domain and leucine-rich repeat protein-3 (NLRP3) inflammasome signaling pathway and the associated cytokines, including tumour necrosis factor α (TNFα), interleukin-1β (IL-1β), and interleukin-18 (IL-18), as novel therapeutic approaches for SSc-ILD. This review highlights that modulating these factors could offer new strategies for treating SSc-ILD.

SARS-CoV-2 infection, the virus responsible for COVID-19, can also contribute to lung injury and fibrosis. Individuals with diabetes and hypertension have been found to be susceptible to lung injury (Fuso et al., 2019; Rajasurya et al., 2020). Zhang et al. found that fibroblasts are upregulated in individuals with diabetes, hypertension, and hypertension-diabetes comorbidity who were infected with SARS-CoV-2, leading to reduced lung function. They identified specific genes associated with enhanced endothelial cell activation in fibroblasts and suggested kringle containing transmembrane protein 1 (*KREMEN1*) as a potential receptor for the activation of fibroblasts. Comparing Pirfenidone and Nintedanib, they propose Nintedanib as a more suitable treatment for COVID-19 patients with diabetes and hypertension and fibrotic lung lesions. These findings provide new insights into the modulation of fibroblasts during SARS-CoV-2 infection in comorbid conditions.

In addition to lung fibrosis and COPD, asthma, a prevalent chronic lung disease characterized by airway hyperresponsiveness and persistent airway inflammation, can also lead to reduced lung function. Globally, approximately 300 million people are affected by asthma. While medication is the primary approach for managing asthma, physical therapy, which includes exercise therapy, respiratory exercises, and muscle training, has proven to be effective (Brusselle and Koppelman, 2022). Zhou et al. has revealed that regular exercise can improve lung function, immune responses, and quality of life in children with asthma. Swimming and aerobic exercise have been identified as particularly beneficial for children with asthma. It is recommended to engage in these activities at least 2 to 3 times per week for a duration of 8 weeks, with each session lasting 40–60 min.

BALB/c and C57BL/6 mouse strains are commonly utilized in respiratory disease research, including studies on asthma. Among these strain, BALB/c mice have been observe to exhibit higher airway responsiveness than C57BL/6 mice (Duguet et al., 2000). Zeng et al. investigated the underlying mechanism using precision-cut lung slices. They found that BALB/c mice exhibited stronger small airway contraction and faster Ca^{2+} oscillations in airway smooth muscle (ASM) cells when exposed to agonists. This was attributed to increased store-operated Ca^{2+} entry (SOCE), resulting from elevated expression of SOCE components (STIM1, Orai1) in BALB/c mice's small airway ASM cells. The mathematical model further supported that the elevated SOC current may lead to enhanced agonist-induced Ca^{2+} oscillations. These findings suggest that the inherently higher SOC activity in BALB/c mice contributes to the enhanced frequency of Ca^{2+} oscillations in ASM cells, stronger small airway contraction, leading to grater airway responsiveness compared to C57BL/6 mice.

In summary, the publications within this Research Topic have the potential to improve our understanding of the cellular and molecular mechanisms involved in lung regeneration, repair, and fibrosis. Furthermore, the papers make valuable contributions towards advancing the treatment options available for lung fibrosis and improving the diagnosis of individuals afflicted by this disease.

Author contributions

CM: Conceptualization, Funding acquisition, Resources, Supervision, Writing–original draft, Writing–review and editing. MY: Writing–original draft, Writing–review and editing. XT: Funding acquisition, Writing–review and editing. SS: Writing–review and editing, Funding acquisition. GB: Writing–review and editing.

Funding

The authors declare financial support was received for the research, authorship, and/or publication of this article. This work was supported by the National Natural Science Foundation of China (82200084 to CM, 82270077 to XT), Natural Science Foundation of Sichuan Province (2023NSFSC1456 to CM), the Fundamental Research Funds for the Central Universities (to CM), Postdoctoral Science Foundation funded project of Sichuan Province (TB2023047 to CM), Sichuan University postdoctoral interdisciplinary Innovation Fund (0020404153020 to CM), Grant-in-Aid for Transformative Research Areas (B) (22H05064 to SS), and the Japan Agency for Medical Research and Development (AMED)-PRIME (JP21gm6210025 to SS).

Acknowledgments

We appreciate all the authors and reviewers who made valuable contributions to this Research Topic. We also appreciate RR from Medical College of Wisconsin, United States, for his editing of the manuscript from the Mo Laboratory at West China Second University Hospital, China.

Conflict of interest

The authors declare that the research was conducted in the absence of any commercial or financial relationships that could be construed as a potential conflict of interest.

The authors declared that they were an editorial board member of Frontiers, at the time of submission. This had no impact on the peer review process and the final decision.

Publisher's note

References

Basil, M. C., Katzen, J., Engler, A. E., Guo, M., Herriges, M. J., Kathiriya, J. J., et al. (2020). The cellular and physiological basis for lung repair and regeneration: past, present, and future. *Cell Stem Cell* 26, 482–502. doi:10.1016/j.stem.2020.03.009

Bhattacharya, M., and Ramachandran, P. (2023). Immunology of human fibrosis. *Nat. Immunol.* 24, 1423–1433. doi:10.1038/s41590-023-01551-9

Brusselle, G. G., and Koppelman, G. H. (2022). Biologic therapies for severe asthma. *N. Engl. J. Med.* 386, 157–171. doi:10.1056/NEJMra2032506

Deng, Y., Huang, X., Hu, Y., Zhong, W., Zhang, H., Mo, C., et al. (2023). Deficiency of endothelial FGFR1 signaling via upregulation of ROCK2 activity aggravated ALI/ARDS. *Front. Immunol.* 14, 1041533. doi:10.3389/fimmu.2023.1041533

Duguet, A., Biyah, K., Minshall, E., Gomes, R., Wang, C.-G., Taoudi-Benchekroun, M., et al. (2000). Bronchial responsiveness among inbred mouse strains: role of airway smooth-muscle shortening velocity. *Am. J. Respir. Crit. care Med.* 161, 839–848. doi:10.1164/ajrccm.161.3.9906054

El Agha, E., and Thannickal, V. J. (2023). The lung mesenchyme in development, regeneration, and fibrosis. *J. Clin. Investigation* 133, e170498. doi:10.1172/JCI170498

Fields, A., Potel, K. N., Cabuhal, R., Aziri, B., Stewart, I. D., and Schock, B. C. (2023). Mediators of systemic sclerosis-associated interstitial lung disease (SSc-ILD): systematic review and meta-analyses. *Thorax* 78, 799–807. doi:10.1136/thorax-2022-219226

Fuso, L., Pitocco, D., and Antonelli-Incalzi, R. (2019). Diabetic lung, an underrated complication from restrictive functional pattern to pulmonary hypertension. *Diabetes/metabolism Res. Rev.* 35, e3159. doi:10.1002/dmrr.3159

Liu, S.-s., Liu, C., Lv, X.-x., Cui, B., Yan, J., Li, Y.-x., et al. (2021). The chemokine CCL1 triggers an AMFR-SPRY1 pathway that promotes differentiation of lung fibroblasts into myofibroblasts and drives pulmonary fibrosis. *Immunity* 54, 2433–2435. doi:10.1016/j.immuni.2021.09.009

Meng, X., Cui, G., and Peng, G. (2023). Lung development and regeneration: newly defined cell types and progenitor status. *Cell Regen.* 12, 5–13. doi:10.1186/s13619-022-00149-0

Moss, B. J., Ryter, S. W., and Rosas, I. O. (2022). Pathogenic mechanisms underlying idiopathic pulmonary fibrosis. *Annu. Rev. Pathology Mech. Dis.* 17, 515–546. doi:10.1146/annurev-pathol-042320-030240

Neupane, A. S., Willson, M., Chojnacki, A. K., Castanheira, F. V. E. S., Morehouse, C., Carestia, A., et al. (2020). Patrolling alveolar macrophages conceal bacteria from the immune system to maintain homeostasis. *Cell* 183, 110–125. doi:10.1016/j.cell.2020.08.020

Podolanczuk, A. J., Thomson, C. C., Remy-Jardin, M., Richeldi, L., Martinez, F. J., Kolb, M., et al. (2023). Idiopathic pulmonary fibrosis: state of the art for 2023. *Eur. Respir. J.* 61, 2200957. doi:10.1183/13993003.00957-2022

Qiu, Y., Mo, C., Xu, S., Chen, L., Ye, W., Kang, Y., et al. (2023). Research progress on perioperative blood-brain barrier damage and its potential mechanism. *Front. Cell Dev. Biol.* 11, 1174043. doi:10.3389/fcell.2023.1174043

Rajasurya, V., Gunasekaran, K., and Surani, S. (2020). Interstitial lung disease and diabetes. *World J. Diabetes* 11, 351–357. doi:10.4239/wjd.v11.i8.351

Rockey, D. C., Bell, P. D., and Hill, J. A. (2015). Fibrosis—a common pathway to organ injury and failure. *N. Engl. J. Med.* 372, 1138–1149. doi:10.1056/NEJMra1300575

Stockwell, B. R. (2022). Ferroptosis turns 10: emerging mechanisms, physiological functions, and therapeutic applications. *Cell* 185, 2401–2421. doi:10.1016/j.cell.2022.06.003

Tang, D., Chen, X., and Kroemer, G. (2022). Cuproptosis: a copper-triggered modality of mitochondrial cell death. *Cell Res.* 32, 417–418. doi:10.1038/s41422-022-00653-7

van der Vaart, J., and Clevers, H. (2021). Airway organoids as models of human disease. *J. Intern. Med.* 289, 604–613. doi:10.1111/joim.13075

Vonk, M. C., Smith, V., Sfikakis, P. P., Cutolo, M., Del Galdo, F., and Seibold, J. R. (2021). Pharmacological treatments for SSc-ILD: systematic review and critical appraisal of the evidence. *Autoimmun. Rev.* 20, 102978. doi:10.1016/j.autrev.2021.102978

Xu, J., Zhou, F., Wang, X., and Mo, C. (2023). Role of ferroptosis in pregnancy related diseases and its therapeutic potential. *Front. Cell Dev. Biol.* 11, 1083838. doi:10.3389/fcell.2023.1083838

Yan, M., Li, H., Xu, S., Wu, J., Li, J., Xiao, C., et al. (2023). Targeting endothelial necroptosis disrupts profibrotic endothelial–hepatic stellate cells crosstalk to alleviate liver fibrosis in nonalcoholic steatohepatitis. *Int. J. Mol. Sci.* 24, 11313. doi:10.3390/ijms241411313

Zhang, J., Zhang, L., Chen, Y., Fang, X., Li, B., and Mo, C. (2023a). The role of cGAS-STING signaling in pulmonary fibrosis and its therapeutic potential. *Front. Immunol.* 14, 1273248. doi:10.3389/fimmu.2023.1273248

Zhou, D., Zhang, J., Xiao, C., Mo, C., and Ding, B. S. (2022). Trimethylamine-N-oxide (TMAO) mediates the crosstalk between the gut microbiota and hepatic vascular niche to alleviate liver fibrosis in nonalcoholic steatohepatitis. *Front. Immunol.* 13, 964477. doi:10.3389/fimmu.2022.964477

Frontiers in Immunology

TYPE Original Research
PUBLISHED 14 April 2023
DOI 10.3389/fimmu.2023.1159856

Check for updates

OPEN ACCESS

EDITED BY
Chunheng Mo,
Sichuan University, China

REVIEWED BY
Xiao Xiao Tang,
First Affiliated Hospital of Guangzhou Medical University, China
Gianluca Bagnato,
University of Messina, Italy

*CORRESPONDENCE
Jixiang Ni
jxnee77@163.com

†These authors have equally contributed to this work

SPECIALTY SECTION
This article was submitted to Inflammation, a section of the journal Frontiers in Immunology

RECEIVED 06 February 2023
ACCEPTED 29 March 2023
PUBLISHED 14 April 2023

CITATION
Zhao T, Wu X, Zhao X, Yao K, Li X and Ni J (2023) Identification and validation of chemokine system-related genes in idiopathic pulmonary fibrosis. *Front. Immunol.* 14:1159856. doi: 10.3389/fimmu.2023.1159856

Identification and validation of chemokine system-related genes in idiopathic pulmonary fibrosis

Tianming Zhao[1†], Xu Wu[1†], Xuelei Zhao[2†], Kecheng Yao[3], Xiaojuan Li[1] and Jixiang Ni[1*]

[1]Department of Respiratory and Critical Care Medicine, The People's Hospital of China Three Gorges University, The First People's Hospital of Yichang, Yichang, China, [2]Department of Gastroenterology, The People's Hospital of China Three Gorges University, The First People's Hospital of Yichang, Yichang, China, [3]Department of Geriatrics, The People's Hospital of China Three Gorges University, The First People's Hospital of Yichang, Yichang, China

Background: Idiopathic pulmonary fibrosis (IPF) is a chronic progressive interstitial lung disease with limited therapeutic options. Recent studies have demonstrated that chemokines play a vital role in IPF pathogenesis. In the present study, we explored whether the gene signature associated with chemokines could be used as a reliable biological marker for patients with IPF.

Methods: Chemokine-related differentially expressed genes (CR-DEGs) in IPF and control lung tissue samples were identified using data from the Gene Expression Omnibus database. A chemokine-related signature of the diagnostic model was established using the LASSO-Cox regression. In addition, unsupervised cluster analysis was conducted using consensus-clustering algorithms. The CIBERSORT algorithm was used to calculate immune cell infiltration across patient subgroups. Finally, we established a mouse model of bleomycin-induced pulmonary fibrosis and a model of fibroblasts treated with TGFβ1. Expression levels of chemokine-related signature genes were determined using real-time quantitative polymerase chain reaction (RT-qPCR).

Results: We established a chemokine-related eleven-gene signature of a diagnostic model consisting of CXCL2, CCRL2, ARRB1, XCL1, GRK5, PPBP, CCL19, CCL13, CCL11, CXCL6, and CXCL13, which could easily distinguish between IPF patients and controls. Additionally, we identified two subtypes of IPF samples based on chemokine-related gene expression. Pulmonary function parameters and stromal scores were significantly higher in subtype 1 than in subtype 2. Several immune cell types, especially plasma cells and macrophages, differ significantly between the two subtypes. RT-qPCR results showed that the expression levels of *Cxcl2* and *Ccl2* increased considerably in bleomycin-induced mice. Meanwhile, *Arrb1*, *Ccrl2*, *Grk5*, and *Ppbp* expression was significantly reduced. Furthermore, multiple chemokine-related genes were altered in TGFβ1 or TNFα-induced fibroblast cells.

Conclusions: A novel chemokine-related eleven-signature of diagnostic model was developed. These genes are potential biomarkers of IPF and may play essential roles in its pathogenesis.

KEYWORDS

chemokine, idiopathic pulmonary fibrosis, gene signature, immune infiltration, biomarker

1 Introduction

Idiopathic pulmonary fibrosis (IPF) is a chronic progressive lung disease characterized by pulmonary scarring (1). The incidence of IPF is increasing, and IPF is a leading cause of death in an aging population (2). The prognosis for IPF is often poor, with an average survival of 3–5 years after diagnosis (1). The incidence and prevalence of IPF were analyzed as 0.09–1.30 per 10,000 and 0.33–4.51 per 10,000, respectively (3). The treatment options for IPF are limited. Pirfenidone and nintedanib are currently FDA-approved oral agents that reduce IPF progression (4, 5). Thus, identifying specific biomarkers, especially for early stage and prompt therapy, is vital for improving the prognosis of patients with IPF.

The pathogenesis of IPF involves multiple environmental risk factors and multi-gene alterations that contribute to epithelial cell damage and apoptosis, recruit immune cells to the site of injury, and activate fibroblasts to secrete extracellular matrix to initiate repair (6). Chemokines play an essential role in injury and repair (7). Chemokines are small-molecular-weight proteins secreted by multiple cell types and are involved in the process of pulmonary fibrosis (8–10). For example, alveolar epithelial cell (AECs) injury increases the expression of both CCL2 and CCL12, and alveolar epithelial cell-specific deletion of CCL12 prevents pulmonary fibrosis in mice, but not in CCL12 null mice. Loss of CCL12 in AECs leads to decreased macrophage recruitment (10). During pulmonary fibrosis, alveolar macrophages secrete multiple chemokines such as CCL18 and CCL1, which directly activate pulmonary fibroblasts and stimulate collagen production (8, 11). CCL18 levels significantly increase in the serum and bronchoalveolar lavage fluid (BALF) of patients with multiple interstitial lung diseases, including IPF (12). Serum CCL18 concentrations >150 ng/mL significantly increased mortality in patients with IPF, indicating that serum CCL18 concentrations are a good predictor of IPF (13). Neutralizing CCL1 or inhibiting CCL1 signaling reduces pulmonary fibrosis *in vitro* and *in vivo*, indicating that CCL1 is a potential therapeutic target for IPF (8). In IPF, various cells express chemokines and chemokine receptors, constituting a complex chemokine system that regulates the pathogenesis of IPF. Thus, the role of chemokine system-related genes in the diagnosis and prognosis of IPF remains unclear and requires further investigation.

In the present study, we identified chemokine-related differentially expressed genes (CR-DEGs) in the control and IPF samples. Based on the least absolute shrinkage and selection operator (LASSO), eleven CR-DEGs were included to establish a diagnostic model in the training and validation sets. In addition, IPF samples were divided into two subgroups based on eleven genes and characterized for each subgroup. Finally, we examined the expression of eleven CR-DEGs in bleomycin-induced injury and TGFβ1-induced pulmonary fibroblasts.

2 Materials and methods

2.1 Data source and processing

The gene expression matrix and clinical data of IPF samples were downloaded from the NCBI GEO database (http://www.ncbi.nlm.nih.gov/geo/) (14). The training cohort consisted of 122 IPF and 91 control samples from GSE47460 [GPL14550 platform]. The validation cohort comprised 112 IPF and 20 control samples from GSE70866 [GPL14550 platform]. GSE47460 [GPL6480 platform] served as a validation cohort. One hundred thirteen chemokine-related genes (CRGs) were extracted from GeneCards (https://www.genecards.org/).

2.2 Identification of the CR-DEGs

Differentially expressed genes (DEGs) were extracted between the IPF and normal samples using the “limma” R package (the absolute value of log2 fold change (log2FC) was more significant than 1, and false discovery rate (FDR) was less than 0.05). We compared the differences between DEGs and CRGs and retained the pooled portion as CR-DEGs. The “pheatmap” R package and “cor” functions were used to draw heatmaps and calculate the correlation between the CR-DEGs. Protein-protein interactions (PPI) between CR-DEGs were predicted using the STRING database. Cytoscape Version 3.0.0 was used to visualize the PPI network (15). Next, we enriched GO biological processes and KEGG signaling for genes in the network using Cluster Profiler version 4.4.4 (16).

2.3 Construction of diagnostic models

Based on the expression levels of CR-DEGs in the GSE47460 [GPL14550 platform] cohort, “rms” R packages were used for univariable logistic regression. We then used LASSO to screen for optimal CR-DEGs. For the GSE47460 [GPL14550 platform] cohort, a CR-DEG-based diagnostic classifier was constructed using the Support Vector Machine (SVM) method. The diagnostic model was evaluated using the ROC curve method in the training cohort (GSE47460 [GPL14550 platform]) and two independent validation cohorts (GSE70866 and GSE47460 [GPL6480 platform]).

2.4 Clinical relevance of CR-DEGs

Clinical information, including age, diffusion capacity of carbon monoxide (dlco), forced vital capacity (fvc), and forced expiratory volume in 1 s (fev1), was extracted from the GSE47460 dataset. Fisher's exact test was used for categorical variables to analyze the distribution of clinical information in the samples. The Kruskal–Wallis test was used to compare continuous data variables, and correlations between the expression levels of CR-DEGs and clinical parameters were calculated using the cor function.

2.5 Analysis of immune infiltration

We used CIBERSORT to estimate the proportional immune cell types in the GSE47460 [GPL14550 platform] samples. We then compared the variability of immune cell distribution in the IPF and control groups using the Kruskal–Wallis test. Correlations between the expression levels of CR-DEGs, which were used to construct diagnosis models and immune cells, were calculated using a cor function.

2.6 Prognostic relevance of diagnostic CR-DEGs

We obtained survival information from the GSE70866 cohort to observe the prognostic relevance of diagnostic CR-DEGs. The IPF samples were divided into two groups (high- and low-expression groups) according to the median gene expression value. The prognostic difference between the high- and low-expression groups was assessed using the Kaplan–Meier curve method (survival package) in the R language, and the p-value was calculated using the log-rank test.

2.7 Analysis of molecular subtype

Based on the expression levels of CR-DEGs constructed for diagnostic models, we performed a consensus clustering analysis of the IPF samples from the GSE47460 [GPL14550 platform] cohort using the "Consensus ClusterPlus" package. The "GSVA" package assessed the chemokine scores for each IPF sample, and then the chemokine scores of the different subtypes were compared using the Kruskal–Wallis test. As described above, we also compared the differences in clinical parameters, immune infiltration, and stromal scores between the subtypes.

2.8 Pathway enrichment analysis in subgroups

All KEGG data were downloaded from the GSEA database. We then quantified each KEGG pathway using the "GSVA" package based on the gene expression levels in the GSE47460 [GPL14550 platform] sample. We then used the "limma" package to screen for differentially expressed genes between subgroups (FDR<0.05 and |log2FC|>0.263). The ClusterProfiler" package was used to perform Gene Ontology (GO), including biological processes (BP), and Kyoto Encyclopedia of Genes and Genomes (KEGG) pathway enrichment analysis.

2.9 Animal model

Eight-week-old male C57BL/6J mice were purchased from the SLRC Laboratory Animal Company (Hunan, China). All animals were kept in an SPF environment at China Three Gorges University. The animal experimental protocol was approved by the Ethics Committee of China Three Gorges University (Approval No. 2022B100A). The animal model of lung fibrosis was established by a single intratracheal administration of bleomycin (2 U/kg, Hisun Pharmaceutical, China) or an equal amount of saline as a control. Mice were sacrificed 21 days after establishment of the mouse model. The body and lung weights were measured. The left lung was embedded in paraffin and stained with Masson's trichrome. The right lung was collected and frozen in liquid nitrogen for real-time quantitative polymerase chain reaction (RT-qPCR).

2.10 Cells culture and treatment

The human embryonic lung fibroblast MRC-5 cell line was purchased from Procell (Wuhan, China) and cultured in Minimum Essential Medium (MEM, Procell) containing non-essential amino acids, 10% fetal bovine serum (FBS, VivaCell) and 1% penicillin-streptomycin (VivaCell) at 37°C with 5% CO_2. MRC-5 cells were treated with TGFβ1 (5 ng/mL), and TNFα (10 ng/mL) for 24 h.

2.11 RT-qPCR

The expression of these core CR-DEGs in fibroblasts stimulated with TGF-β1 and TNF-α or bleomycin-treated lung tissue was further verified using RT-qPCR. Total RNA was isolated using TRIZOL. The cDNA was synthesized using a cDNA synthesis kit (Vazyme, Nanjing, China). RT-qPCR was performed using the Taq Pro Universal SYBR qPCR Master Mix (Vazyme, Nanjing, China). *GAPDH* or *ACTB* was used as the reference gene. The relative fold-change was calculated using the $2^{-\triangle\triangle Ct}$ method.

2.12 Western blot analysis

Western blot analysis was performed to detect protein level of GRK5, ARRB1, and CCRL2 in fibroblasts stimulated with TGF-β1 and TNF-α. Briefly, MRC-5 cells were lysed on ice using radioimmune precipitation assay (RIPA) lysis buffer (Servicebio, Wuhan, China). Protein concentration was measured using BCA protein assay kit. Protein extracts (20 ug) were separated by SDS-polyacrylamide gels (SDS-PAGE), transferred to PVDF membranes. Membranes were then incubated with primary antibodies against α-SMA (1:1000, Cell Signaling Technology, MA, USA), FN1 (1:2000, Proteintech, Wuhan, China), Tubulin (1:2000, Santa Cruz, CA, USA), GRK5 (1:1000, Proteintech, Wuhan, China), ARRB1 (1:1000, Proteintech, Wuhan, China), CCRL2 (1:3000, Proteintech, Wuhan, China) overnight at 4°C. Horseradish peroxidase (HRP)-conjugated anti-mouse or anti-rabbit whole IgG secondary antibodies (1:5000, Birmingham, AL, USA) was identify the primary antibody. Protein bands were detected using Super ECL Star kit (US Everbright, Suzhou, China).

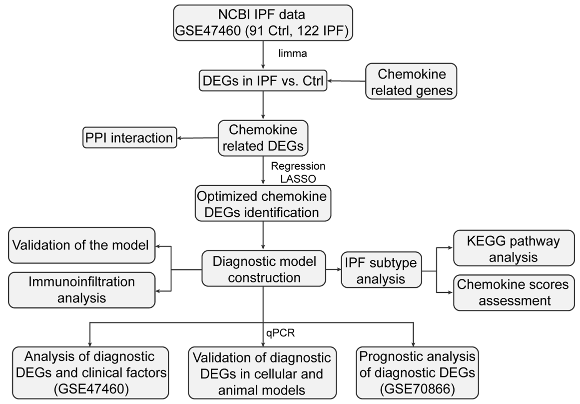

FIGURE 1
Flow diagram of this study.

2.13 Statistical analysis

Statistical analysis was performed using the R software (version 3.6.1) and GraphPad Prism software (version 8.0). Different R packages were used to analyze the gene expression profiles. Data from RT-qPCR were presented as “mean ± standard error of mean (SEM)” or “mean ± standard deviation (SD)”. An Independent samples t-test was used to compare the treatment and control groups. Statistical significance was set at p<0.05.

3 Results

3.1 Identification of chemokine-related differentially expressed genes

The workflow is illustrated in Figure 1. We investigated the DEGs in 122 IPF and 91 normal tissue samples (CTRL) from GS47460 [GPL14550 platform]. These specimens were obtained surgically and were diagnosed as having IPF or being controls by clinical history, CT scan, or surgical pathology. The baseline characteristics of the IPF and control individuals are shown in Table 1. As shown in the volcano map, 891 DEGs (306 downregulated and 585 upregulated) were identified (Figure 2A). In total, 113 CRGs were retrieved from the GeneCards database (Table S1). Thirty-four CR-DEGs were identified by investigating the intersection of the DEGs and CRGs (Figure 2B). The heatmap showed 34 CR-DEGs in IPF and control samples (Figure 2C). Chemokine receptors often play an essential role in the binding of specific chemokines. Based on this, we performed a correlation analysis between the CR-DEGs (Figure 2D). Additionally, we constructed a PPI network of CR-DEGs using the STING database. Among these CR-DEGs, CCL13, CCL11, CCL7, CXCL13, GRK5, ARRB1, CCRL2, and CXCL2 with the highest degrees were considered hub genes in this network (Figure S1). Biological processes of GO enrichment analysis revealed that CR-DEGs were mainly involved in cell chemotaxis, response to chemokines, chemokine-mediated signaling pathways, etc. (Figure S2A). The enrichment analysis of KEGG pathways included the chemokine signaling pathway, cytokine-cytokine receptor interaction, and IL-17 signaling pathway (Figure S2B).

3.2 Construction of diagnostic model based on chemokine-related hub genes

We performed univariate logistic regression analysis of 34 CR-DEGs (Figure 3A). Next, we used LASSO to screen for optimal CR-DEGs. Eleven CR-DEGs were subjected to LASSO Cox regression analysis to construct a diagnostic model (Figures 3B, C). The

TABLE 1 The baseline characteristics of the study subjects.

Clinical features	IPF (N=122)	CTRL (N=91)	*P value*
Gender			0.0013
Female	41	51	
Male	81	40	
Age	64.51 ± 8.40	63.79±11.49	0.615
Predicted dlco (%)	49.51±18.73	82.86±16.44	< 0.001
Predicted fev1 (%)	71.05±17.51	94.58±12.97	< 0.001
Predicted fvc (%)	64.28±14.62	94.46±13.11	< 0.001

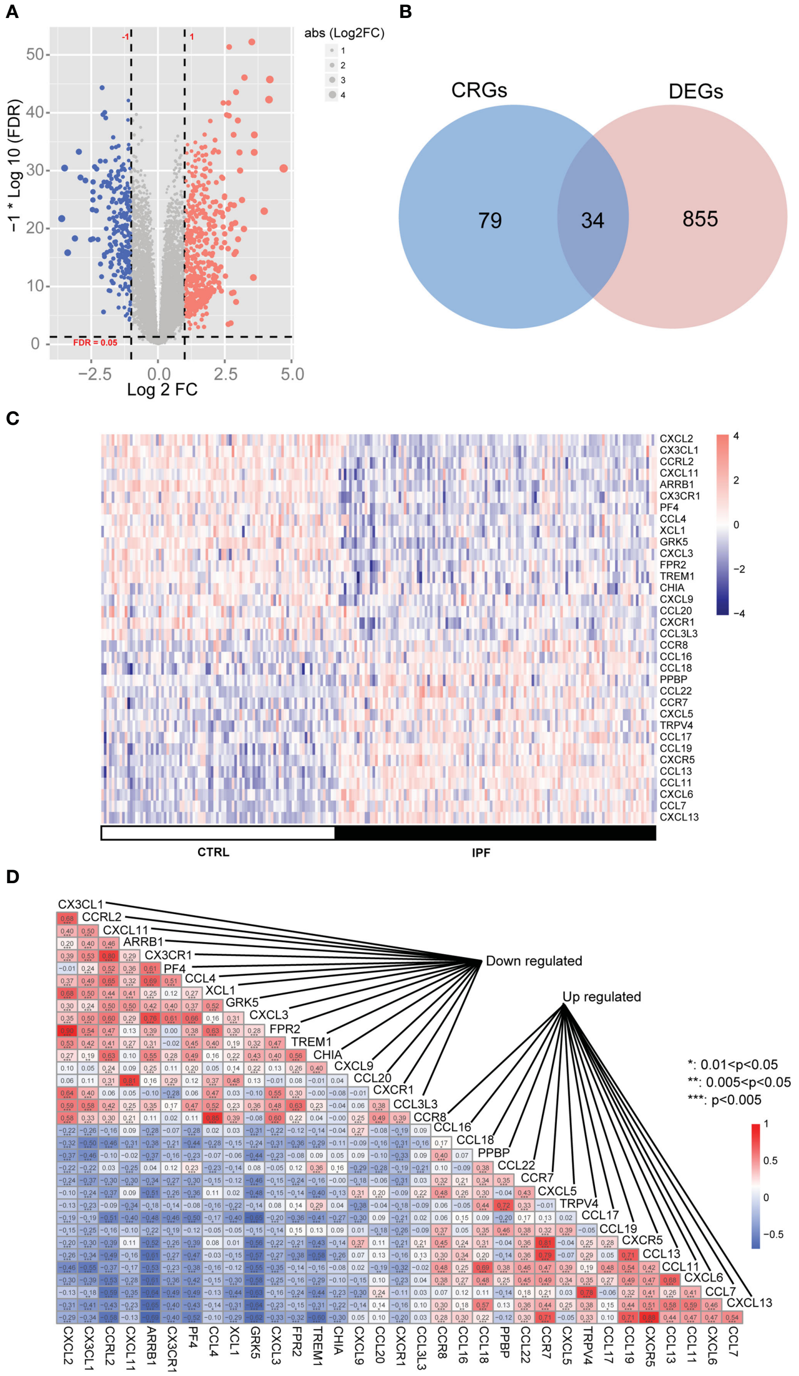

FIGURE 2

The differentially expressed chemokine-related genes (CRs) in IPF cohort. **(A)** Volcano plot of differentially expressed genes (DEGs). **(B)** Venn diagram of DEGs and CRs. **(C)** Heatmap of CR-DEGs in IPF samples. **(D)** Heatmap of correlation between CR-DEGs.

heatmap showed that eleven CR-DEGs in the diagnostic model had significant differences in precision between the IPF and control samples in the training cohort (GS47460 [GPL14550 platform]) (Figure 3D) and two external validation cohorts (GSE70866 and GS47460 [GPL6480 platform]) (Figures 3E, F). Figures 3G–I show the ROC curves of the eleven CR-DEGs diagnostic models in the GS47460 [GPL14550 platform], GSE70866, and GS47460 [GPL6480 platform] datasets, respectively. Eleven CR-DEGs were significantly associated with clinical parameters in patients, such as age, dlco, fev1, and fvc (Figure 4A). For example, ARRB1 expression was significantly positively correlated with dlco, indicating that higher ARRB1 expression is associated with better lung function. In contrast, CXCL6 expression was significantly negatively correlated with dlco, suggesting that CXCL6 is a marker of poor lung function (Figure 4A). Therefore, these results suggest that the eleven CR-DEGs signatures may serve as potential diagnostic factors in IPF patients. Based on the median values, patients with IPF from the GSE70866 cohort were divided into two groups. The association

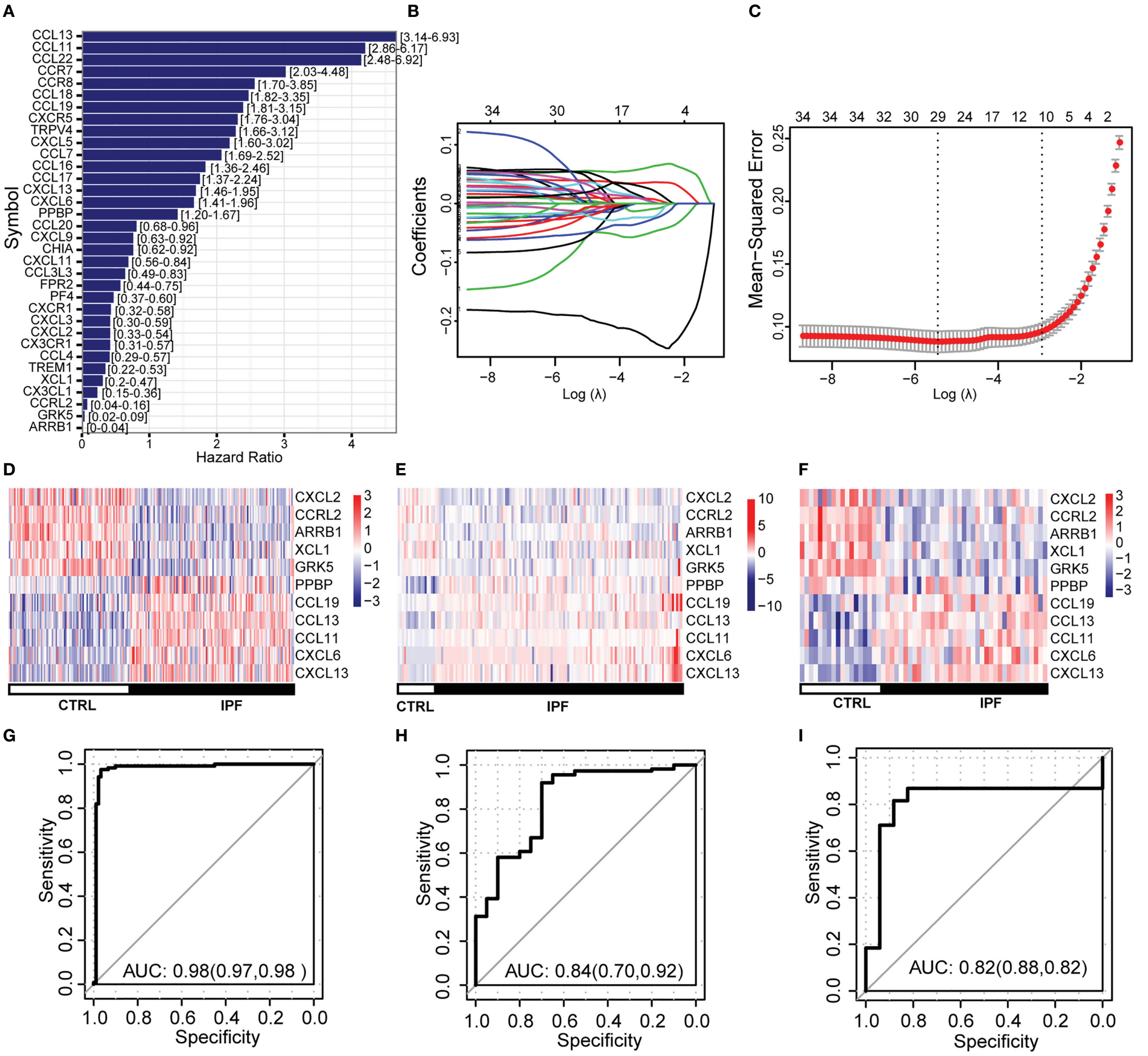

FIGURE 3
Construction and validation of diagnostic models based on CR-DEGs. **(A)** The logistic regression analysis of CR-DEGs. **(B)** Diagnostic model construction using a least absolute shrinkage and selection operator (LASSO) Cox regression model. **(C)** Coefficient distribution plots to select the optimum lambda value. **(D–F)** Heatmap of the gene-expression profiles of model-related CR-DEGs in the training **(D)** and external validation cohorts **(E, F)**. **(G–I)** ROC curves of diagnostic models in training **(G)** and external validation cohorts **(H, I)**.

between gene expression and outcome was assessed using Kaplan–Meier curves. Six genes (ARRB1, CCRL2, CXCL2, CCL13, PPBP, and GRK5) showed a prognostic value. In bronchoalveolar lavage (BAL) cells, high expression of CCRL2, CXCL2, CCL13, PPBP, and GRK5 was significantly associated with shorter survival times. High ARRB1 expression was associated with better outcomes (Figures 4B–G).

3.3 CR-DEGs and immune cell infiltration

The CIBERSORT algorithm was used to assess the immune microenvironment of the GSE GS47460 [GPL14550 platform] dataset. A boxplot indicated that the infiltration of multiple immune cells was significantly different between IPF and control samples (Figure 5A). For example, plasma cells, naïve CD4$^+$ T cells, macrophages (M0 and M2), and activated mast cells infiltrated significantly higher levels in the IPF tissue (Figure 5A). Next, we explored the relationship between eleven CR-DEGs and immune cell infiltration. The results suggest that eleven CR-DEGs were significantly associated with the infiltration level of immune cells (Figure 5B).

3.4 Subtype based on the diagnosis of CR-DEGs

To explore the biological characteristics of chemokine-related genes, IPF samples were classified into two clusters (subtype 1 and

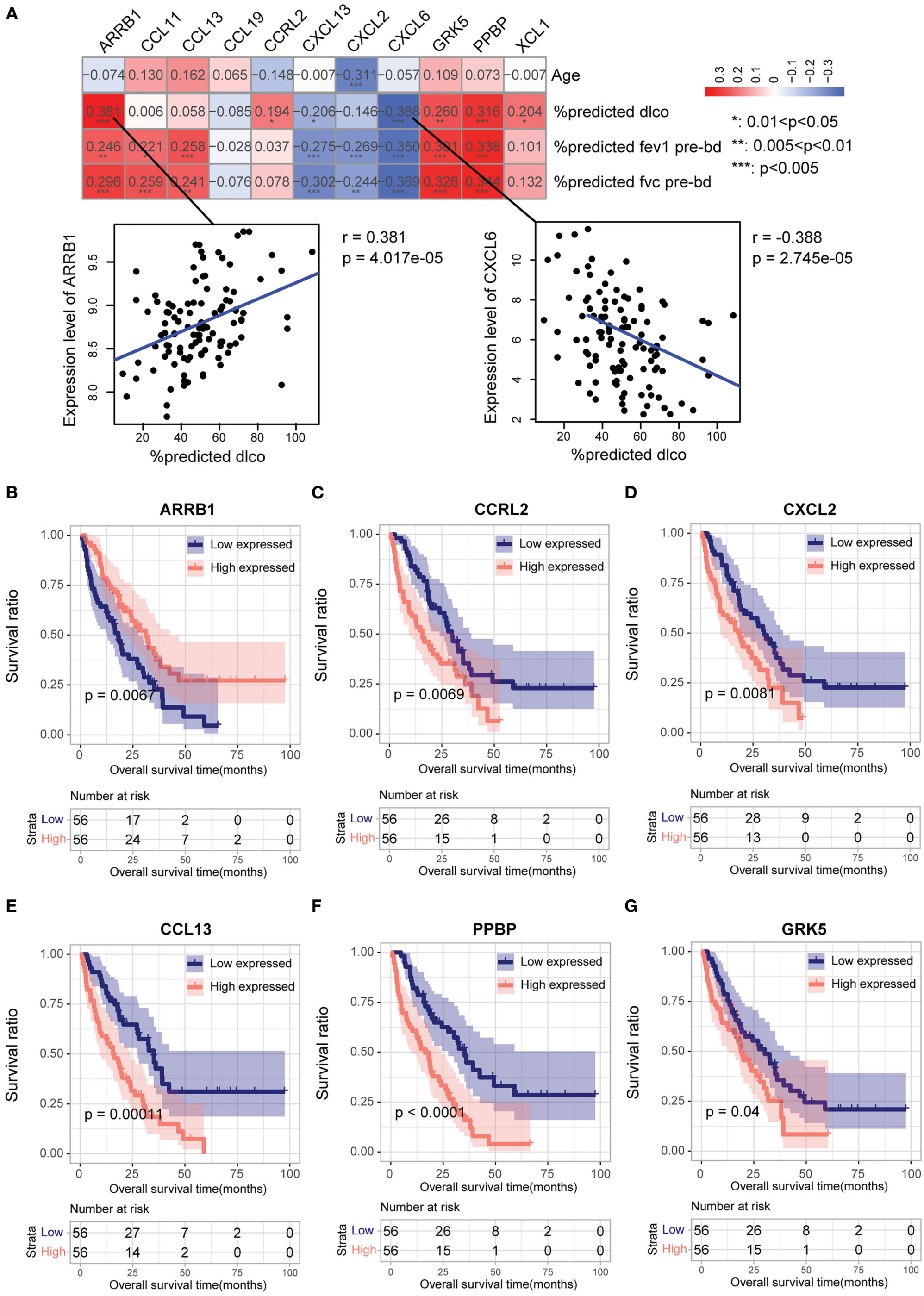

FIGURE 4

Association of clinical parameters and prognostic value of eleven CR-DEGs in IPF patients. **(A)** Correlation between eleven CR-DEGs and age, dlco, fev1, and fvc. **(B–G)**. K-M analysis and the predictive value of ARRB1 **(B)**, CCRL2 **(C)**, CXCL2 **(D)**, CCL13 **(E)**, PPBP **(F)**, and GRK5 **(G)** for the survival in the BALF of patients with IPF.

subtype 2) using the "ConsensusClusterPlus" package in R, according to eleven CR-DEGs expression levels. Subtypes 1 and 2 contained 81 and 41 IPF samples, respectively (Figure 6A). The chemokine score for each sample was assessed using the GSVA algorithm. As shown in Figure 6B, the chemokine score was significantly higher for subtype 1 than for subtype 2. The heatmap shows the expression patterns of eleven CR-DEGs in subtypes 1 and 2 (Figure 6C). Pulmonary function parameters (dlco, fev1, and fvc) and stromal scores were significantly higher in subtype 1 than in subtype 2 (Figures 6D–G). In addition, immune infiltration analysis showed that the levels of infiltration of multiple immune cells differed significantly between the two subtypes (Figure 6H).

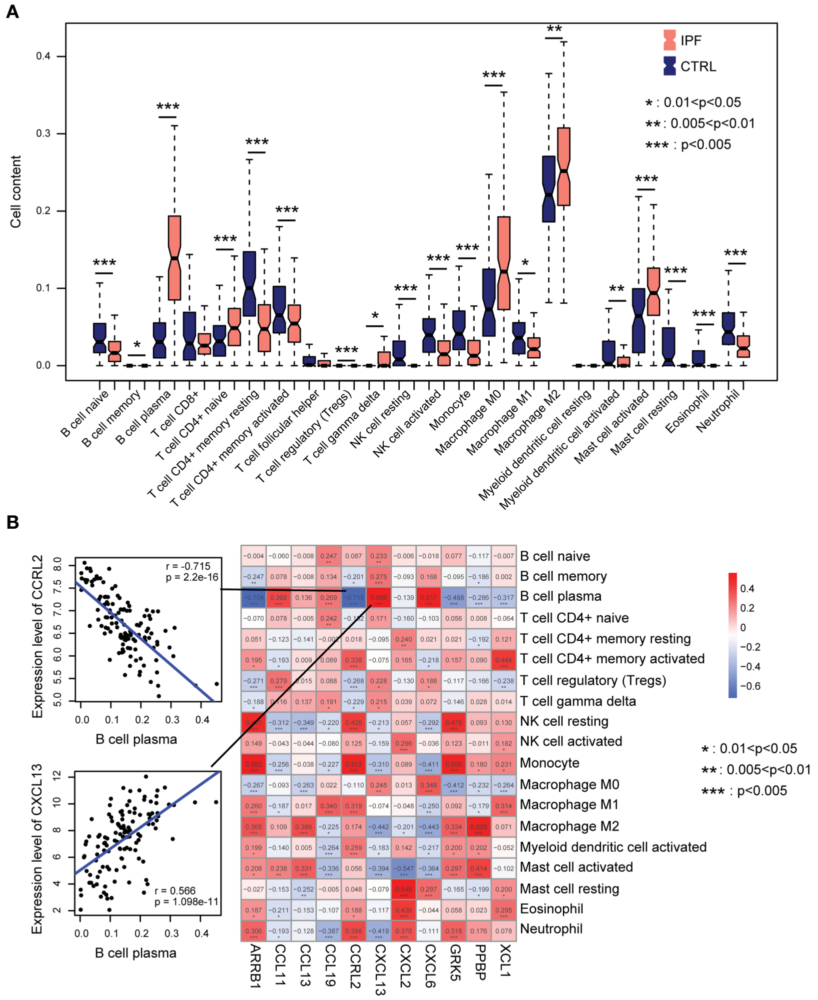

FIGURE 5
Immune cell infiltration. **(A)** Distribution of immune cells in normal and IPF lung tissue. **(B)** Correlation between eleven CR-DEGs expression levels and levels of infiltration immune cells.

3.5 Functional enrichment analysis

To further investigate changes in biological function between subtypes based on the expression levels of the eleven CR-DEGs, we performed GSEA for subtypes 1 and 2. The significantly enriched pathways in subtypes 1 and 2 are shown in Figure 7A. Subsequently, GSEA was performed for these two subtypes. The results indicated that the samples in subtype 1 were significantly enriched in unsaturated fatty acid biosynthesis, glycosaminoglycan degradation, and snare interactions in vesicular transport. Subtype 2 was significantly enriched in ribosomes (Figure 7B).

3.6 Validation of model gene expression in TGFβ1- or TNFα-treated lung fibroblast cells

Upon stimulation with various cytokines, pulmonary fibroblasts are transformed into myofibroblasts that synthesize large amounts of the extracellular matrix. TGF-β1 and TNF-α, well-known profibrotic and proinflammatory cytokines, are widely used to induce fibroblast-to-myofibroblast transformation (17, 18). The mRNA levels of the eleven CR-DEGs were estimated using RT-qPCR. Primer sequences are listed in Table S2. Treatment of MRC-5 cells with TGF-β1 (5 ng/mL for 24 h) significantly upregulated ACTA2 (encoding α-SMA) and FN1 (encoding fibronectin) expression (Figure 8A), suggesting that TGF-β1 promotes fibroblast-to-myofibroblast transformation. Additionally, the expression of several chemokines and receptors decreased, including CXCL2, CCRL2, ARRB1, GRK5, CXCL6, CCL13 (human only), and CCL11. Stimulation of MRC-5 cells with TNF-α (10 ng/mL for 24 h) resulted in a significant increase in CXCL2, CCRL2, and CXCL6 expression, whereas ARRB1, GRK5, CCL13, CCL11, CCL19, and CXCL13 expression was significantly decreased (Figures 8B–K). XCL1 was not detected in the MRC-5 cells. Western blot revealed elevated of α-SMA and FN1, as well as down-regulated GRK5, ARRB1 in TGFβ1-treated lung fibroblasts (Figures 8L–P, Figure S3).

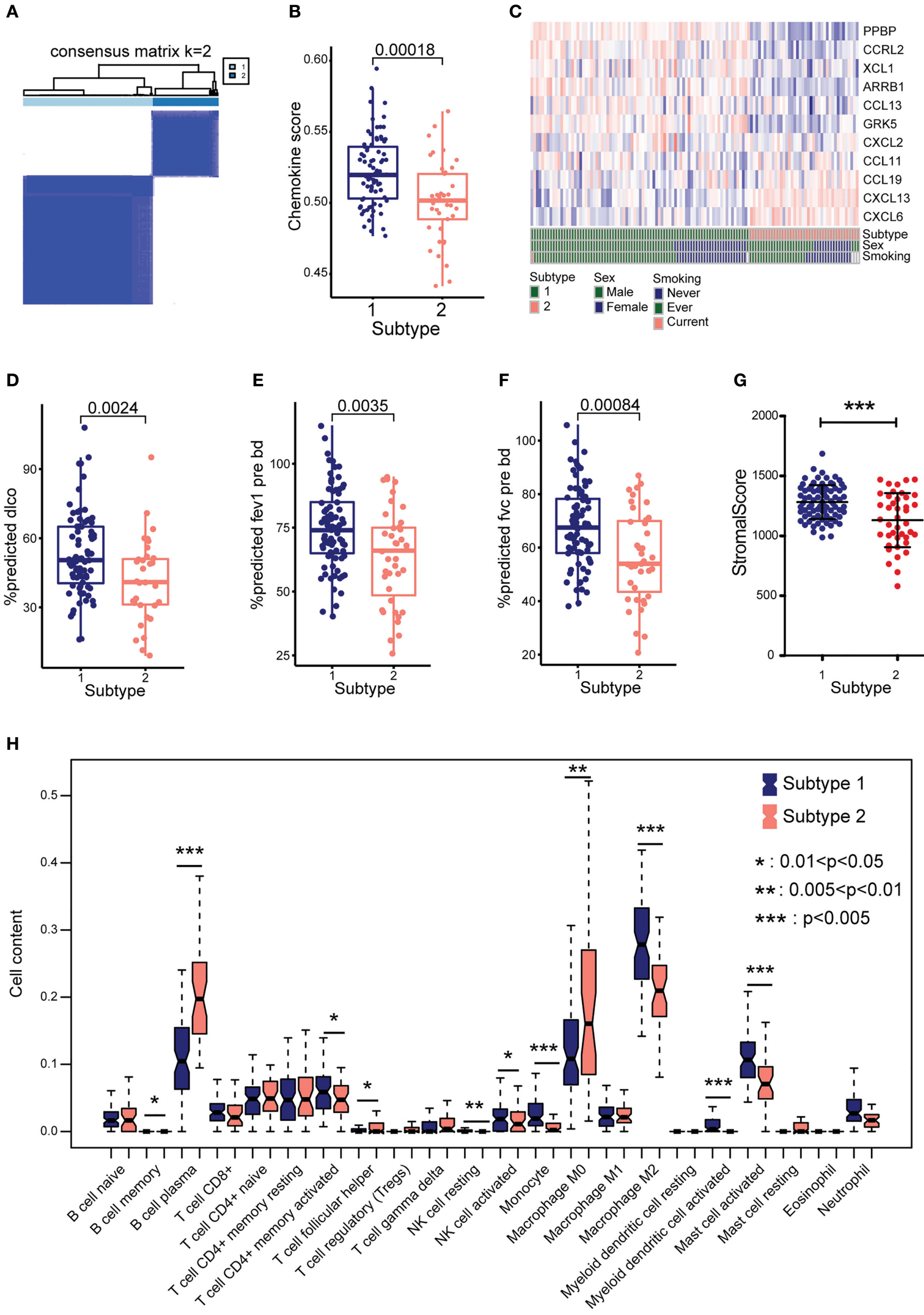

FIGURE 6
Identify different subtypes based on eleven CR-DEGs. **(A)** Hierarchical map of subtype analysis. **(B)** The chemokine score between the two subtypes. **(C)** Distribution of the eleven CR-DEGs in GSE47460 cohorts in subtype, sex, and smoking. **(D)** The pulmonary function parameters, dlco **(D)**, fev1 **(E)**, and fvc **(F)** in two subtypes. **(G)** Stromal score in two subtypes. **(H)** The proportion of 22 types of immune cells in two subtypes.

3.7 Validation of model gene expression in bleomycin induced-pulmonary fibrosis model

Bleomycin-induced murine pulmonary fibrosis is the most representative and commonly used experimental model for IPF studies (19). We further validated model gene expression in BLM-induced pulmonary fibrosis. We established a model of pulmonary fibrosis by intratracheal injection of bleomycin (2 U/kg). The mice were sacrificed on day 21, and lung tissues were harvested (Figure 9A). The lung index was significantly increased in mice treated with bleomycin (Figure 9B). Masson staining showed that bleomycin significantly increased collagen deposition (Figure 9C). The fibrosis marker genes *Col1a1*, *Acta2*, and *Fn1* were also significantly upregulated in bleomycin-induced mice (Figure 9D). These results suggest that the pulmonary fibrosis model was

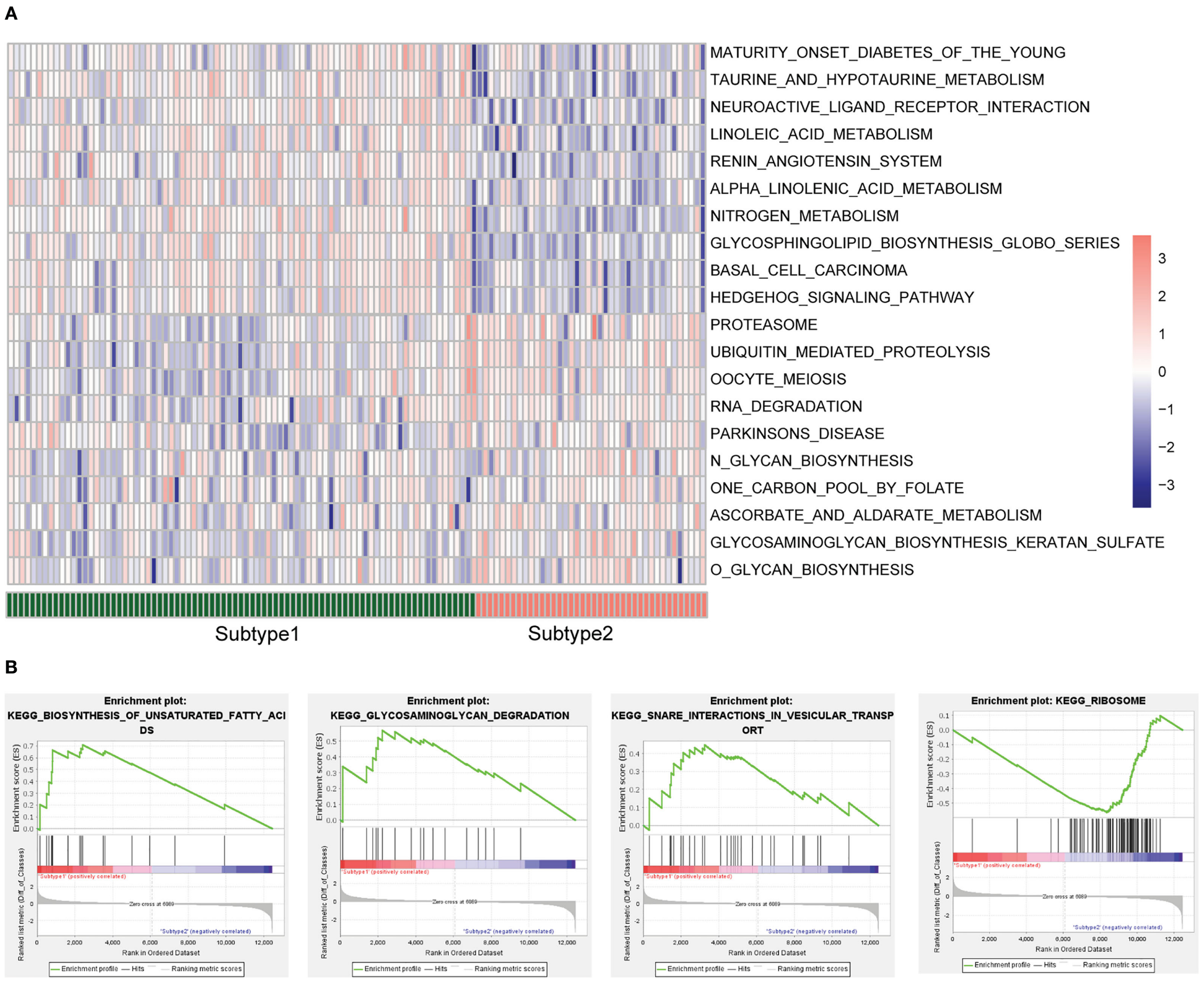

FIGURE 7
Enrichment analysis between the two subtypes. **(A)** GSVA enrichment analysis. **(B)** GSEA enrichment analysis.

successfully established. Next, validation of the model genes mRNA levels was validated using RT-qPCR. Primer sequences are listed in Table S2. The results demonstrated that Cxcl2 and Ccl2 (human homolog CCL13) expression were significantly increased in bleomycin-induced mice (Figures 9E, F). Meanwhile, Arrb1, Ccrl2, Grk5, and Ppbp levels were significantly reduced (Figures 9G–J). Cxcl13, Ccl11, Ccl19, Xcl1, and Cxcl5 (human homolog CXCL6) mRNA levels did not change between the two groups of mice (Figures 9K–O).

4 Discussion

Idiopathic pulmonary fibrosis is a chronic, progressive, and fatal disease characterized by alveolar epithelial injury, immune cell recruitment, and fibroblast activation despite the application of anti-fibrotic therapy. Accumulating evidence indicates that injured epithelial cells and abnormally activated macrophages secrete chemokines that induce fibroblast expansion and activation (6). Chemokine and chemokine receptor signals play a role in cell migration, activation, and response to lung injury repair, including IPF (8, 10, 20, 21). Antibodies that neutralize chemokines may contribute to treating IPF (8). In the lung tissues, many cells secrete chemokines or express chemokine receptors. The analysis of chemokines and receptors may be conducive to diagnosing and treating IPF, even when evaluating the prognosis of patients with IPF. Therefore, establishing a multi-gene diagnostic model for patients with IPF based on the chemokine system is necessary.

In the present study, 34 CR-DEGs were screened from the GSE47460 dataset, containing 112 IPF and 91 control samples. Eleven CR-DEGs signatures were identified using the LASSO regression model to construct a diagnosis IPF model. The diagnosis model easily distinguished between IPF and control samples, highlighting that the chemokine system differs between patients with IPF and control individuals. In addition, we explored the prognostic role of the eleven IPF genes in the GSE70866 dataset. The results suggest that ARRB1, CCRL2, CXCL2, CCL13, PPBP, and GRK5 are better factors for determining the prognosis of IPF. Furthermore, consensus clustering was used to classify patients with IPF into two subgroups based on the expression levels of eleven CR-DEGs. Finally, we evaluated the expression of eleven CR-DEGs in a

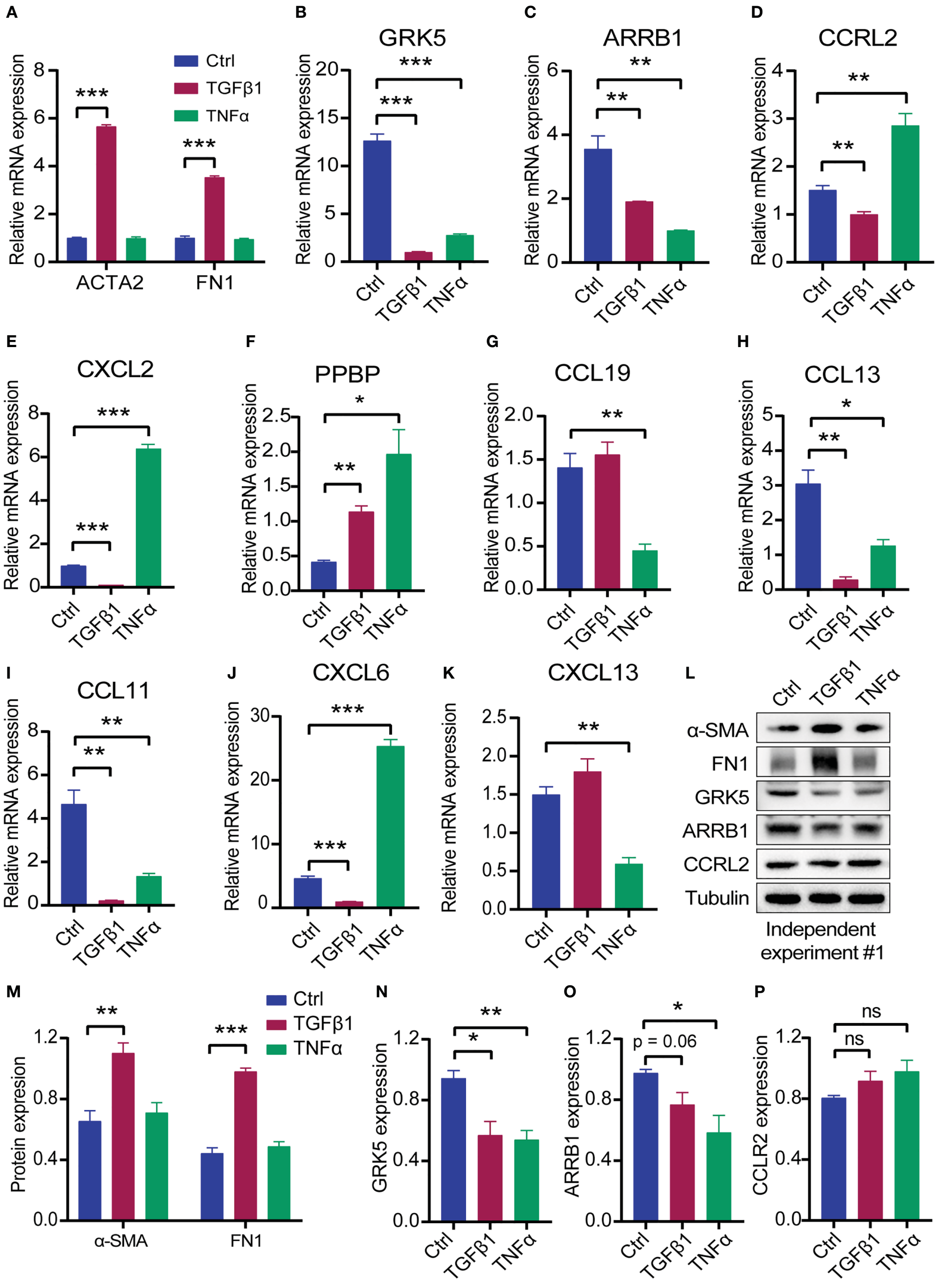

FIGURE 8
The expression of the eleven CR-DEGs in MRC-5 treated with TGFβ1 or TNFα for 24 h. **(A)** mRNA levels of ACTA2 and FN1 in control, TGFβ1, and TNFα group. **(B–K)** mRNA levels of CXCL2 **(B)**, CCRL2 **(C)**, ARRB1 **(D)**, GRK5 **(E)**, PPBP **(F)**, CCL19 **(G)**, CCL13 **(H)**, CCL11 **(I)**, CXCL6 **(J)**, and CXCL13 **(K)** in control, TGFβ1, and TNFα group, **(L)** Protein levels of α-SMA, FN1, GRK5, ARRB1, and CCRL2. **(M-P)** Quantitative analysis of α-SMA, FN1 **(M)**, GRK5 **(N)**, ARRB1 **(O)**, and CCRL2 **(P)**. Values were expressed as mean ± SEM, *p < 0.05, **p < 0.01, ***p < 0.001. t test was used. Ctrl, control; ns, not significant difference.

bleomycin-induced pulmonary fibrosis model and in TGFβ1-activated human lung fibroblasts. Although preclinical models of bleomycin-induced pulmonary fibrosis are the most commonly experimental models to investigate the mechanisms of pulmonary fibrosis, there are differences with IPF, such as recovery from bleomycin-induced pulmonary fibrosis. Consistent with the transcriptome data of IPF lung tissue, Arrb1, Ccrl2, and Grk5 mRNA levels are significantly reduced in a bleomycin-induced

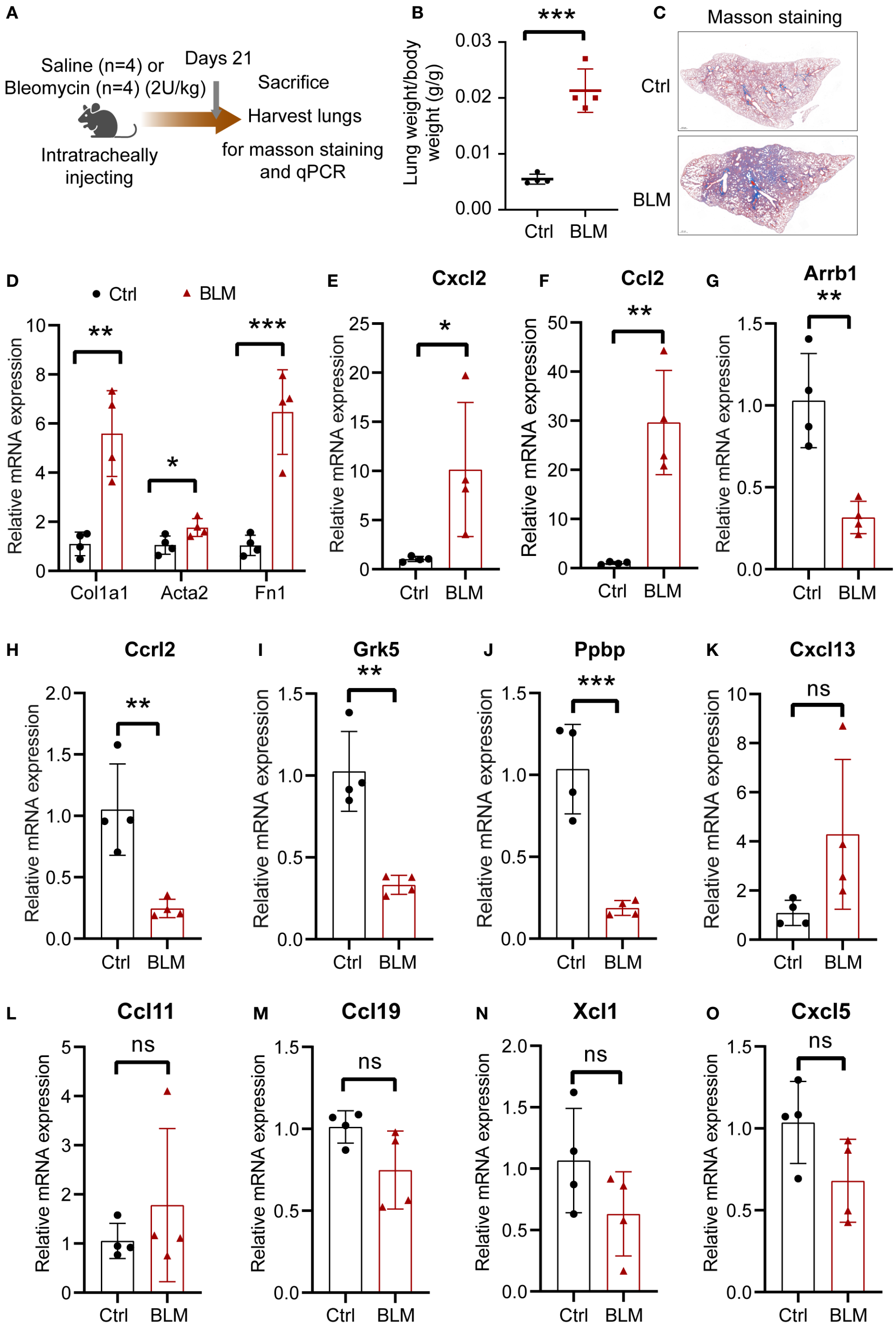

FIGURE 9
The expression of the eleven CR-DEGs in bleomycin-induced lung fibrosis. **(A)** Schematic diagram of bleomycin-induced lung fibrosis. **(B)** Lung index (lung weight/body weight). **(C)** Representative images of Masson's trichrome staining of the lung section. **(D)** mRNA levels of Col1a1, Acta2, and Fn1 in lung tissue. **(E-O)** mRNA levels of Cxcl2 **(E)**, Ccl2 **(F)**, Arrb1 **(G)**, Ccrl2 **(H)**, Grk5 **(I)**, Ppbp **(J)**, Cxcl13 **(K)**, Ccl11 **(L)**, Ccl19 **(M)**, Xcl1 **(N)**, and Cxcl5 **(O)** in control and bleomycin group.. Values were expressed as mean ± SD (n = 4), *p < 0.05, **p < 0.01, ***p < 0.001. t test was used. Ctrl, control; BLM, bleomycin; ns, not significant difference.

mouse model that should be investigated further. The lack of changes in Cxcl13, Ccl11, Ccl19, Xcl1, and Cxcl5 mRNA levels may be due to differences in bleomycin-induced pulmonary fibrosis and IPF, although models of bleomycin-induced pulmonary fibrosis are the most common experimental models for investigating IPF.

A previous study reported that PADI4, IGFBP7, and GADD45A serve as biomarkers for IPF, which may contribute to the diagnosis of IPF (22). This is the first study to establish and validate a diagnostic model using eleven chemokine-associated genes (CXCL2, CCRL2, ARRB1, XCL1, GRK5, PPBP, CCL19, CCL13, CCL11, CXCL6, and CXCL13). Among the eleven CR-DEGs, some have been studied in lung injury. CXCL2 is significantly upregulated in mouse lung tissue in a bleomycin-induced model of pulmonary fibrosis, and 5-azacytidine (a DNA methyltransferase inhibitor) reduces CXCL2 expression (23). The neutralization of CXCL2 reduced hydroxyproline in the lung tissue of bleomycin-induced mice, but did not reduce lung neutrophil infiltration. Interestingly, stimulation with CXCL2 did not promote the proliferation of lung fibroblasts or collagen expression (20). In our study, CXCL2 expression levels were inversely correlated with lung function parameters. High expression of CXCL2 in alveolar lavage fluid cells from patients with IPF suggests a poor prognosis. Interestingly, CXCL2 expression is reduced in IPF lung tissue, possibly due to different extents across cell types.

CCRL2 is a seven-transmembrane protein expressed in epithelial cells, endothelial cells, and a variety of leukocytes. CCRL2 is upregulated under inflammatory conditions and recruits CXCR2-mediated neutrophils at sites of inflammation (24). Additional studies have demonstrated that CCRL2 deficiency worsens obesity and insulin resistance by increasing macrophage infiltration into adipose tissue (25). CCRL2 was downregulated in IPF samples, bleomycin-induced pulmonary fibrosis, and TGFβ1-induced fibroblast. ARRB1, initially thought to be a negative regulator of G-protein-coupled receptor signaling, has been shown to regulate cellular functions and is involved in various physiological processes, including inflammation, immune responses, and tumorigenesis (26, 27).

Deletion of Arrb1 significantly inhibited autophagy and induced neuronal apoptosis and necrosis in a model of cerebral ischemia (28). Autophagy is a highly conserved intracellular process involved in cellular degradation and recycling that has been found to delay the pathological progression of IPF (29). XCL1 and its receptor (XCR1) are significant regulators of dendritic and T-cell immune responses. For example, T cell-derived XCL1 contributes to intestinal XCR1$^+$ DC activation and migration (30). Mice deficient in XCL1 or XCR1 have attenuated CD8$^+$ T-cell responses and lack the ability to generate regulatory T cells. However, the role of XCL1-mediated immune responses in IPF has not been previously reported.

GRK5 has been reported to be highly expressed in the cardiac fibroblast. Nuclear translocation of GRK5 results in fibroblast activation. Fibroblast-specific deletion of GRK5 attenuates myocardial fibrosis and hypertrophy after chronic Ang II infusion or ischemic injury (31). GRK5 expression was significantly reduced in fibroblasts from the IPF cohort and TGFβ1-treated fibroblasts. Thus, the role of RGK5 in IPF pathogenesis warrants further investigation. PPBP, also known as CXCL7, is expressed by multiple cells, including platelets, neutrophils, natural killer cells, lymphocytes, and megakaryocytes (32). It has been found that CXCL7 regulates various processes, including glucose metabolism, mitogenesis, extracellular matrix and plasminogen activator synthesis (33). Proteomic analysis of serum extracellular vesicles showed that PPBP could represent a potential biomarker of liver fibrosis in patients with chronic hepatitis C (34). Recent evidence suggests that PPBP is upregulated in the serum of COVID-19 patients compared to influenza and serves as a potential biomarker for the severity of COVID-19 (35). The role of increased PPBP in IPF pathogenesis remains to be determined.

Our findings were consistent with those previously reported. CCL19 has been reported to be highly expressed in the lung tissue of patients with IPF, which facilitates the recruitment and accumulation of dendritic cells to fibrotic lung and sustains chronic inflammation, driving IPF development (36). Plasma CCL13 and CXCL13 are prognostic markers of IPF, and a higher concentration of CXCL13 is associated with higher all-cause mortality (37). CXCL6 has been reported to be upregulated in IPF-derived BAL. CXCL6 mRNA levels significantly increased on day 1 after bleomycin treatment, and then gradually decreased to normal levels. The inflammatory response induced by CXCL6 promoted the progression of pulmonary fibrosis. CXCL6 antibody neutralization attenuates early lung inflammation and prevents pulmonary fibrosis after bleomycin administration (38). Taken together, our findings support the ongoing assessment of the prognostic potential of chemokines as biomarkers in future IPF trials.

Increasing evidence suggests that immune cells are involved in the pathogenesis of IPF (39–42). Immune cells produce chemokines and cytokines that regulate fibroblast phenotypes. Alveolar macrophages and CD4$^+$ T cells secrete CCL1, which promotes the differentiation of lung fibroblasts into myofibroblasts and contributes to pulmonary fibrosis (8). High levels of CD138 plasma cells have been demonstrated in the lung tissues of IPF patients and in mouse models of bleomycin-induced pulmonary fibrosis. Treatment of mice with bortezomib resulted in the depletion of plasma cells, which attenuated the development of bleomycin-induced pulmonary fibrosis, suggesting that plasma cells are essential effector cells in the pathogenesis of pulmonary fibrosis (43). In the current study, we also observed higher levels of plasma and macrophages (M0 and M2) in the IPF cohort than in the control cohort. Subtype analysis showed a decrease in dlco, fev1, and fvc in subtype 2, which indicated that patients with subtype 2 had more severe disease. Immune cell infiltration revealed increased levels of plasma cells and M0 macrophages in subtype 2 tumors. Further research is required to determine the exact mechanism by which plasma cells and macrophages promote IPF progression.

Despite this, several limitations of this study still exist. First, lung tissue specimens from patients with IPF were not available to validate the analysis, despite using a bleomycin-induced lung fibrosis model and a TGFβ1-induced cell model. Second, not only do the mRNA levels of hub genes need to be verified, but the expression levels of these genes also need to be confirmed to further understand the molecular mechanisms of IPF. Third, to gain a comprehensive understanding of the nature of chemokines and their receptors in IPF, especially their unique roles in different cell types, further functional and mechanistic investigations are necessary to determine the potential role of chemokine-associated genes in IPF pathogenesis.

In conclusion, our study established and validated a chemokine system-related eleven-gene signature in a diagnostic model for IPF. The model could serve as a diagnostic biomarker and contribute to a better understanding of the role of chemokines in IPF pathogenesis. Moreover, we validated hub gene expression levels by RT-qPCR in bleomycin-induced pulmonary fibrosis and a TGFβ1-induced cell model. Further studies are required to clarify these findings.

Data availability statement

The original contributions presented in the study are included in the article/Supplementary Material. Further inquiries can be directed to the corresponding author.

Ethics statement

The animal study was reviewed and approved by Ethics Committee of China Three Gorges University (Approval No. 2022B100A).

Author contributions

TZ developed the concept and designed this study. TZ and XW carried out the data analysis. TZ, XW, and XZ contributed to animal and cell experiment. TZ, KY, XL and JN wrote and edited the manuscript. All authors contribute to the article and approved the submitted version.

Funding

This work has been supported by Natural Science Foundation of Hubei Province (2019CFB745), Health Commission of Hubei Province scientific research project (WJ2021M067).

Acknowledgments

We sincerely thank the researchers who created and maintained GEO data.

Conflict of interest

The authors declare that the research was conducted in the absence of any commercial or financial relationships that could be construed as a potential conflict of interest.

Publisher's note

Supplementary material

The Supplementary Material for this article can be found online at: https://www.frontiersin.org/articles/10.3389/fimmu.2023.1159856/full#supplementary-material

SUPPLEMENTARY FIGURE 1
PPI network of CR-DEGs using the STING database.

SUPPLEMENTARY FIGURE 2
GO and KEGG enrichment analysis of CR-DEGs. **(A)** GO enrichment analysis of CR-DEGs, including BP. **(B)** KEGG enrichment analysis of CR-DEGs.

SUPPLEMENTARY FIGURE 3
Independent experiments of treatment of MRC-5 with TGFβ1 or TNFα for 24 h.

References

1. Martinez FJ, Collard HR, Pardo A, Raghu G, Richeldi L, Selman M, et al. Idiopathic pulmonary fibrosis. *Nat Rev Dis Primers* (2017) 3:17074. doi: 10.1038/nrdp.2017.74

2. Henderson NC, Rieder F, Wynn TA. Fibrosis: From mechanisms to medicines. *Nature* (2020) 587(7835):555–66. doi: 10.1038/s41586-020-2938-9

3. Maher TM, Bendstrup E, Dron L, Langley J, Smith G, Khalid JM, et al. Global incidence and prevalence of idiopathic pulmonary fibrosis. *Respir Res* (2021) 22(1):197. doi: 10.1186/s12931-021-01791-z

4. Li R, Jia Y, Kong X, Nie Y, Deng Y, Liu Y. Novel drug delivery systems and disease models for pulmonary fibrosis. *J Controlled release Off J Controlled Release Soc* (2022) 348:95–114. doi: 10.1016/j.jconrel.2022.05.039

5. Richeldi L, du Bois RM, Raghu G, Azuma A, Brown KK, Costabel U, et al. Efficacy and safety of nintedanib in idiopathic pulmonary fibrosis. *New Engl J Med* (2014) 370 (22):2071–82. doi: 10.1056/NEJMoa1402584

6. Moss BJ, Ryter SW, Rosas IO. Pathogenic mechanisms underlying idiopathic pulmonary fibrosis. *Annu Rev Pathol* (2022) 17:515–46. doi: 10.1146/annurev-pathol-042320-030240

7. Strieter RM, Gomperts BN, Keane MP. The role of cxc chemokines in pulmonary fibrosis. *J Clin Invest* (2007) 117(3):549–56. doi: 10.1172/jci30562

8. Liu SS, Liu C, Lv XX, Cui B, Yan J, Li YX, et al. The chemokine Ccl1 triggers an amfr-Spry1 pathway that promotes differentiation of lung fibroblasts into myofibroblasts and drives pulmonary fibrosis. *Immunity* (2021) 54(9):2042–56.e8. doi: 10.1016/j.immuni.2021.06.008

9. Affandi AJ, Carvalheiro T, Ottria A, de Haan JJ, Brans MAD, Brandt MM, et al. Cxcl4 drives fibrosis by promoting several key cellular and molecular processes. *Cell Rep* (2022) 38(1):110189. doi: 10.1016/j.celrep.2021.110189

10. Yang J, Agarwal M, Ling S, Teitz-Tennenbaum S, Zemans RL, Osterholzer JJ, et al. Diverse injury pathways induce alveolar epithelial cell Ccl2/12, which promotes lung fibrosis. *Am J Respir Cell Mol Biol* (2020) 62(5):622–32. doi: 10.1165/rcmb.2019-0297OC

11. Prasse A, Pechkovsky DV, Toews GB, Jungraithmayr W, Kollert F, Goldmann T, et al. A vicious circle of alveolar macrophages and fibroblasts perpetuates pulmonary fibrosis *Via* Ccl18. *Am J Respir Crit Care Med* (2006) 173(7):781–92. doi: 10.1164/rccm.200509-1518OC

12. Cai M, Bonella F, He X, Sixt SU, Sarria R, Guzman J, et al. Ccl18 in serum, bal fluid and alveolar macrophage culture supernatant in interstitial lung diseases. *Respir Med* (2013) 107(9):1444–52. doi: 10.1016/j.rmed.2013.06.004

13. Prasse A, Probst C, Bargagli E, Zissel G, Toews GB, Flaherty KR, et al. Serum cc-chemokine ligand 18 concentration predicts outcome in idiopathic pulmonary fibrosis. *Am J Respir Crit Care Med* (2009) 179(8):717–23. doi: 10.1164/rccm.200808-1201OC

14. Barrett T, Wilhite SE, Ledoux P, Evangelista C, Kim IF, Tomashevsky M, et al. Ncbi geo: Archive for functional genomics data sets–update. *Nucleic Acids Res* (2013) 41(Database issue):D991–5. doi: 10.1093/nar/gks1193

15. Shannon P, Markiel A, Ozier O, Baliga NS, Wang JT, Ramage D, et al. Cytoscape: A software environment for integrated models of biomolecular interaction networks. *Genome Res* (2003) 13(11):2498–504. doi: 10.1101/gr.1239303

16. Yu G, Wang LG, Han Y, He QY. Clusterprofiler: An r package for comparing biological themes among gene clusters. *Omics J Integr Biol* (2012) 16(5):284–7. doi: 10.1089/omi.2011.0118

17. Frangogiannis N. Transforming growth factor-B in tissue fibrosis. *J Exp Med* (2020) 217(3):e20190103. doi: 10.1084/jem.20190103

18. Zhang C, Wu Z, Li JW, Tan K, Yang W, Zhao H, et al. Discharge may not be the end of treatment: Pay attention to pulmonary fibrosis caused by severe covid-19. *J Med Virol* (2021) 93(3):1378–86. doi: 10.1002/jmv.26634

19. D'Alessandro-Gabazza CN, Yasuma T, Kobayashi T, Toda M, Abdel-Hamid AM, Fujimoto H, et al. Inhibition of lung microbiota-derived proapoptotic peptides ameliorates acute exacerbation of pulmonary fibrosis. *Nat Commun* (2022) 13(1):1558. doi: 10.1038/s41467-022-29064-3

20. Keane MP, Belperio JA, Moore TA, Moore BB, Arenberg DA, Smith RE, et al. Neutralization of the cxc chemokine, macrophage inflammatory protein-2, attenuates bleomycin-induced pulmonary fibrosis. *J Immunol (Baltimore Md 1950)* (1999) 162 (9):5511–8. doi: 10.4049/jimmunol.162.9.5511

21. Ma Z, Ma C, Zhang Q, Bai Y, Mu K, Liu X, et al. Role of Cxcl16 in blm-induced epithelial-mesenchymal transition in human A549 cells. *Respir Res* (2021) 22(1):42. doi: 10.1186/s12931-021-01646-7

22. Li K, Liu P, Zhang W, Liu X, Tanino Y, Koga Y, et al. Bioinformatic identification and analysis of immune-related chromatin regulatory genes as potential biomarkers in idiopathic pulmonary fibrosis. *Ann Trans Med* (2022) 10 (16):896. doi: 10.21037/atm-22-3700

23. Lu CH, Chen CM, Ma J, Wu CJ, Chen LC, Kuo ML. DNA Methyltransferase inhibitor alleviates bleomycin-induced pulmonary inflammation. *Int Immunopharmacol* (2020) 84:106542. doi: 10.1016/j.intimp.2020.106542

24. Del Prete A, Martínez-Muñoz L, Mazzon C, Toffali L, Sozio F, Za L, et al. The atypical receptor Ccrl2 is required for Cxcr2-dependent neutrophil recruitment and tissue damage. *Blood* (2017) 130(10):1223–34. doi: 10.1182/blood-2017-04-777680

25. Xu M, Wang YM, Li WQ, Huang CL, Li J, Xie WH, et al. Ccrl2 deficiency deteriorates obesity and insulin resistance through increasing adipose tissue macrophages infiltration. *Genes Dis* (2022) 9(2):429–42. doi: 10.1016/j.gendis.2020.08.009

26. DeWire SM, Ahn S, Lefkowitz RJ, Shenoy SK. Beta-arrestins and cell signaling. *Annu Rev Physiol* (2007) 69:483–510. doi: 10.1146/annurev.physiol.69.022405.154749

27. Lei Y, Xu X, Liu H, Chen L, Zhou H, Jiang J, et al. Hbx induces hepatocellular carcinogenesis through Arrb1-mediated autophagy to drive the G(1)/S cycle. *Autophagy* (2021) 17(12):4423–41. doi: 10.1080/15548627.2021.1917948

28. Wang P, Xu TY, Wei K, Guan YF, Wang X, Xu H, et al. Arrb1/B-Arrestin-1 mediates neuroprotection through coordination of Becn1-dependent autophagy in cerebral ischemia. *Autophagy* (2014) 10(9):1535–48. doi: 10.4161/auto.29203

29. Yue YL, Zhang MY, Liu JY, Fang LJ, Qu YQ. The role of autophagy in idiopathic pulmonary fibrosis: From mechanisms to therapies. *Ther Adv Respir Dis* (2022) 16:17534666221140972. doi: 10.1177/17534666221140972

30. Ohta T, Sugiyama M, Hemmi H, Yamazaki C, Okura S, Sasaki I, et al. Crucial roles of Xcr1-expressing dendritic cells and the Xcr1-Xcl1 chemokine axis in intestinal immune homeostasis. *Sci Rep* (2016) 6:23505. doi: 10.1038/srep23505

31. Eguchi A, Coleman R, Gresham K, Gao E, Ibetti J, Chuprun JK, et al. Grk5 is a regulator of fibroblast activation and cardiac fibrosis. *Proc Natl Acad Sci USA* (2021) 118(5):e2012854118. doi: 10.1073/pnas.2012854118

32. Wu Q, Tu H, Li J. Multifaceted roles of chemokine c-X-C motif ligand 7 in inflammatory diseases and cancer. *Front Pharmacol* (2022) 13:914730. doi: 10.3389/fphar.2022.914730

33. Hristov M, Zernecke A, Bidzhekov K, Liehn EA, Shagdarsuren E, Ludwig A, et al. Importance of cxc chemokine receptor 2 in the homing of human peripheral blood endothelial progenitor cells to sites of arterial injury. *Circ Res* (2007) 100(4):590–7. doi: 10.1161/01.res.0000259043.42571.68

34. Shirai K, Hikita H, Sakane S, Narumi R, Adachi J, Doi A, et al. Serum amyloid p component and pro-platelet basic protein in extracellular vesicles or serum are novel markers of liver fibrosis in chronic hepatitis c patients. *PloS One* (2022) 17(7):e0271020. doi: 10.1371/journal.pone.0271020

35. Wismans LV, Lopuhaä B, de Koning W, Moeniralam H, van Oosterhout M, Ambarus C, et al. Increase of mast cells in covid-19 pneumonia may contribute to pulmonary fibrosis and thrombosis. *Histopathology* (2023) 82(3):407–19. doi: 10.1111/his.14838

36. Marchal-Sommé J, Uzunhan Y, Marchand-Adam S, Kambouchner M, Valeyre D, Crestani B, et al. Dendritic cells accumulate in human fibrotic interstitial lung disease. *Am J Respir Crit Care Med* (2007) 176(10):1007–14. doi: 10.1164/rccm.200609-1347OC

37. Neighbors M, Cabanski CR, Ramalingam TR, Sheng XR, Tew GW, Gu C, et al. Prognostic and predictive biomarkers for patients with idiopathic pulmonary fibrosis treated with pirfenidone: Post-hoc assessment of the capacity and ascend trials. *Lancet Respir Med* (2018) 6(8):615–26. doi: 10.1016/s2213-2600(18)30185-1

38. Besnard AG, Struyf S, Guabiraba R, Fauconnier L, Rouxel N, Proost P, et al. Cxcl6 antibody neutralization prevents lung inflammation and fibrosis in mice in the bleomycin model. *J Leukocyte Biol* (2013) 94(6):1317–23. doi: 10.1189/jlb.0313140

39. Heukels P, Moor CC, von der Thüsen JH, Wijsenbeek MS, Kool M. Inflammation and immunity in ipf pathogenesis and treatment. *Respir Med* (2019) 147:79–91. doi: 10.1016/j.rmed.2018.12.015

40. She YX, Yu QY, Tang XX. Role of interleukins in the pathogenesis of pulmonary fibrosis. *Cell Death Discov* (2021) 7(1):52. doi: 10.1038/s41420-021-00437-9

41. Fraser E, Denney L, Antanaviciute A, Blirando K, Vuppusetty C, Zheng Y, et al. Multi-modal characterization of monocytes in idiopathic pulmonary fibrosis reveals a primed type I interferon immune phenotype. *Front Immunol* (2021) 12:623430. doi: 10.3389/fimmu.2021.623430

42. Serezani APM, Pascoalino BD, Bazzano JMR, Vowell KN, Tanjore H, Taylor CJ, et al. Multiplatform single-cell analysis identifies immune cell types enhanced in pulmonary fibrosis. *Am J Respir Cell Mol Biol* (2022) 67(1):50–60. doi: 10.1165/rcmb.2021-0418OC

43. Prêle CM, Miles T, Pearce DR, O'Donoghue RJ, Grainge C, Barrett L, et al. Plasma cell but not Cd20-mediated b-cell depletion protects from bleomycin-induced lung fibrosis. *Eur Respir J* (2022) 60(5):2101469. doi: 10.1183/13993003.01469-2021

Frontiers in Immunology

TYPE Original Research
PUBLISHED 17 May 2023
DOI 10.3389/fimmu.2023.1171445

OPEN ACCESS

EDITED BY
Chunheng Mo,
Sichuan University, China

REVIEWED BY
Jian Yang,
Sichuan University, China
Hong Wang,
Hebei University of Chinese Medicine,
China
Xiuli Zhang,
Nathan Kline Institute for Psychiatric
Research, United States
Xiaoyu Su,
University of Chicago Medicine,
United States

*CORRESPONDENCE
Ting Cai
✉ caiting@ucas.ac.cn
Ruitian Liu
✉ rtliu@ipe.ac.cn

†These authors have contributed equally to this work

RECEIVED 22 February 2023
ACCEPTED 05 May 2023
PUBLISHED 17 May 2023

CITATION
Shi X, Pan Z, Cai W, Zhang Y, Duo J, Liu R and Cai T (2023) Identification and immunological characterization of cuproptosis-related molecular clusters in idiopathic pulmonary fibrosis disease. *Front. Immunol.* 14:1171445. doi: 10.3389/fimmu.2023.1171445

Identification and immunological characterization of cuproptosis-related molecular clusters in idiopathic pulmonary fibrosis disease

Xuefeng Shi[1,2,3†], Zhilei Pan[2†], Weixiu Cai[2], Yuhao Zhang[4], Jie Duo[2], Ruitian Liu[3*] and Ting Cai[1*]

[1]Department of Experimental Medical Science, Ningbo No.2 Hospital, Ningbo, China, [2]Department of Pulmonary and Critial Care medicine, Qinghai provincial people's hospital, Xining, China, [3]State Key Laboratory of Biochemical Engineering, Institute of Process Engineering, Chinese Academy of Sciences, Beijing, China, [4]Cancer Center, Department of Neurosurgery, Zhejiang Provincial People's Hospital, Affiliated People's Hospital, Hangzhou Medical College, Hangzhou, China

Background: Idiopathic pulmonary fibrosis (IPF) has attracted considerable attention worldwide and is challenging to diagnose. Cuproptosis is a new form of cell death that seems to be associated with various diseases. However, whether cuproptosis-related genes (CRGs) play a role in regulating IPF disease is unknown. This study aims to analyze the effect of CRGs on the progression of IPF and identify possible biomarkers.

Methods: Based on the GSE38958 dataset, we systematically evaluated the differentially expressed CRGs and immune characteristics of IPF disease. We then explored the cuproptosis-related molecular clusters, the related immune cell infiltration, and the biological characteristics analysis. Subsequently, a weighted gene co-expression network analysis (WGCNA) was performed to identify cluster-specific differentially expressed genes. Lastly, the eXtreme Gradient Boosting (XGB) machine-learning model was chosen for the analysis of prediction and external datasets validated the predictive efficiency.

Results: Nine differentially expressed CRGs were identified between healthy and IPF patients. IPF patients showed higher monocytes and monophages M0 infiltration and lower naive B cells and memory resting T CD4 cells infiltration than healthy individuals. A positive relationship was found between activated dendritic cells and CRGs of LIPT1, LIAS, GLS, and DBT. We also identified cuproptosis subtypes in IPF patients. Go and KEGG pathways analysis demonstrated that cluster-specific differentially expressed genes in Cluster 2 were closely related to monocyte aggregation, ubiquitin ligase complex, and ubiquitin-mediated proteolysis, among others. We also constructed an XGB machine model to diagnose IPF, presenting the best performance with a relatively lower residual and higher area under the curve (AUC= 0.700) and validated by external validation datasets (GSE33566, AUC = 0.700). The analysis of the nomogram model demonstrated that XKR6, MLLT3, CD40LG, and HK3 might be used to diagnose IPF disease. Further analysis revealed that CD40LG was significantly associated with IPF.

Conclusion: Our study systematically illustrated the complicated relationship between cuproptosis and IPF disease, and constructed an effective model for the diagnosis of IPF disease patients.

KEYWORDS

idiopathic pulmonary fibrosis disease, cuproptosis, machine learning, immune infiltration, molecular clusters

1 Introduction

IPF is among the most severe form of interstitial pneumonia, characterized by chronic and progressive lung scars and usual interstitial pneumonia (1). IPF has a poor prognosis, with a median life expectancy of only 2-3 years from diagnosis (2). Epidemiological studies of North America, the US, and Europe demonstrated that the number of IPF patients increased, placing a growing economic burden on global health care (1). Currently, the primary drugs used to treat IPF are pirfenidone and nidanib. Nevertheless, there are some limitations in preventing disease progression and improving the quality of life of patients because of the treatment efficacy of Individual differences, and side effects (gastrointestinal intolerance, skin reactions and diarrhea) caused by the Nintedanib and Prefenidone (3). IPF is the result of various mechanisms. Alveolar epithelial injury and infiltration of inflammatory cells, such as neutrophils, macrophages, and lymphocytes, are the primary causes of the destruction of lung tissue structure, alveolar atrophy and collapse, and regression of pulmonary vessels (4). The accumulation of extracellular matrix in lung tissue leads to fibroblast foci and collagen fiber reconstruction (5). In addition, the development of IPF is favored by the interaction of epithelial-mesenchymal transition (EMT), interleukin, TGF-β, and oxidative stress.

Cuproptosis, a novel unique non-apoptotic programmed cell death, targets and leads the aggregation of fatty acylated components and the loss of Fe-S cluster-containing proteins, causing proteotoxic stress and cell death (6). At present, more articles reveled the cuproptosis-related genes (CRGs) as a bio-marker play an important role in the development of disease, such as stomach adenocarcinoma (STAD), hepatocellular carcinoma (HCC) and head and neck squamous carcinoma (HNSC) (7–9). Furthermore, copper is essential for all living organisms and serves as a catalyst, antioxidant defense, autophagy, and even arouses immune activation (10). Notably, copper homeostasis strongly correlates with the concentration of T cells, neutrophils, and macrophages (11). In the development of pulmonary fibrosis, H2O2 was increased in alveolar macrophages due to the translocation of Cu and Zn-SOD to the mitochondrial intermembrane space (12). In addition, NLRP3, a cuproptosis gene, was involved in TGF-β and EMT signaling pathways and promoted fibrosis progression (13, 14). Therefore, we hypothesize that cuproptosis-related genes (CRGs) may play a role in developing IPF. This study investigated the underlying mechanism and immune cell infiltration on IPF and analyzed the effect of CRGs on IPF. In this study, the underlying mechanism and immune cell infiltration of IPF was investigated, and the effect of CRGs on IPF was analyzed.

2 Materials and methods

2.1 Raw data acquisition and processing

Three datasets (GSE38958, GSE28042, and GSE33566) were downloaded from the database of the website GEO (GEO, www.ncbi.nlm.nih.gov/geo). Database GSE38958 (platform GPL5175), which includes 45 healthy and 70 IPF blood samples, was selected to analyze the relationship between CRGs and IPF and construct the machine learning model to diagnose IPF. Datasets GSE28042 (GPL6480 platform) (containing 19 healthy and 75 IPF blood samples) and GSE33566 (GPL6480) (containing 30 healthy and 93 IPF blood samples) were used for the validation of the IPF prediction model and following analysis. The three datasets were processed with limma package and normalized using the normalizeBetweenArrays method.

2.2 CRGs difference expression and correlation analysis

According to Peter Tsvetkov's report (6), 19 cuprotosis-related genes were reported and analyzed, including NFE2L2, NLRP3, ATP7B, ATP7A, SLC31A1, FDX1, LIAS, LIPT1, LIPT2, DLD, DLAT, PDHA1, PDHB, MTF1, GLS, CDKN2A, DBT, GCSH, and DLST. These genes were selected for analysis of CRGs expression in the blood of 45 healthy and 70 IPF patients. The differentially expressed cuprotosis-related genes was analyzed by the wilcox.test, and p-values < 0.05 was considered to be significantly different. The heatmap and boxplot were exhibited using R packages heatmap and ggpubr. Then, the conspicuous expression of CRGs in IPF was selected for correlation analysis. The results were exhibited using the R packages corrplot (version 0.92) and circlize (15). *P*-values below 0.05 represented a significant correlation.

2.3 Relationship between cuproptosis-related genes expression and immunity

CIBERSORT R package (16) and LM22 signature matrix were applied to esimate the relative abundance of 22 types of immune cells infiltrated in IPF patients. Correlations between CRGs and immune cells infiltration level in IPF were performed using the R packages tidyverse (17), ggplot2 (18), and reshape2. The sum of the 22 immune cells proportions in each sample was 1 (16), and $p < 0.05$ represented a significant correlation.

2.4 IPF patients classification analysis

The R package ConsensusClusterPlus (19) and the k-means algorithm with 1,000 iterations were applied to classify 70 IPF samples into different clusters based on the differentially expressed CRGs profile acquired from 2.2. The maximum subtype k was 9 and the optimal clusters numeber was comprehensively evaluated based on the result of the cumulative distribution function (CDF) curve, consensus matrix and consistent cluster score (> 0.9).

2.5 Gene set variation analysis

GSVA, a non-parametric unsupervised analytical method, is mainly used to evaluate the results of gene enrichment by R packages limma, GSEABase, and GSVA. We downloaded “c2.cp.kegg.v7.4.symbols” and “c5.go.bp.v7.5.1.symbols” from the MSigDB website database. Finally, the top 10 GO and KEGG pathways were selected for statistical analysis and ridge mapping. The absolute value of t value of GSVA score more than 2 was considered as significantly altered.

2.6 Weighted gene co-expression network analysis analysis

Co-expression modules were identified by the R package WGCNA (20). The top 25% of genes with the highest variance were used for subsequent WGCNA analysis. We then constructed an adjacency matrix with the optimal soft power value and converted it into a topological overlap matrix (TOM). Based on the hierarchical clustering tree algorithm, the modules were determined using the TOM dissimilarity measure (1-TOM) and the minimum module size was set to 100. Each module was assigned a random color. Module eigengene represented the gene expression profiles in one module. The correlation between genes, clinical phenotype, modules, and disease status were also identified. The modular significance showed the relationship between modules and disease status. Gene significance was described as the correlation between a gene with the clinical phenotype.

2.7 Construction and verification of multiple machine learning model

Four machine-learning models: Support Vector Machines (SVM), XGB, generalized linear model (GLM), and Random Forest (RF) models were built by the R package caret, and all the models worked with default parameters and assessed *via* 5-fold cross-validation. Data were randomly divided into a training set (70%, N=81) and a test set (30%, N=35). Interpretive analysis of the 4 models was performed by the DALEX package (21), and then the cumulative residual distribution map and boxplot distribution map of these machine-learning models were visualized. The ROC curves were obtained and visualized using the pROC R package. Next, the optimal learning model was determined, and the top 4 key genes were selected as the predictive genes related to the IPF. Subsequently, the ability of the predictive model was validated with GSE33566 using the ROC analysis. In addition, we performed the correlation between four key genes and TGF-β and constructed a gene-gene interaction network by the GeneMANIA website for key genes (http://www.genemania.org). R package rms was used to build a nomogram model, and the predictive power of the nomogram model was tested by the calibration curve and decision curve analysis (DCA).

2.8 The analysis of clinical features

To determine the relationship between key genes and clinical indicators associated with IPF, including age, diffusing capacity of the lung for carbon monoxide (DLCO), and FVC, the spearman correlation analysis was performed to explore the correlations. R packages ggplot2, ggpubr (version 0.4.0), and ggExtra (version 0.10.0) were used to draw the scatter plot. $P < 0.05$ represented a significant correlation and R represented a correlation coefficient.

3 Results

3.1 CRGs expression and immune activation in IPF

We systematically analyzed the differentially expressed curproptosis genes between healthy and IPF patients using the GSE38958 database. There were 9 CRGs with significant differences in IPF patients including, NLRP3, ATP7B, ATP7A, SLC31A1, FDX1, LIAS, LIPT1, DLAT, GLS, CDKN2A, and DBT. Among them, 3 CRGs in IPF samples were higher than that in healthy subjects, including NLRP3, SLC31A1, and CDKN2A, while others exhibited a lower expression, especially GLS (Figures 1A, B). The location of 9 CRGs on chromosomes is shown in Figure 1C. We also performed the correlation analysis among the 9 CRGs to examine whether these genes play an essential functional role in the

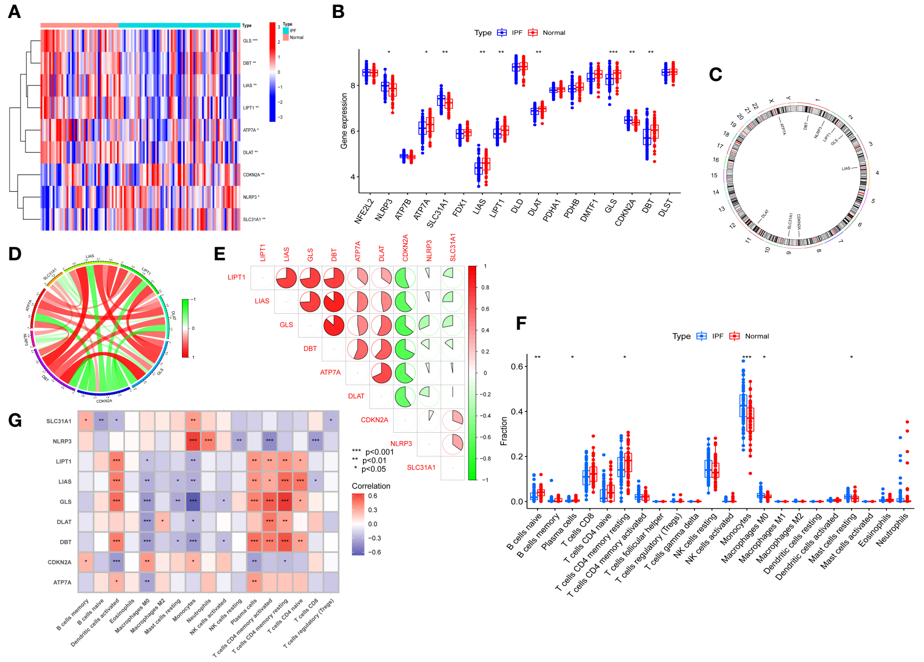

FIGURE 1

CRGs expression and immune cells infiltration in IPF. **(A)** Significantly differential expressed CRGs between normal individuals and IPF patients -Heatmap. **(B)** The CRGs expression between Normal group and IPF group. **(C)** The location of 9 CRGs on chromosomes. **(D)** Correlation of differentially expressed CRGs - Cyclograph. **(E)** Correlation of differentially expressed CRGs, red and green represent positive correlation and negative correlation, respectively-Pie chart. **(F)** The relative percent of immune cells in Normal and IPF groups. **(G)** The differentially expressed CRGs expression in immune cells. *p< 0.05, **p< 0.01, ***p< 0.001.

progression of IPF. The results showed an apparent synergistic effect among the LIPT1, LIAS, GLS, DBT, ATP7A, and DLAT, and the most robust antagonistic effect was found between CDKN2A and LIPT1, LIAS, GLS, DBT, ATP7A and DLAT (Figure 1E). The Cyclograph was constructed to detect further the relationships of the differentially expressed CRGs (Figure 1D).

We estimated the relative percent of 22 types of immune cells in healthy and IPF patients to find immune cell infiltration differences. The boxplot results revealed that IPF patients had higher immune cell infiltration of Monocytes and Monophages M0 than healthy subjects but lower naive B cells and memory resting T cells CD4 infiltration (Figure 1F). Meanwhile, we also examined the correlation between CRGs and immune infiltration. The results showed a strong positive relationship between activated dendritic cells and LIPT1, LIAS, GLS, and DBT. In addition, these four genes also showed a positive relationship with plasma cells, memory activated and resting T Cells CD4, and naive T cells CD4. However, a negative relationship was found between the macrophages M0 and LIPT1, LIAS, GLS, DLAT, DBT, and ATP7A. The monocytes displayed the most robust positive relationship with NLRP3 and a negative relationship with GLS (Figure 1G).

3.2 Identification of cuproptosis related IPF subtypes

To elucidate the cuproptosis-related expression patterns in IPF, we classified 70 IPF samples based on differentially expressed CRGs. The cluster numbers were most stable when the k value was set to two (k = 2). Moreover, the CDF curves fluctuated within a minimum range at a consensus index of 0.2 to 0.8 (Figures 2A, E). When k = 2 to 9, the area under the CDF curves exhibited the difference between the two CDF curves (k and k-1) (Figure 2D). Furthermore, the consistency score of each subtype was >0.9 only when k = 2. (Figure 2C). Furthermore, the two clusters showed significant differences (Figure 2B).

3.3 CRGs and immune cell infiltration in different cuproptosis related IPF subtypes

The differences in immune cell infiltration and differentially expressed CRGs were also examined in different cuproptosis-related IPF subgroups, and there were 9 differentially expressed CRGs between Cluster 1 and Cluster 2. ATP7A, LIAS, LIPT1, DLAT, GLS, and DBT overexpressed in Cluster 1, and CDKN2A overexpressed in Cluster 2 (Figures 3A, B). Moreover, Cluster 1 exhibited higher immune cell infiltration of naive T cells CD4, memory resting and activated T cells CD4, but a lower level of monocytes, macrophages M0, and resting mast cells (Figure 3C).

3.4 GSVA analysis

To explore the GO function and KEGG pathway in different clusters, the GSCA algorithm was applied to quantify the test value of

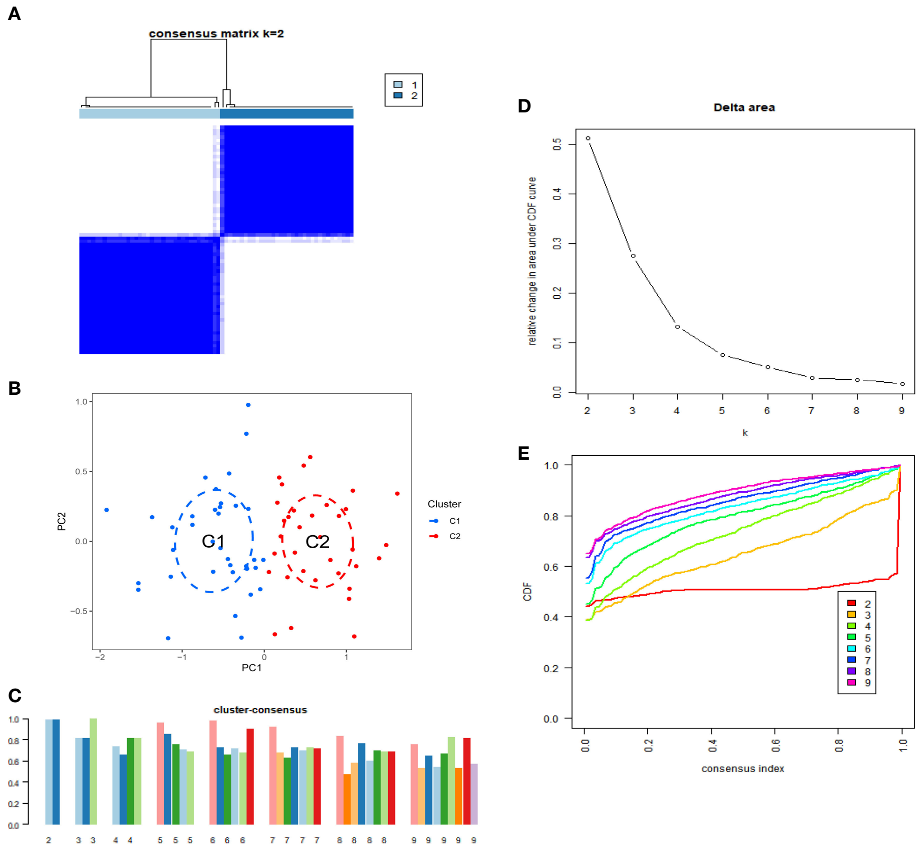

FIGURE 2
Identification of cuproptosis-related IPF subtype. **(A)** Consensus matrix when k=2. **(B)** CDF delta area curves when k was ranged 2 to 9. **(C)** Representative cumulative distribution function (CDF) curves. **(D)** The score of consensus clustering. **(E)** Principal component analysis (PCA) of two subtypes.

GSVA between clusters. The results of GO analysis indicated that Cluster 2 IPF group was enriched in the ubiquitin ligase complex, ubiquitin mediated proteolysis, tRNA methylation, monocyte aggregation, nucleotide sugar metabolic process, cell-cell adhesion *via* plasma membrane adhesion molecules, circulatory system development, myotube differentiation, and synaptic membrane, among others (Figure 4A). KEGG pathway enrichment showed that Cluster 2 IPF was enriched in aminoacyl tRNA biosynthesis, RNA polymerase, and calcium signaling pathway, among others (Figure 4B).

3.5 WGCNA co-expression analysis

To find out the essential gene modules related to the IPF, the co-expression network and modules were constructed using the WGCNA algorithm, and the top 25% of differently expressed genes were opted to further analysis. When the optimal value of soft power was set to 5, the co-expressed gene modules were identified, and R^2 was equal to 0.92 (Figure 5A). Thus, 8 distinct modules with different colors were obtained, and the topological overlap matrix was displayed (Figures 5B–D). The yellow module strongly correlated with the IPF with a correlation coefficient of 0.6 and *p* value of 9×e-24 (Figure 5E). A total of 253 genes were in the yellow module, as shown in Figure 5F.

We also used the R package WGCNA to analyze the correlations between cuproptosis clusters and critical genes modules. The scale-free network was ensured when β = 4 (scare-free R^2 = 0.97) (Figure 6A). There were 8 significant modules determined (Figures 6B–D), and the turquoise module had the highest relationship with IPF (Figure 6E). The scatter plot portrayed the relationship between members in the turquoise module and the significant gene of Cluster 2 (Figure 6F).

3.6 Establishment and evaluation of machine learning

To identify specific genes with a high diagnostic capacity for IPF, 66 core genes (Figure 7A) were used to train a machine-learning model with different methods, including SVM, XGB, GLM, and RF. XGB and GLM models displayed a relatively low residual (Figures 7B, E). Subsequently, the top 10 feature variables of each method were ranked according to the root mean square error (RMSE, Figure 7D). Moreover, all four machine learning models were evaluated for the discriminative performance by calculating receiver operating characteristic (ROC) curves, and all the performance of models were compared by AUC-ROC value (RF, AUC = 0.729; SVM, AUC = 0.630; XGB, AUC= 0.700; GLM, AUC=

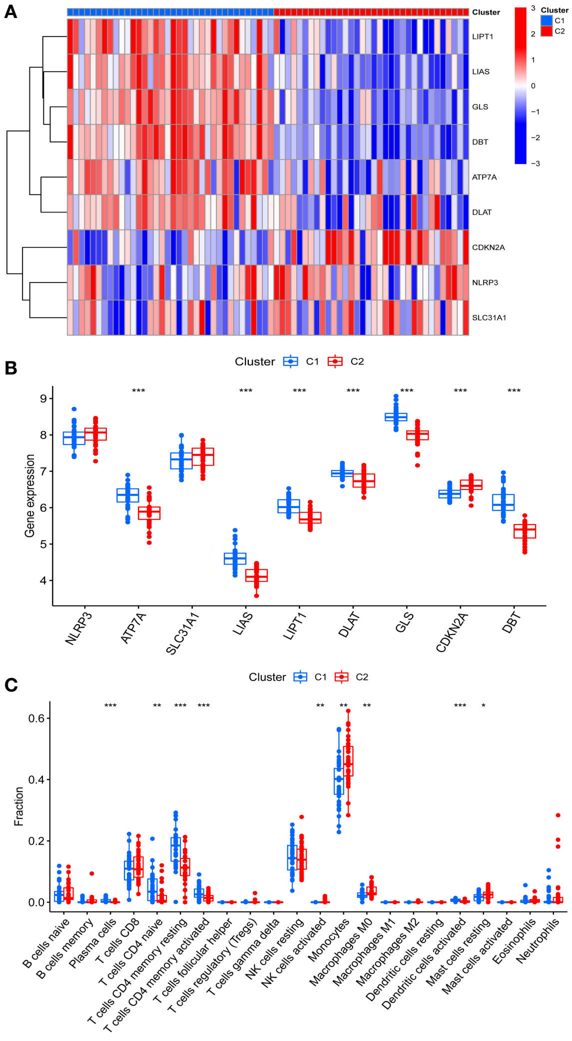

FIGURE 3
Identification of CRGs expression and immune characteristics between the two cuproptosis related IPF subtype (clusters). **(A)** CRGs expression between the two cuproptosis related IPF clusters - Heatmap. **(B)** CRGs expression between the two cuproptosis related IPF clusters. **(C)** The relative percent of 22 infiltrated immune cells between two cuproptosis related IPF clusters. *$p< 0.05$, **$p< 0.01$, ***$p< 0.001$.

0.599, Figure 7C). Above all, the XGB model was the best model to distinguish IPF. Moreover, the 4 genes, including XKR6, MLLT3, CD40LG and HK3, were applied as predictor genes for further analysis.

To further assess the predictive efficiency of the XGB model a clinical nomogram was created, which assigns all risk factors to points and judges the IPF risk according to the total points (Figure 8D). The R package rms made the calibration curve and DCA to assess the predictive efficiency of the nomogram model. Results showed that the nomogram had high accuracy in diagnosing IPF, with the predicted probability presenting a small error and the decision curve of the model far from the curve of all models (Figures 8A, B). We then validated the 4-gene prediction model with ROC analysis, which showed satisfactory performance with an AUC value of 0.7 in the GSE33566 database (healthy vs. IPF patients) (Figure 8C). The results indicated that our diagnosis model is effectively distinguishes IPF from healthy patients.

3.7 The relationship analysis between clinical characteristics and the 4 critical genes

To explore the correlation between clinical characteristics and the 4 most critical genes, we enrolled them in the GSE38958 databases to validate the correlation between the predictor genes and clinical characteristics. DLCO was selected as the factor related to IPF. The results revealed that 3 genes exhibited a positive correlation with DLCO (p < 0.05, CD40LG, R = 0.35; XKR6, R = 0.29; MLLT3, R = 0.36), except HK3 (R = -0.44, p < 0.01) (Figures 9A–D).

We also constructed the heatmap portraying the correlation between the 4 genes and genes related to TGF-β in the GSE38958 and GSE33566 databases. Two databases showed that XKR6, MLLT3, and CD40LG had a negative correlation with TGFβ1, while HK3 presented a positive relationship (Figure 9E, F).

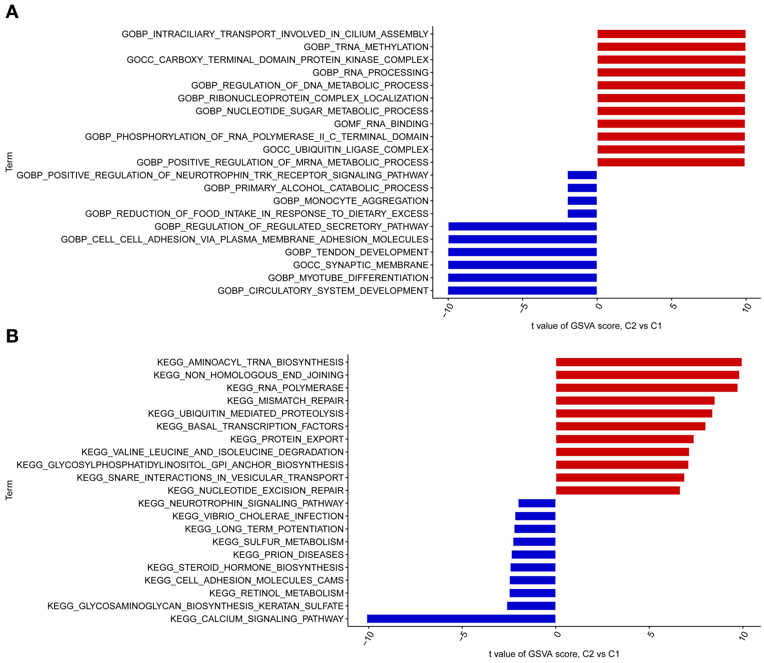

FIGURE 4
GO enrichment and KEGG pathway enrichment between the two cuproptosis related IPF subtype (clusters). **(A)** GO enrichment. **(B)** KEGG pathway enrichment.

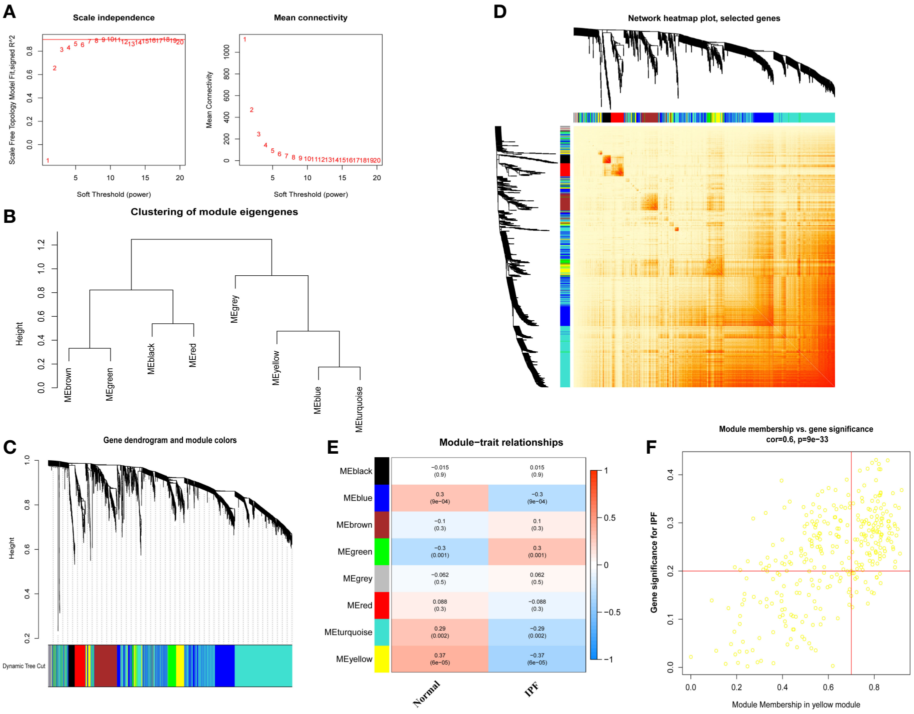

FIGURE 5
Co-expression network of differential expressed genes between IPF patients and normal individuals. **(A)** Exponential curve fitting and mean connectivity of power value. **(B)** The correlation between different modules in dendrogram. **(C)** Gene clustering dendrogram with dynamic identification of modules. Different colors show distinct co-expression modules. **(D)** Network heatmap of the correlation among 8 modules. **(E)** Module-trait relationships. Each row represents a module; each column represents a clinical status. **(F)** Scatter plot between module membership in yellow module and the gene significance for IPF.

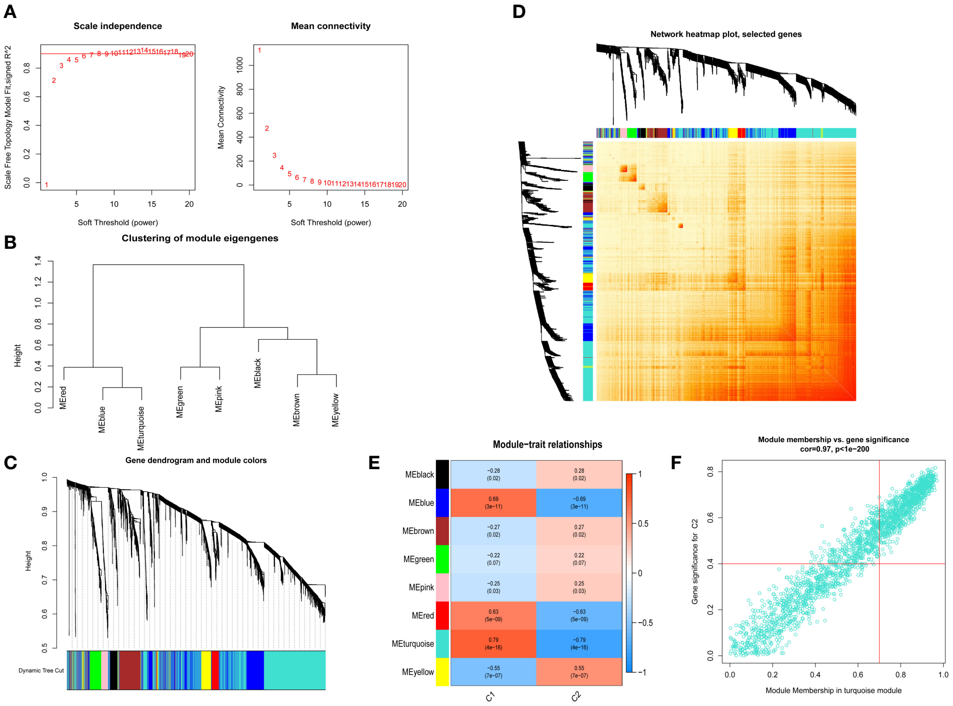

FIGURE 6
Co-expression network of differential expressed genes between two cuproptosis related IPF clusters. **(A)** Exponential curve fitting of power value. **(B)** The correlation between different modules in dendrogram. **(C)** Gene clustering dendrogram with dynamic identification of modules. Different colors show distinct co-expression modules. **(D)** Network heatmap of the correlation among 8 modules. **(E)** Module-trait relationships. Each row represents a module; each column represents a clinical status. C1 and C2 represent cluster 1 and cluster 2, respectively. **(F)** Scatter plot between module membership in turquoise module and the gene significance for cluster 2.

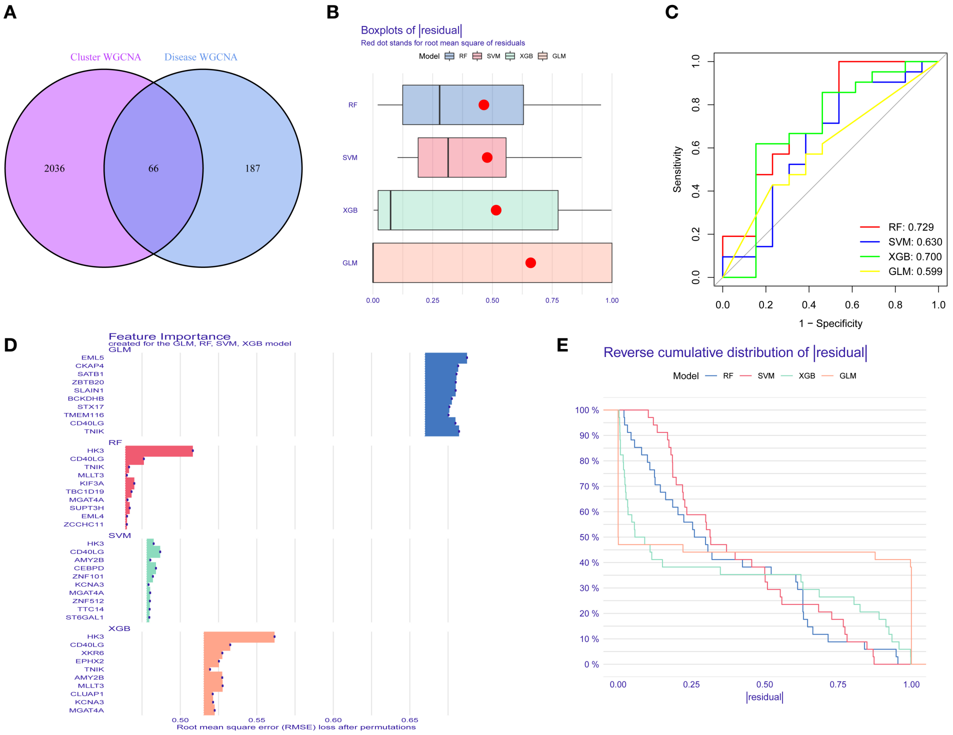

FIGURE 7
The construction and verification of Study machine learning. **(A)** The core gene of differently expressed gene in IPF and IPF clusters. **(B)** Boxplots of four machine learning models. **(C)** ROC analysis of machine learning models. **(D)** Top gene of four models. **(E)** Cumulative residual distribution of XGB, RF, GLM and SVM machine learning models.

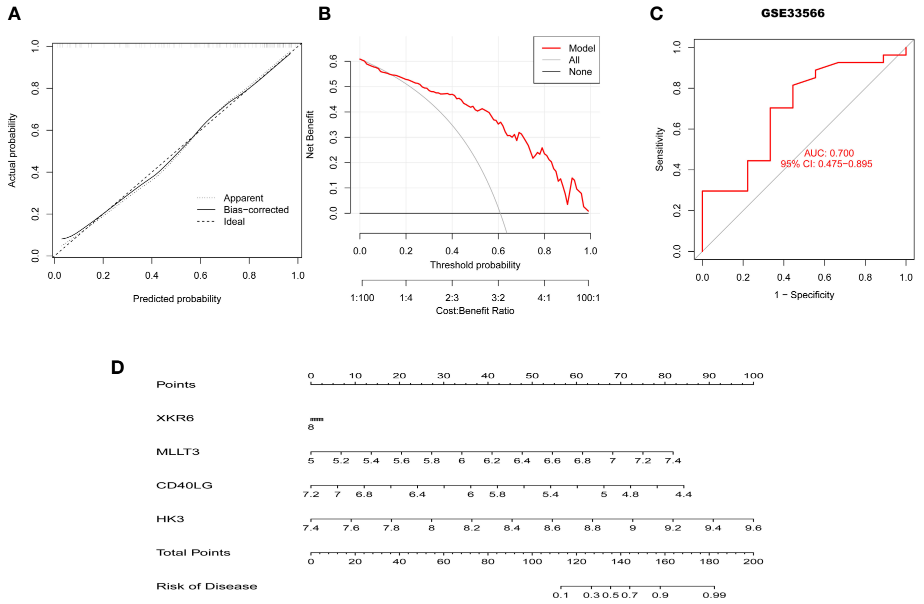

FIGURE 8
Validation of the 4-gene-based XGB model. **(A, B)** Predictive efficiency of the nomogram model by the DCA **(A)** and calibration curve **(B)**. **(C)** ROC curve of the 4-gene-based XGB model in the GSE33566. **(D)** The construction of nomogram for predicting the rate of IPF based on the 4-gene-based XGB model.

Meanwhile, the gene-gene interaction network for CD40LG was constructed using GeneMANIA, and the functions with high significance were selected to display (Figure 9G). Moreover, the function and pathways analysis revealed that CD40LG was prominently enriched in tumor necrosis factor (TNF) receptor binding, TNF-mediated signaling pathway, CD40 receptor complex, NF-κB signaling pathway, and cytokine and regulation of immune effector process (Figure 9H).

4 Discussion

IPF is a progressive and irreversible lung disease with different etiology. There is no effective treatment but lung transplantation for IPF patients (22). A new mechanism, copper-dependent cell death, has been reported to be strongly associated with disease progression through the aggregation of lipoylated mitochondrial enzymes and loss of iron-suffer cluster proteins (6). As there was no study about the role of CRGs in IPF patients blood, more studies needed to analysis the relationship between CRGs and IPF in blood samples, and the correlation between CRGs and immune cells in IPF patients. Therefore, we sought to clarify the role of CRGs in the progression of IPF and the effect on the immune microenvironment of IPF patients, which may provide a novel treatment approach for IPF. Additionally, gene signatures related to cuproptosis were used to predict IPF subtypes, and define biomarkers for the diagnosis of IPF.

It's reported that the CRGs, such as FDX1, LIAS, DLD, PDHA1, PDHB, DLAT, and LIPT1, were down-regulated in the lung tissues of pulmonary fibrosis mouse model, and the same results were obtained via analysis of lung tissues scRNA-seq data for human pulmonary fibrosis (23). In our study, differential expression analysis showed that there were 9 different expressed CRGs in blood samples of IPF patients compared with healthy individuals, suggesting that CRGs may participate in the development of IPF. Of the 9 CRGs, NLRP3, SLC31A1, and CDKN2A were upregulated in IPF, while ATP7A, LIAS, LIPT1, DLAT, GLS, and DBT were downregulated in IPF patients than healthy subjects. It also has been reported that the overactivation of NLRP3 in IPF patients leads to the increased production of Class I of collagens (24, 25), and NLRP3 inflammasome can promote fibrosis *via* pathways involving TGF-β1 and EMT (26). Besides, CDKN2A, a cell cycle negative regulator, is involved in the progression of dysregulated epithelial cell senescence and triggering the activation of fibroblasts and myofibroblasts in IPF patients (27, 28).Therefore, CRGs may attend to the progression of IPF, but more studies are needed.

Subsequently, we further calculated the correlation between the CRGs to clarify the relationship between cuproptosis regulators and IPF. There was an apparent synergistic effect among LIPT1, LIAS, GLS, DBT, ATP7A, and DLAT, and a robust antagonistic effect between CDKN2A and LIPT1, LIAS, GLS, DBT, ATP7A, and DLAT in IPF patients. Moreover, the abundance of immune cells differed between healthy subjects and IPF patients. In this study, IPF patients exhibited high infiltration levels of monocytes, which was consistent with previous studies, and can be considered a biomarker for assessing IPF patients (29). Further, based on the expression landscapes of CRGs, we used unsupervised cluster analysis to illustrate the different cuproptosis regulation patterns in IPF patients. Two distinct cuproptosis-related clusters were identified. We found that most CRGs were downregulated in the Cluster 2 IPF

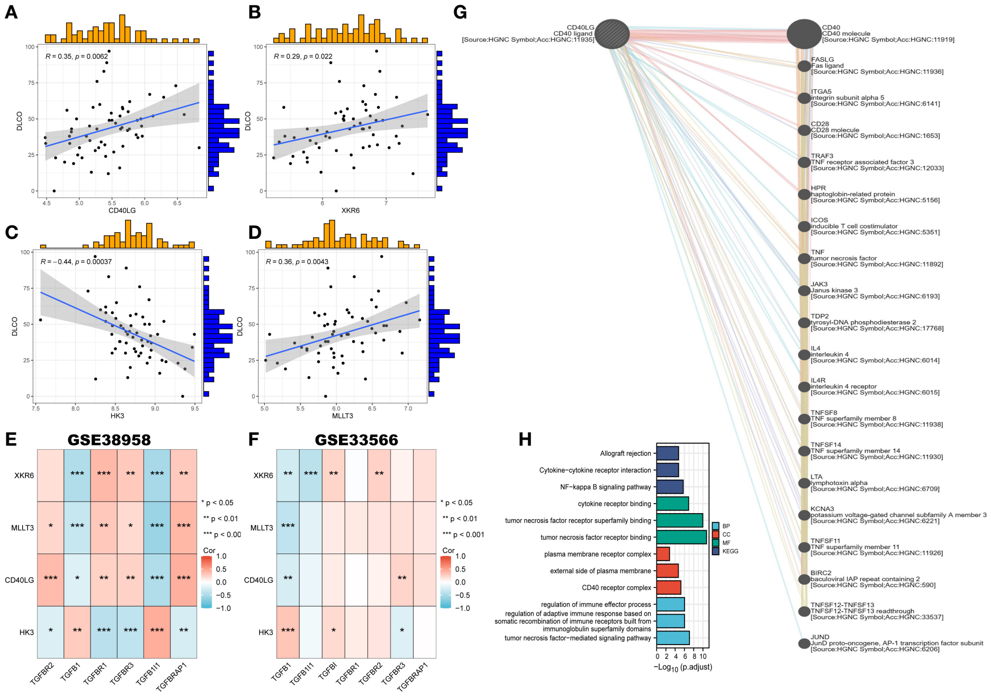

FIGURE 9
Correlation of clinical characteristics with CRGs based on two datasets and the construction of gene-gene network. **(A–D)** The correlation between key genes and DLCO. **(E, F)** The correlation between four key genes and TGF-β in GSE38958 **(E)** and GSE33566 **(F)**. **(G)** The gene-gene interaction network of CD40LG from GeneMANIA. **(H)** Go enrichment and KEGG pathway enrichment for genes related to CD40LG.

group. In addition, the cluster 2 group had a high infiltration of monocytes and macrophages M0, and low infiltration of naive T cells CD4 and memory resting and activated T cells CD4. Elevated monocyte counts in IPF have been associated with worse outcomes (30, 31). Growing data also shows monocyte-derived cells in lungs display discrete profibrotic phenotypes characterized by the expression of markers of alternative macrophage activation (32). In addition, macrophages are activated by activators such as IFN-γ, IL-10, or IL-3, acquiring profibrotic phenotype (33). Even more, macrophages can be polarized to M1 or M2 by these chemokines and release TGF-β and IL-10 to regulate endothelial cell proliferation, fibroblast activation, angiogenesis, and extracellular matrix (ECM) deposition to facilitate fibrosis formation (34, 35). Few T cells are in the fibrotic lung compared to the healthy lung (36). Above all, we believe that cluster 2 IPF patients are more likely to have worse outcomes, but more studies are needed. GO enrichment showed that the Cluster 2 IPF group was enriched in the ubiquitin ligase complex, ubiquitin-mediated proteolysis, tRNA methylation, monocyte aggregation, nucleotide sugar metabolic process, cell-cell adhesion *via* plasma membrane adhesion molecules, circulatory system development, myotube differentiation, and synaptic membrane, among others. KEGG pathway enrichment showed that Cluster 2 IPF was enriched in aminoacyl tRNA biosynthesis, RNA polymerase, calcium signaling pathway, and other pathways.

The performance of 4 selected machine-learning models (RF, SVM, GLM, and XGB) was compared and selected based on the high predictive efficacy in the testing cohort. Results showed that the XGB-based machine-learning model had the best performance in predicting the IPF. We then selected 4 critical genes (XKR6, MLLT3, CD40LG, and HK3) to construct a 4-gene-based XGBand nomogram models. The constructed 4-gene-based XGB model could accurately predict IPF, validated in other external datasets (AUC = 0.700), which provides new insights into the diagnosis of IPF. The nomogram was established for the diagnosis of IPF, exhibiting effective predictive efficacy with possible clinical application. Next, we analyzed the correlations between the clinical characteristics of IPF and 4 critical genes. DLCO was used to evaluate the diffusing capacity of the lung for carbon monoxide and aiding in IPF diagnosis. Our result revealed that only DLCO strongly correlated with the selected 4 genes. Additionally, an increasing number of studies have confirmed that TGF-β1 is a fundamental pathological mechanism, which contributes to the progression of IPF by promoting the transformation of fibroblast into myofibroblast, epithelial cells into mesenchymal cells, the production of collagen, filamentous actin, and α-SMA (37). Therefore, we performed a correlation analysis between these 4 predictor genes and TGF-β in two databases. The results suggested that HK3 was positively associated with TGF-β1, while the other 3 predictor genes were negatively correlated with TGF-β1 levels. Overall, the 4-gene-based XGB model is a satisfactory indicator of the diagnosis of IPF.

We also constructed a gene-gene network and performed Go and KEGG analyses of similar genes related to the 4 critical genes.

GO analysis of CD40LG showed that tumor necrosis and NF-κB were primarily enriched. Many studies have demonstrated that the tumor necrosis factor is primarily produced by macrophages and monocytes linked to a number of pulmonary inflammatory diseases, including IPF (38, 39). It also has been widely reported that NF-κB is one of the essential pathways in the progression of IPF, and blockade of NF-κB prevented lung fibroblast-mediated IL-6, IL-8, and CXCL6 cytokine secretion as well as accumulation of profibrotic factors (40). Meanwhile, regulation of the immune and tumor necrosis factor-mediated signaling pathways are enriched in KEGG. Therefore, CD40LG may correlated with the progression of IPF and the immune system. HK3, one of the 4 critical genes, is a protein-coding gene related to the glycolysis pathway. It has been observed that glycolysis reprogramming drives fibroblast activation when macrophages direct the metabolic fate of adjacent cells, implying that HK3 may be influenced in the development of IPF (41). MLLT3, as a critical gene, acts upstream of or within the negative or positive regulation of the canonical Wnt pathway, which has been reported to be associated with lung fibroblast activation, differentiation, and dysregulation of repairing processes (42). Although the correlation between IPF and MLLT3 has not been reported, we believe that MLLT3 may play a role in regulating the Wnt signaling pathway to participate in the progression of IPF. In addition, the correlation of XKR6 with IPF has not been reported. However, the mechanism of the 4 critical genes in regulating IPF progression needs more studies.

This study has some limitations. Firstly, more IPF samples are needed to demonstrate the correlation between CRGs and IPF disease or immune cells infiltration. Secondly, it is necessary to do more experiments to clarify the regulation and mechanism of the 4 critical genes identified and CRGs in the progression of IPF. Lastly, more clinical features are required to confirm the validity of the predictive model.

5 Conclusions

In conclusion, our study clarified that CRGs might play a role in IPF progression. We also showed the correlation between CRGs and immune cell infiltration, and elucidated the significance of immune heterogeneity in IPF patients with distinct cuproptosis clusters. The prognostic model based on the 4 critical genes may allow a new way to predict the prognosis of IPF.

Data availability statement

The original contributions presented in the study are included in the article/supplementary material. Further inquiries can be directed to the corresponding authors.

Author contributions

XS and ZP wrote and revised the manuscript. YZ, WC and JD collected the original data and visualized the final results. XS provided the funding. TC and RL supervised the study. The final manuscript was read and approved by all authors. All authors contributed to the article and approved the submitted version.

Funding

This research was funded by the National Nature Science Foundation of China (NO. 81960020), 2022 Kunlun Elite of Qinghai Province High-End Innovation and Entrepreneurship leading Talents (NO.2022), Qinghai Clinical Research Center for Respiratory Diseases (NO. 2019-SF-L4) and 2022 Provincial Key Clinical Specialty Project: Respiratory and Critical Care Department (NO.2022).

Conflict of interest

The authors declare that the research was conducted in the absence of any commercial or financial relationships that could be construed as a potential conflict of interest

Publisher's note

References

1. Barratt SL, Creamer A, Hayton C. Idiopathic pulmonary fibrosis (IPF): an overview. *J Clin Med* (2018) 7(8):201. doi: 10.3390/jcm7080201

2. Raghu G, Collard HR, Egan JJ, Martinez FJ, Behr J, Brown KK, et al. An official ATS/ERS/JRS/ALAT statement: idiopathic pulmonary fibrosis: evidence-based guidelines for diagnosis and management. *Am J Respir Crit Care Med* (2011) 183 (6):788–824. doi: 10.1164/rccm.201506-1063ST

3. Spagnolo P, Kropski JA, Jones MG, Lee JS, Rossi G, Karampitsakos T, et al. Idiopathic pulmonary fibrosis: disease mechanisms and drug development. *Pharmacol Ther* (2021) 222:107798. doi: 10.1016/j.pharmthera.2020.107798

4. Desai O, Winkler J, Minasyan M, et al. The role of immune and inflammatory cells in idiopathic pulmonary fibrosis. *Front Med (Lausanne)* (2018) 5:43. doi: 10.3389/fmed.2018.00043

5. Thannickal VJ, Toews GB, White ES, Herzog EL. Mechanisms of pulmonary fibrosis. *Annu Rev Med* (2004) 55:395–417. doi: 10.1146/annurev.med.55.091902.103810

6. Tsvetkov P, Coy S, Petrova B, Dreishpoon M, Verma A, Abdusamad M, et al. Copper induces cell death by targeting lipoylated TCA cycle proteins. *Science* (2022) 375(6586):1254–61. doi: 10.1126/science.abf0529

7. Li X, Jiang P, Li R, Wu B, Zhao K, Li S, et al. Analysis of cuproptosis in hepatocellular carcinoma using multi-omics reveals a comprehensive HCC landscape and the immune patterns of cuproptosis. *Front Oncol* (2022) 12:1009036. doi: 10.3389/fonc.2022.1009036

8. Tang S, Zhao L, Wu X-B, Wang Z, Cai LY, Pan D, et al. Identification of a novel cuproptosis-related gene signature for prognostic implication in head and neck squamous carcinomas. *Cancers* (2022) 14(16):3986. doi: 10.3390/cancers14163986

9. Tu H, Zhang Q, Xue L, Bao J. Cuproptosis-related lncRNA gene signature establishes a prognostic model of gastric adenocarcinoma and evaluate the effect of antineoplastic drugs. *Genes* (2022) 13:2214. doi: 10.3390/genes13122214

10. Wang F, Lin H, Su Q, Li C. Cuproptosis-related lncRNA predict prognosis and immune response of lung adenocarcinoma. *World J Surg Oncol* (2022) 20(1):275. doi: 10.1186/s12957-022-02727-7

11. Percival SS. Copper and immunity. *Am J Clin Nutr* (1998) 67(5):1064S–8S. doi: 10.1093/ajcn/67.5.1064S

12. He C, Murthy S, McCormick ML, Spitz DR, Ryan AJ, Carter AB. Mitochondrial Cu,Zn-superoxide dismutase mediates pulmonary fibrosis by augmenting H2O2 generation. *J Biol Chem* (2011) 286(17):15597–607. doi: 10.1074/jbc.M110.187377

13. Tian R, Zhu Y, Yao J, Meng X, Wang J, Xie H, et al. NLRP3 participates in the regulation of EMT in bleomycin-induced pulmonary fibrosis. *Exp Cell Res* (2017) 357:328–34. doi: 10.1016/j.yexcr.2017.05.028

14. Stout-Delgado HW, Cho SJ, Chu SG, Mitzel DN, Villalba J, El-Chemaly S, et al. Age-dependent susceptibility to pulmonary fibrosis is associated with NLRP3 inflammasome activation. *Am J Respir Cell Mol Biol* (2016) 55:252–63. doi: 10.1165/rcmb.2015-0222OC

15. Gu Z, Gu L, Eils R, Schlesner M, Brors B. Circlize implements and enhances circular visualization in r. *Bioinformatics* (2014) 30(19):2811–2. doi: 10.1093/bioinformatics/btu393

16. Newman A, Liu C, Green M, Gentles AJ, Feng W, Xu Y, et al. Robust enumeration of cell subsets from tissue expression profiles. *Nat Methods* (2015) 12:453–7. doi: 10.1038/nmeth.3337

17. Wickham H, Averick M, Bryan J, Chang W, McGowan L, François R, et al. Welcome to the tidyverse. *J Open Source Softw* (2019) 4:1686. doi: 10.21105/joss.01686

18. Wickham H. *ggplot2 - elegant graphics for data analysis*. Springer Publishing Company, Incorporated. (2009) 260 p.

19. Wilkerson MD, Hayes DN. ConsensusClusterPlus: a class discovery tool with confidence assessments and item tracking. *Bioinformatics* (2010) 26:1572–3. doi: 10.1093/bioinformatics/btq170

20. Langfelder P, Horvath S. WGCNA: an r package for weighted correlation network analysis. *BMC Bioinf* (2008) 9:559. doi: 10.1186/1471-2105-9-559

21. Biecek P. Dalex: explainers for complex predictive models in r. *J Mach Learn Res* (2018) 19(84):1–5. doi: 10.48550/arXiv.1806.08915

22. Hennion N, Desseyn JL, Gottrand F, Wémeau-Stervinou L, Gouyer V. Fibrose pulmonaire idiopathique. *Med Sci (Paris)*(2022) 38(6-7):579–84. doi: 10.1051/medsci/2022084

23. Li G, Peng L, Wu M, Zhao Y, Cheng Z, Li G. Appropriate level of cuproptosis may be involved in alleviating pulmonary fibrosis. *Front Immunol* (2022) 13:1039510. doi: 10.3389/fimmu.2022.1039510

24. Colunga Biancatelli RML, Solopov PA, Catravas JD. The inflammasome NLR family pyrin domain-containing protein 3 (NLRP3) as a novel therapeutic target for idiopathic pulmonary fibrosis. *Am J Pathol* (2022) 192(6):837–46. doi: 10.1016/j.ajpath.2022.03.003

25. Moss BJ, Ryter SW, Rosas IO. Pathogenic mechanisms underlying idiopathic pulmonary fibrosis. *Annu Rev Pathol* (2022) 17:515–46. doi: 10.1146/annurev-pathol-042320-030240

26. Justet A, Zhao AY, Kaminski N. From COVID to fibrosis: lessons from single-cell analyses of the human lung. *Hum Genomics* (2022) 16(1):20. doi: 10.1186/s40246-022-00393-0

27. Kreuter M, Lee JS, Tzouvelekis A, et al. Monocyte count as a prognostic biomarker in patients with idiopathic pulmonary fibrosis. *Am J Respir Crit Care Med* (2021) 204(1):74–81. doi: 10.1164/rccm.202003-0669OC

28. Iyonaga KT, Akeya M, Saita N, Sakamoto O, Yoshimura T, Ando M, et al. Monocyte chemoattractant protein-1 in idiopathic pulmonary fibrosis and other interstitial lung diseases. *Hum Pathol* (1994) 25:455–63. doi: 10.1016/0046-8177(94)90117-1

29. Bergeron A, Soler P, Kambouchner M, Loiseau P, Milleron B, Valeyre D, et al. Cytokine profiles in idiopathic pulmonary fibrosis suggest an important role for TGF-β and IL-10. *Eur Respir J* (2003) 22:69–76. doi: 10.1183/09031936.03.00014703

30. Mathai SK, Gulati M, Peng X, Russell TR, Shaw AC, Rubinowitz AN, et al. Circulating monocytes from systemic sclerosis patients with interstitial lung disease show an enhanced profibrotic phenotype. *Lab Invest* (2010) 90:812–23. doi: 10.1038/labinvest.2010.73

31. Prasse A, Probst C, Bargagli E, Zissel G, Toews GB, Flaherty KR, et al. Serum CC chemokine ligand-18 con-centration predicts outcome in idiopathic pulmonary fibrosis. *Am J Respir . Crit Care Med* (2009) 179:717–23. doi: 10.1164/rccm.200808-1201OC

32. Capelli A, Di Stefano A, Gnemmi I, Donner CF. CCR5 expression and CC chemokine levels in idiopathic pulmonary fibrosis. *Eur Respir J* (2005) 25:701–7. doi: 10.1183/09031936.05.00082604

33. Wick G, Grundtman C, Mayerl C, Wimpissinger TF, Feichtinger J, Zelger B, et al. The immunology of fibrosis. *Annu Rev Immunol* (2013) 31:107–35. doi: 10.1146/annurev-immunol-032712-095937

34. Nuovo GJ, Hagood JS, Magro CM, Chin N, Kapil R, Davis L, et al. The distribution of immunomodulatory cells in the lungs of patients with idiopathic pulmonary fibrosis. *Mod Pathol* (2012) 25:416–33. doi: 10.1038/modpathol.2011.166

35. Inui N, Sakai S, Kitagawa M. Molecular pathogenesis of pulmonary fibrosis, with focus on pathways related to TGF-β and the ubiquitin-proteasome pathway. *Int J Mol Sci* (2021) 22(11):6107. doi: 10.3390/ijms22116107

36. Li S, Zhao J, Shang D, Kass DJ, Zhao Y. Ubiquitination and deubiquitination emerge as players in idiopathic pulmonary fibrosis pathogenesis and treatment. *JCI Insight* (2018) 3(10):e120362. doi: 10.1172/jci.insight.120362

37. Suzuki J, Hamada E, Shodai T, Kamoshida G, Kudo S, Itoh S, et al. Cytokine secretion from human monocytes potentiated by p-selectin-mediated cell adhesion. *Int Arch Allergy Immunol* (2013) 160:152–60. doi: 10.1159/000339857

38. Malaviya R, Laskin JD, Laskin DL. Anti-TNFα therapy in inflammatory lung diseases. *Pharmacol Ther* (2017) 180:90–8. doi: 10.1016/j.pharmthera.2017.06.008

39. Aggarwal BB, Gupta SC, Kim JH. Historical perspectives on tumor necrosis factor and its superfamily: 25 years later, a golden journey. *Blood* (2012) 119:651–65. doi: 10.1182/blood-2011-04-325225

40. Sieber P, Schäfer A, Lieberherr R, Caimi SL, Lüthi U, Ryge J, et al. NF-κB drives epithelial-mesenchymal mechanisms of lung fibrosis in a translational lung cell model. *JCI Insight* (2022) 8(3):e154719. doi: 10.1172/jci.insight.154719

41. Xie N, Tan Z, Banerjee S, Cui H, Ge J, Liu RM, et al. Glycolytic reprogramming in myofibroblast differentiation and lung fibrosis. *Am J Respir Crit Care Med* (2015) 192(12):1462–74. doi: 10.1164/rccm.201504-0780OC

42. Königshoff M, Balsara N, Pfaff EM, Kramer M, Chrobak I, Seeger W, et al. Functional wnt signaling is increased in idiopathic pulmonary fibrosis. *PloS One* (2008) 3:e2142. doi: 10.1371/journal.pone.0002142

frontiers | Frontiers in Cell and Developmental Biology

TYPE Original Research
PUBLISHED 05 June 2023
DOI 10.3389/fcell.2023.1202573

OPEN ACCESS

EDITED BY
Chunheng Mo,
Sichuan University, China

REVIEWED BY
Yan Bai,
Massachusetts General Hospital and Harvard Medical School, United States
Chan Young Park,
Ulsan National Institute of Science and Technology, Republic of Korea
Yihua Lin,
First Affiliated Hospital of Xiamen University, China

*CORRESPONDENCE
Jun Chen,
✉ junchen@scu.edu.cn
Yongchun Shen,
✉ shen_yongchun@126.com

†These authors have contributed equally to this work and share first authorship

RECEIVED 08 April 2023
ACCEPTED 26 May 2023
PUBLISHED 05 June 2023

CITATION
Zeng Z, Cheng M, Li M, Wang T, Wen F, Sanderson MJ, Sneyd J, Shen Y and Chen J (2023), Inherent differences of small airway contraction and Ca^{2+} oscillations in airway smooth muscle cells between BALB/c and C57BL/6 mouse strains.
Front. Cell Dev. Biol. 11:1202573.
doi: 10.3389/fcell.2023.1202573

Inherent differences of small airway contraction and Ca^{2+} oscillations in airway smooth muscle cells between BALB/c and C57BL/6 mouse strains

Zijian Zeng[1†], Mengxin Cheng[1†], Meng Li[1†], Tao Wang[1], Fuqiang Wen[1], Michael J. Sanderson[2], James Sneyd[3], Yongchun Shen[1]* and Jun Chen[1]*

[1]Department of Pulmonary and Critical Care Medicine, West China Hospital, Sichuan University and Division of Pulmonary Diseases, State Key Laboratory of Biotherapy, Chengdu, Sichuan, China, [2]Department of Microbiology and Physiological Systems, University of Massachusetts Medical School, Worcester, MA, United States, [3]Department of Mathematics, The University of Auckland, Auckland, New Zealand

BALB/c and C57BL/6 mouse strains are widely used as animal model in studies of respiratory diseases, such as asthma. Asthma is characterized by airway hyperresponsiveness, which is eventually resulted from the excessive airway smooth muscle (ASM) contraction mediated by Ca^{2+} oscillations in ASM cells. It is reported that BALB/c mice have inherently higher airway responsiveness, but show no different contractive response of tracheal ring as compared to C57BL/6 mice. However, whether the different airway responsiveness is due to the different extents of small airway contraction, and what's underlying mechanism remains unknown. Here, we assess agonist-induced small airway contraction and Ca^{2+} oscillations in ASM cells between BALB/c and C57BL/6 mice by using precision-cut lung slices (PCLS). We found that BALB/c mice showed an intrinsically stronger extent of small airway narrowing and faster Ca^{2+} oscillations in ASM cells in response to agonists. These differences were associated with a higher magnitude of Ca^{2+} influx via store-operated Ca^{2+} entry (SOCE), as a result of increased expression of SOCE components (STIM1, Orai1) in the ASM cells of small airway of BALB/c mice. An established mathematical model and experimental results suggested that the increased SOC current could result in increased agonist-induced Ca^{2+} oscillations. Therefore, the inherently higher SOC underlies the increased Ca^{2+} oscillation frequency in ASM cells and stronger small airway contraction in BALB/c mice, thus higher airway responsiveness in BALB/c than C57BL/6 mouse strain.

KEYWORDS

airway smooth muscle, asthma, precision-cut lung slices, Ca^{2+} oscillations, airway hyperresponsiveness

1 Introduction

Asthma is clinically characterized by airway hyperresponsiveness (AHR), a phenomenon of excessive airway narrowing in response to agonists. Although AHR might result from hypertrophy and hyperplasia of airway smooth muscle (ASM) induced by airway inflammation (Bentley and Hershenson, 2008), the contractility of ASM itself also contributes to AHR. ASM contraction is driven by the phosphorylation of myosin light-chain (MLC) via the activation of MLC kinase, which is induced by the binding of calmodulin and intracellular calcium (Sieck et al., 2001). Previous reports have shown that agonist-induced ASM contraction is accompanied by repetitive waves of increased intracellular calcium concentration ($[Ca^{2+}]_i$) of ASM, termed Ca^{2+} oscillations, the frequency of Ca^{2+} oscillations determines the extent of ASM contraction (Prakash et al., 1998; Perez and Sanderson, 2005). Notably, the sustained Ca^{2+} oscillations cause a small and continual loss of Ca^{2+} across the plasma membrane (PM) via PM Ca^{2+} ATPases (PMCA) and Na^+/Ca^{2+} exchanger (NCX). Therefore, the maintenance of agonist-induced Ca^{2+} oscillations and ASM contraction requires an influx of extracellular Ca^{2+}. We has demonstrated that this influx occurs mainly via store-operated calcium entry (SOCE) (Chen and Sanderson, 2017), which involves a PM-resident Ca^{2+} channel called Orai1, and a sarcoplasmic reticulum (SR) membrane-spanning Ca^{2+}-sensing protein called stromal interaction molecule 1 (STIM1) (Prakriya and Lewis, 2015).

Mouse is commonly proposed as an experimental animal model to investigate the pathogenesis of AHR. Different mouse strains were used to measure airway reactivity, therefore, the inherent differences among mouse strains have been observed. For example, two widely used mouse strains, BALB/c and C57BL/6, have been demonstrated to display substantial differences in the distribution of inflammatory cells, expression of proinflammatory cytokines, ASM mass, and subepithelial collagen and fibronectin deposition after acute or chronic exposure to allergens (Gueders et al., 2009; Van Hove et al., 2009). It is worth noting that BALB/c mice showed stronger agonist-induced airway responsiveness and increased shortening velocity of ASM than C57BL/6 mice (Duguet et al., 2000). However, BALB/c and C57BL/6 mice show no difference in the contractive response of tracheal ring segments to agonists (Safholm et al., 2011), indicating that tracheal contraction might not account for the different airway responsiveness. Recently, small airway contraction has been increasingly acknowledged in the pathogenies of AHR (Kjellberg et al., 2016; Stenberg et al., 2017). Nevertheless, it is still unclear whether BALB/c and C57BL/6 mice have inherent differences in the small airway contractility and whether the Ca^{2+} oscillations regulated by the magnitude of SOCE contributes to these differences.

In this study, we used an established precision-cut lung slices (PCLS) to access the agonist-induced contraction of the small airway and Ca^{2+} oscillations of ASM cells in BALB/c and C57BL/6 mice. We report that BALB/c mice show an inherently stronger extent of small airway narrowing and a higher frequency of Ca^{2+} oscillation in ASM cells in response to agonists, which might be associated with an increased Ca^{2+} influx via SOCE.

2 Methods and materials

2.1 Animals

Age matched female C57BL/6 mice and BALB/c mice (8–12 weeks with bodyweight of 19–22 g) were purchased from Charles River Breeding Laboratories (Needham, MA, United States) and GemPharmatech Co. Ltd (Nanjing, Jiangsu, China). The mice were bred in a specific pathogen free environment. The adequate number of mice was estimated by a power analysis. All protocols were in accordance with the Guide for the Care and Use of Laboratory Animals and approved by the Institutional Animal Care and Use Committee of University of Massachusetts Medical School and West China Hospital (approval number: 2018049A).

2.2 Reagents

Hanks' Balanced Salt Solution (HBSS) was prepared by supplementing 20 mM HEPES buffer and adjusted to pH 7.4 (sHBSS). Hanks' 0-Ca^{2+} solution (0-Ca^{2+} sHBSS) was prepared with no-Ca^{2+} HBSS supplemented with 1 mM Na_2H_2-EGTA, 20 mM HEPES and 0.9 mM $MgSO_4$. Oregon Green 488 BAPTA-1 a.m. was purchased from Life Technologies (Grand Island, NY, United States). Ryanodine was purchased from Abcam Inc (Cambridge, MA, United States), other reagents were purchased from either Sigma-Aldrich (St. Louis, MO, United States) or Thermo Fisher Scientific (Pittsburgh, PA, United States).

2.3 Precision-cut lung slices (PCLS)

The detailed protocol has been previously described (Perez and Sanderson, 2005). 1.8% low melting point agarose was prepared in sHBSS. Mice were killed by cervical dislocation, and the lung was inflated with ~1 mL 1.8% low melting point agarose via an intratracheal catheter at 37°C, 0.3 mL air was injected subsequently to flush the agarose within the airway into the distal alveoli. The cardiac lobe was disassembled after gelling agarose with 4°C sHBSS, and sectioned into 180 μm thick PCLS by a vibratome (VF-300, Precisionary Instruments, Greenville, NC, United States). As the slicing might stimulate a spontaneous airway contraction in PCLS preparation, all experiments were performed on the second day of slicing when the airways were fully relaxed. The PCLS were maintained in DMEM supplemented with antibiotics at 10% CO_2 and 37°C for up to 2 days, within the periods the contractility of small airway remains unchanged. The experiments were performed at 37°C, and repeated at room temperature, in a custom-made, temperature-controlled microscope enclosure as described previously (Bai and Sanderson, 2009).

2.4 Airway contraction and relaxation

The detailed protocol has been previously described (Chen and Sanderson, 2017). The PCLS were held down by a 200 μm nylon mesh with a hole aligned over a selected airway on a cover-glass. To make a perfusion chamber, a smaller cover-glass was placed on the top of the nylon mesh and the side edges were sealed with silicone grease. We used two different agonists, methacholine (MCh) and 5-hydroxytryptamine (5-HT), which bind to their respective cell-surface receptors and activate different downstream G protein-coupled pathways to trigger airway contraction.

The contraction assay was performed by giving increasing doses (100, 200, 400, 800, 2000 nM) of MCh/5-HT sequentially with washing-out of agonists by sHBSS between each dose. The extent of airway narrowing in response to the agonists was determined by the change in lumen area, which was recorded by a CCD camera at 1 image per 2 s on an inverted microscope (Nikon Diaphot or Olympus IX71). The area of the lumen was calculated by using ImageJ, and then normalized by the formula: Area (%) = 100% * Lumen area at a certain time/Initial lumen area.

To compare the extent of airway narrowing between BALB/c and C57BL/6 mice, the extent of airway contraction was defined and calculated by the formula: airway contraction (%) = 100% *(Initial lumen area-lumen area at a certain time)/Initial lumen area. Then a dose-response curve was plotted by using the extent of airway contraction in response to increasing doses of agonists at sequential timepoints (5, 15, 25, 35 and 45 min) of the contraction assay. For each assay, 6 BALB/c mice and 6 C57BL/6 mice were used, 1–2 PCLS were obtained from each mouse, 2 randomly selected airways in each PCLS were assessed, and specific sample sizes were reported in the figure legends.

2.5 Intracellular Ca^{2+} signaling

The detailed protocol has been previously described (Chen and Sanderson, 2017). The PCLS were loaded with 20 μM Oregon Green (OG) 488 BAPTA-1-AM supplemented with 0.1% Pluronic F-127 and 200 μM sulfobromophthalein (SB) at 30°C for 1 h, and then placed in 200 μM SB at room temperature for 30 min to allow the de-esterification of OG. After washing the PCLS with sHBSS in the perfusion chamber, the intracellular Ca^{2+} signaling of a single ASM cell in the PCLS was recorded by a custom-built, video-rate scanning 2-photon laser microscope at a rate of 15 images per second. The change in fluorescence intensity in an interest region (8 × 10 pixels) of an ASM cell was analyzed by Video Savant 4 (IO Industries, Montreal, Canada) with custom-written code. The fluorescence intensity at a particular time (F_t) was normalized to the initial time (F_0) as F_t/F_0. For each assay, five to six BALB/c mice and five to six C57BL/6 mice were used, 1–2 PCLS were obtained from each mouse, two to three randomly selected ASM cells in each PCLS were assessed, and specific sample sizes were reported in the figure legends.

2.6 SOCE-activated PCLS

The validation of SOCE-activated PCLS has been reported (Bai and Sanderson, 2006). Briefly, the PCLS was treated with 20 mM caffeine and 50 μM ryanodine simultaneously for 5 min, followed by a thorough washout with sHBSS. This treatment gates the ryanodine receptors (RyR) of SR in an open state and leads to a decreased Ca^{2+} concentration in SR ($[Ca^{2+}]_{SR}$), activating SOCE to induce Ca^{2+} influx. The SOCE-activated PCLS remains viable for at least 5 h, during this time the $[Ca^{2+}]_{SR}$ is kept in a low level due to the persistent opening of RyR, and consequently the activation of SOCE is sustained and irreversible. As a result, the $[Ca^{2+}]_i$ is determined by the extracellular Ca^{2+} concentration ($[Ca^{2+}]_e$) via SOC influx.

2.7 Immunofluorescence

Mice were anesthetized with intraperitoneal injection of 2.5% sodium pentobarbital, and subsequently euthanized through exsanguination from the right ventricle to collect lung tissue. The left lung was inflated and preserved with 10% formaldehyde solution, followed by paraffin embedding and slicing. We employed tyramide signal amplification (TSA) principle for immunofluorescence staining, by using a multiplex fluorescence kit and following the guidelines provided by the manufacturer (RS0035, Immunoway). Briefly, the lung sections underwent dewaxing and rehydration, followed by antigen retrieval. Protein blocking was performed using peroxidase blocking solution for 30 min before each of the three staining cycles. Primary antibodies against Na^+/K^+ ATPase (NKA, 1:200, YT2973, Immunoway), α-smooth muscle actin (α-SMA, 1:200, 19245S, CST), STIM1 (1:200, ET1612-53, Huabio), and Orai1 (1:200, ER 1803–11, Huabio) were applied to the lung sections respectively for 2 h at room temperature. Then horseradish peroxidase (HRP)-labeled rabbit secondary antibodies were applied to the lung sections for 20 min, followed by incubation with TSA opal fluorophore (Opal 488, Opal 594 or Opal 647) for 10 min at room temperature. The antibody-TSA complex was removed through a heat-mediated antigen retrieval process using Tris/EDTA buffer (pH 9.0) during each staining cycle. Then the lung sections were counterstained with DAPI (P36931, Invitrogen). The immunofluorescence images were captured by Nikon A1R MP confocal microscope. We conducted a negative control to rule out the possibility of spontaneous fluorescence and non-specific signals by staining lung sections with vehicle instead of primary antibodies. The α-SMA (conjugated to Opal 488) was used to identify ASM cells. The fluorescence intensity of NKA (conjugated to Opal 594) was used as an internal control. We then quantified the fluorescence density of Orai1 and STIM1 (both conjugated to Opal 647) by normalizing the fluorescence intensity of Orai1/STIM1 to that of NKA in the same region of interest of ASM cells using ImageJ. Three BALB/c mice and three C57BL/6 mice were used for each staining, and two to three lung sections were obtained from each mouse. Three randomly selected ASM cells in each lung section were analyzed in a blinded manner, the specific sample sizes were reported in the figure legends.

2.8 Statistics

Data were statistically analyzed and plotted by GraphPad Prism 7.00 (GraphPad Software Inc., San Diego, CA, United States). For the comparison of two groups, the distribution of data was first tested by the Shapiro-Wilk normality test or KS normality test, and then the data were compared using the Unpaired *t*-test or Mann-Whitney test. For the comparison of dose-response curves, nonlinear regression analysis was performed first, and then the best-fits values, including the bottom, top and concentration for 50% of

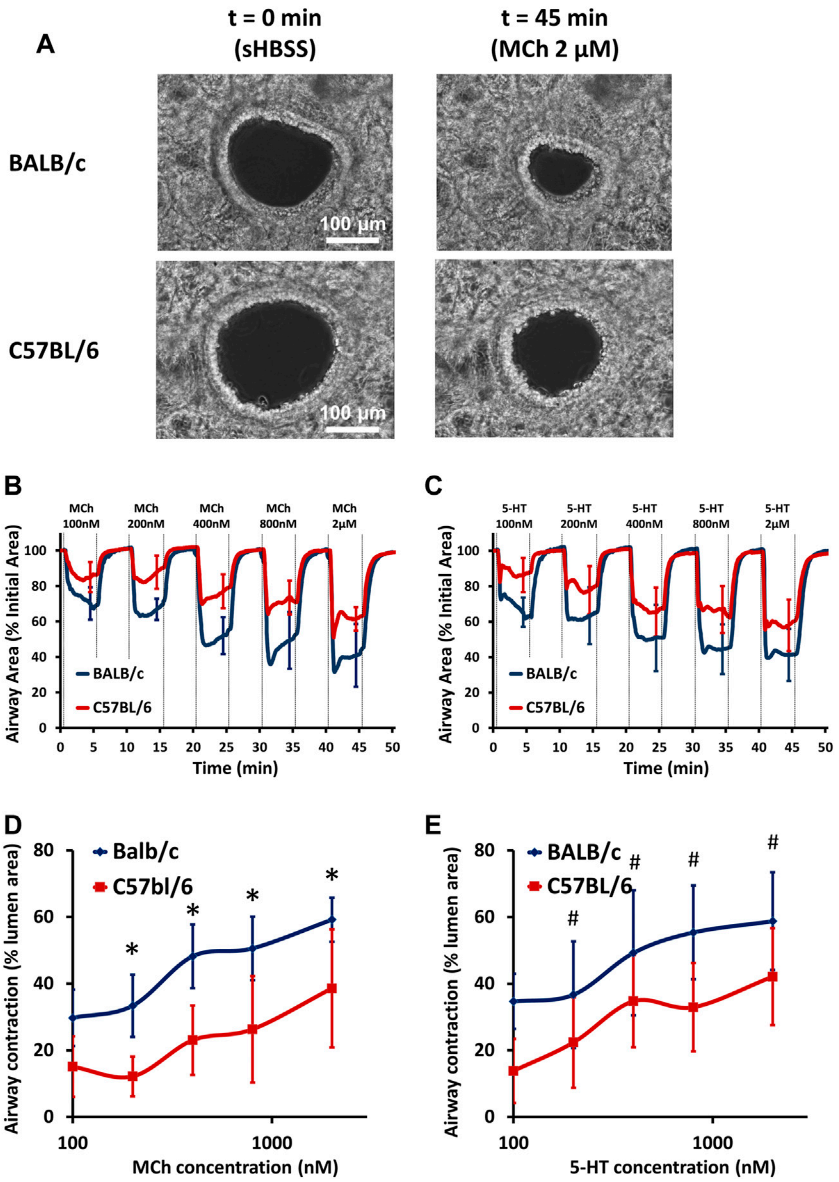

FIGURE 1
BALB/c mice show stronger airway contraction than C57BL/6 mice. **(A)** Representative phase-contrast images of 2 small airways in PCLS derived from BALB/c and C57BL/6 mice under resting conditions (left panel, scale bar = 100 μm) and exposed to 2 μM MCh (right panel) at 37°C. **(B–C)** The contraction assay show small airway contraction in response to increasing doses of MCh and 5-HT, respectively, at 37°C in PCLS derived from BALB/c (BLUE line) and C57BL/6 (RED line) mice. **(D–E)** The comparison of dose-response curves to MCh (D) and 5-HT (E) between BALB/c (BLUE line) and C57BL/6 (RED line) mice. Data are presented as the mean ± SD, **p* < 0.0001 in (D), #*p* < 0.0001 in (E). Data are obtained from 14 airways in 8 PCLS of 6 BALB/c mice, and 12 airways in 6 PCLS of 6 C57BL/6 mice, respectively.

the maximal effect (EC50) of the curves, were compared between groups. Data are presented as the mean ± SD, the sample sizes and numbers of mice used in experiments were reported in the figure legends; a value of $p < 0.05$ was considered significant.

2.9 Mathematical model

The mathematical model has been reported previously and well validated in stimulating the dynamic structure of Ca^{2+} oscillations in the ASM of PCLS (Wang et al., 2010; Croisier et al., 2013; Croisier et al., 2015; Sneyd et al., 2017). In brief, the dynamics of intracellular Ca^{2+} concentration ($c = [Ca^{2+}]_i$) and the SR Ca^{2+} concentration ($c_s = [Ca^{2+}]_{SR}$) are modelled by:

$$\frac{dc}{dt} = J_{in} - J_{PMCA} + J_{rel} - J_{SERCA}$$

$$\frac{dc_s}{dt} = \gamma (J_{SERCA} - J_{rel})$$

where J_{in} accounts for the Ca^{2+} influx, primarily through SOCE, while J_{PMCA} and J_{SERCA} represent the Ca^{2+} fluxes through the PMCA and SR Ca^{2+} ATPases (SERCA) pumps, respectively. J_{rel}, on the other hand,

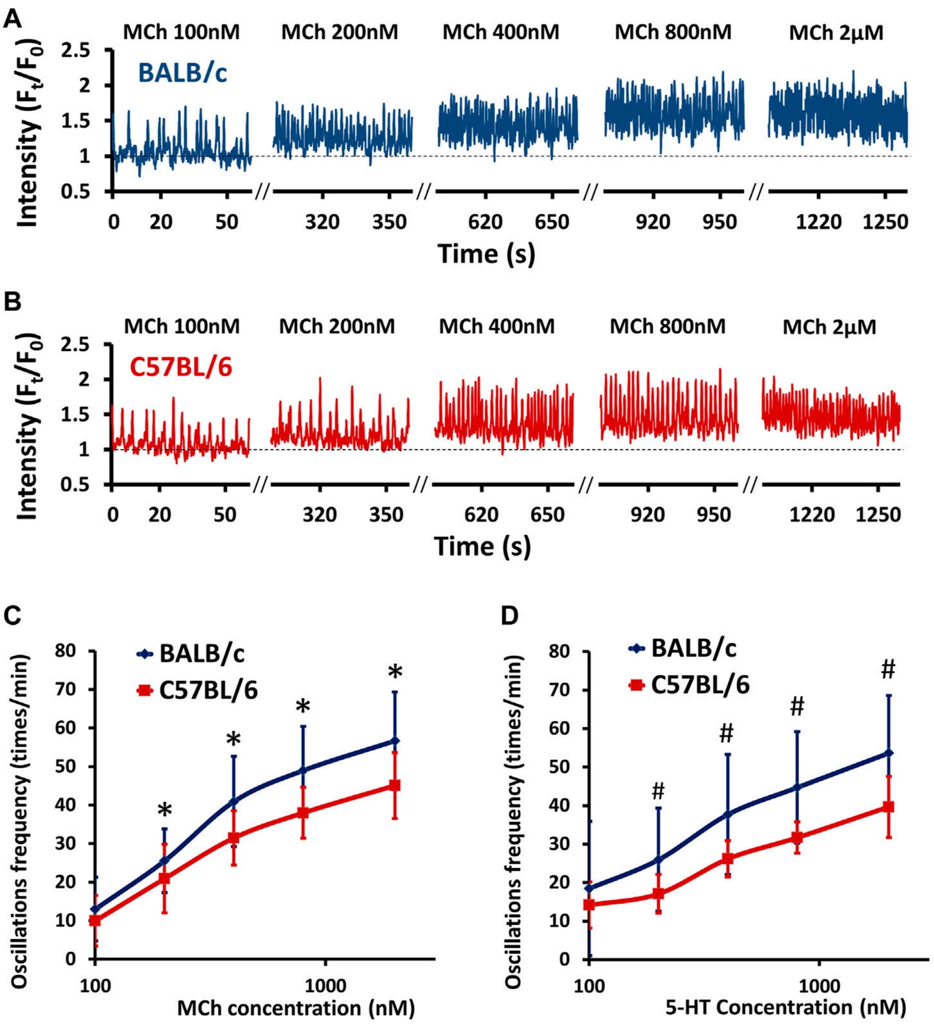

FIGURE 2
BALB/c mice show an increased agonist-induced Ca^{2+} oscillation frequency in ASM cells compared to C57BL/6 mice. **(A–B)** Representative traces show Ca^{2+} oscillations of ASM cells in PCLS derived from BALB/c (A, BLUE line) and C57BL/6 (B, RED line) mice in response to increasing doses of MCh at 37°C. **(C–D)** The comparison of dose-response curves to MCh (C) and 5-HT (D) between BALB/c (BLUE line) and C57BL/6 (RED line) mice. Data are presented as the mean ± SD, $*p < 0.0001$ in (C), $\#p < 0.0001$ in (D). Data are obtained from 18 ASM cells in 9 PCLS of 6 BALB/c mice, and15 ASM cells in 7 PCLS of 6 C57BL/6 mice, respectively.

models the efflux of Ca^{2+} from the SR through inositol trisphosphate (IP_3) receptors (IP_3R) and RyR. The comprehensive description of the mathematical model is provided in the supplement.

3 Results

3.1 BALB/c mice showed stronger agonist-induced small airway contraction than C57BL/6 mice

To assess the extent of "small airway" narrowing, we distinguished airway generation as reported previously (Bai et al., 2007): the first airway generation was defined as the most distal airway that had an intact epithelium with ciliated cells, and then the next airway generation was identified when another airway branch merged into the airway. By sequentially cutting the PCLS from the cardiac lobe, 7–10 intrapulmonary generations of airways can be obtained. We defined "small airway" as airway generation four to five with a lumen diameter of approximately 0.2mm, which showed the strongest contraction compared to other airway generations (Bai et al., 2007). As the extent of small airway narrowing might be also affected by extracellular matrix tethering, which is mainly determined by the presence of agarose in the parenchymal spaces (Hiorns et al., 2016), we used an identical concentration of agarose (with identical stiffness after gelling) and carefully chose airways from similar positions in the same lobe of mice.

The extent of small airway narrowing in PCLS derived from BALB/c and C57BL/6 mice was visualized (Figure 1A) and analyzed (Figures 1B–E and Supplementary Figure S1) respectively. No pre-contraction of airways was observed in either BALB/c or C57BL/6 PCLS as previously reported (Chen et al., 2017). Both MCh (Figure 1B) and 5-HT (Figure 1C) induced dose-dependent small airway narrowing (as reflected by the change in airway lumen area) in the PCLS of

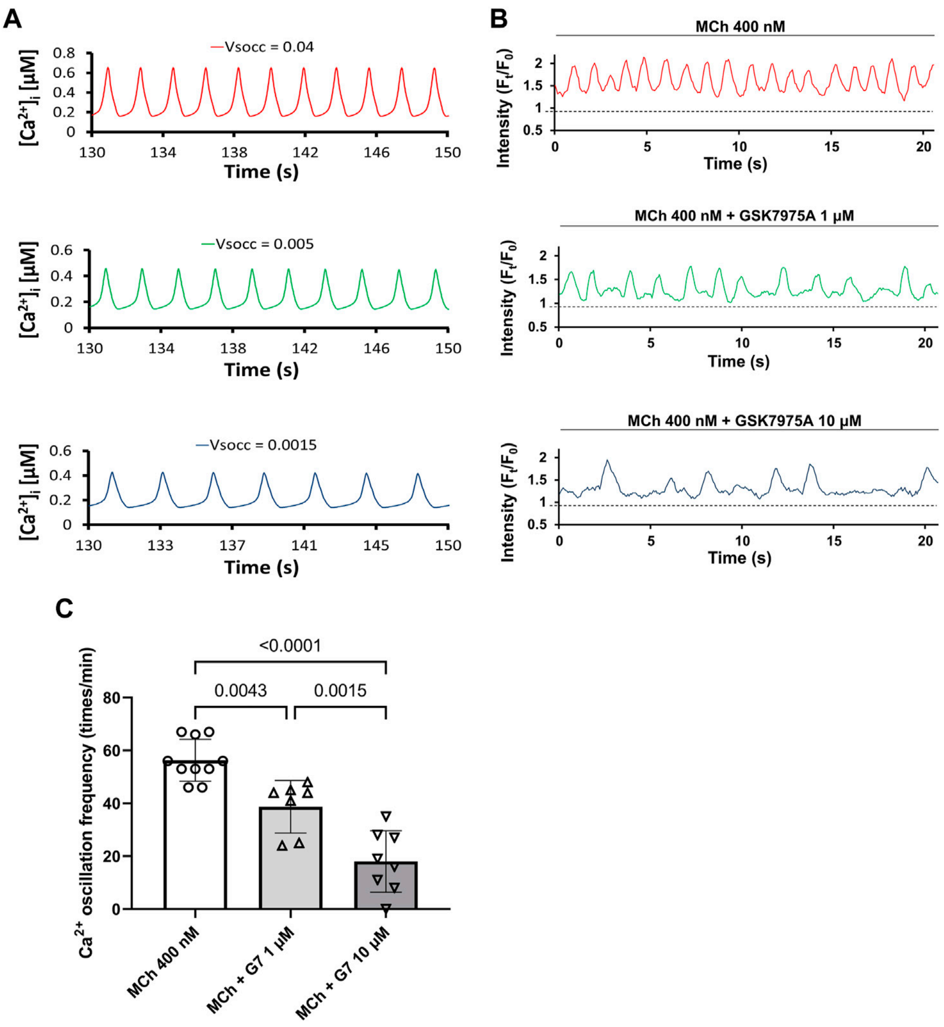

FIGURE 3
Reduced SOC current (V_{SOCC}) leads to slower Ca^{2+} oscillations in ASM cells. **(A)** Mathematical model predicts that decreased V_{SOCC} might lead to decreased Ca^{2+} oscillations in ASM cells. **(B)** The frequency of MCh (400 nM) induced Ca^{2+} oscillations in ASM cells of PCLS decreased when SOCE is inhibited by 1 μM and 10 μM GSK7975A (G7) respectively. **(C)** There are significant differences among Ca^{2+} oscillation frequency induced by 400 nM MCh, MCh +1 μM G7 and MCh +10 μM G7. Data are presented as the mean ± SD. For each bar in (C), seven to eight ASM cells obtained from 6 PCLS in 3 BALB/c mice are evaluated.

BALB/c and C57BL/6 mice at 37°C. Compared to C57BL/6 mice, the extent of small airway narrowing in BALB/c mice was significantly stronger upon stimulation with both MCh (Figures 1B,D) and 5-HT (Figures 1C,E) at all concentrations tested (100–2000 nM), suggesting an overall increased small airway contraction in BALB/c mice. A similar pattern of increased airway contraction in BALB/c mice was also seen at room temperature (Supplementary Figure S1). These results demonstrate an intrinsically stronger small airway contraction in BALB/c mice than in C57BL/6 mice.

3.2 BALB/c mice showed higher Ca^{2+} oscillation frequency in ASM cells than C57BL/6 mice

Agonist-induced small airway contraction is largely induced by the contraction of ASM itself, which is mediated by intracellular Ca^{2+} oscillations (Perez and Sanderson, 2005). Therefore, we examined the intrinsic difference in Ca^{2+} oscillations of ASM cells stimulated by MCh and 5-HT. No spontaneous Ca^{2+} signaling was observed in ASM cells derived from either BALB/c or C57BL/6 PCLS as previously reported (Chen et al., 2017). In the presence of both MCh and 5-HT at 37°C, ASM cells exhibited periodic Ca^{2+} waves propagating along the length of the cells (Figures 2A,B), accompanied by ASM contraction. In the ASM cells of both BALB/c and C57BL/6 mice, MCh induced a dose-dependent increase in Ca^{2+} oscillation frequency (Figures 2A,B). Compared to C57BL/6 mice, the ASM cells derived from BALB/c mice showed significantly increased Ca^{2+} oscillation frequency upon stimulation with both MCh (Figures 2A–C) and 5-HT (Figure 2D) at all concentrations tested (100–2000 nM). A similar pattern of higher Ca^{2+} oscillation frequency in ASM cells of BALB/c mice was also noted at room temperature (Supplementary Figure S2). These results demonstrate an intrinsically higher Ca^{2+} oscillation

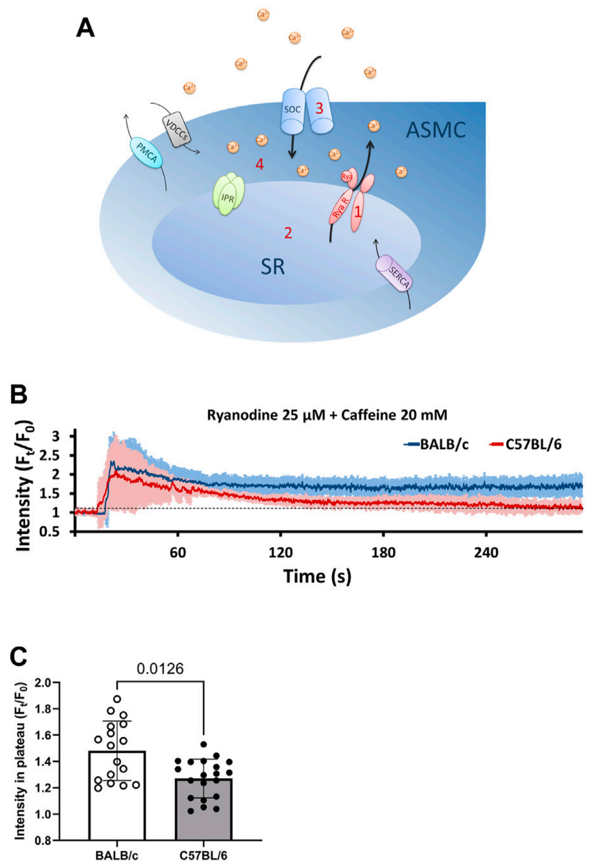

FIGURE 4
BALB/c mice show higher levels of $[Ca^{2+}]_i$ in SOCE-activated ASM cells than C57BL/6 mice. **(A)** A sketch illustrates the development of SOCE-activated ASM cells: **1**, PCLS were treated with 25 μM ryanodine (Rya) and 20 mM caffeine simultaneously to "lock" the ryanodine receptors (RyR) of SR in an open state; **2**, Opening of RyR leads to the depletion of SR Ca^{2+}; **3**, Ca^{2+} depletion in SR induces Ca^{2+} influx through SOC to form SOCE; **4,** The steady level of $[Ca^{2+}]_i$ in SOCE-activated ASM cells results from a dynamic balance of Ca^{2+} influx through SOCE, Ca^{2+} efflux from SR through RyR, Ca^{2+} uptake to the SR by SERCA, and Ca^{2+} efflux through plasma membrane Ca^{2+} ATPase (PCMA) and Na^+/Ca^{2+} exchanger (NCX). **(B)** SOCE-activated PCLS is prepared by exposing PCLS to a cocktail of 25 μM ryanodine and 20 mM caffeine at 37°C, ASM cells from BALB/c mice (BLUE line) show a higher steady level of $[Ca^{2+}]_i$ than those from C57BL/6 mice (RED line). Each point of the line represents the mean ± SD of the intensity at selected time points (F_t) normalized to the initial intensity at the beginning time (F_0). **(C)** Comparison of steady levels (F_t/F_0) in SOCE-activated ASM cells derived from BALB/c and C57BL/6 mice. Data are presented as the mean ± SD, $p = 0.0126$. Data are obtained from 17 ASM cells of 5 BALB/c mice, and 20 ASM cells of 5 C57BL/6 mice, respectively.

frequency in ASM cells of BALB/c mice than in those of C57BL/6 mice.

3.3 The frequency of agonist-induced Ca^{2+} oscillation depends on the magnitude of SOCE

As SOCE is required for sustained agonist-induced Ca^{2+} oscillations in ASM (Chen and Sanderson, 2017), an inherently higher SOC current might contribute to the increased Ca^{2+} oscillations and thus stronger ASM contraction observed in BALB/c mice. Accordingly, we used an established mathematical model to predict the potential contribution of SOC current to the agonist-induced Ca^{2+} oscillations in ASM cells. As Figure 3A showed, the mathematical model predicted that the decreased magnitude of SOC current (V_{SOCC}) reduced the frequency of Ca^{2+} oscillation. This prediction was validated in experiment that the blockage of SOCE by 1 μM and 10 μM GSK7975A, a specific inhibitor targets SCOE (Chen and Sanderson, 2017), significantly reduced MCh-induced Ca^{2+} oscillation frequency in a dose-dependent way in ASM cells of PCLS (Figures 3B,C). Therefore, both the mathematical model and experimental results suggested that SOCE magnitude regulates the Ca^{2+} oscillations frequency in ASM cells.

3.4 BALB/c mice showed higher $[Ca^{2+}]_i$ in SOCE-activated ASM cells, which might be SOC current-dependent

To further investigate the possible increased magnitude of SOCE in ASM cells of BALB/c mice, we utilized a model called "SOCE-activated PCLS". The rationale of SOCE-activated PCLS has been described previously (Bai and Sanderson, 2006; Chen and Sanderson, 2017). Briefly, PCLS is treated with ryanodine and caffeine simultaneously. While caffeine stimulates RyR opening, ryanodine irreversibly locks the RyR in a submaximal open state, which results in constitutive Ca^{2+} efflux from SR and consequently decreased $[Ca^{2+}]_{SR}$. This activates and maintains the SOCE to induce Ca^{2+} influx (Figure 4A). The treatment first induces an immediate transient increase of $[Ca^{2+}]_i$ caused by Ca^{2+} released from the SR through RyR opening, followed by a sustained elevation of $[Ca^{2+}]_i$ (Figure 4B). The steady level of this elevated $[Ca^{2+}]_i$ results from a dynamic balance of Ca^{2+} influx through SOCE (SOC current, P_{SOC}), Ca^{2+} efflux from SR through RyR (P_{RyR}), Ca^{2+} uptake to the SR by SERCA (P_{SERCA}), and intercellular Ca^{2+} efflux through plasma membrane Ca^{2+} ATPase (PCMA) and Na^+/Ca^{2+} exchanger (NCX) (P_{PCMA} and P_{NCX}, Figure 4A). As previously validated (Bai and Sanderson, 2006), the SOCE-activated PCLS presents an irreversible decrease of $[Ca^{2+}]_{SR}$ due to the constant opening of RyR and thus sustained activation of SOCE for at least 5 h since treatment of ryanodine and caffeine.

We used the mathematical model to predict the contribution of P_{RyR}, P_{SOC} and P_{SERCA} to the steady level of elevated $[Ca^{2+}]_i$ in SOCE-activated ASM cells. As Supplementary Figure S3A, B show, with either a given P_{RyR} or a given P_{SERCA}, the steady level of $[Ca^{2+}]_i$ changes little as P_{SERCA} or P_{RyR} increased. On the other hand, with a given P_{RyR}, increased P_{SOC} leads to an increased $[Ca^{2+}]_i$ (Supplementary Figure S3C), indicating that the steady level of $[Ca^{2+}]_i$ is mainly determined by the P_{SOC} in SOCE-activated ASM cells. Interestingly, the influence of P_{RyR} on the steady level of $[Ca^{2+}]_i$ is only evidenced when the P_{SOC} is sufficient (Supplementary Figure S3D), indicating that the contribution of P_{RyR} to $[Ca^{2+}]$i also depends on P_{SOC}.

Accordantly, our experimental results showed that when exposed to the same $[Ca^{2+}]_e$, the steady level of $[Ca^{2+}]_i$ in SOCE-activated ASM cells derived from BALB/c PCLS was significantly

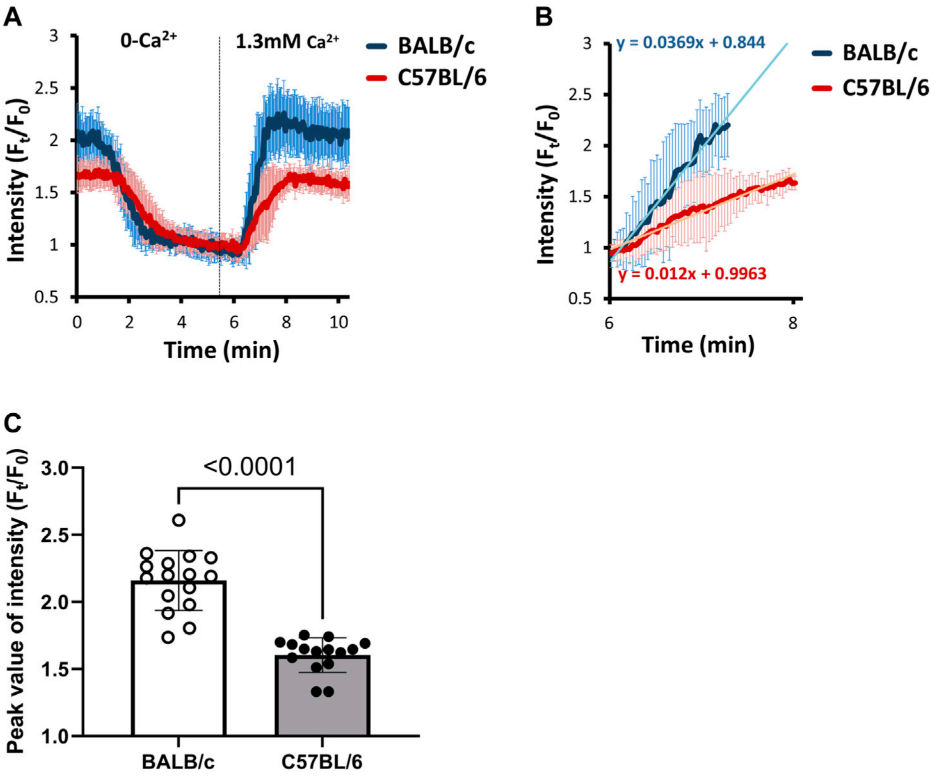

FIGURE 5
BALB/c mice show faster and higher SOC currents in SOCE-activated ASM cells than C57BL/6 mice. **(A)** The SOC current is evaluated by removing extracellular Ca^{2+} first to empty the $[Ca^{2+}]_i$ and $[Ca^{2+}]_{SR}$ in SOCE-activated ASM cells, and then adding back 1.3 mM Ca^{2+} to assess the transient Ca^{2+} influx via SOCE. Each point of the line represents the mean ± SD of the intensity at selected time points (F_t) normalized to the initial intensity at the beginning time (F_0). The SOC current was further quantified and compared by measuring **(B)** the rate of Ca^{2+} entry and **(C)** the peak value of Ca^{2+} influx. Data are presented as the mean ± SD, $p < 0.0001$ in **(C)**. Data are obtained from 16 ASM cells in 8 PCLS of 5 BALB/c mice, and 15 ASM cells in 7 PCLS of 5 C57BL/6 mice.

higher than that observed in C57BL/6 PCLS (Figures 4B,C). This observation suggested a completely different dynamic balance of Ca^{2+} influx and efflux in SOCE-activated ASM cells between BALB/c and C57BL/6 mice. As this steady level of $[Ca^{2+}]_i$ is mainly determined by P_{SOC}, it is assumed that the magnitude of SOCE in ASM cells of BALB/c mice is higher than those of C57BL/6 mice.

3.5 BALB/c mice showed higher SOC current in ASM cells than C57BL/6 mice

To further evaluate the SOC current in ASM cells, we removed the extracellular Ca^{2+} (by giving 0-Ca^{2+} sHBSS) to the SOCE-activated ASM cells firstly to decrease the $[Ca^{2+}]_i$ and $[Ca^{2+}]_{SR}$. As shown in Figure 5A, 0-Ca^{2+} sHBSS induced decreased $[Ca^{2+}]_i$ within 5 min. As previously described, the $[Ca^{2+}]_i$ is primarily determined by the SOC influx in the SOCE-activated ASM cells, we then added back 1.3 mM Ca^{2+} to assess the transient Ca^{2+} influx via SOCE (Figure 5A). The SOC current was quantified and compared by measuring the rate of Ca^{2+} entry (Figure 5B) and the peak value of Ca^{2+} influx (Figure 5C). The results showed that both the rate of Ca^{2+} entry and the peak value of Ca^{2+} influx via SOCE were significantly higher in ASM cells of BALB/c mice than those of C57BL/6 mice, suggesting that the ASM cells of BALB/c mice have a higher SOC current.

3.6 BALB/c mice show increased expression of STIM1 and Orai1 in ASM cells of small airways compared to C57BL/6 mice

To support a higher P_{SOCE} observed in ASM cells of BALB/c mice, we used semiquantitative immunofluorescent method to assess the expression of Orai1 and STIM1, two essential component proteins of SOCE, in the ASM cells of small airway derived from BALB/c and C57BL/6 mice. We used fluorescent intensity of NKA, a commonly used membrane marker, as the internal control to normalize the fluorescent intensity of Orai1 and STIM1 respectively (Figure 6A) in ASM cells labeled with α-smooth muscle actin (α-SMA). The results showed that the ASM cells of small airways obtained from BALB/c mice have higher intensity ratio of STIM1/NKA and Orai1/NKA respectively than those of C57BL/6 mice, indicating a relatively higher expression of essential elements of SOCE in ASM cells of BALB/c mice, in line with the larger SOC current observed in ASM cells of BALB/c mice.

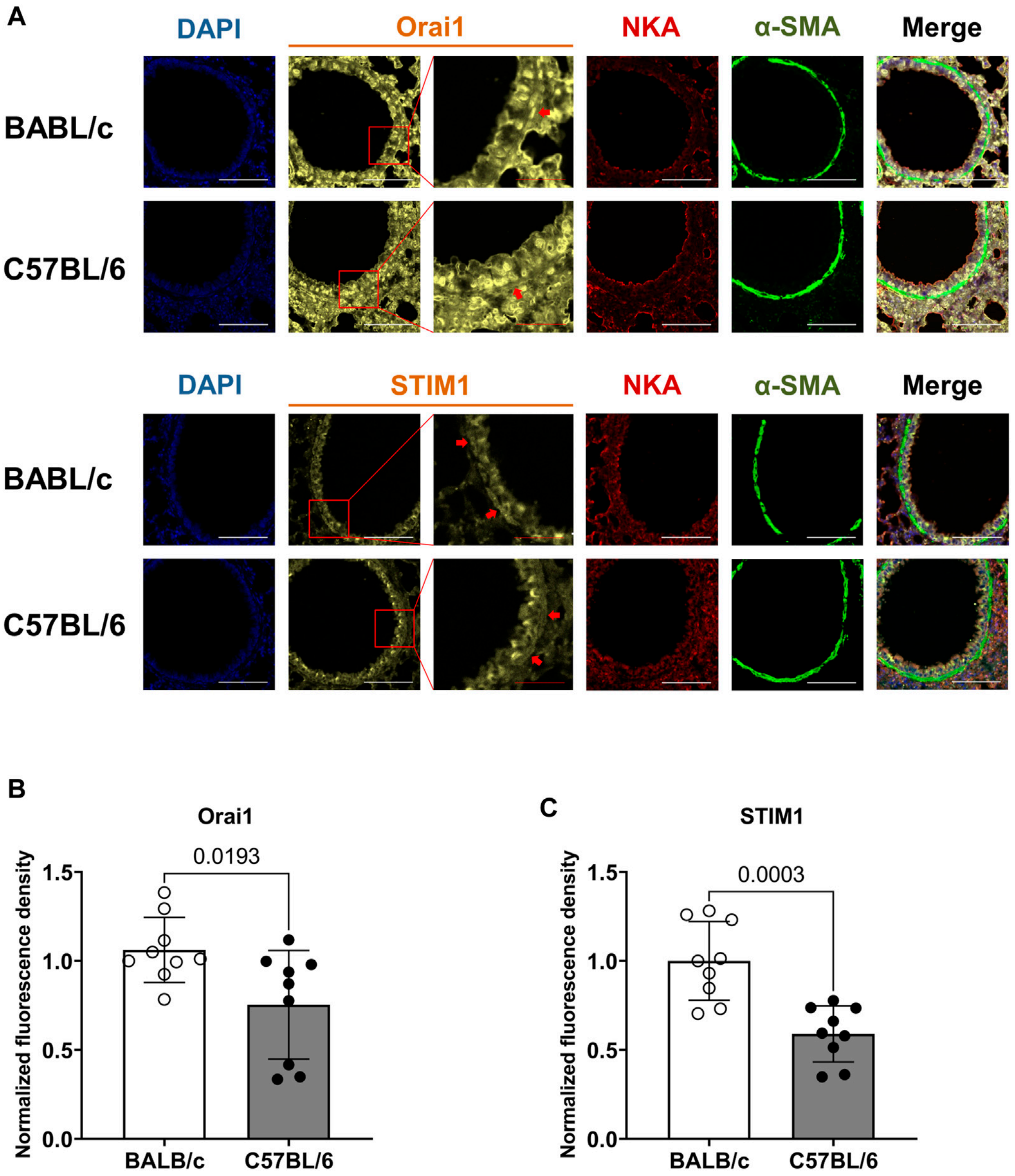

FIGURE 6
BALB/c mice show increased expression of Orai1 and STIM1, two essential component proteins of SOCE, in ASM cells of small airway compared to C57BL/6 mice. **(A)** The representative fluorescent images show the co-staining of DAPI, Orai1 or STIM1, Na$^+$/K$^+$ ATPase (NKA) and α-smooth muscle actin (α-SMA) in ASM cells of BALB/c and C57BL/6 mice; the fluorescent intensity of Orai1 or STIM1 were normalized to that of NKA in the same region of interest within ASM cells, which was identified by α-SMA; The red arrows indicate the representative ASM cells of interest used for analysis; White scale bar: 100 μm, red scale bar: 25 μm. **(B–C)** A comparison of the normalized fluorescent density of Orai1 (B) and STIM1 (C) in ASM cells derived from BALB/c and C57BL/6 mice, respectively. Data are presented as the mean ± SD, $p = 0.0193$ in (B), $p = 0.0003$ in (C). The bar in (B) represents 9 ASM cells obtained from 6 slices in three BALB/c mice, and 9 ASM cells obtained from 8 slices in three C57BL/6 mice; the bar in (C) represents 9 ASM cells obtained from 7 slices in three BALB/c mice, and 9 ASM cells obtained from 9 slices in three C57BL/6 mice.

4 Discussion

It is well known that airway responses appear differently among mouse strains, such as the contraction response to agonists (Levitt and Mitzner, 1988), IgE response to allergens (Larsen et al., 1992), force-velocity response in sensitized tracheal smooth muscle (TSM) strips (Fan et al., 1997), and different shortening velocities of ASM in both central and peripheral airways before or after sensitization with antigens (Duguet et al., 2000; Wagers et al., 2007). As BALB/c and C57BL/6 mice are widely used as animal models in studies of asthma and AHR, it is essential to characterize their innate differences in the airway response. Although BALB/c mice showed a higher agonist-induced airway response than C57BL/6 mice as assessed *in vivo* (Duguet et al., 2000), they showed no different response in the isometric tension of tracheal ring to agonists (Safholm et al., 2011). We hypothesized that the small airway contraction of BALB/c mice might differ from that of C57BL/6 mice, which could explain their different airway responses. Here, by using PCLS, a useful tool to investigate ASM physiology in relatively small airways *in situ*, we show that BALB/c mice have stronger extent of small airway narrowing and increased Ca^{2+} oscillation frequency in ASM cells in response to agonists than C57BL/6 mice. These observations are consistent with the increased airway response and ASM shortening velocity observed in BALB/c mice. As inspired by the increased steady level of $[Ca^{2+}]_i$ observed in SOCE-activated ASM cells derived from BALB/c mice, we further show that ASM cells derived from BALB/c mice have inherently higher Ca^{2+} influx via SOCE and increased expressions of Orai1 and STIM1 compared to those derived from C57BL/6 mice. Furthermore, both the mathematical model and the experimental results suggest that decreased SOC current leads to decreased frequency of Ca^{2+} oscillation in ASM cells. Therefore, the inherently higher SOC current resulting from increased expression of Orai1 and STIM1 might account for the higher frequency of Ca^{2+} oscillation and stronger contraction of ASM cells in BALB/c mice than in C57BL/6 mice.

Previous studies have demonstrated that the agonist-induced Ca^{2+} oscillations are generated by the cyclic release and re-uptake of Ca^{2+} from and to the SR (Wright et al., 2013). Specifically, agonist (such as MCh and 5-HT) binds to their respective cell-surface receptors and activates the different downstream G protein-coupled pathways to produce IP_3, which binds IP_3R to release Ca^{2+} from the SR into the cytoplasm; Ca^{2+} in the cytoplasm is pumped back into the SR by SERCA (Prakash et al., 2009). Ca^{2+} efflux from the SR might also occur via RyR (Croisier et al., 2015). During Ca^{2+} oscillations, the cytoplasmic Ca^{2+} continually loss via PMCA and NCX, therefore, an in-time supplementation of intracellular Ca^{2+} is essential for the sustained agonist-induced Ca^{2+} oscillations in ASM. We have demonstrated that SOCE, rather than voltage-gated Ca^{2+} channels, is the major Ca^{2+} influx pathway for sustaining agonist-induced Ca^{2+} oscillations in ASM cells (Chen and Sanderson, 2017).

The molecular basis of SOCE (Orai1 and STIM1) has been well demonstrated (Prakriya and Lewis, 2015). STIM1 senses the decreased $[Ca^{2+}]_{SR}$, and then oligomerizes and translocates to a region near the PM, where it interacts with Orai1 to generate a local Ca^{2+} influx current to replenish the Ca^{2+} lost in ASM cells (Croisier et al., 2013). Previous studies reported that the expressions of STIM1 and Orai1 are increased in ASM cells derived from experimental asthmatic mice (Spinelli et al., 2012; Qiu et al., 2017). In addition, STIM1 and Orai1-mediated SOCE has been associated with the proliferation of ASM cells (Zou et al., 2011). Furthermore, STIM1 is required for ASM remodeling through metabolic and transcriptional reprogramming and cytokine secretion (Johnson et al., 2022). In the present study, we demonstrate that inherently higher SOC current might induce increased Ca^{2+} oscillation frequency in ASM cell, leading to increase of $[Ca^{2+}]_i$ due to spatial and temporal integration, and thus resulting in stronger contraction. These results together highlight the regulatory role of SOCE in the Ca^{2+} oscillations of ASM cells and the contraction of ASM, which is closely associated with AHR.

It is worth noting that agonist-induced airway contraction is not only determined by the Ca^{2+} oscillations of ASM cells. Previously, we reported that both the Ca^{2+} oscillation frequency and the Ca^{2+} sensitivity of ASM cells contribute to innate ASM contractility (Bergner and Sanderson, 2003; Bai and Sanderson, 2009), whether the Ca^{2+} sensitivity of ASM cells in BALB/c mice differs from that in C57BL/6 mice is still unknown and worth further investigation. In addition, it is reported that different SERCA expression (Chen et al., 2017), IP_3R receptor density (Narayanan et al., 2012) and imbalance of GPCR-derived signals (Wright et al., 2013) could affect the agonist-induced Ca^{2+} oscillation frequency, whether BALB/c and C57BL/6 mice have different SERCA or IP_3R expression might need further investigation. Furthermore, it has been reported that the contractile protein content in ASM cells (Ammit et al., 2000), the tone of ASM cells themself (Fairbank et al., 2008), and the extracellular matrix stiffness (Polio et al., 2019) also exert impacts on airway contractility, however, whether these factors contribute to the different extents of small airway narrowing between BALB/c and C57BL/6 mice is unclear, but beyond our scope here. Finally, the absolute quantification of Orai1 and STIM1 protein expression in the ASM cells of small airway should be investigated in future study.

Taken together, our findings demonstrate that, as compared to C57BL/6 mice, BALB/c mice have inherently higher small airway contraction along with increased agonist-induced Ca^{2+} oscillation frequency, which might result from higher SOCE influx due to increased expression of Orai1 and STIM1 in ASM cells. These results suggest that an increased SOC current in ASM itself might lead to a higher Ca^{2+} oscillation frequency and stronger airway contraction, highlighting the importance of SOCE in understanding the mechanisms of AHR.

Data availability statement

The original contributions presented in the study are included in the article/Supplementary Material, further inquiries can be directed to the corresponding author.

Ethics statement

The animal study was reviewed and approved by Institutional Animal Care and Use Committee of University of Massachusetts Medical School and West China Hospital (approval number: 2018049A).

Author contributions

JC and YS conceived and supervised the research project and wrote the manuscript. ZZ, MC and ML performed the experiments and analyzed the data. TW, FW, MS and JS helped with image acquisition and data analysis. Project administration and funding acquisition by JC and YS. All authors contributed to the article and approved the submitted version.

Funding

This work was supported by Natural Science Foundation of China (NSFC) under Grant number 81800015, 82170046; China Postdoctoral Science Foundation under Grant number

2019T120851, 2018M643501; Natural Science Foundation of Sichuan Province under Grant number 2022NSFSC0603; Fundamental Research Funds for the Central Universities (2018SCU12028, the Postdoctoral Foundation of Sichuan University).

Conflict of interest

The authors declare that the research was conducted in the absence of any commercial or financial relationships that could be construed as a potential conflict of interest.

The handling editor, CM, declared a shared parent affiliation with the authors ZZ, MC, ML, TW, FW, YS and JC at the time of review.

Publisher's note

Supplementary material

The Supplementary Material for this article can be found online at: https://www.frontiersin.org/articles/10.3389/fcell.2023.1202573/full#supplementary-material

References

Ammit, A., Armour, C., and Black, J. (2000). Smooth-muscle myosin light-chain kinase content is increased in human sensitized airways. *Am. J. Respir. Crit. care Med.* 161, 257–263. doi:10.1164/ajrccm.161.1.9901005

Bai, Y., and Sanderson, M. J. (2006). Modulation of the Ca2+ sensitivity of airway smooth muscle cells in murine lung slices. *Am. J. Physiol. Lung Cell. Mol. Physiol.* 291, L208–L221. doi:10.1152/ajplung.00494.2005

Bai, Y., and Sanderson, M. J. (2009). The contribution of Ca2+ signaling and Ca2+ sensitivity to the regulation of airway smooth muscle contraction is different in rats and mice. *Am. J. Physiol. Lung Cell. Mol. Physiol.* 296, L947–L958. doi:10.1152/ajplung.90288.2008

Bai, Y., Zhang, M., and Sanderson, M. (2007). Contractility and Ca2+ signaling of smooth muscle cells in different generations of mouse airways. *Am. J. Respir. Cell. Mol. Biol.* 36, 122–130. doi:10.1165/rcmb.2006-0036OC

Bentley, J. K., and Hershenson, M. B. (2008). Airway smooth muscle growth in asthma: Proliferation, hypertrophy, and migration. *Proc. Am. Thorac. Soc.* 5, 89–96. doi:10.1513/pats.200705-063VS

Bergner, A., and Sanderson, M. J. (2003). Airway contractility and smooth muscle Ca(2+) signaling in lung slices from different mouse strains. *J. Appl. Physiol.* 95, 1325–1332. doi:10.1152/japplphysiol.00272.2003

Chen, J., Miller, M., Unno, H., Rosenthal, P., Sanderson, M. J., and Broide, D. H. (2017). Orosomucoid-like 3 (ORMDL3) upregulates airway smooth muscle proliferation, contraction, and Ca(2+) oscillations in asthma. *J. Allergy Clin. Immunol.* 142, 207–218. doi:10.1016/j.jaci.2017.08.015

Chen, J., and Sanderson, M. J. (2017). Store-operated calcium entry is required for sustained contraction and Ca(2+) oscillations of airway smooth muscle. *J. Physiol.* 595, 3203–3218. doi:10.1113/JP272694

Croisier, H., Tan, X., Chen, J., Sneyd, J., Sanderson, M. J., and Brook, B. S. (2015). Ryanodine receptor sensitization results in abnormal calcium signaling in airway smooth muscle cells. *Am. J. Respir. Cell. Mol. Biol.* 53, 703–711. doi:10.1165/rcmb.2014-0386OC

Croisier, H., Tan, X., Perez-Zoghbi, J. F., Sanderson, M. J., Sneyd, J., and Brook, B. S. (2013). Activation of store-operated calcium entry in airway smooth muscle cells: Insight from a mathematical model. *PLoS One* 8, e69598. doi:10.1371/journal.pone.0069598

Duguet, A., Biyah, K., Minshall, E., Gomes, R., Wang, C. G., Taoudi-Benchekroun, M., et al. (2000). Bronchial responsiveness among inbred mouse strains. Role of airway smooth-muscle shortening velocity. *Am. J. Respir. Crit. Care Med.* 161, 839–848. doi:10.1164/ajrccm.161.3.9906054

Fairbank, N., Connolly, S., Mackinnon, J., Wehry, K., Deng, L., and Maksym, G. (2008). Airway smooth muscle cell tone amplifies contractile function in the presence of chronic cyclic strain. *Am. J. physiology Lung Cell. Mol. physiology* 295, L479–L488. doi:10.1152/ajplung.00421.2007

Fan, T., Yang, M., Halayko, A., Mohapatra, S. S., and Stephens, N. L. (1997). Airway responsiveness in two inbred strains of mouse disparate in IgE and IL-4 production. *Am. J. Respir. Cell. Mol. Biol.* 17, 156–163. doi:10.1165/ajrcmb.17.2.2628

Gueders, M. M., Paulissen, G., Crahay, C., Quesada-Calvo, F., Hacha, J., Van Hove, C., et al. (2009). Mouse models of asthma: A comparison between C57bl/6 and BALB/c strains regarding bronchial responsiveness, inflammation, and cytokine production. *Inflamm. Res.* 58, 845–854. doi:10.1007/s00011-009-0054-2

Hiorns, J., Bidan, C., Jensen, O., Gosens, R., Kistemaker, L., Fredberg, J., et al. (2016). Airway and parenchymal strains during bronchoconstriction in the precision cut lung slice. *Front. physiology* 7, 309. doi:10.3389/fphys.2016.00309

Johnson, M. T., Xin, P., Benson, J. C., Pathak, T., Walter, V., Emrich, S. M., et al. (2022). STIM1 is a core trigger of airway smooth muscle remodeling and hyperresponsiveness in asthma. *Proc. Natl. Acad. Sci. U. S. A.* 119, 118. doi:10.1073/pnas.2114557118

Kjellberg, S., Houltz, B. K., Zetterstrom, O., Robinson, P. D., and Gustafsson, P. M. (2016). Clinical characteristics of adult asthma associated with small airway dysfunction. *Respir. Med.* 117, 92–102. doi:10.1016/j.rmed.2016.05.028

Larsen, G. L., Renz, H., Loader, J. E., Bradley, K. L., and Gelfand, E. W. (1992). Airway response to electrical field stimulation in sensitized inbred mice. Passive transfer of increased responsiveness with peribronchial lymph nodes. *J. Clin. Invest.* 89, 747–752. doi:10.1172/JCI115651

Levitt, R. C., and Mitzner, W. (1988). Expression of airway hyperreactivity to acetylcholine as a simple autosomal recessive trait in mice. *FASEB J.* 2, 2605–2608. doi:10.1096/fasebj.2.10.3384240

Narayanan, D., Adebiyi, A., and Jaggar, J. H. (2012). Inositol trisphosphate receptors in smooth muscle cells. *Am. J. Physiol. Heart Circ. Physiol.* 302, H2190–H2210. doi:10.1152/ajpheart.01146.2011

Perez, J. F., and Sanderson, M. J. (2005). The frequency of calcium oscillations induced by 5-HT, ACH, and KCl determine the contraction of smooth muscle cells of intrapulmonary bronchioles. *J. Gen. Physiol.* 125, 535–553. doi:10.1085/jgp.200409216

Polio, S., Stasiak, S., Jamieson, R., Balestrini, J., Krishnan, R., and Parameswaran, H. (2019). Extracellular matrix stiffness regulates human airway smooth muscle contraction by altering the cell-cell coupling. *Sci. Rep.* 9, 9564. doi:10.1038/s41598-019-45716-9

Prakash, Y., Kannan, M., Walseth, T., and Sieck, G. (1998). Role of cyclic ADP-ribose in the regulation of [Ca2+]i in porcine tracheal smooth muscle. *Am. J. physiology* 274, C1653–C1660. doi:10.1152/ajpcell.1998.274.6.C1653

Prakash, Y. S., Sathish, V., Thompson, M. A., Pabelick, C. M., and Sieck, G. C. (2009). Asthma and sarcoplasmic reticulum Ca2+ reuptake in airway smooth muscle. *Am. J. Physiol. Lung Cell. Mol. Physiol.* 297, L794. doi:10.1152/ajplung.00237.2009

Prakriya, M., and Lewis, R. S. (2015). Store-operated calcium channels. *Physiol. Rev.* 95, 1383–1436. doi:10.1152/physrev.00020.2014

Qiu, C., Liu, W., Shi, F., Fen, M., Ren, L., and Qi, H. (2017). Silencing of β1 integrin regulates airway remodeling by regulating the transcription of SOCE-associated genes in asthmatic mice. *Mol. Med. Rep.* 16, 2645–2651. doi:10.3892/mmr.2017.6863

Safholm, J., Lovdahl, C., Swedin, L., Boels, P. J., Dahlen, S. E., Arner, A., et al. (2011). Inflammation-induced airway smooth muscle responsiveness is strain dependent in mice. *Pulm. Pharmacol. Ther.* 24, 361–366. doi:10.1016/j.pupt.2011.01.001

Sieck, G., Han, Y., Pabelick, C., and Prakash, Y. (2001). Temporal aspects of excitation-contraction coupling in airway smooth muscle. *J. Appl. physiology* 91, 2266–2274. doi:10.1152/jappl.2001.91.5.2266

Sneyd, J., Han, J., Wang, L., Chen, J., Yang, X., Tanimura, A., et al. (2017). On the dynamical structure of calcium oscillations. *Proc. Natl. Acad. Sci. U. S. A.* 114, 1456–1461. doi:10.1073/pnas.1614613114

Spinelli, A. M., Gonzalez-Cobos, J. C., Zhang, X., Motiani, R. K., Rowan, S., Zhang, W., et al. (2012). Airway smooth muscle STIM1 and Orai1 are upregulated in asthmatic mice and mediate PDGF-activated SOCE, CRAC currents, proliferation, and migration. *Pflugers Arch.* 464, 481–492. doi:10.1007/s00424-012-1160-5

Stenberg, H., Diamant, Z., Ankerst, J., Bjermer, L., and Tufvesson, E. (2017). Small airway involvement in the late allergic response in asthma. *Clin. Exp. Allergy* 47, 1555–1565. doi:10.1111/cea.13036

Van Hove, C. L., Maes, T., Cataldo, D. D., Gueders, M. M., Palmans, E., Joos, G. F., et al. (2009). Comparison of acute inflammatory and chronic structural asthma-like responses between C57BL/6 and BALB/c mice. *Int. Arch. Allergy Immunol.* 149, 195–207. doi:10.1159/000199715

Wagers, S. S., Haverkamp, H. C., Bates, J. H., Norton, R. J., Thompson-Figueroa, J. A., Sullivan, M. J., et al. (2007). Intrinsic and antigen-induced airway hyperresponsiveness are the result of diverse physiological mechanisms. *J. Appl. Physiol.* 102, 221–230. doi:10.1152/japplphysiol.01385.2005

Wang, I. Y., Bai, Y., Sanderson, M. J., and Sneyd, J. (2010). A mathematical analysis of agonist- and KCl-induced Ca(2+) oscillations in mouse airway smooth muscle cells. *Biophys. J.* 98, 1170–1181. doi:10.1016/j.bpj.2009.12.4273

Wright, D. B., Tripathi, S., Sikarwar, A., Santosh, K. T., Perez-Zoghbi, J., Ojo, O. O., et al. (2013). Regulation of GPCR-mediated smooth muscle contraction: Implications for asthma and pulmonary hypertension. *Pulm. Pharmacol. Ther.* 26, 121–131. doi:10.1016/j.pupt.2012.06.005

Zou, J. J., Gao, Y. D., Geng, S., and Yang, J. (2011). Role of STIM1/Orai1-mediated store-operated Ca^{2+} entry in airway smooth muscle cell proliferation. *J. Appl. Physiol.* 110, 1256–1263. doi:10.1152/japplphysiol.01124.2010

frontiers | Frontiers in Cell and Developmental Biology

TYPE Original Research
PUBLISHED 10 July 2023
DOI 10.3389/fcell.2023.1192929

EDITED BY
Chunheng Mo,
Sichuan University, China

REVIEWED BY
Sarah Ashley,
Royal Children's Hospital, Australia
Jing Zhang,
Sichuan University, China

*CORRESPONDENCE
Linyuan Zhou,
✉ 1515878990@qq.com

†These authors have contributed equally to this work

RECEIVED 24 March 2023
ACCEPTED 24 May 2023
PUBLISHED 10 July 2023

CITATION
Zhou L and Xu H (2023), Feasibility of exercise therapy for children with asthma: a meta-analysis.
Front. Cell Dev. Biol. 11:1192929.
doi: 10.3389/fcell.2023.1192929

Feasibility of exercise therapy for children with asthma: a meta-analysis

Linyuan Zhou*† and Haofu Xu†

Special Operation College of PLA, Guangzhou, China

Background: Although numerous studies have demonstrated the clear benefits of exercise for people with asthma, controversy remains. This study evaluated the effects of sustained exercise types on lung function and quality of life in patients with asthma.

Methods: We searched PubMed, EMBASE, Web of Science, Cochrane Library, China National Knowledge Infrastructure (CNKI), and Wanfang database since January 2000 to August 2022 .included randomized controlled trials (RCTs) of asthmatic children intervened with exercise. The outcomes were lung function and asthma-related quality of life. Fixed-effects model ($I2 \leq 50\%$) or random-effects model ($I2 > 50\%$) was applied to calculate the pooled effects. Funnel plots were quantified to present publication bias, and a P value <0.05 was statistically significant.

Results: Eventually, 15 trials conformed to the selection criteria. The exercise group significantly improved lung function (FEV1 and FVC) in asthmatic children compared with the control group. Forced Expiratory Volume in 1 Second (MD = 2.12, 95%CI = 0.70, 3.53; $p = 0.003$; $I^2 = 15\%$); Forced Vital Capacity (MD = 2.78, 95%CI = 1.26, 4.31; $p = 0.0004$; $I^2 = 56\%$). The immune system markers IL-6 and TNF-α, were significantly reduced in the exercise group. Interleukin-6 (MD = –0.49, 95%CI = –0.81, –0.17; $p = 0.003$; $I^2=0\%$); tumor necrosis factor-α (MD = –0.54, 95%CI = –0.92, –0.15; $p = 0.006$; $I^2 = 0\%$). That quality of life (PAQLQ) was significantly improved in children with asthma in the exercise group. PAQLQ-Total score (MD = 1.06, 95%CI = 0.46, 1.66; $p = 0.006$; $I^2 = 94\%$); PAQLQ-Emotional (MD = 0.91, 95%CI = 0.76, 1.06; $p<0.00001$; $I^2 = 90\%$); PAQLQ-symptoms (MD = 0.87, 95%CI = 0.71, 1.02; $p<0.00001$; $I^2 = 95\%$); PAQLQ-activities (MD = 1.20, 95%CI = 0.58, 1.82; $p = 0.00001$; $I^2 = 93\%$). Meta-analysis showed significant improvements in body composition in the exercise group. BMI (MD = –2.42, 95%CI = –4.40, 0.44; $p = 0.02$; $I^2 = 85\%$).

Conclusions: This meta-analysis demonstrated the effectiveness of exercise in improving pulmonary function index (FEV1, FVC), immune system (IL-6, TNF-α, Feno), exercise ability (6MWT), body composition (BMI), and quality of life (PAQLQ) in asthmatic children. Asthmatic children should regularly participate in physical exercise.

KEYWORDS

asthma, exercise therapy, children, lung function, immune system

1 Introduction

Asthma is one of the most common chronic diseases among adults and children all around the world. Asthma is a heterogeneous disease characterized by chronic airway inflammation and airway hyperresponsiveness. The chronic inflammation causes associated airway hyperresponsiveness that leads to recurrent wheezing, cough, breathlessness, and chest tightness, which often triggers attacks or exacerbates at night and in the early morning. Around 300 million people of all ages experience asthma and related complications, and about 250,000 people die from asthma each year (Bousquet and Khaltaev, 2007). Experts predict that 100 million people will still live with asthma in 2025. The prevalence of childhood asthma in China soared from 1.09% in 1990 to 3.02% in 2010 (BAO Yixiao et al., 2016). However, standardized treatment of asthma is mature and has been used globally for many years. With the introduction of the GINA program and the implementation of the guidelines for the prevention and treatment of childhood asthma in China, the early diagnosis and management of childhood asthma in Chinese pediatricians have been enhanced. However, the overall control of childhood asthma is still poor (Sha Li et al., 2016). The Third National Childhood Asthma Epidemiological Survey in China showed that 77% of children with asthma had an acute episode in the past year (LIU Chuanhe et al., 2013). Medication has long been the primary means of asthma control, but physical therapy is another effective means. Physical therapy mainly includes exercise therapy, respiratory exercise, and muscle training (Wang et al., 2019).

Although some scholars have conducted systematic reviews and meta-analyses on the effects of physical therapy on childhood asthma, these scholars did not exclude adults in the research process. Also, they lumped together three different physical therapy methods: exercise therapy, respiratory exercise and respiratory muscle training (Wang et al., 2019; hang et al., 2021; YANG Yiyun et al., 2021). Compared with respiratory exercise and respiratory muscle training, exercise therapy is more social and recreational, and exercise therapy can better promote children’s physical development. Exercise therapy has also been shown as safe and effective, and the benefits of regular exercise are significant for children with asthma (Lang, 2019). Therefore, this meta-analysis only focused on children and excluded respiratory exercise and muscle training. This study aimed to show the effects of different exercise intensity, no exercise modes, and other exercise intervention times on children’s lung function and quality of life and to provide recommendations and references for pediatricians to treat and control children’s asthma using exercise therapy.

2 Methods

This meta-analysis was performed following the statement of the Preferred Reporting Items for Systematic Review and Meta-Analysis (PRISMA) guidelines (Moher et al., 2009) in order to provide comprehensive and transparent reporting of methods and results.

2.1 Search strategy

Electronic article searches were conducted between January 2000 and August 2022 in PubMed, Cochrane Library, Web of Science, EMBASE, China National Knowledge Infrastructure (CNKI), and Wanfang database. The language of articles was English and Chinese. The search terms in this review were a combination of exercise intervention terms AND asthma related terms AND adolescent population terms. Figure 1 provides the keywords and search strategy. Three researchers independently screened titles, abstracts, and full-text articles of potentially relevant studies. We further searched for additional relevant articles in Google Scholar and identified potential references for inclusion from previous systematic review and meta-analyses.

2.2 Eligibility criteria

The inclusion criteria for studies are as follows: 1) Participants: Participants should have asthma diagnosed by well-defined or internationally recognized criteria, and they should not be older than 18 or younger than 6, regardless of gender, ethnicity, or region. 2) Intervention type: We included studies with an exercise training intervention in children with asthma, and the intervention period less than 2 weeks were acceptable. 3) Outcome: At least one of the four main outcomes (lung function, airway inflammation, exercise ability, and health and life quality) had to be reported to be included. The specific outcome measures of lung function were Forced Vital Capacity (FVC), Forced Expiratory Volume in 1 Second (FEV1), and Peak Expiratory Flow (PEF). The exercise capacity outcome measure was six walk minute test (6WMT). The airway inflammation indicators were tumor necrosis factor-α (TNF-α), Interleukin- 6 (IL-6), and Fractional exhaled nitric oxide (FeNO). The health and life quality outcomes were Pediatric Asthma Quality of Life Questionnaire (PAQLQ) and Body Mass Index (BMI). 4) Study design: We included randomized controlled trials that compared exercise training interventions with no intervention.

2.3 Studies screening and data extraction

Two authors independently evaluated all studies for potential eligibility. In the case of disagreement, a third party adjudicated whether a study met the inclusion criteria. The documents were transferred to a third researcher for adjudication if they disagreed. For each study, data were extracted regarding the first author’s last name, year of publication, country, participants characteristics (mean age, sample size), exercise intervention (type, duration, frequency, intensity), and the mean values of two time points (pre- and post-intervention) with corresponding standard deviations. The outcome measures were: FVC, FeV1, PEF, 6WMT, TNF-α, IL-6, FeNO, BMI, PAQLQ-Total score, PAQLQ-Emotional score, PAQLQ-symptoms score, and PAQLQ-activities score. When there was insufficient information the research team attempted to contact the corresponding author. Tables 1, 2 provides detailed information on these studies.

2.4 Study selection

We searched identified 53,865 articles, including 45,042 articles from PubMed, 1,253 articles from the Cochrane Library studies, 6,285 articles from the Embase studies, 809 articles from the Web of Science studies, 198 articles from the WanFang, and 278 articles from the CNKI.47,162 duplicate articles eliminated. By reading the

TABLE 1 Exercise Program details of eligible studies.

Author	Years	Exercise	Duration (weeks) x Frequency(d/wk)	Time (minutes)	Intensity
Winn	2021	HIIT	16x3	30	90%HR_{max}
Qiong Chen	2020	Aerobic Exercise	12x3	40-60	1~4wk50–60%HR_{max} 5~12wk60–70%HR_{max}
Jing Tan	2019	Exercise	12x3	20-30	No
Abdelbasset	2018	Aerobic Exercise	10x3	40	50–70%HR_{max}
Carew	2017	Swimming,Football And Basketball	6x1	40	No
Jia Li	2016	HIIT and Aerobic exercise	8x3	40	90%VO_{2peak} and 50% VO_{2peak}
Latorre-Roman	2014	Combined Training	12x3	60	No
Andrade	2014	Aerobic Exercise	6x3	1~2wk 20 3~6wk 30	70–80%HR_{max}
Kader	2013	Aerobic Exercise	8X4	25-45	60–80%HR_{max}
Onur	2011	Aerobic Exercise	8x2	45	80%HR_{max}
Wicher	2010	Swimming	12x2	60	No
JengShing Wang	2009	Swimming	6x3	50	No
Basaran	2006	Basketball	8x3	60	No
Counil	2003	Aerobic Exercise	6x3	45	No
Weisgerber	2003	Swimming	5-6x3	45	No

title and abstract, six thousand five hundred seventy-three irrelevant documents were removed. There were 130 to read, 115 to delete, and 15 included in the Meta-analysis. Figure 2 shows a flow chart of the search screening process (Counil et al., 2003; Weisgerber et al., 2003; Basaran et al., 2006; WANG and HUNG, 2009; Wicher et al., 2010; Onur et al., 2011; El-Kader et al., 2013; de Andrade et al., 2014; Latorre-Román et al., 2014; Jia et al., 2016; Abdelbasset et al., 2018; Carew and Cox, 2018; Jing et al., 2019; Chen et al., 2020; Winn et al., 2021).

2.5 Risk of bias in studies

Two reviewers independently assessed each included study using the Cochrane risk of bias tool. For RCTs, the Cochrane Collaboration Guideline specifies six domains, including bias arising from the randomization process, bias owing to deviations from intended interventions, bias owing to missing outcome data, bias in measurement of the outcome, bias in selection of the reported, and other biases (Higgins et al., 2011). Risk of bias was stated as "low risk," "high risk," or "unclear."

Risk of bias are provided in Table 2. 6/15 studies described the randomization method of the subjects in detail. 2/15 studies described the allocation concealment scheme of the subjects in detail. 2/15 studies blinded patients and experimenters, and 3/15 studies blinded outcome evaluators. 10/15 studies reported the integrity of the results in detail, 1 study did not report the number of lost visits in detail, and 4 studies had too many lost visits, which affected data integrity. 13/15 studies reported the results of the data in detail, and 2 studies did not report the results. There was no other bias in 14/15 studies.

2.6 Publication bias

Publication bias was assessed by funnel plot and Egger test. First, funnel plot was drawn by Stata 17 software, and then Egger test was carried out. When $p>0.05$, there was no publication bias. The risk of bias is summarized in Figure 3 and Figure 4.

2.7 Statistical analysis

A meta-analysis was performed using ReMan software (version 5.3) to evaluate the effect of exercise intervention on children with asthma. Effect sizes for main outcomes are expressed as standardized mean differences (SMD). If the standard deviation was not reported, it was estimated from the reported standard error, the 95% confidence interval, interquartile range or *p*-value related to the pertinent number of participants. To better interpret SMD, we used Hedges "gas small (0.2), medium (0.5) and large (0.8) (Cohen, 2013)." The heterogeneity between trial results was tested for I2 statistics. I2 values of <25%, 25%–50%, and >50% are acknowledged to represent small, medium, and large amounts of heterogeneity (Higgins and Thompson, 2002).

If heterogeneity is greater than 50%, a sensitivity analysis will be performed. Moreover, two analyses with subgroups were studied: exercise type (HIIT, Swimming, Ball, Aerobic exercise) and frequency of the exercise intervention (≤8 weeks vs. > 8 weeks).

TABLE 2 Demographics and outcomes.

Author	years	Participants	Age (years)	Gender	BMI	Overcomes				
						Lung function	Athletic ability	Immune system	Body composition	Quality of life
Winn	2021	E(29) C(68)	E(13.1±1.0) C(12.9±1.2)	78M & 77F	22.7±4.7	FEV1% FVC% PEF%	No	FeNO	BMI	PAQLQ
Qiong Chen	2020	E(20) C(20)	E(11.4 ± 2.8) C(12.1 ± 3.4)	14M & 26F	No	FVC% FEV1% PEF%	6MWT	No	No	PAQLQ
Jing Tan	2019	E(80) C(76)	E(8.2 ± 2.1) C(8.1 ± 2.1)	97M & 59F	No	FVC% FEV1% PEF%	No	No	No	No
Abdelbasset	2018	E(19) C(19)	E(9.8 ± 2.3) C(11.7 ± 2.3)	23M & 15F	21.3±3.0	FEV1% FVC%	6MWT	No	BMI	PAQLQ
Carew	2017	E(29) C(12)	E(13.5 ± 1.8) C(12.0 ± 3.1)	24M & 17F	No	FVC% FEV1% PEF%	No	No	No	No
Jia Li	2016	E(29) C(12)	E(12.5 ± 1.6) C(10.8 ± 1.3)	26M & 15F	18.3±2.0 18.2±3.2	FVC% FEV1% PEF%	6MWT	IL-6 TNF-α FeNO	BMI	No
Latorre-Roman	2014	E(58) C(47)	E(11.5 ± 1.0) C(11.5 ± 1.4)	Not Described	17.49±2.8	No	6MWT	No	BMI	PAQLQ
Andrade	2014	E(10) C(17)	E(11.7 ± 2.3) C(11.4 ± 2.3)	15M & 12F	No	No	6MWT	No	No	PAQLQ
Kader	2013	E(40) C(40)	E(13.2 ± 3.5) C(12.6 ± 3.2)	42M & 38F	27.15 ± 2.38	No	No	IL-6 TNF-α	BMI	No
Onur	2011	E(30) C(13)	E(9.8 ± 1.8) C(10.3 ± 2.0)	28M & 15F	No	FEV1% FVC%	No	No	No	No
Wicher	2010	E(30) C(31)	E(10.4 ± 3.1) C(10.9 ± 2.6)	27M & 34F	No	FEV1% FVC%	No	No	No	No
JengShing Wang	2009	E(15) C(15)	E(9-11) C(9-11)	20M & 10F	No	FEV1% FVC%	No	No	No	No
Basaran	2006	E(31) C(31)	E(10.4 ± 2.2) C(10.5 ± 2.1)	40M & 22F	No	FEV1% FVC% PEF%	6MWT	No	No	PAQLQ
Counil	2003	E(7) C(7)	E(13.9 ± 0.8) C(14.0 ± 0.6)	14M	No	FEV1%	No	No	No	No
Weisgerber	2003	E(5) C(3)	E(8.4 ± 1.5) C(7.3 ± 0.6)	4M & 4F	No	FEV1% FVC% PEF%	No	No	No	No

FEV1, Forced Expiratory Volume in 1 Second; FVC, Forced Vital Capacity; PEF, Peak Expiratory Flow; 6MWT, 6-min walking test; IL-6, Interleukin- 6; TNF-α tumor necrosis factor-α; FeNO, Fractional Exhaled Nitric Oxide; BMI, Body Mass Index; PAQLQ, Paediatric Asthma Quality of Life Questionnaire.

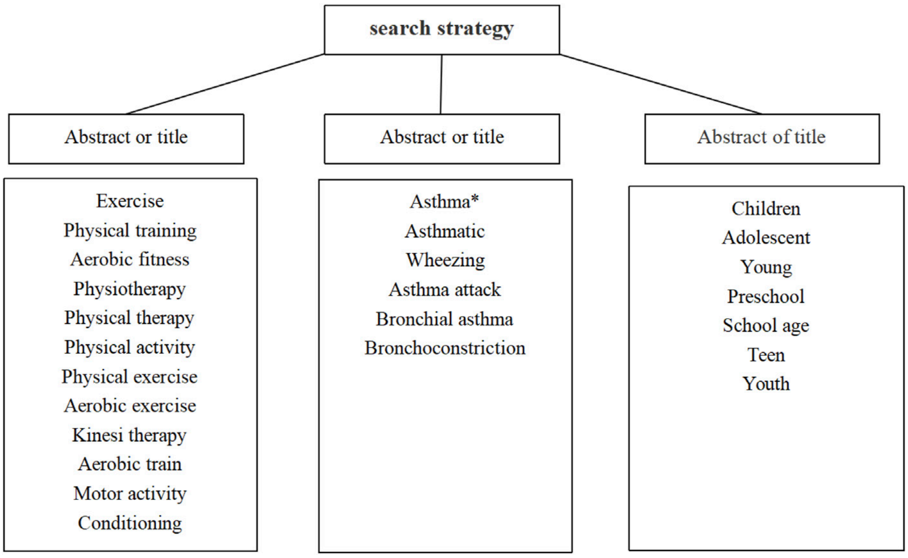

FIGURE 1
A search strategy for English database using the following keywords b and search strategy using the following keywords to search Chinese databases.

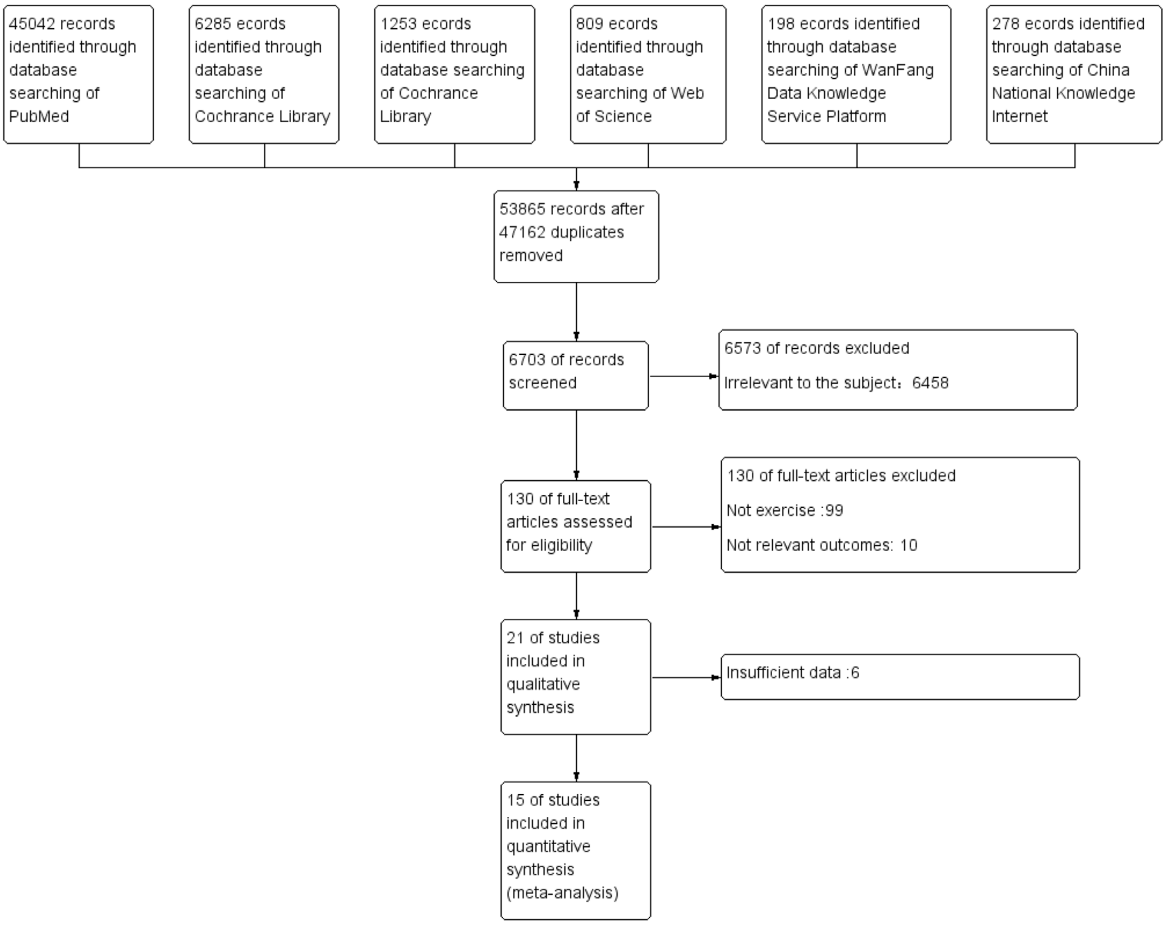

FIGURE 2
Search screening process.

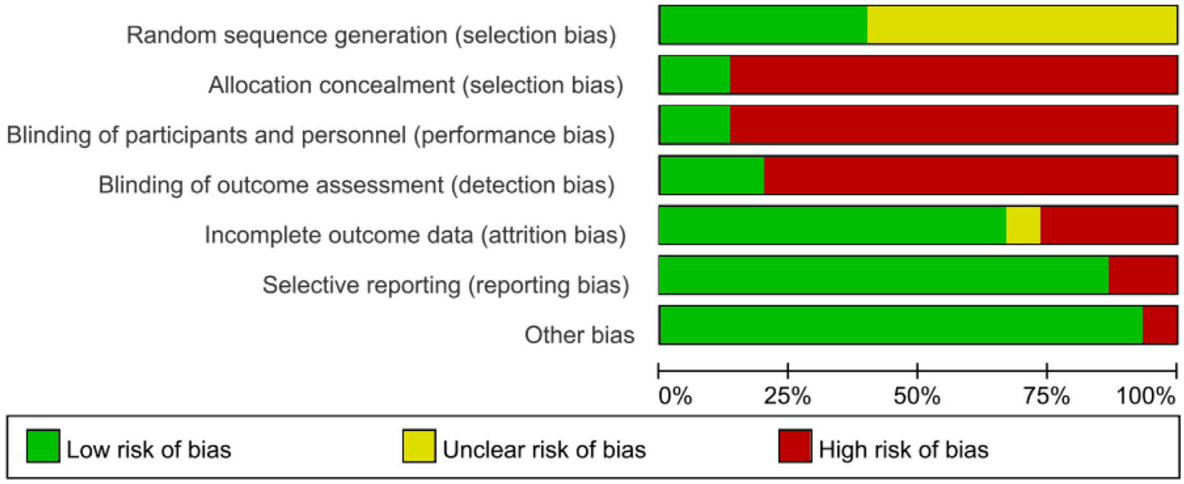

FIGURE 3
Overall risk bias evaluation.

3 Meta-analysis

3.1 Effects of exercise on lung function in children with asthma

Meta-analysis showed that the exercise group significantly improved lung function (FEV1 and FVC) in asthmatic children compared with the control group, but exercise did not improve PEF alone significantly. Forced Expiratory Volume in 1 Second (MD = 2.12, 95% CI = 0.70, 3.53; $p = 0.003$; $I^2 = 15\%$); Forced Vital Capacity (MD = 2.78, 95% CI = 1.26, 4.31; $p = 0.0004$; $I^2 = 56\%$), Peak Expiratory Flow (MD = 1.84, 95% CI = −2.83, 6.51; $p = 0.44$; $I^2 = 72\%$) (Figure 5).

The results of the subgroup analysis showed that aerobic exercise and swimming significantly improved lung function (FEV1 and FVC) in children with asthma and that HIIT and ball exercise improvements were not significant. Exercise intervention of over 8 weeks significantly improved lung function (FEV1 and FVC) in children with asthma, and exercise intervention effects of less than 8 weeks were not significant. The exercise was insignificant in children with asthma (PEF) (Table 4).

Effects of different exercise modes on FEV1 in asthmatic children. Swimming (MD = 5.98, 95% CI = 0.85, 11.11; $p = 0.02$; $I^2 = 0\%$); Aerobic exercise (MD = 2.89, 95% CI = 0.58, 5.19; $p = 0.01$; I2 = 57%); Ball (MD = 0.79, 95% CI = −3.94, 5.51; $p = 0.74$; $I^2 = 0\%$); HIIT (MD = −0.95, 95% CI = 5.83, 3.92; $p = 0.70$; $I^2 = 0\%$). Effects of different exercise modes on FVC in asthmatic children. Swimming (MD = 11.07, 95% CI = 6.33, 15.82; $p < 0.00001$; $I^2 = 24\%$); Aerobic exercise (MD = 5.06, 95% CI = 1.57, 8.54; $p = 0.004$; I2 = 30%); Ball (MD = 0.77, 95% CI = −3.88, 5.43; $p = 0.74$; $I^2 = 0\%$); HIIT (MD = 0.80, 95% CI = −4.28, 5.89; $p = 0.76$; $I^2 = 46\%$). Effects of different exercise modes on PEF in asthmatic children: Swimming (MD = 2.49, 95% CI = −7.80, 12.78; $p = 0.64$; $I^2 = 0\%$); Aerobic exercise (MD = 0.61, 95% CI = 4.26, 5.49; $p = 0.8$; $I^2 = 0\%$); Ball (MD = 0.06, 95% CI = −5.94, 6.07; $p = 0.98$; $I^2 = 0\%$); HIIT (MD = −1.34, 95% CI = −6.63, 3.9; $p = 0.62$; $I^2 = 46\%$).

Influence of different exercise intervention cycles on FEV1 in asthmatic children. More than 8 weeks (MD = 2.89, 95% CI = 1.09, 4.69; $p = 0.02$; $I^2 = 55\%$); less than 8 weeks (MD = 0.85, 95% CI = 1.45, 3.15; $p = 0.47$; $I^2 = 0\%$). Influence of different exercise intervention cycles on FVC in asthmatic children. More than 8 weeks (MD = 5.88, 95% CI = −1.30, 10.46; $p = 0.01$; $I^2 = 56\%$); less than 8 weeks (MD = 0.70, 95% CI = −2.32, 3.71; $p = 0.65$; $I^2 = 78\%$). Influence of different exercise intervention cycles on PEF in asthmatic children. More than 8 weeks (MD = 4.65, 95% CI = −3.68, 12.98; $p = 0.89$; $I^2 = 0\%$); less than 8 weeks (MD = −0.27, 95% CI = −3.93, 3.39; $p = 0.27$; $I^2 = 85\%$).

3.2 Effects of exercise on the immune system in children with asthma

Meta-analysis showed that the immune system markers, IL-6 and TNF-α, were significantly reduced in the exercise group. However, exercise did not significantly improve FeNO in asthmatic children: Interleukin-6 (MD = −0.49, 95% CI = −0.81, −0.17; $p = 0.003$; $I^2 = 0\%$); tumor necrosis factor-α (MD = −0.54, 95% CI = −0.92, −0.15; $p = 0.006$; $I^2 = 0\%$); Fractional exhaled nitric oxide (MD = −2.45, 95% CI = −11.91, 7.02; $p = 0.61$; $I^2 = 0\%$) (Table 3).

3.3 Effects of exercise on the quality of life index in children with asthma

Meta-analysis showed that quality of life (PAQLQ) was significantly improved in children with asthma in the exercise group. PAQLQ-Total score (MD = 1.06, 95% CI = 0.46, 1.66; $p = 0.006$; $I^2 = 94\%$); PAQLQ-Emotional (MD = 0.91, 95% CI = 0.76, 1.06; $p < 0.00001$; $I^2 = 90\%$); PAQLQ-symptoms (MD = 0.87, 95% CI = 0.71, 1.02; $p < 0.00001$; $I^2 = 95\%$); PAQLQ-activities (MD = 1.20, 95% CI = 0.58, 1.82; $p = 0.00001$; $I^2 = 93\%$) (Table 3).

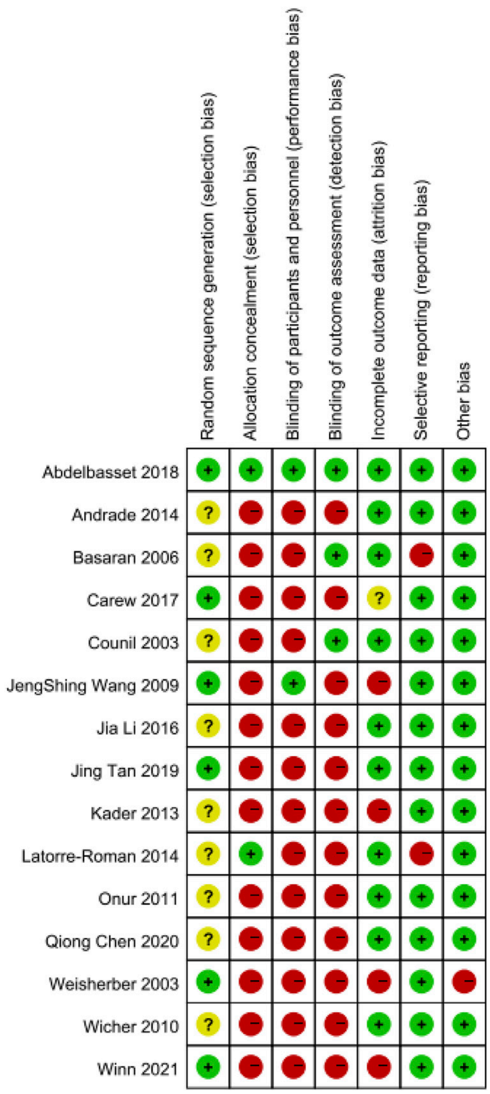

	Random sequence generation (selection bias)	Allocation concealment (selection bias)	Binding of participants and personnel (performance bias)	Binding of outcome assessment (detection bias)	Incomplete outcome data (attrition bias)	Selective reporting (reporting bias)	Other bias
Abdelbasset 2018	+	+	+	+	+	+	+
Andrade 2014	?	−	−	−	+	+	+
Basaran 2006	?	−	−	+	+	−	+
Carew 2017	+	−	−	−	?	+	+
Counil 2003	?	−	−	+	+	+	+
JengShing Wang 2009	+	−	+	−	−	+	+
Jia Li 2016	?	−	−	−	+	+	+
Jing Tan 2019	+	−	−	−	+	+	+
Kader 2013	?	−	−	−	−	+	+
Latorre-Roman 2014	?	+	−	−	+	−	+
Onur 2011	?	−	−	−	+	+	+
Qiong Chen 2020	?	−	−	−	+	+	+
Weisherber 2003	+	−	−	−	−	+	−
Wicher 2010	?	−	−	−	+	+	+
Winn 2021	+	−	−	−	−	+	+

FIGURE 4
Overall risk bias summary.

3.4 Effects of exercise on motor ability and body composition in children with asthma

Meta-analysis showed significant improvements in body composition in the exercise group. BMI (MD = −2.42, 95% CI = −4.40, 0.44; p = 0.02; I^2 = 85%) (Table 3). Subgroup analysis showed that aerobic exercise significantly improved BMI in children with asthma, and exercise intervention for less than 8 weeks significantly improved BMI in children with asthma (Table 4).

Effects of different exercise modes on BMI in asthmatic children. Aerobic exercise (MD = −3.12, 95% CI = −5.58, −0.66; p = 0.01; I^2 = 78%); HIIT (MD = −0.06, 95% CI = −5.58, −0.66; p = 0.96; I^2 = 43%); Influence of different exercise intervention cycles on BMI in asthmatic children. More than 8 weeks (MD = −1.90, 95%CI-5.15, 1.35; p = 0.25; I^2 = 85%); less than 8 weeks (MD = −2.99, 95% CI = −5.70, −0.28; p = 0.03; I^2 = 77%).

The meta-analysis showed a significant improvement in 6WMT in the exercise group. 6WMT (MD = 115.33, 95% CI = 54.64, 176.02; p = 0.0002; I^2 = 94%).

4 Discussion

This meta-analysis demonstrated the effectiveness of exercise in improving pulmonary function index (FEV1, FVC), immune system (IL-6, TNF-α, Feno), exercise ability (6MWT), body composition (BMI), and quality of life (PAQLQ) in asthmatic children. Asthmatic children should regularly participate in physical exercise.

4.1 Effects on lung function

GINA (Global Initiative for Asthma) recommends exercise therapy as a treatment for children with asthma (Bateman et al., 2008). Exercise is also an integral part of the treatment of children with asthma. Exercise-induced asthma is the main reason why most parents ban their asthmatic children from participating in the exercise (de Valois Correia et al., 2012). The effect of exercise on the lung function of children with asthma has been controversial in the past. However, a growing number of published studies have shown that children with asthma can benefit from regular exercise training (Higgins and Thompson, 2002; Higgins et al., 2011; Cohen, 2013). Our meta-analysis shows that exercise intervention can effectively improve pulmonary function parameters FEV1 and FVC in asthmatic children. This is consistent with Xinggui Wu and coworkers' conclusion (Wu et al., 2020). FEV1 is an essential index of airway function, which reflects airway patency, airway function, and respiratory muscle strength, and used to evaluate the degree of airway obstruction and lesion in asthmatic patients (Alfrayh et al., 2014). FVC reflected the vital capacity of asthmatic patients and be used to assess whether the patients had dysfunction of ventilation. The increase of FEV1 and FVC indicated that exercise could improve airway ventilation function and alleviate asthma symptoms in children with asthma. Our results reinforce previous findings (Wu et al., 2020). Exercise can effectively improve the lung function of children with asthma, which is of great clinical significance. Our meta-analysis results showed that exercise had no significant improving effect on PEF in asthmatic children. This is inconsistent with Xinggui Wu and coworkers' conclusion (Wu et al., 2020). Due to age differences in subjects, our study focused primarily on 7- to 12-year-old asthmatic children and did not include adults. This suggests that exercise intervention may have different effects on PEF in patients of different ages.

There is no consensus as to which exercise program is most beneficial for children with asthma. Hence, our study used a subgroup analysis of exercise patterns and cycles. We examined the effects of swimming, aerobic exercise, ball games, and HIIT exercise on lung function in children with asthma. We found that swimming and aerobic exercise significantly improved asthmatic children's pulmonary function index (FEV1, FVC), while ball and HIIT exercise had little effect on FEV1 FVC in asthmatic children. HIIT and ball games did not significantly improve FEV1. This is inconsistent with the findings of Ertürk et al. (2021), which showed that long-term application of HIIT

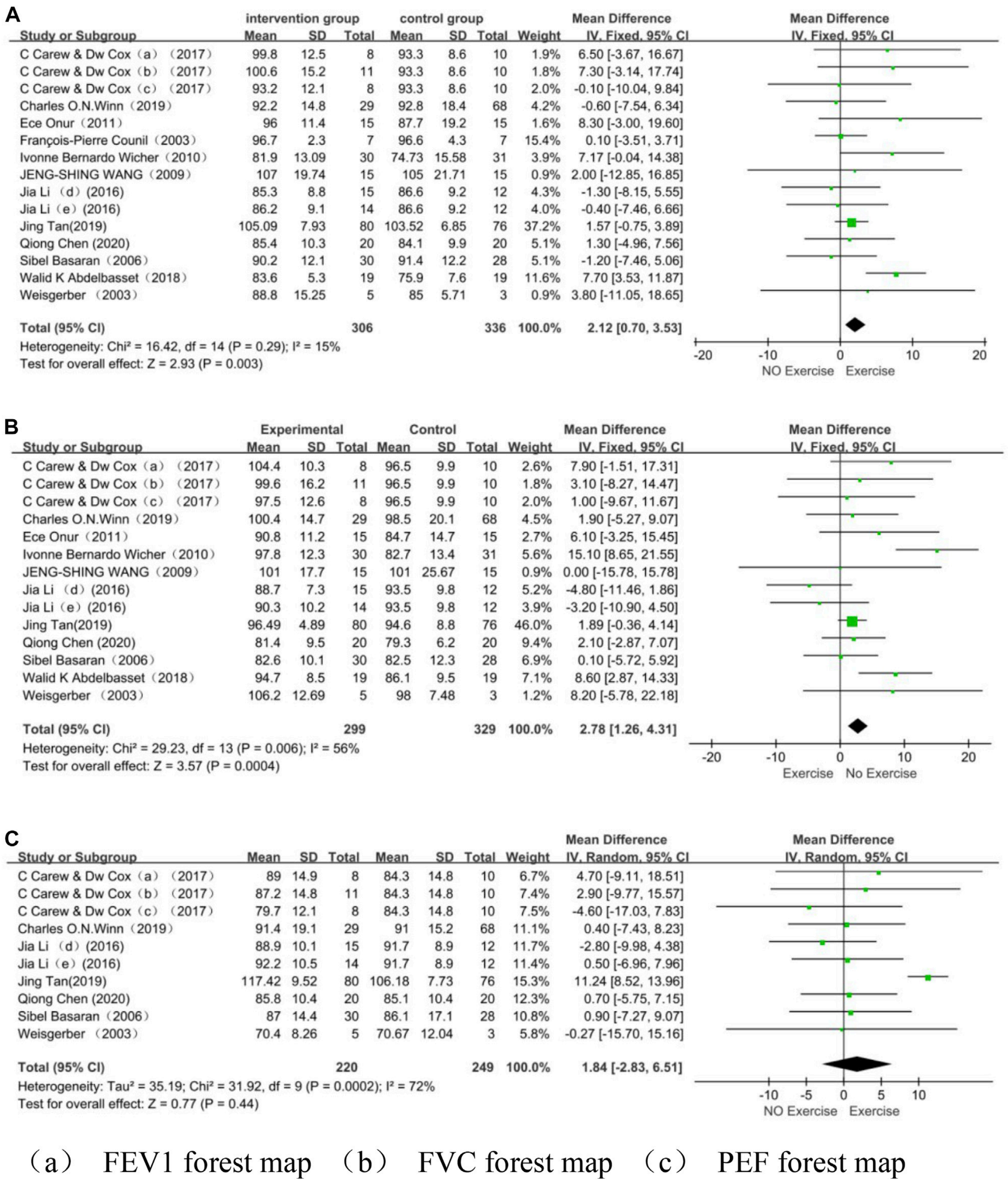

A

Study or Subgroup	intervention group Mean	SD	Total	control group Mean	SD	Total	Weight	Mean Difference IV, Fixed, 95% CI
C Carew & Dw Cox（a）（2017）	99.8	12.5	8	93.3	8.6	10	1.9%	6.50 [-3.67, 16.67]
C Carew & Dw Cox（b）（2017）	100.6	15.2	11	93.3	8.6	10	1.8%	7.30 [-3.14, 17.74]
C Carew & Dw Cox（c）（2017）	93.2	12.1	8	93.3	8.6	10	2.0%	-0.10 [-10.04, 9.84]
Charles O.N.Winn（2019）	92.2	14.8	29	92.8	18.4	68	4.2%	-0.60 [-7.54, 6.34]
Ece Onur（2011）	96	11.4	15	87.7	19.2	15	1.6%	8.30 [-3.00, 19.60]
François-Pierre Counil（2003）	96.7	2.3	7	96.6	4.3	7	15.4%	0.10 [-3.51, 3.71]
Ivonne Bernardo Wicher（2010）	81.9	13.09	30	74.73	15.58	31	3.9%	7.17 [-0.04, 14.38]
JENG-SHING WANG（2009）	107	19.74	15	105	21.71	15	0.9%	2.00 [-12.85, 16.85]
Jia Li（d）(2016)	85.3	8.8	15	86.6	9.2	12	4.3%	-1.30 [-8.15, 5.55]
Jia Li（e）(2016)	86.2	9.1	14	86.6	9.2	12	4.0%	-0.40 [-7.46, 6.66]
Jing Tan(2019)	105.09	7.93	80	103.52	6.85	76	37.2%	1.57 [-0.75, 3.89]
Qiong Chen (2020)	85.4	10.3	20	84.1	9.9	20	5.1%	1.30 [-4.96, 7.56]
Sibel Basaran（2006）	90.2	12.1	30	91.4	12.2	28	5.1%	-1.20 [-7.46, 5.06]
Walid K Abdelbasset（2018）	83.6	5.3	19	75.9	7.6	19	11.6%	7.70 [3.53, 11.87]
Weisgerber（2003）	88.8	15.25	5	85	5.71	3	0.9%	3.80 [-11.05, 18.65]
Total (95% CI)			**306**			**336**	**100.0%**	**2.12 [0.70, 3.53]**

Heterogeneity: Chi² = 16.42, df = 14 (P = 0.29); I² = 15%
Test for overall effect: Z = 2.93 (P = 0.003)

B

Study or Subgroup	Experimental Mean	SD	Total	Control Mean	SD	Total	Weight	Mean Difference IV, Fixed, 95% CI
C Carew & Dw Cox（a）（2017）	104.4	10.3	8	96.5	9.9	10	2.6%	7.90 [-1.51, 17.31]
C Carew & Dw Cox（b）（2017）	99.6	16.2	11	96.5	9.9	10	1.8%	3.10 [-8.27, 14.47]
C Carew & Dw Cox（c）（2017）	97.5	12.6	8	96.5	9.9	10	2.0%	1.00 [-9.67, 11.67]
Charles O.N.Winn（2019）	100.4	14.7	29	98.5	20.1	68	4.5%	1.90 [-5.27, 9.07]
Ece Onur（2011）	90.8	11.2	15	84.7	14.7	15	2.7%	6.10 [-3.25, 15.45]
Ivonne Bernardo Wicher（2010）	97.8	12.3	30	82.7	13.4	31	5.6%	15.10 [8.65, 21.55]
JENG-SHING WANG（2009）	101	17.7	15	101	25.67	15	0.9%	0.00 [-15.78, 15.78]
Jia Li（d）(2016)	88.7	7.3	15	93.5	9.8	12	5.2%	-4.80 [-11.46, 1.86]
Jia Li（e）(2016)	90.3	10.2	14	93.5	9.8	12	3.9%	-3.20 [-10.90, 4.50]
Jing Tan(2019)	96.49	4.89	80	94.6	8.8	76	46.0%	1.89 [-0.36, 4.14]
Qiong Chen (2020)	81.4	9.5	20	79.3	6.2	20	9.4%	2.10 [-2.87, 7.07]
Sibel Basaran（2006）	82.6	10.1	30	82.5	12.3	28	6.9%	0.10 [-5.72, 5.92]
Walid K Abdelbasset（2018）	94.7	8.5	19	86.1	9.5	19	7.1%	8.60 [2.87, 14.33]
Weisgerber（2003）	106.2	12.69	5	98	7.48	3	1.2%	8.20 [-5.78, 22.18]
Total (95% CI)			**299**			**329**	**100.0%**	**2.78 [1.26, 4.31]**

Heterogeneity: Chi² = 29.23, df = 13 (P = 0.006); I² = 56%
Test for overall effect: Z = 3.57 (P = 0.0004)

C

Study or Subgroup	Mean	SD	Total	Mean	SD	Total	Weight	Mean Difference IV, Random, 95% CI
C Carew & Dw Cox（a）（2017）	89	14.9	8	84.3	14.8	10	6.7%	4.70 [-9.11, 18.51]
C Carew & Dw Cox（b）（2017）	87.2	14.8	11	84.3	14.8	10	7.4%	2.90 [-9.77, 15.57]
C Carew & Dw Cox（c）（2017）	79.7	12.1	8	84.3	14.8	10	7.5%	-4.60 [-17.03, 7.83]
Charles O.N.Winn（2019）	91.4	19.1	29	91	15.2	68	11.1%	0.40 [-7.43, 8.23]
Jia Li（d）(2016)	88.9	10.1	15	91.7	8.9	12	11.7%	-2.80 [-9.98, 4.38]
Jia Li（e）(2016)	92.2	10.5	14	91.7	8.9	12	11.4%	0.50 [-6.96, 7.96]
Jing Tan(2019)	117.42	9.52	80	106.18	7.73	76	15.3%	11.24 [8.52, 13.96]
Qiong Chen (2020)	85.8	10.4	20	85.1	10.4	20	12.3%	0.70 [-5.75, 7.15]
Sibel Basaran（2006）	87	14.4	30	86.1	17.1	28	10.8%	0.90 [-7.27, 9.07]
Weisgerber（2003）	70.4	8.26	5	70.67	12.04	3	5.8%	-0.27 [-15.70, 15.16]
Total (95% CI)			**220**			**249**	**100.0%**	**1.84 [-2.83, 6.51]**

Heterogeneity: Tau² = 35.19; Chi² = 31.92, df = 9 (P = 0.0002); I² = 72%
Test for overall effect: Z = 0.77 (P = 0.44)

FIGURE 5
(A) FEV1 forest map **(B)** FVC forest map **(C)** PEF forest map.

in patients with asthma can achieve better results in lung function and VO2max. This is probably due to the exclusion of two training structures, SIT and RST, into the HIIT study. A recent study showed that the effects of interval sprint training on airway responsiveness are similar to those of aerobic exercise (Good et al., 2019). HIIT training structure based on intermittent sprint training may be more effective in FEV1 of asthmatic children. Ball exercise did not improve FEV1 significantly, possibly due to the short period of

TABLE 3 Effects of exercise on lung function, immune system, body composition, exercise capacity and quality of life in children with asthma.

	Study(*n*)	Participants(*n*)	MD (95% CI)	I^2 (%)	*p*-value
Lung function					
FEV1	15	642	2.12 (0.70,3.53)	15	0.003
FVC	14	628	2.78 (1.26,4.31)	56	0.0004
PEF	10	513	1.84 (V2.83,6.51)	72	0.44
Immune system					
IL-6	3	132	−0.49 (−0.81, −0.17)	0	0.003
TNF-α	3	132	−0.54 (−0.92, −0.15)	0	0.006
FeNO	3	151	−2.45 (−11.91,7.02)	0	0.61
Body composition					
BMI	6	372	−2.42 (−4.40,0.44)	85	0.02
Exercise capacity					
6WMT	7	320	115.33 (54.64,176.02)	94	0.0002
The Quality of life index					
PAQLQ-Total score	6	370	1.06 (0.46,1.66)	94	0.006
PAQLQ-Emotional	6	370	0.91 (0.76,1.06)	90	<0.00001
PAQLQ-symptoms	6	370	0.87 (0.71,1.02)	95	<0.00001
PAQLQ-activities	6	370	1.20 (0.58,1.82)	93	0.00001

exercise included in the study (all less than 8 weeks) and the undetermined intensity of the exercise. Studies have shown that the average heart rate of children participating in ball exercise is higher than aerobic exercise. Ball exercise intervention significantly improves children's performance in intermittent exercise and reduces cardiovascular stress during submaximal exercise (Bendiksen et al., 2014). This suggests that the HIIT structure should be given more weight in intermittent sprint training, and the intensity of exercise should be paid more attention to in the future. For the analysis of intervention time, we chose the intervention time of 8 weeks as the node, divided into more than 8 weeks, less than or equal to 8 weeks. By comparing the intervention time, we found that more than 8 weeks of intervention time significantly improved pulmonary function index (FEV1, FVC) in children with asthma. The American Thoracic Society/European Respiratory Association recommends 2-3 exercises per week of 30 min each for at least 8 weeks (Rochester et al., 2015). We suggest that children with asthma choose aerobic exercise and swimming as exercise mode, each 30–40 min, and stick to 8 weeks.

4.2 Effects on the immune system

Asthma is characterized by the limitation of variable airflow secondary to airway narrowing, airway wall thickening, and mucus accumulation. Airway narrowing is the result of chronic airway inflammation secondary to plasma extravasation and influx of inflammatory cells (such as eosinophil granulocyte, neutrophil, lymphocyte, macrophages and mast cells), and airway hyperresponsiveness (AHR) is an important physiological feature of asthma (Boonpiyathad et al., 2019). AHR may act directly with TNF-α on airway smooth muscle, or release cysteinyl leukotriene C4, D4 indirectly.

TNF-α is produced mainly by macrophages and mast cells and promotes neutrophil (Brightling et al., 2008). IL-6 is secreted by non-white blood cells. Compared with allergic asthma, IL-6 levels are also influenced by viral infection, obesity and increased intrinsic asthma (Simpson et al., 2013; Berry et al., 2006). There was a negative correlation between the level of IL-6 in saliva and the predicted percentage of FEV1. The increase of serum IL-6 in obese asthma patients was related to the impairment of lung function (Raundhal et al., 2015; Lee et al., 2011). The expression of IL-6 and TNF-α in asthmatic patients is closely related to the severity of asthma symptoms. IL-6 and TNF-α are involved in the inflammatory reaction of asthma (Luyu, 2013). We found that exercise intervention can effectively reduce IL-6 and TNF-α levels in children with asthma. This may be due to reduced proinflammatory cytokine release and increased release of anti-inflammatory cytokines (IL-10) (Brüggemann et al., 2015). Fractional Exhaled Nitric Oxide is closely related to airway hyperresponsiveness and airway inflammation, suggesting that airway inflammatory state is an indicator of asthma inflammation (Ricciardolo et al., 2015). We found that the effects of exercise intervention on FeNo were not significant, as is consistent with Toennesen et al. (2018)'s results. This may be due to a certain overlap of FeNO levels between asthmatic and non-asthmatic children, which does not effectively distinguish the different types

TABLE 4 Subgroup analysis.

	Subgroup		Study	95% CI	*p*-Value	Chi-squared (I2) (%)
FEV1	Sport	Swimming	4	5.98 (0.85,11.11)	0.02*	0
		Aerobic exercise	5	2.89 (0.58,5.19)	0.01*	57
		Ball	3	0.79 (−3.94,5.51)	0.74	0
		HIIT	2	−0.95 (5.83,3.92)	0.70	0
FVC	Sport	Swimming	4	11.07 (6.33,15.82)	<0.00001*	24
		Aerobic exercise	3	5.06 (1.57,8.54)	0.004*	30
		Ball	3	0.77 (−3.88,5.43)	0.74	0
		HIIT	2	0.80 (−4.28,5.89)	0.76	46
PEF	Sport	Swimming	2	2.49 (−7.80,12.78)	0.64	0
		Aerobic exercise	2	0.61 (4.26,5.49)	0.8	0
		Ball	3	0.06 (−5.94,6.07)	0.98	0
		HIIT	2	−1.34 (−6.63,3.95)	0.62	0
BMI	Sport	Aerobic exercise	3	−3.12 (−5.58,-0.66)	0.01*	78
		HIIT	2	−0.06 (−5.58,-0.66)	0.96	43
FEV1	Time	≤8 weeks	10	0.85 (1.45,3.15)	0.47	0
		>8 weeks	5	2.89 (1.09,4.69)	0.002*	55
FVC	Time	≤8 weeks	9	0.70 (−2.32,3.71)	0.65	78
		>8 weeks	5	5.88 (−1.30,10.46)	0.01*	56
PEF	Time	≤8 weeks	7	−0.27 (−3.93,3.39)	0.27	85
		>8 weeks	3	4.65 (−3.68,12.98)	0.89	0
BMI	Time	≤8 weeks	3	−2.99 (−5.70,-0.28)	0.03*	77
		>8 weeks	3	−1.90 (−5.15,1.35)	0.25	85

of allergic disease population. The effects of exercise on improving FeNo in children with asthma need further confirmation.

4.3 Effects on motor ability and body composition and quality of life

Eating Habits and physical activity have a significant impact on the quality of life of children and adolescents. Poor eating habits and low level of physical activity can lead to childhood obesity and affect the quality of life of children (Martins et al., 2021). The global prevalence of obesity has increased over the past 30 years, resulting in an increase in the incidence and clinical manifestations of many respiratory diseases. In the United States, about 19 per cent of children aged 6–11 are obese, and the proportion of severely obese children was 5.2% (Hales et al., 2018). Asthma is one of the most typical diseases associated with obesity, and among obese children, asthma is also exacerbated and poorly controlled, the quality of life is also reduced, and physical activity is severely inadequate or below the minimum physical activity level (Okubo et al., 2016; Holderness et al., 2017; Kupkina et al., 2020). Studies have shown that children with asthma have higher BMI and higher rates of obesity than other children (Glazebrook et al., 2006). Having a high BMI can also reduce the quality of life in children with asthma (Kupkina et al., 2020). Our meta-analysis shows that exercise interventions can be effective in reducing BMI in children with asthma. We have also carried on the subgroup analysis to the movement pattern and the movement cycle. We found that aerobic exercise was more effective than HIIT, and the possible reason may be that HIIT exercise requires higher cardiopulmonary capacity of asthmatic children, and the intensity of HIIT exercise is higher, which leads to poor effect of HIIT exercise intervention in asthmatic children. We also found that exercise cycles of less than 8 weeks were significantly more effective. The reason for this result was that the subjects in Kader (2013) had a higher BMI. When excluded this article, more than 8 weeks' exercise cycle were found to be effective in improving BMI in children with asthma. Indeed, the heterogeneity between the studies impacts the interpretation of the associations with >8 weeks cycles, which also reminds us to be more cautious in the subsequent studies. At the same time, we found that the quality of life and exercise ability of asthmatic children improved significantly after exercise intervention, and the total score (emotional, symptom, activities) of all four parts of the questionnaire improved significantly, and the walking distance of 6 WMT increased significantly. These results suggest that exercise interventions can reduce BMI, improve quality of life, and improve exercise performance in asthmatic children, and these three trends occur at the same time. This is due to the increase of physical activity in asthmatic children, the decrease of BMI in asthmatic children caused by the increase of energy expenditure, and increased participation brought about by regular physical activity. Subjects' quality of life scores may also be partially biased, because although we think it is a relatively objective evaluation method, it is also derived from subjects' subjective evaluation, and studies with large sample size can reduce the bias.

The decrease of BMI and the increase of exercise ability have a good effect on the quality of life of children with asthma (Holderness et al., 2017). A high BMI affects immune cells in adipose tissue, leading to an increase in macrophages, mainly pro-inflammatory phenotypes, and an increase in other pro-inflammatory factors (such as TNF-α and Il-6) in obesity (Bulló et al., 2003). Adipose tissue is an important source of mast cell progenitor cells, and mast cells are the key mediators of allergy (Poglio et al., 2010). These factors may lead to asthma symptoms in children with asthma. Regular exercise over a long period of time can effectively reduce the BMI of asthmatic children and promote the release of anti-inflammatory factors (such as IL-4 and IL-5), thereby reducing the symptoms of asthma (Bantulà et al., 2021). Quality of life is a multidimensional concept that includes physical, psychological, emotional and social wellbeing. The positive effects of sports on children are not only reflected in physiology, but also demonstrated by the improved quality of life in children with asthma. Studies show that the higher the physical activity level of asthmatic children, the better their quality of life (Basso et al., 2013). A number of factors limit the participation of asthmatic children in physical activities: their own limited understanding of the symptoms, parents' concerns about the risks of physical activity, and family values of physical activity. These factors reduce children's levels of physical activity and athletic ability (Williams et al., 2008). Studies have shown that exercise does not worsen symptoms in children with asthma, but improves the quality of life in children with asthma (Furtado et al., 2019). All the studies included in this meta-analysis showed a significant improvement in the 6 WMT distance of asthmatic children after exercise intervention, indicating that exercise intervention improved the exercise ability of asthmatic children. Recently, a meta-analysis found that cardiorespiratory fitness (CRF) and muscular fitness (MF) were positively correlated with the quality of life in asthmatic children, and higher CRE and MF could improve the relationship between asthmatic children and their peers and families (Bermejo-Cantarero et al., 2021). Therefore, reasonable and effective exercise can significantly improve the body composition, exercise capacity and quality of life of children with asthma, which can be used as a reference for clinical exercise rehabilitation.

4.4 Limitations

This study has certain limitations. First of all, the literature included in the experimental methods was not blindly included, because the way of exercise intervention is difficult to implement double-blind method. Second, the inclusion of the study used different ways of exercise intervention and different cycle, and the difference of exercise time may be the source of clinical difference. Finally, although some indexes were based on random effect model, there were still some heterogeneities between some studies.

5 Conclusion

Exercise intervention can effectively improve the pulmonary function index (FEV1 and FVC) and the immune system (IL-6 and TNF-α) of asthmatic children, improve the quality of life and exercise ability of asthmatic children and effectively reduce the BMI of asthmatic children. We found that swimming and aerobic exercise were more effective in helping children with asthma than other types of exercise, with a duration of at least 8 weeks, 2 to 3 times per week, and 40–60 min of exercise each time.

Data availability statement

The raw data supporting the conclusion of this article will be made available by the authors, without undue reservation.

Author contributions

LZ conceived the project, designed, and supervised the experiments. LZ and HX analyzed the data and wrote the manuscript with input from all the authors. All authors contributed to the article and approved the submitted version.

Funding

This work was supported by the Fundamental Research Funds for the Central Universities.

Conflict of interest

The authors declare that the research was conducted in the absence of any commercial or financial relationships that could be construed as a potential conflict of interest.

Publisher's note

References

Abdelbasset, W. K., Alsubaie, S. F., Tantawy, S. A., Elyazed, T. I. A., and Kamel, D. M. (2018). Evaluating pulmonary function, aerobic capacity, and pediatric quality of life following a 10-week aerobic exercise training in school-aged asthmatics: A randomized controlled trial. *Patient Prefer. adherence* 12, 1015–1023. doi:10.2147/PPA.S159622

Alfrayh, A., Khoja, T., Alhusain, K., Alshehri, S., Gad, A., and Madani, M. (2014). *FEV1 and FVC pulmonary function reference values among 6-18-year-old children: A multi-centre study in Saudi arabia*.

Brüggemann, T. R., Ávila, L. C. M., Fortkamp, B., Greiffo, F. R., Bobinski, F., Mazzardo-Martins, L., et al. (2015). Effects of swimming on the inflammatory and redox response in a model of allergic asthma. *Int. J. sports Med.* 36 (07), 579–584. doi:10.1055/s-0034-1395588

Bantulà, M., Roca-Ferrer, J., Arismendi, E., and Picado, C. (2021). Asthma and obesity: Two diseases on the rise and bridged by inflammation. *J. Clin. Med.* 10 (2), 169. doi:10.3390/jcm10020169

Bao Yixiao, C. A., Zhou, F. U., Li, Changchong, Liu, Chuanhe, Xiang, Li, Shang, Yunxiao, et al. (2016). Guidelines for diagnosis, prevention and treatment of bronchial asthma in children (2016 edition). *Chin. J. Pediatr.* 54 (03), 167–181.

Basaran, S., Guler-Uysal, F., Ergen, N., Seydaoglu, G. Ü. L. Ş. A. H., Bingol-Karakoç, G., and Altintas, D. (2006). Effects of physical exercise on quality of life, exercise capacity and pulmonary function in children with asthma. *J. rehabilitation Med.* 38 (2), 130–135. doi:10.1080/16501970500476142

Basso, R. P., Jamami, M., Labadessa, I. G., Regueiro, E. M. G., Pessoa, B. V., Oliveira, A. D. D., Jr, et al. (2013). Relationship between exercise capacity and quality of life in adolescents with asthma. *J. Bras. Pneumol.* 39, 121–127. doi:10.1590/s1806-37132013000200002

Bateman, E. D., Hurd, S. S., Barnes, P. J., Bousquet, J., Drazen, J. M., FitzGerald, M., et al. (2008). Global strategy for asthma management and prevention: GINA executive summary. *Eur. Respir. J.* 31 (1), 143–178. doi:10.1183/09031936.00138707

Bendiksen, M., Williams, C. A., Hornstrup, T., Clausen, H., Kloppenborg, J., Shumikhin, D., et al. (2014). Heart rate response and fitness effects of various types of physical education for 8-to 9-year-old schoolchildren. *Eur. J. sport Sci.* 14 (8), 861–869. doi:10.1080/17461391.2014.884168

Bermejo-Cantarero, A., Álvarez-Bueno, C., Martínez-Vizcaino, V., Redondo-Tébar, A., Pozuelo-Carrascosa, D. P., and Sánchez-López, M. (2021). Relationship between both cardiorespiratory and muscular fitness and health-related quality of life in children and adolescents: A systematic review and meta-analysis of observational studies. *Health Qual. life outcomes* 19 (1), 127–215. doi:10.1186/s12955-021-01766-0

Berry, M. A., Hargadon, B., Shelley, M., Parker, D., Shaw, D. E., Green, R. H., et al. (2006). Evidence of a role of tumor necrosis factor alpha in refractory asthma. *N. Engl. J. Med.* 354 (7), 697–708. doi:10.1056/NEJMoa050580

Boonpiyathad, T., Sözener, Z. C., Satitsuksanoa, P., and Akdis, C. A. (2019). "Immunologic mechanisms in asthma," in *Seminars in immunology* (Cambridge, MA: Academic Press), 46, 101333.

Bousquet, J., and Khaltaev, N. (2007). *Global surveillance, prevention and control of chronic respiratory diseases: A comprehensive approach*. Switzerland: WHO.

Brightling, C., Berry, M., and Amrani, Y. (2008). Targeting TNF-alpha: A novel therapeutic approach for asthma. *J. Allergy Clin. Immunol.* 121 (1), 5–10. doi:10.1016/j.jaci.2007.10.028

Bulló, M., García-Lorda, P., Megias, I., and Salas-Salvadó, J. (2003). Systemic inflammation, adipose tissue tumor necrosis factor, and leptin expression. *Obes. Res.* 11 (4), 525–531. doi:10.1038/oby.2003.74

Carew, C., and Cox, D. W. (2018). Laps or lengths? The effects of different exercise programs on asthma control in children. *J. Asthma* 55 (8), 877–881. doi:10.1080/02770903.2017.1373806

Chen, Q., FengQin, W., Xin, S., and Ruan, J. (2020). Low-complexity rate-distortion optimization of sampling rate and bit-depth for compressed sensing of images. *J. GuangZhou Sport Univ.* 40 (5), 125–128. doi:10.3390/e22010125

Cohen, J. (2013). *Statistical power analysis for the behavioral sciences*. England, UK: Routledge.

Counil, F. P., Varray, A., Matecki, S., Beurey, A., Marchal, P., Voisin, M., et al. (2003). Training of aerobic and anaerobic fitness in children with asthma. *J. Pediatr.* 142 (2), 179–184. doi:10.1067/mpd.2003.83

de Andrade, L. B., Britto, M. C., Lucena-Silva, N., Gomes, R. G., and Figueroa, J. N. (2014). The efficacy of aerobic training in improving the inflammatory component of asthmatic children. Randomized trial. *Respir. Med.* 108 (10), 1438–1445. doi:10.1016/j.rmed.2014.07.009

de Valois Correia, M. A., Rizzo, J. A., Sarinho, S. W., Sarinho, E. S. C., Medeiros, D., and Assis, F. (2012). Effect of exercise-induced bronchospasm and parental beliefs on physical activity of asthmatic adolescents from a tropical region. *Ann. Allergy, Asthma & Immunol.* 108 (4), 249–253. doi:10.1016/j.anai.2012.01.016

El-Kader, M. S., Al-Jiffri, O., and Ashmawy, E. M. (2013). Impact of weight loss on markers of systemic inflammation in obese Saudi children with asthma. *Afr. health Sci.* 13 (3), 682–688. doi:10.4314/ahs.v13i3.23

Ertürk, G., Günday, Ç., Evrendilek, H., Sağır, K., and Aslan, G. K. (2021). Effects of high intensity interval training and sprint interval training in patients with asthma: A systematic review. *J. Asthma* 59, 2292–2304. doi:10.1080/02770903.2021.1999470

Furtado, P. R., Maciel, Á. C. C., Barbosa, R. R. T., da Silva, A. A. M., de Freitas, D. A., and de Mendonça, K. M. P. P. (2019). Association between quality of life, severity of asthma, sleep disorders and exercise capacity in children with asthma: A cross-sectional study. *Braz. J. Phys. Ther.* 23 (1), 12–18. doi:10.1016/j.bjpt.2018.08.010

Glazebrook, C., McPherson, A. C., Macdonald, I. A., Swift, J. A., Ramsay, C., Newbould, R., et al. (2006). Asthma as a barrier to children's physical activity: Implications for body mass index and mental health. *Pediatrics* 118 (6), 2443–2449. doi:10.1542/peds.2006-1846

Good, J., Viana, E., Burgomaster, K. A., and Dogra, S. (2019). Acute responses to sprint-interval and continuous exercise in adults with and without exercise-induced bronchoconstriction. *J. Sports Sci.* 37 (2), 212–220. doi:10.1080/02640414.2018.1488520

Hales, C. M., Fryar, C. D., Carroll, M. D., Freedman, D. S., and Ogden, C. L. (2018). Trends in obesity and severe obesity prevalence in US youth and adults by sex and age, 2007-2008 to 2015-2016. *Jama* 319 (16), 1723–1725. doi:10.1001/jama.2018.3060

hang, W., Wang, Q., Liu, L., Yang, W., and Liu, H. (2021). Effects of physical therapy on lung function in children with asthma: A systematic review and meta-analysis. *Pediatr. Res.* 89 (6), 1343–1351. doi:10.1038/s41390-020-0874-x

Higgins, J. P., Altman, D. G., Gøtzsche, P. C., Jüni, P., Moher, D., Oxman, A. D., et al. (2011). The Cochrane Collaboration's tool for assessing risk of bias in randomised trials. *Bmj* 343, d5928. doi:10.1136/bmj.d5928

Higgins, J. P., and Thompson, S. G. (2002). Quantifying heterogeneity in a meta-analysis. *Statistics Med.* 21 (11), 1539–1558. doi:10.1002/sim.1186

Holderness, H., Chin, N., Ossip, D. J., Fagnano, M., Reznik, M., and Halterman, J. S. (2017). Physical activity, restrictions in activity, and body mass index among urban children with persistent asthma. *Ann. Allergy, Asthma & Immunol.* 118 (4), 433–438. doi:10.1016/j.anai.2017.01.014

Jia, L., XingQiao, W., Jun, L., and Jie, Z. (2016). Effects of high-intensity interval training and moderate-intensity continuous training on management of asthmatic children. *J. Beijing Sport Univ.* 39 (10), 58–64.

Jing, T., ChengJun, L., JunMing, H., Zhuxia, L., YinLan, L., Chang, S., et al. (2019). Application of exercise prescriptions in the control of asthma. *Chin. J. Child Health Care* 27 (12), 1331.

Kupkina, A. V., Volosovets, O. P., Kryvopustov, S. P., Prokhorova, M. P., and Mozyrska, O. V. (2020). *The impact of overweight and obesity on the quality of life in children with bronchial asthma*.

Lang, J. E. (2019). The impact of exercise on asthma. *Curr. Opin. Allergy Clin. Immunol.* 19 (2), 118–125. doi:10.1097/ACI.0000000000000510

Latorre-Román, P. Á., Navarro-Martínez, A. V., and García-Pinillos, F. (2014). The effectiveness of an indoor intermittent training program for improving lung function, physical capacity, body composition and quality of life in children with asthma. *J. Asthma* 51 (5), 544–551. doi:10.3109/02770903.2014.888573

Lee, B. J., Moon, H. G., Shin, T. S., Jeon, S. G., Lee, E. Y., Gho, Y. S., et al. (2011). Protective effects of basic fibroblast growth factor in the development of emphysema induced by interferon-γ. *Exp. Mol. Med.* 43 (4), 169–178. doi:10.3858/emm.2011.43.4.018

Liu Chuanhe, H. J., and Shang, Yunxiao.Chinese Center for Disease Control and Prevention (2013). Third nationwide survey of childhood asthma in urban areas of China. *Chin. J. Pediatr.* 51 (10), 729–735.

Luyu, Y. (2013). Correlation between the levels of IL-6,TNF-α and IL-10 in serum and airway inflammation of patients with bronchial asthma. *Jouranl Clin. Pulm. Med.* 18 (08), 1389–1391.

Martins, E., Fernandes, R., Mendes, F., Magalhães, C., and Araújo, P. (2021). Food intake, physical activity and quality of life among children and youth. *Work* 69 (2), 475–484. doi:10.3233/WOR-213492

Moher, D., Liberati, A., Tetzlaff, J., and Altman, D. G.PRISMA Group (2009). Preferred reporting items for systematic reviews and meta-analyses: The PRISMA statement. *Ann. Intern. Med.* 151 (4), 264–269, W64. doi:10.7326/0003-4819-151-4-200908180-00135

Okubo, Y., Nochioka, K., Hataya, H., Sakakibara, H., Terakawa, T., and Testa, M. (2016). Burden of obesity on pediatric inpatients with acute asthma exacerbation in the United States. *J. Allergy Clin. Immunol. Pract.* 4 (6), 1227–1231. doi:10.1016/j.jaip.2016.06.004

Onur, E., Kabaroğlu, C., Günay, Ö., Var, A., Yilmaz, Ö., Dündar, P., et al. (2011). The beneficial effects of physical exercise on antioxidant status in asthmatic children. *Allergologia Immunopathol.* 39 (2), 90–95. doi:10.1016/j.aller.2010.04.006

Poglio, S., De Toni-Costes, F., Arnaud, E., Laharrague, P., Espinosa, E., Casteilla, L., et al. (2010). Adipose tissue as a dedicated reservoir of functional mast cell progenitors. *Stem Cells* 28 (11), 2065–2072. doi:10.1002/stem.523

Raundhal, M., Morse, C., Khare, A., Oriss, T. B., Milosevic, J., Trudeau, J., et al. (2015). High IFN-γ and low SLPI mark severe asthma in mice and humans. *J. Clin. investigation* 125 (8), 3037–3050. doi:10.1172/JCI80911

Ricciardolo, F. L., Sorbello, V., and Ciprandi, G. (2015). “FeNO as biomarker for asthma phenotyping and management,” in *Allergy and asthma proceedings* (East Providence, RI: OceanSide Publications Inc), 36, e1–e8.1

Rochester, C. L., Vogiatzis, I., Holland, A. E., Lareau, S. C., Marciniuk, D. D., Puhan, M. A., et al. (2015). An official American thoracic society/European respiratory society policy statement: Enhancing implementation, use, and delivery of pulmonary rehabilitation. *Am. J. Respir. Crit. care Med.* 192 (11), 1373–1386. doi:10.1164/rccm.201510-1966ST

Sha Li, L. C., Shao, Mingjun, and Chen, Yuzhi (2016). Ten years comparison of diagnosis and treatment of asthma in urban children in China. *Chin. J. Pediatr.* 54 (3), 182–186. doi:10.3760/cma.j.issn.0578-1310.2016.03.005

Simpson, J. L., Gibson, P. G., Yang, I. A., Upham, J., James, A., Reynolds, P. N., et al.AMAZES Study Research Group (2013). Impaired macrophage phagocytosis in non-eosinophilic asthma. *Clin. Exp. Allergy* 43 (1), 29–35. doi:10.1111/j.1365-2222.2012.04075.x

Toennesen, L. L., Soerensen, E. D., Hostrup, M., Porsbjerg, C., Bangsbo, J., and Backer, V. (2018). Feasibility of high-intensity training in asthma. *Eur. Clin. Respir. J.* 5 (1), 1468714. doi:10.1080/20018525.2018.1468714

Wang, J. S., and Hung, W. P. (2009). The effects of a swimming intervention for children with asthma. *Respirology* 14 (6), 838–842. doi:10.1111/j.1440-1843.2009.01567.x

Wang, Q., Zhang, W., Liu, L., Yang, W., and Liu, H. (2019). Effects of physical therapy on lung function in children with asthma: Study protocol for a systematic review and meta-analysis. *Med. Baltim.* 98 (15), e15226. doi:10.1097/MD.0000000000015226

Weisgerber, M. C., Guill, M., Weisgerber, J. M., and Butler, H. (2003). Benefits of swimming in asthma: Effect of a session of swimming lessons on symptoms and PFTs with review of the literature. *J. Asthma* 40 (5), 453–464. doi:10.1081/jas-120018706

Wicher, I. B., Ribeiro, M. Â. G. D. O., Marmo, D. B., Santos, C. I. D. S., Toro, A. A. D. C., Mendes, R. T., et al. (2010). Effects of swimming on spirometric parameters and bronchial hyperresponsiveness in children and adolescents with moderate persistent atopic asthma. *J. Pediatr.* 86, 384–390. doi:10.2223/JPED.2022

Williams, B., Powell, A., Hoskins, G., and Neville, R. (2008). Exploring and explaining low participation in physical activity among children and young people with asthma: A review. *BMC Fam. Pract.* 9 (1), 40–11. doi:10.1186/1471-2296-9-40

Winn, C. O., Mackintosh, K. A., Eddolls, W. T., Stratton, G., Wilson, A. M., McNarry, M. A., et al. (2021). Effect of high-intensity interval training in adolescents with asthma: The eXercise for Asthma with Commando Joe’s®(X4ACJ) trial. *J. Sport Health Sci.* 10 (4), 488–498. doi:10.1016/j.jshs.2019.05.009

Wu, X., Gao, S., and Lian, Y. (2020). Effects of continuous aerobic exercise on lung function and quality of life with asthma: A systematic review and meta-analysis. *J. Thorac. Dis.* 12 (9), 4781–4795. doi:10.21037/jtd-19-2813

Yang Yiyun, S. X., Chen, rong, Sun, Xinxin, and Liao, Yuexia (2021). Effects of physical exercise on lung function, aerobic capacity and quality of life in asthmatic children: A meta analysis of a randomized controlled trial. *Hubei Sports Sci.* 40 (05), 435–441.

Frontiers in Cell and Developmental Biology

TYPE Original Research
PUBLISHED 08 September 2023
DOI 10.3389/fcell.2023.1268621

EDITED BY
Chunheng Mo,
Sichuan University, China

REVIEWED BY
Chiwei Xu,
The Rockefeller University, United States
Dengcheng Zhou,
Sichuan University, China

*CORRESPONDENCE
Lara Gentemann,
✉ gentemann@iqo.uni-hannover.de
Stefan Kalies,
✉ kalies@iqo.uni-hannover.de

RECEIVED 28 July 2023
ACCEPTED 24 August 2023
PUBLISHED 08 September 2023

CITATION
Gentemann L, Donath S, Seidler AE, Patyk L, Buettner M, Heisterkamp A and Kalies S (2023), Mimicking acute airway tissue damage using femtosecond laser nanosurgery in airway organoids. *Front. Cell Dev. Biol.* 11:1268621. doi: 10.3389/fcell.2023.1268621

Mimicking acute airway tissue damage using femtosecond laser nanosurgery in airway organoids

Lara Gentemann[1,2,3]*, Sören Donath[1,2], Anna E. Seidler[1,2], Lara Patyk[1,2], Manuela Buettner[4], Alexander Heisterkamp[1,2,3,5] and Stefan Kalies[1,2,3,5]*

[1]Institute of Quantum Optics, Leibniz University Hannover, Hannover, Germany, [2]Lower Saxony Center for Biomedical Engineering, Implant Research and Development, Hannover, Germany, [3]REBIRTH Research Center for Translational Regenerative Medicine, Hannover, Germany, [4]Institute for Laboratory Animal Science, Hannover Medical School, Hannover, Germany, [5]German Center for Lung Research (DZL), Gießen, Germany

Airway organoids derived from adult murine epithelial cells represent a complex 3D *in vitro* system mimicking the airway epithelial tissue's native cell composition and physiological properties. In combination with a precise damage induction via femtosecond laser-based nanosurgery, this model might allow for the examination of intra- and intercellular dynamics in the course of repair processes with a high spatio-temporal resolution, which can hardly be reached using *in vivo* approaches. For characterization of the organoids' response to single or multiple-cell ablation, we first analyzed overall organoid survival and found that airway organoids were capable of efficiently repairing damage induced by femtosecond laser-based ablation of a single to ten cells within 24 h. An EdU staining assay further revealed a steady proliferative potential of airway organoid cells. Especially in the case of ablation of five cells, proliferation was enhanced within the first 4 h upon damage induction, whereas ablation of ten cells was followed by a slight decrease in proliferation within this time frame. Analyzing individual trajectories of single cells within airway organoids, we found an increased migratory behavior in cells within close proximity to the ablation site following the ablation of ten, but not five cells. Bulk RNA sequencing and subsequent enrichment analysis revealed the differential expression of sets of genes involved in the regulation of epithelial repair, distinct signaling pathway activities such as Notch signaling, as well as cell migration after laser-based ablation. Together, our findings demonstrate that organoid repair upon ablation of ten cells involves key processes by which native airway epithelial wound healing is regulated. This marks the herein presented *in vitro* damage model suitable to study repair processes following localized airway injury, thereby posing a novel approach to gain insights into the mechanisms driving epithelial repair on a single-cell level.

KEYWORDS

airway organoids, acute lung damage, epithelial repair, laser-based nanosurgery, femtosecond laser

1 Introduction

Due to its physiological function, the lung is constantly exposed to external, airborne hazards such as pollutants or viruses. While this can lead to acute irritation of the lung epithelial tissue, long-term or high-dosage exposures might induce chronic inflammatory conditions (Vernooy et al., 2002; Guo et al., 2018). These pathologies are often accompanied by high rates of tissue damage, which, at a certain point, cannot be repaired by endogenous regeneration mechanisms anymore, making pulmonary diseases one of the world's leading causes of death (Hogan et al., 2014; Barkauskas et al., 2017). While, under homeostatic conditions, the airway epithelium represents a rather quiescent tissue, it unleashes a remarkable regenerative potential with high lineage plasticity upon injury (Rao Tata and Rajagopal, 2017; Wu et al., 2022). In this context, several studies have identified Trp63$^+$, Krt5$^+$ basal cells as the airway epithelium's resident stem cells serving for self-renewal and as progenitors during repair (Rock et al., 2010; Wu et al., 2022). The balance between basal cell maintenance or differentiation is regulated by the dynamic activity of different signaling pathways. Especially Notch signaling controls the fate of basal as well as their derivative luminal secretory cells during homeostasis and following injury (Tsao et al., 2009; Rock et al., 2011; Xing et al., 2012; Mori et al., 2015; Pardo-Saganta et al., 2015). While luminal Krt8$^+$, Scgb1a1$^+$ secretory cells can give rise to multiciliated cells under low Notch activity, the maintenance of their secretory cell state is regulated by juxtacrine Notch signals derived from basal cells (Pardo-Saganta et al., 2015). Besides their capability to further differentiate, secretory cells were shown to be able to fully restore an ablated basal cell population by dedifferentiation, thereby acting as a backup progenitor cell population (Rawlins et al., 2009; Tata et al., 2013; Wu et al., 2022). Still, on the cellular level, it has yet to be solved which events are necessary for effective repair or, *vice versa*, finally lead to the aforementioned pathologies (Barkauskas et al., 2017).

To gain a better understanding of how early endogenous regeneration and repair processes occur and how these could be controlled or regulated to ultimately enable the development of cell-based therapeutics, it is essential to study the fate of single cells upon injury. In this context, the advancement of appropriate model systems is indispensable. Organotypic models, such as stem cell-derived, self-assembled organoids, mimic the native tissue's complex three-dimensional structure and cell heterogeneity as well as interaction, thereby resembling its biological properties to a high extent (Clevers, 2016; Barkauskas et al., 2017). For *in vitro* regeneration studies of airway epithelial tissue, several injury models have been developed, which, in a majority of cases, are based on the application of either naphthalene, sulfur dioxide, or on ionizing radiation (Borthwick et al., 2001; Hsu et al., 2014). These methods induce broad and rather unspecific damage. To study localized acute injury and reaction, the spatially selective ablation of only a limited number of cells is desirable. This would allow the identification of events specifically triggered in cells close to the injury site, potentially serving as essential factors for repair. One possible approach for such a targeted and precise damage induction in cellular systems is the employment of femtosecond laser nanosurgery (König et al., 1999; Heisterkamp et al., 2005; Vogel et al., 2005; Müller et al., 2021). Based on non-linear optical effects within biological material, this method generates a low-density plasma of free electrons which causes the bonds between molecules to break (Vogel et al., 2005). Femtosecond laser nanosurgery outperforms other manipulation techniques due to its very high spatial selectivity. As there is negligible heating and confinement of all effects to the focal volume, precise 3D application is possible without adverse effects to surrounding cells (Cheng et al., 2021; Liang and Vogel, 2022). In the context of organoids, femtosecond laser nanosurgery has previously been applied to selectively ablate single cells and study the neighboring cells' reparative response in colonoids (Donath et al., 2022).

Here, we apply targeted femtosecond laser-based nanosurgery in combination with state-of-the-art imaging technologies such as multiphoton or confocal microscopy to better understand epithelial repair in airway organoids (see Figure 1). The precise ablation of a single or up to ten cells enabled the investigation of the individual cells' damage response dependent on their distance to the injured site in terms of their migratory and proliferative behavior. Moreover, we conducted RNA sequencing to support our findings on a molecular level and to identify further factors and processes functionally involved in epithelial repair after localized injury in airway organoid.

2 Materials and methods

2.1 Isolation and preparation of airway organoids

The protocol for the isolation of airway epithelial cells was based on the work of Rabata et al. (2017). The experiments complied with the German Animal Protection Act (§4, TierSchG) and were approved by the local institutional advisory committee for animal care and research and by the Lower Saxony State Office for Consumer Protection and Food Safety (file number 42500/1H).

C57BL/6J wildtype mice (both sexes, 10–14 weeks) were sacrificed by CO_2 inhalation and subsequent cervical dislocation. The lungs were collected and kept in 1× Dulbecco's phosphate-buffered saline (DPBS, Sigma-Aldrich, MO, United States). Under sterile conditions, the tissue was cut into small pieces which were then transferred into freshly prepared and prewarmed (37°C) digestion solution (DMEM, high glucose (Sigma-Aldrich, MO, United States) supplemented with 3 mg/mL collagenase A (Sigma-Aldrich, MO, United States), 2 mg/mL trypsin (Sigma-Aldrich, MO, United States), 5% fetal calf serum (Pan Biotech, Germany), 5 μg/mL insulin (Sigma-Aldrich, MO, United States), 1× Cellshield (Biochrom, Germany)). After incubation of 1 h at 37°C under constant agitation, the cell suspension was centrifuged for 5 min at 450 × g and 4°C, followed by two subsequent erylysis steps for 2 min and 30 s, respectively, using Red Blood Cell Lysis Buffer (155 mM NH_4Cl, 12 mM $NaHCO_3$, 0.1 mM EDTA in ddH_2O, pH 7.4). DNA digestion was conducted in DMEM supplemented with 20 U/mL DNase I (Sigma-Aldrich, MO, United States) for 3 min at room temperature (RT). To decrease the number of stromal cells, the cell suspension was subjected to differential centrifugation three times for 10 s each, at 450 × g and 4°C. The organoid-forming epithelial cells, concentrated in the cell pellet, were further

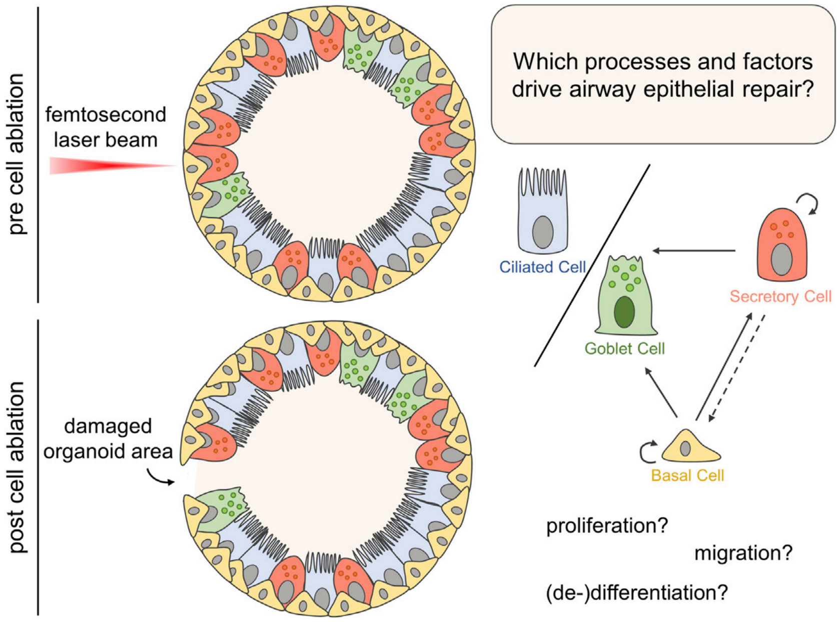

FIGURE 1
Airway organoids, mimicking the structure of proximal airway epithelial tissue mainly composed of basal as well as luminal secretory, ciliated, and goblet cells, were subjected to femtosecond laser-based nanosurgery for targeted ablation of a single or up to ten cells. Subsequently, multiphoton or confocal microscopy was employed to study the organoid's response to the damage in terms of structural integrity, proliferation, migration and changes in gene expression to identify processes driving the epithelial repair.

dissociated into a single-cell solution by incubation in 1× TrypLE Select (Thermo Fisher Scientific, MA, United States) for 10 min at RT and passed through a 40 µm cell strainer (VWR, PA, United States). The cells were resuspended in Cultrex Reduced Growth Factor Basement Membrane Extract (BME), Type R1 (R&D Systems, MN, United States) at a concentration of 2.5 × 10^6 cells/mL and plated in domes of 30 µL/well in a 24-well plate (Costar® Cell Culture Plate, Corning Incorporate™, NY, United States of America) preheated to 37°C. After a subsequent incubation of the plated cells for 30 min at 37°C, 5% CO_2 for gelation of the Cultrex, organoid growth medium (DMEM, high glucose, GlutaMAX™, pyruvate (Thermo Fisher Scientific, MA, United States of America) with 50% L-WRN-supernatant (ATCC® CRL3276™ in DMEM, high glucose, GlutaMAX™, pyruvate plus 10% fetal calf serum), 1× N2 (Invitrogen, CA, United States of America), 1× B27 (Invitrogen, CA, United States), 50 ng/µL recombinant mouse epidermal growth factor (Sigma-Aldrich, MO, United States), 10 µM Y-27632 (Tocris, Bristol, United Kingdom), 1× Cellshield (Biochrom, Berlin, Germany)) was added and the cells were kept at 37°C, 5% CO_2 and a humidified atmosphere. During the first few passages (2–3 weeks), remaining non-epithelial cells that were initially seeded together with epithelial organoid-forming cells gradually underwent cell death, as previously described by Chiu et al. for a similar culture model (Chiu et al., 2022). While organoid culture was accompanied by an adherent stromal cell monolayer, solely airway epithelial organoids grew within Cultrex embedding. These airway organoids were characterized by a basal cell layer positive for Trp63 and cytokeratin 5 (CK5), and a luminal CK8-positive differentiated cell layer including ciliated cells (acetylated alpha-tubulin-positive) (Supplementary Figure S1, Supplementary Video S1, Supplementary Files S1–S3).

2.2 Airway organoid culture and transduction

Airway organoids were cultured in growth medium at 37°C, 5% $CO_{2,}$ and a humidified atmosphere as described above. Medium was changed every 2–3 days and organoids were passaged every 10–14 days. Genetic modification of organoid cells, allowing the expression of a fluorescent protein, was achieved via lentiviral transduction. Lentiviral particles were produced via third-generation split packaging protocol in HEK293T cells (DSMZ, Germany) as previously described (Schambach et al., 2006). The transfer plasmid contained the sequence for expression of a histone 2A-mCherry fusion protein under control of a Trp63 promoter, which was amplified from human genomic DNA as previously described (Lanza et al., 2006). Lentiviral transduction was performed based on a protocol previously described for employment in intestinal organoids by van Lidth de Jeude and colleagues (Van Lidth De Jeude et al., 2015).

2.3 Laser setup, imaging, and manipulation

For laser-based nanosurgery applications, including multiphoton imaging as well as manipulation, a Chameleon Ultra II laser system with a pulse length of 140 fs and a repetition rate of 80 MHz, previously described (Müller et al., 2019), was employed.

Organoids labeled by histone 2A (H2A)-mCherry fusion protein were visualized at an excitation wavelength of 730 nm and emission was detected by a photomultiplier tube (Hamamatsu Photonics, Japan) using an emission filter at 607 ± 18 nm. Cell ablation was conducted with a wavelength of 730 nm, a pulse energy of 0.9 nJ, and a dissection speed of 15 μm/s.

2.4 Analysis of organoid morphology, cell proliferation, and migration

2.4.1 Analysis of organoid morphology and cell migration

For analysis of organoid morphology and cell migration, organoids were transferred to a glass-bottom dish (μ-Dish 35 mm, high Grid-500 Glass, Ibidi, Germany). Therefore, Cultrex was dissolved and airway organoids were selectively pulled out of the suspension under a transmitted light microscope using a 20 μL pipette, followed by embedding into fresh Cultrex and covering with growth medium. The following day, the medium was changed to FluoroBrite™ DMEM (Thermo Fisher Scientific, MA, United States), and laser nanosurgery was conducted yielding ablation of either none (control), a single, two, five, or ten cells per organoid. Following cell ablation, two-photon microscopy images (z-stacks in the range of ±10 μm from the ablation plane with a step-size of 2 μm) were captured every 30 min over 4–6 h, and again at 24 h post-ablation. Organoids were kept under culture conditions (37°C, 5% CO_2) throughout the experimental procedure.

For analysis of the impact of cell ablation on organoid morphology, organoid growth was quantitively determined using a custom Fiji macro calculating the mean organoid diameter. For this, the organoid's minor and major axes on each of ten images captured per time point (ten z-slices in distances of 2 μm) were measured and subsequently averaged for each time point to obtain the diameter.

As airway organoids are characterized by a nearly centrosymmetric structure, we decided to quantify data using a 2D representation. Thus, for analysis of cell migration within organoids, maximum intensity projections of the captured z-stacks (±6 μm from ablation plane with a step-size of 2 μm) were generated for every point in time via Fiji. Using Fiji TrackMate plugin in combination with Stardist detector (Schmidt et al., 2018; Ershov et al., 2022), all cells were detected via their fluorescently labeled nuclei and subsequent employment of LAP Tracker identified the individual cells' trajectories. To obtain data on every single cell's migratory behavior in dependence on their distance from the ablation site, track data was further processed by a custom Matlab script.

2.4.2 Analysis of cell proliferation

For analysis of cell proliferation within airway organoids, an EdU assay was performed as described previously by Donath et al. (2022). Briefly, organoids were transferred to a glass-bottom dish (μ-Dish 35 mm, high Grid-500 Glass, Ibidi, Germany) as described in Section 2.4.1. The following day, medium was changed to FluoroBrite™ DMEM (Thermo Fisher Scientific, MA, United States) supplemented with 10 μM 5-Ethynyl-2-deoxyuridine (5-EdU, Jena Bioscience, Germany) and organoids were incubated at 37°C, 5% CO_2 for 2 h. Subsequent laser nanosurgery was conducted for ablation of either none (control), five or ten cells per organoid. At 4 h post cell ablation, organoids were fixed by incubation with 4% Roti®-Histofix (Carl Roth, Germany) supplemented with 1% glutaraldehyde (Carl Roth, Germany) for 20 min at RT. Cell permeabilization was conducted by incubation in 0.5% Triton X-100 (Carl Roth, Germany) in DPBS (Sigma-Aldrich, MO, United States) for 20 min at RT. A subsequent click-chemistry-mediated staining reaction was achieved by incubation of organoids in the reaction mix (1 mM Cu_2SO_4 (Jena Bioscience, Germany), 10 mM sodium ascorbate (Jena Bioscience, Germany), 8 μM 5-FAM Azide (Biomol, Germany) diluted in DPBS (Sigma-Aldrich, MO, United States)) for 1 h at 37°C in the dark, leading to fluorescent visualization of EdU that was incorporated into the DNA. Nuclear counterstaining was conducted using NucSpot® 650 (final 1×, Biotium Inc., United States). Multi-channel z-stacks in the range of ±8 μm from the ablation plane with a step-size of 2 μm were captured by confocal laser scanning microscopy (Leica TCS SP5). As described in Section 2.4.1, for analysis, 2D representations of image data was used. Therefore, image data were processed using Fiji to generate a z-projection (sum slices), which was then used for nuclei detection of both EdU-positive as well as all cells via Fiji Stardist (Schmidt et al., 2018). The relative proliferation rate, defined as the ratio of EdU-positive to all cells, was determined and, using a custom Matlab script, was put into relation to the cells' distances from the ablation site.

2.5 Transcriptome analysis via bulk RNA sequencing

For transcriptome analysis, 45 organoids were transferred to a glass-bottom dish (μ-Dish 35 mm, high Grid-500 Glass, Ibidi, Germany). The following day, medium was replaced by FluoroBrite™ DMEM (Gibco, United States), and laser-based ablation of ten neighboring cells within each organoid was conducted. Another dish with 45 organoids prepared analogously and kept under the same experimental conditions remained untreated as control. The organoids were incubated at 37°C, 5% CO_2 and a humidified atmosphere for 4.5 h after cell ablation, followed by organoid harvesting using Cultrex® 3D Culture Cell Harvesting Kit (Trevigen, MD, United States) according to the manufacturer's protocol. After final centrifugation for 5 min at 850 × g and 4°C, organoids were resuspended in 1× DNA/RNA Shield™ (Zymo Research, CA, United States) and stored at −80 °C until all samples were collected. RNA isolation was conducted using *Quick*-RNA™ Microprep Kit (R1050, Zymo Research, CA, United States) following the manufacturer's instructions. Subsequent library generation, RNA sequencing run, raw data processing, and differential expression analysis were performed by the Genomic core facility of Hannover Medical School.

2.5.1 Library generation, quality control, and quantification

150 ng of total RNA per sample were utilized as input for mRNA enrichment procedure with 'NEBNext® Poly(A) mRNA Magnetic Isolation Module' (E7490L; New England Biolabs) followed by stranded cDNA library generation using "NEBNext® Ultra II

Directional RNA Library Prep Kit for Illumina" (E7760L; New England Biolabs). All steps were performed as recommended in the user manual E7760 (Version 1.0_02-2017; NEB) except that all reactions were downscaled to 2/3 of initial volumes.

cDNA libraries were barcoded by dual indexing approach, using "NEBNext Multiplex Oligos for Illumina–96 Unique Dual Index Primer Pairs" (6440S; New England Biolabs). All generated cDNA libraries were amplified with 10 cycles of final PCR.

One additional purification step was introduced at the end of the standard procedure, using 1.2x "Agencourt® AMPure® XP Beads" (#A63881; Beckman Coulter, Inc.). Fragment length distribution of individual libraries was monitored using "Bioanalyzer High Sensitivity DNA Assay" (5,067-4626; Agilent Technologies). Quantification of libraries was performed by use of the "Qubit® dsDNA HS Assay Kit" (Q32854; ThermoFisher Scientific).

2.5.2 Library denaturation and sequencing run

Equal molar amounts of individually barcoded libraries were pooled for a common sequencing run in which each analyzed library constituted 16.7% of overall flowcell/run capacity. The library pool was denatured with NaOH and was finally diluted to 1.8 p.m. according to the Denature and Dilute Libraries Guide (Document # 15048776 v02; Illumina). 1.3 mL of the denatured pool was loaded on an Illumina NextSeq 550 sequencer using a Mid Output Flowcell (130 M cluster) for 2 × 75 bp paired-end reads (20024904; Illumina). Sequencing was performed with the following settings: Sequence reads 1 and 2 with 76 bases each; Index reads 1 and 2 with 8 bases each.

2.5.3 BCL to FASTQ conversion

BCL files were converted to FASTQ files using bcl2fastq Conversion Software version v2.20.0.422 (Illumina).

2.5.4 Raw data processing and quality control

Raw data processing was conducted by use of nfcore/rnaseq (version 1.4.2) which is a bioinformatics best-practice analysis pipeline used for RNA sequencing data at the National Genomics Infrastructure at SciLifeLab Stockholm, Sweden. The pipeline uses Nextflow, a bioinformatics workflow tool. It pre-processes raw data from FastQ inputs, aligns the reads and performs extensive quality-control on the results. The genome reference and annotation data were taken from GENCODE.org (*Mus musculus*; GRCm38. p6).

2.5.5 Normalization and differential expression analysis

Normalization and differential expression analysis was performed on the internal Galaxy (version 20.05) instance of the RCU Genomics, Hannover Medical School, Germany with DESeq2 (Galaxy Tool Version 2.11.40.6) with default settings except for "Output normalized counts table", which was set to "Yes" and all additional filters were disabled ("Turn off outliers replacement", "Turn off outliers filtering", and "Turn off independent filtering" set "Yes"). The different conditions were selected as primary factor whereas the batch was used as secondary factor in DESeq2 analyses (two factor design).

2.5.6 Gene ontology enrichment analysis

Gene ontology enrichment analysis was performed on the basis of all DEGs (p-adj <0.05) using Cytoscape software (version 3.9.1) (Shannon et al., 2003) and StringApp (Doncheva et al., 2019).

2.6 Image analysis and statistics

All image data analysis was performed via Fiji (Schindelin et al., 2012), including Stardist (Schmidt et al., 2018) and TrackMate (Ershov et al., 2022) plugins. Further data analysis, including graphical representation, was conducted using Matlab software (version 2022a) and OriginPro 2021b (version 9.8.5.201, OriginLab Corporation, Northampton, MA, United States).

Statistical analysis was performed using Microsoft Excel (Microsoft Corporation, Redmond, WA, United States). Student's unpaired *t*-test and One-Way ANOVA were used to test for significant differences between groups, thereby applying a significance level of $\alpha = 0.05$.

3 Results

3.1 Local cell death has no consequences for organoid survival and long-term morphology

As described by Donath et al., native colonic epithelial repair processes can be observed in colonoids on a cellular level upon femtosecond laser-based ablation of as little as a single cell (Donath et al., 2022). Based on this, we aimed to generate an airway organoid damage model allowing for the examination of endogenous repair mechanisms on a single-cell level, triggered by highly localized injury induction via ablation of few cells.

Initially, to study how local cell death affects the overall viability and morphology of airway organoids, femtosecond laser-mediated damage was induced on a single-cell level, and organoids were tracked using multiphoton microscopy over a subsequent period of 24 h. Untreated organoids kept under the same experimental conditions served as control.

Upon ablation of either a single or multiple (two, five, or ten) neighboring cells, the overall organoid viability within 24 h post cell ablation, determined by microscopic examination of the organoid's structural integrity, was closely 100% and did not differ from the survival rate observed in control organoids (Figure 2). For either condition, cell ablation immediately led to a strong autofluorescence signal within the damage site. Subsequently, a shedding of the dead cell/s into the organoid's lumen and an invagination of cells surrounding the damaged area was observed within 1 h. While the injured area showed at least a partial repair at 4 h post laser-based ablation, especially in the case of ablation of five or ten cells, the damage site was still clearly visible at this point in time (Figure 2A). Independent of the extent of damage, the observed gap within the cell layer was closed within 24 h after laser treatment, the structural integrity was restored. Representative timelines of organoids subjected to ablation of either a single or ten cells, captured in the period from pre until 24 h post ablation via multiphoton microscopy, are shown in Figure 2A. Color-labeled

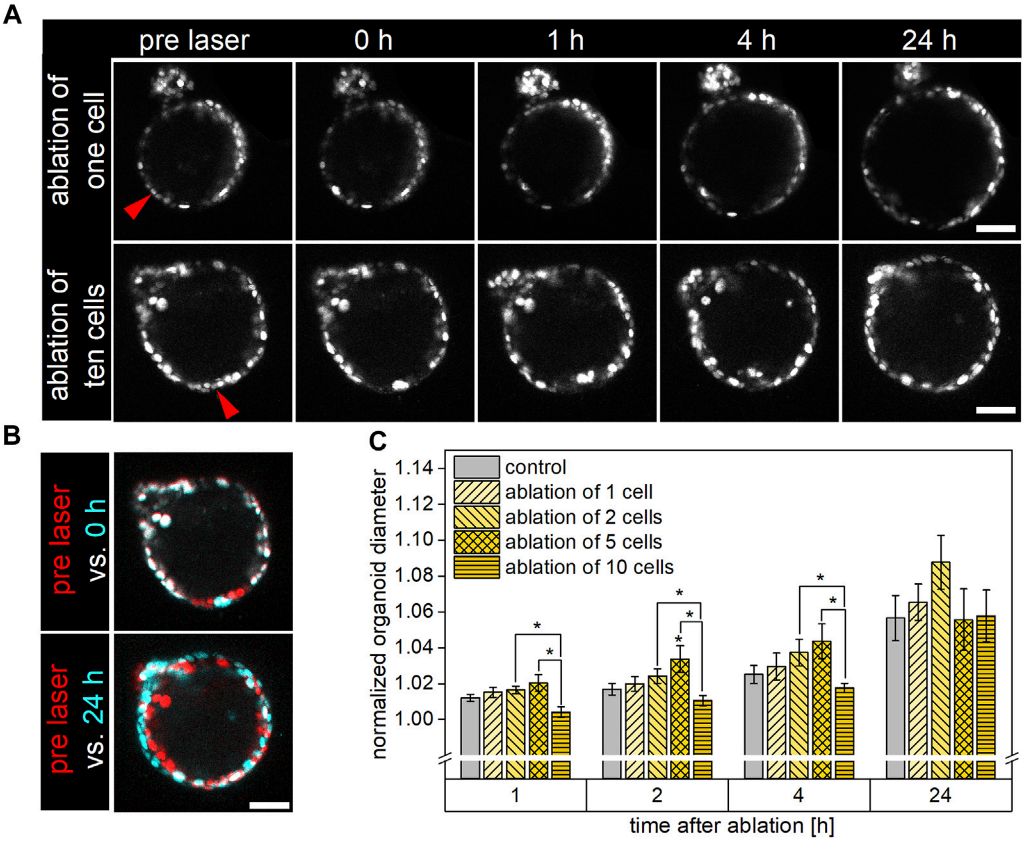

FIGURE 2
Influence of single or multiple cell ablation on morphology, structural integrity, and growth behavior of airway organoids. The organoids' structural integrity was restored within 24 h post cell ablation independent of the extent of damage. Organoids subjected to the ablation of five cells showed an increased growth potential in the early phase after damage induction, while ablation of ten cells tended to decelerate organoid growth within this time. **(A)**: Representative timelines showing organoids pre, as well as 0, 1, 4, and 24 h post ablation of either a single (top row) or ten neighboring (bottom row) cells. Red arrows indicate ablation site. Scale bar: 50 µm. **(B)**: Color-labeled overlays of organoid images captured pre (red) and post (cyan) laser manipulation. Immediately following cell ablation (top), red- and cyan-colored cells indicate the damage area, in which the cyan-colored signal originates from strong autofluorescence of ablated cells. At 24 h post laser ablation (bottom), the organoid had grown, indicated by non-overlapping red and cyan color-labeled cells. Scale bar: 50 µm. **(C)**: Relative diameter of control organoids as well as of organoids subjected to ablation of either a single, two, five, or ten cells at 1, 2, 4, and 24 h post laser manipulation. Data shown represent mean ± SEM, $n \geq 6$ per condition, *: $p < 0.05$, statistics refer to control if not stated otherwise.

image overlays of the organoid pre laser treatment (red) and either of the subsequent captures (cyan) served for better visualization of the damage site and potential morphological changes in the course of repair (Figure 2B).

For examination of the impact of cell ablation on organoid morphology, organoid growth was quantitively analyzed using a custom Fiji macro that determined the mean organoid diameter. For this, the organoid's minor and major axes on each of the ten images captured per time point (ten z-slices in distances of 2 µm) were measured and subsequently averaged for each time point to obtain the diameter. For these experiments, organoids with an initial diameter of 148 ± 4 µm were used, and growth to a mean diameter of 157 ± 5 µm was observed within 24 h. For further analysis and better comparison between the groups, all raw data were normalized to the respective organoid's initial size pre ablation.

The changes over time of the normalized organoid's mean diameters of each group are depicted in Figure 2C. It was found that, within 24 h, the organoids' diameters of the different conditions increased by 5.7% ± 1.3%, 6.5% ± 1.0%, 8.8% ± 1.5%, 5.6% ± 1.7% and 5.8% ± 1.4% in case of control, ablation of a single, two, five, and ten cells, respectively, with no statistically significant differences between any two conditions. In the early period of repair, especially ablation of five cells slightly promoted the organoids' growth potential compared to the control. In this context, control organoid diameter increases to 101.2% ± 0.2%, subsequently to 101.7% ± 0.3%, and further to 102.5% ± 0.5% after one, two, and 4 h were measured. In comparison, organoids subjected to ablation of five cells had grown to 102.0% ± 0.5% ($p = 0.09$), 103.4% ± 0.7% ($p = 0.03$), and 104.4% ± 1.0% ($p = 0.19$) of their original diameter at the same time points. On the contrary, ablation of ten cells seemed to arrest organoid growth within the first 4 h post laser treatment. In this case, only minor increases in organoid diameter to 100.4% ± 0.3% ($p = 0.08$) and subsequently to 101.1% ± 0.3% and to 101.8% ± 0.3% after one, two, and 4 h after ablation were determined. These changes in size were less than those observed for the control group ($p > 0.05$) as well as for organoids subjected to two- or five-cell-ablation ($p < 0.05$).

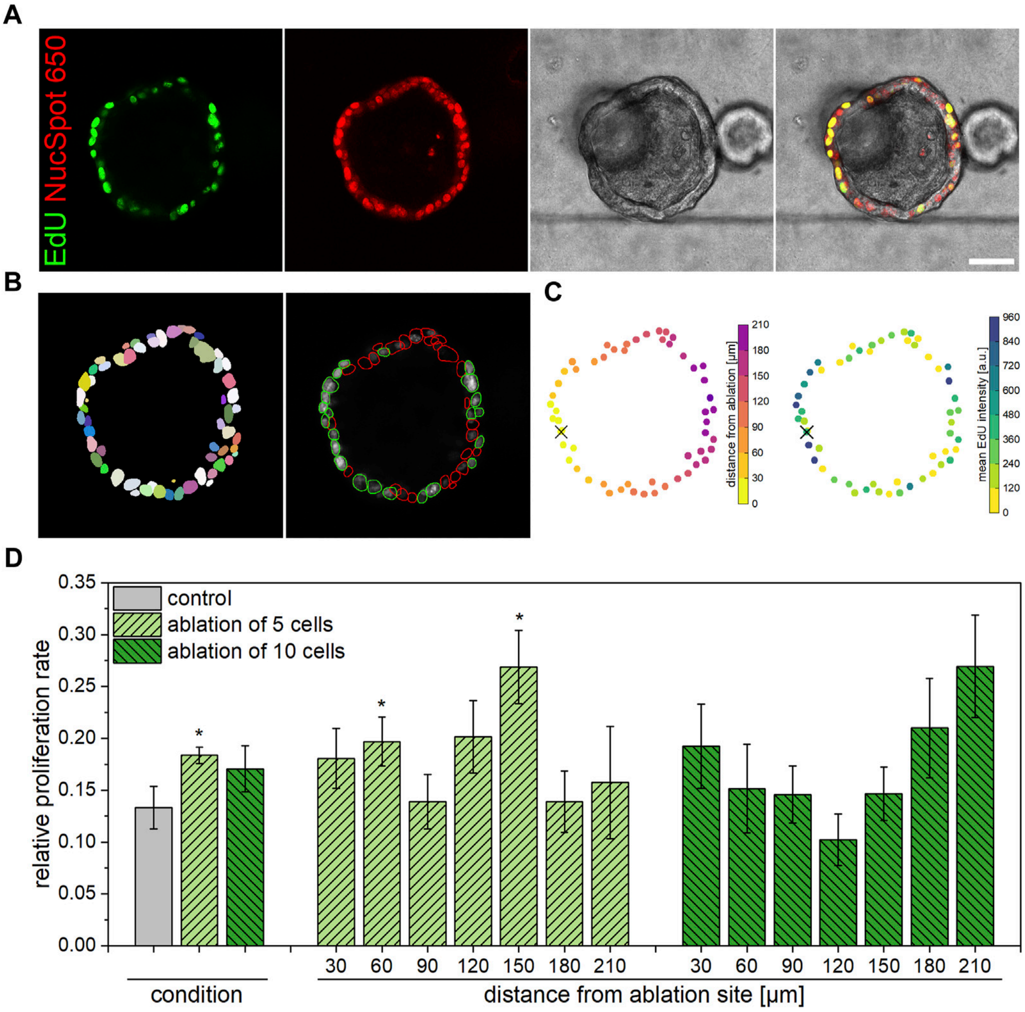

FIGURE 3
Influence of multiple cell ablation on proliferation within airway organoids. Ablation of five cells induced an enhanced proliferative behavior within 4 h post laser nanosurgery in cells within close proximity as well as at an intermediate distance to the ablation site. **(A)**: Representative confocal microscopy images showing an organoid 4 h post ablation of ten cells, stained for EdU incorporation (green) and all nuclei (red). Scale bar: 50 µm. **(B)**: Images obtained from Fiji analysis workflow showing detection of all cells via Stardist (left) and subsequent determination of EdU-positive (green circling) vs. all cells (red circling) (right). **(C)**: Images obtained from Matlab analysis workflow showing the distance from ablation site (left) and the mean EdU staining intensity (right) of each cell. Cross indicates center of ablation site. **(D)**: Relative location-independent (left) and location-dependent (right) proliferation rate of control organoids as well as of organoids subjected to ablation of either five or ten cells at 4 h post laser manipulation. Data shown represents mean ± SEM, $n \geq 8$ per condition, *: $p < 0.05$, statistic refers to control if not stated otherwise.

In conclusion, laser-based ablation of up to ten cells did not affect the overall viability or mid-term (24 h) growth potential of airway organoids, while enhanced or decelerated organoid size increases were observed in the early repair period in case of ablation of five or ten cells, respectively.

3.2 Cell death leads to increased proliferation in airway organoids dependent on the extent of damage

Next, we aimed for a more detailed investigation of cell proliferation—a major contributing factor of organoid growth and epithelial restitution (Crosby and Waters, 2010)—within organoids following laser-based nanosurgery. For this, an EdU assay was performed to fluorescently label cells that underwent cell cycle S-phase within 4 h post cell ablation (Kotogány et al., 2010). As previous morphological analyses revealed that ablation of five or ten cells led to the most pronounced alterations in organoid growth behavior within 4 h post laser treatment, these conditions were chosen to examine the proliferation of individual cells within airway organoids. Organoids kept under the same experimental conditions without being subjected to laser nanosurgery served as control.

Qualitatively, confocal microscopy images of fixed organoids stained for EdU incorporation with nuclear counterstain show the extent of proliferative cells within each organoid, representatively illustrated in Figure 3A. For quantitative analysis of the relative proliferation rate within each organoid, Fiji Stardist plugin (Schmidt et al., 2018) was employed to recognize all as well as EdU positive cells only (Figure 3B) in images acquired via confocal microscopy. A

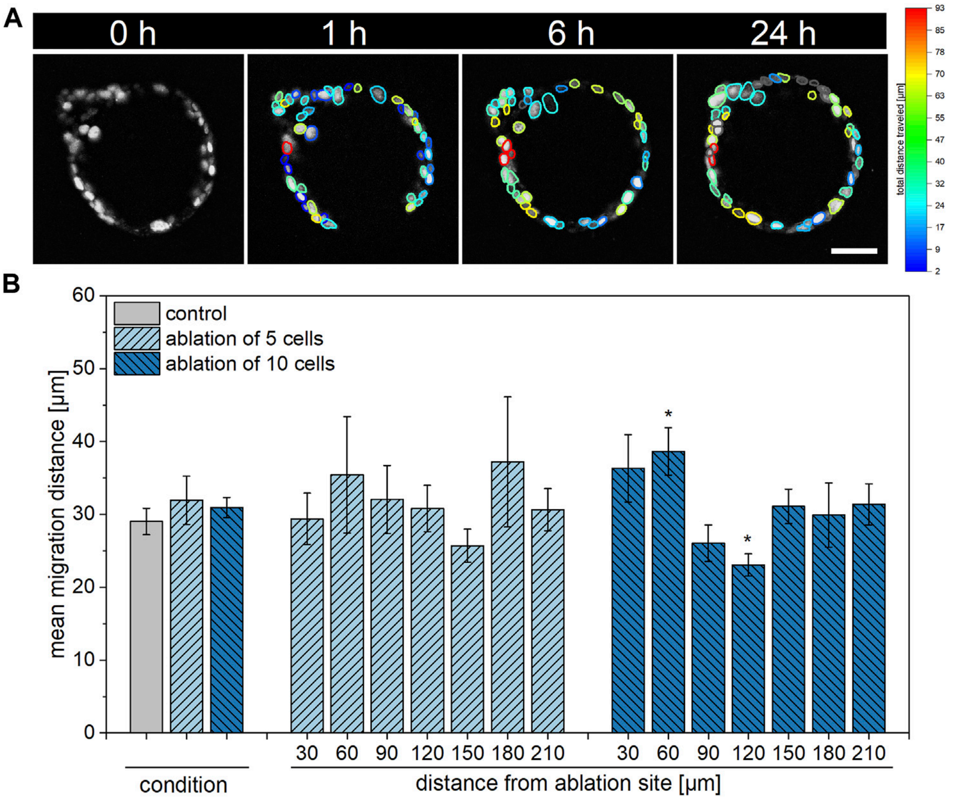

FIGURE 4
Influence of multiple cell ablation on single cell migration distance within airway organoids. Alterations in migratory behavior of cells in close proximity to or at an intermediate distance from the ablation site were detected in organoids subjected to ablation of ten cells. **(A)**: Representative timeline showing an organoid 0, 1, 4, and 24 h post ablation of ten cells with visualization of each cell's total distance travelled as detected by TrackMate. Scale bar: 50 µm. **(B)**: Relative location-independent (left) and location-dependent (right) mean migration distance of control organoids as well as of organoids subjected to ablation of either five or ten cells at 24 h post laser manipulation. Data shown represents mean ± SEM, *n* ≥ 8 per condition, *: *p* < 0.05, statistic refers to control if not stated otherwise.

subsequent application of a custom MatLab script fitted all organoid cells to a circle, in which the distance from the ablation site of each cell was determined (Figure 3C). Further, the script supplied data on the relative proliferation rate in dependence on the distance from the ablation site for each condition. As presented in Figure 3D, it was found that the overall proliferation rate in organoids subjected to ablation of five cells amounts to 18.4% ± 0.8% at 4 h post laser treatment, which represents a significant increase in comparison to untreated organoids (13.3% ± 2.1%, $p = 0.04$). It can further be observed that, in the case of ablation of five cells, an enhanced number of proliferative cells is located either in close proximity to or in an intermediate distance to the ablation site. In this context, proliferation rates of 19.7% ± 2.4% and 26.9% ± 3.5% were measured at distances from the ablation site of 30–60 µm and 120–150 µm, respectively. However, compared to the control, no significant alterations of the proliferation rate were detected for organoids subjected to ten-cell-ablation in either case of overall or location-dependent analysis. Against expectations gained from previous morphological analyses, the location-independent proliferation rate of organoids in which ten cells were ablated amounted to 17.1% ± 2.2%, which was slightly higher than the one determined for control organoids ($p = 0.18$). Also, similar to the observations made for organoids subjected to ablation of five cells, tendencies for enhanced proliferation rates in direct proximity to the ablation site (19.2% ± 4.1% at distances of 0–30 µm, $p = 0.13$) as well as further away (26.9% ± 4.9% at distances of 180–210 µm, $p = 0.05$) were detected in organoids after ablation of ten cells.

In conclusion, it was found that especially ablation of five cells induced an enhanced proliferation rate within airway organoids in the early phase of damage repair. In this context, the observed broad induction of cell proliferation is attributable to locally significantly increased proliferation events in cells in close proximity to as well as in an intermediate distance from the ablation site.

3.3 Large-area damage results in increased localized migration

As epithelial restitution generally depends on both cell proliferation as well as migration (Zahm et al., 1997), we next aimed to examine the migratory behavior of organoid cells within 24 h post laser treatment. For this, images of organoids subjected to ablation of either no (control), five or ten cells acquired via multiphoton microscopy were analyzed using Fiji Stardist (Schmidt et al., 2018) and Trackmate (Ershov et al., 2022) plugins. The achieved track results, illustrated as the maximum distance traveled in Figure 4A, were employed in a custom Matlab

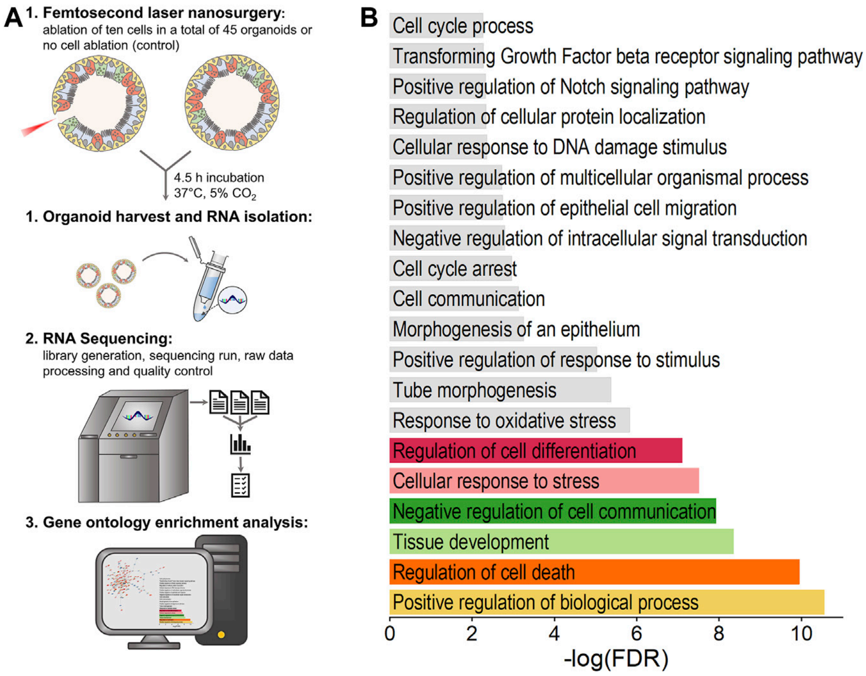

FIGURE 5
Influence of ablation of ten cells on airway organoids' transcriptome. Both genes related to damage induction as well as to repair mechanisms were found to be differentially expressed. **(A)**: Schematic illustration of experimental procedure for transcriptome analysis. **(B)**: Biological processes significantly affected by laser treatment as determined by gene ontology enrichment analysis using STRING database. Data analysis was performed on the basis of RNA-seq data obtained from $n = 6$ samples per group.

script. Analogous to the handling of EdU data, the script fitted all organoid cells to a circle, in which the distance from the ablation site of each cell was determined and data of the migrated distance of each cell in dependence on the distance from the ablation site was supplied.

As represented in Figure 4B, organoid cells of all conditions showed similar migration behavior when analyzed location-independently with mean migration distances of 29.1 ± 1.8 µm, 32.0 ± 3.3 µm and 30.9 ± 1.4 µm within control organoids or after ablation of five or ten cells, respectively, within 24 h. Upon ablation of five cells, migratory activity was not found to be locally enhanced or reduced at 24 h post laser treatment in a significant manner. On the contrary, in comparison to the control, ablation of ten cells led to an increased migration distance of 38.7 ± 3.2 µm of cells within a distance of 30–60 µm from the ablation site ($p = 0.02$). Further, a decrease in migration distance to 23.1 ± 1.5 µm was observed in cells within an intermediate distance from the ablation site of 90–120 µm ($p = 0.02$).

Taken together, alterations in migratory behavior of cells were found in a location-dependent manner in response to ablation of ten, but not five cells.

3.4 Transcriptome analysis reveals the influence of cell ablation on migration, differentiation, and further developmental processes next to cell death and stress pathways

To gain further insights into the functional processes affected by laser-based damage induction and subsequent repair mechanisms, we compared the transcriptomes of organoid cells of untreated condition and post cell ablation via bulk RNA sequencing. According to previous results, which indicated both migration as well as proliferation as driving processes of repair in the case of ablation of ten cells, this condition was chosen for RNA sequencing. A schematic representation of the experimental procedure is shown in Figure 5A.

In relation to the total number of cells an organoid is composed of, ablation of ten cells represents a rather small and highly localized injury. Thus, we expected that, primarily, cells in close proximity to the damage site are involved in early repair processes, which would lead to relatively small changes in the overall measured expression profiles of treated *versus* untreated organoids. We therefore decided to include all differentially expressed genes (DEGs) with a p-adjusted <0.05 for analysis, independently of their determined fold change. In this context, we identified a total of 218 mRNA transcripts, including 129 upregulated and 89 downregulated transcripts, that were differentially expressed in the laser-treated group compared to the control. Notably, these DEGs included *Trp63* (p-adj = 4.79E-9) and *Sox2* (p-adj = 2.54E-2), both of which play a pivotal role in the maintenance of airway epithelial basal cells (Ochieng et al., 2014), while *Krt8* as the gene coding for a general marker of luminal cell types of the airway epithelium (Rock et al., 2009) was not found to be significantly dysregulated (FC = 0.10, p-adj = 0.26).

Subsequent gene ontology (GO) enrichment analysis using STRING database was performed based on all DEGs, which yielded 85 significantly enriched GO terms for biological processes (FDR <0.05), partially displayed in Figure 5B. It was found that, on the one hand, the analyzed DEGs are involved in the positive regulation of biological process (FDR = 2.80E-11, 73 genes, e.g., *Cdc45*, *Tmprss2*, *Plin2*, *Pabpc1*, *Ier3*), regulation of cell death (FDR = 1.13E-10, 37 genes, e.g., *Ier3*, *Nqo1*, *Robo1*, *Xdh*, *Cyp1b1*), cellular response to stress (FDR = 3.12E-8, 31 genes, e.g., *Cdc45*, *Ier3*, *Nqo1*, *Atf6b*, *Robo1*) and response to oxidative stress (FDR = 1.49E-6, 15 genes, e.g., *Nqo1*, *Cyp1b1*, *Pycr1*, *Pcna*, *Slc7a11*), which can all be directly linked to damage induction. On the other hand, the GO biological processes of tissue development (FDR = 4.53E-9, 35 genes, e.g., *Lgr5*, *Vcl*, *Robo1*, *Cyp1b1*, *Hbegf*), regulation of cell differentiation (FDR = 7.96E-8, 34 genes, e.g., *Ptprg*, *Vcl*, *Robo1*, *Xdh*, *Ddit3*), tube morphogenesis (FDR = 4.19E-6, 19 genes, e.g., *Lgr5*, *Robo1*, *Cyp1b1*, *Hbegf*, *Epha7*) and positive regulation of epithelial cell migration (FDR = 1.80E-3, 7 genes, e.g., *Hbegf*, *Ptgs2*, *Tgfb2*, *Sema5a*, *Plcg2*) were determined to be significantly enriched upon laser-based cell ablation. Further, enrichment analysis identified overall cell communication (FDR = 7.50E-4, 43 genes, e.g., *Ier3*, *Stk38*, *Atf6b*, *Lgr5*, *Robo1*) as well as Notch (FDR = 4.70E-3, 4 genes, *Robo1*, *Tgfb2*, *Sox2*, *Trp63*) and transforming growth factor beta (TGF-beta) receptor (FDR = 5.30E-3, 5 genes, *Ltbp4*, *Tgfb2*, *Jun*, *Trp53*, *Skil*) signaling pathways as specifically regulated in response to laser treatment. The involvement of genes in the top six significant GO biological processes as well as their fold-change determined by RNA-seq is illustrated in Supplementary Figure S2.

In conclusion, despite the presumably minor number of cells involved in the early repair processes of airway organoids upon laser-based ablation, changes in expression of genes related to both damage induction as well as cellular regenerative responses were detected.

4 Discussion

Especially chronic pulmonary diseases can cause severe damage in airway epithelial tissue, often finally leading to conditions, in which endogenous regeneration mechanisms fail to repair (Rock and Königshoff, 2012; Barkauskas et al., 2017). Unfortunately, effective medication targeting early cellular injury responses, thereby supporting the cells' native homeostasis and repair programs, have yet to be developed as the underlying mechanisms are still not fully understood (Barkauskas et al., 2017). To enable studying such mechanisms on the long-term, we established an *in vitro* damage model which enables the precise application of injury to airway epithelial cells within self-assembled organoids, allowing for subsequent tracking of triggered repair processes in a close-to-native, multicellular 3D environment via state-of-the-art microscopy techniques.

For the characterization of early repair processes induced in airway organoids upon targeted ablation of a single or up to ten cells, the effects of femtosecond laser-based manipulation on the organoids' structural integrity as well as the cells' migratory and proliferative behavior were studied. Airway epithelial tissue is described to unleash a remarkable endogenous regeneration potential upon injury (Rao Tata and Rajagopal, 2017). Based on this, we expected a fast and efficient repair of the gap within the cell layer restoring the epithelium's structural integrity, induced by targeted ablation. This was observed in nearly all studied organoids (within 4–10 h post laser-based injury infliction). The obtained data show that both migration and proliferation are potentially involved in the airway organoids' repair process following laser-based nanosurgery. This indicates that targeted cell ablation might induce a cellular program with similar mechanisms occurring during epithelial restitution upon injury in native lung tissue (Crosby and Waters, 2010). It was shown that the employed airway organoids are generally characterized by a consistent growth behavior, which is in good agreement with published data of similar cultures (Rabata et al., 2017; Sachs et al., 2019; Ekanger et al., 2022). Still, the underlying enhanced proliferation rate compared to the native tissue's properties needs to be taken into consideration when employing this model for regeneration studies. In this context, on the one hand, the data suggest that ablation of five cells or less, posing a very small damage area, results in a fast repair dominated by early cell proliferation. On the other hand, cell cycle progress might be paused in an early phase upon ablation of ten cells, thereby enabling migration of nearby cells to take part in restoring the epithelial barrier. Notably, according to previous publications, one of the first and also most important processes that characterize repair of injured airway epithelial tissue is cell migration rather than proliferation (Erjefält et al., 1995; Zahm et al., 1997; Puchelle et al., 2006). Thus, the sequence of events occurring upon ablation of ten cells mimics the described procedure of epithelial wound healing, marking this as a potentially suitable model for studying early repair processes *in vitro*.

The results obtained by image analysis are further supported by the transcriptomic changes within airway organoids upon laser-based ablation of ten cells revealed by RNA-seq, which indicate the enrichment of the processes of cell cycle arrest and positive regulation of epithelial cell migration in the early phase of repair. Notably, also a variety of genes directly linked to epithelial repair were found to be differentially expressed. Among these, we found *Trp63* to be significantly upregulated upon cell ablation. It was previously shown that *Trp63* acts as a positive regulator of a set of genes functionally associated with epithelial differentiation and repair and necessary for wound healing (Warner et al., 2013). In good agreement with Warner et al., the described target genes such as *CTNNB1* (beta-catenin), *EGFR,* and *JAG1* (Jagged1) were not determined to be significantly differentially expressed, potentially attributable to a saturation of Trp63 signaling (Warner et al., 2013). Also, an increase in the number of basal cells, of which the expression of *Trp63* is a major characteristic, could have contributed to the determined upregulation. Since, in accordance with the EdU assay, we did not find cell proliferation to be specifically enhanced after the ablation of ten cells, dedifferentiation processes of secretory cells might be involved in the restoration of the epithelial barrier. In this context, YAP-1 was described to act as an important transcriptional coactivator regulating the occurrence of a dedifferentiation program in secretory cells and would be an interesting candidate to focus on in further studies (Zhao et al., 2014). As the mechanism of secretory cell dedifferentiation has only been observed after the elimination of a majority of the basal cell population though (Rawlins et al., 2009; Tata et al., 2013), further experiments will be necessary to evaluate whether localized cell ablation analogously induces local dedifferentiation effects.

The positive regulation of Notch signaling pathway, which was determined to be enriched upon cell ablation, might have different effects. On the one hand, Notch signaling was reported to support the maintenance of basal cells (Carraro et al., 2020), while on the other hand, Pardo-Saganta et al. found that basal cells support the maintenance of their progenies' secretory cell state also by Notch signaling (Pardo-Saganta et al., 2015).

Moreover, we showed that TGF-beta signaling was enriched in airway organoids upon targeted damage induction. TGF-beta is generally known to contribute to various regulatory functions including cell growth, migration, and differentiation (Zhao and Young, 1996; Beck et al., 2003). The physiological production of TGF-beta in airway epithelial cells under homeostatic conditions was shown to increase upon injury, suggesting that cytokine plays a role in wound healing (Thompson et al., 2006). While Thompson et al. demonstrated that TGF-beta2 contributes to the modulation of subepithelial extracellular matrix homeostasis (Thompson et al., 2006), Ito et al. further described TGF-beta as a stimulator of airway epithelial repair after mechanical injury (Ito et al., 2011). In this context, it was found that TGF-beta induces the production of HB-EGF in airway epithelial cells, which subsequently leads to phosphorylation of EGFR and thus autocrine activation of EGF signaling as key factor in the repair process (Ito et al., 2011). In good agreement with this, the expression of both TGF-beta2 and HB-EGF were determined to be upregulated in airway organoids upon cell ablation.

In conclusion, the employment of femtosecond laser-based nanosurgery for targeted cell ablation in airway organoids poses a novel approach for the investigation of cellular damage responses in the course of early epithelial repair after cellular lung injury. This method creates the possibility to reduce animal experiments and have a fine tempo-spatial resolution of the repair process and underlying mechanisms of airway epithelium. We showed that ablation of ten neighboring cells induces a repair program including cell migration and subsequent proliferation in airway organoids, thereby potentially resembling the mechanisms of epithelial restitution in native tissue. Further functional analyses revealed the involvement of Notch and TGF-beta signaling activity previously described to regulate epithelial repair in airways. Based on these findings, future experiments utilizing a lentiviral Notch signaling activity reporter allowing for the tracking of dynamic signaling levels in individual cells via live imaging are of high interest.

Together, the herein described *in vitro* 3D damage model of airway organoids can be employed to further enlighten the intra- and intercellular mechanisms induced by local injury and necessary for efficient epithelial repair. By combining the culture of airway epithelial cells with, e.g., immune cells such as macrophages, an even more complex model system can be designed and applied for translational studies.

Data availability statement

The datasets presented in this study can be found in online repositories. The names of the repository/repositories and accession number(s) can be found below: NCBI GEO, under GSE241237.

Ethics statement

Ethical approval was not required for the studies on humans in accordance with the local legislation and institutional requirements because only commercially available established cell lines were used. The animal study was approved by Lower Saxony State Office for Consumer Protection and Food Safety (reference number 42500/1H). The study was conducted in accordance with the local legislation and institutional requirements.

Author contributions

LG: Conceptualization, Formal Analysis, Investigation, Methodology, Validation, Visualization, Writing–original draft, Writing–review and editing, Data curation. SD: Writing–review and editing, Investigation, Methodology, Validation. AS: Writing–review and editing, Investigation, Methodology, Validation. LP: Writing–review and editing, Investigation. MB: Funding acquisition, Writing–review and editing, Formal Analysis, Methodology, Resources. AH: Funding acquisition, Project administration, Writing–review and editing, Resources. SK: Conceptualization, Formal Analysis, Funding acquisition, Investigation, Methodology, Project administration, Software, Supervision, Writing–original draft, Writing–review and editing, Data curation, Resources, Validation, Visualization.

Funding

The authors declare financial support was received for the research, authorship, and/or publication of this article. AH received funding by the biomedical research in endstage and obstructive lung disease Hannover (BREATH) from the German Center for Lung Research (DZL, 82DZL002B3). SK, MB, and AH received funding by the REBIRTH Research Center for Translational Regenerative Medicine (ZN3440, State of Lower Saxony Ministry of Science and Culture (Nieders. Vorab)). The publication of this article was funded by the Open Access Fund of Leibniz University Hannover.

Acknowledgments

RNA library preparation, sequencing, raw data processing, quality control, normalization and differential expression analysis was performed by the Genomic core facility of Hannover Medical School. We thank Maria Mellin, Puja Pandey and Anja Siebert (all Hannover Medical School) for providing conditioned culture medium.

Conflict of interest

The authors declare that the research was conducted in the absence of any commercial or financial relationships that could be construed as a potential conflict of interest.

Publisher's note

Supplementary material

The Supplementary Material for this article can be found online at: https://www.frontiersin.org/articles/10.3389/fcell.2023.1268621/full#supplementary-material

References

Barkauskas, C. E., Chung, M. I., Fioret, B., Gao, X., Katsura, H., and Hogan, B. L. M. (2017). Lung organoids: current uses and future promise. *Dev* 144, 986–997. doi:10.1242/dev.140103

Beck, P. L., Rosenberg, I. M., Xavier, R. J., Koh, T., Wong, J. F., and Podolsky, D. K. (2003). Transforming growth factor-β mediates intestinal healing and susceptibility to injury *in vitro* and *in vivo* through epithelial cells. *Am. J. Pathol.* 162, 597–608. doi:10.1016/S0002-9440(10)63853-9

Borthwick, D. W., Shahbazian, M., Krantz, Q. T., Dorin, J. R., and Randell, S. H. (2001). Evidence for stem-cell niches in the tracheal epithelium. *Am. J. Respir. Cell Mol. Biol.* 24, 662–670. doi:10.1165/ajrcmb.24.6.4217

Carraro, G., Mulay, A., Yao, C., Mizuno, T., Konda, B., Petrov, M., et al. (2020). Single-cell reconstruction of human basal cell diversity in normal and idiopathic pulmonary fibrosis lungs. *Am. J. Respir. Crit. Care Med.* 202, 1540–1550. doi:10.1164/rccm.201904-0792OC

Cheng, Z., Han, Y., Wei, B., Lai, B., Li, B., Cui, M., et al. (2021). Probing neuronal functions with precise and targeted laser ablation in the living cortex. *Optica* 8, 1559. doi:10.1364/OPTICA.433562

Chiu, M. C., Li, C., Liu, X., Yu, Y., Huang, J., Wan, Z., et al. (2022). A bipotential organoid model of respiratory epithelium recapitulates high infectivity of SARS-CoV-2 Omicron variant. *Cell Discov.* 8, 57. doi:10.1038/s41421-022-00422-1

Clevers, H. (2016). Modeling development and disease with organoids. *Cell* 165, 1586–1597. doi:10.1016/j.cell.2016.05.082

Crosby, L. M., and Waters, C. M. (2010). Epithelial repair mechanisms in the lung. *Am. J. Physiol. - Lung Cell. Mol. Physiol.* 298, L715–L731. doi:10.1152/ajplung.00361.2009

Donath, S., Angerstein, L., Gentemann, L., Müller, D., Seidler, A. E., Jesinghaus, C., et al. (2022). Investigation of colonic regeneration via precise damage application using femtosecond laser-based nanosurgery. *Cells* 11, 1143. doi:10.3390/cells11071143

Doncheva, N. T., Morris, J. H., Gorodkin, J., and Jensen, L. J. (2019). Cytoscape StringApp: network analysis and visualization of proteomics data. *J. Proteome Res.* 18, 623–632. doi:10.1021/acs.jproteome.8b00702

Ekanger, C. T., Zhou, F., Bohan, D., Lotsberg, M. L., Ramnefjell, M., Hoareau, L., et al. (2022). Human organotypic airway and lung organoid cells of bronchiolar and alveolar differentiation are permissive to infection by influenza and SARS-CoV-2 respiratory virus. *Front. Cell. Infect. Microbiol.* 12, 841447–841523. doi:10.3389/fcimb.2022.841447

Erjefält, J. S., Erjefält, I., Sundler, F., and Persson, C. G. A. (1995). *In vivo* restitution of airway epithelium. *Cell Tissue Res.* 281, 305–316. doi:10.1007/BF00583399

Ershov, D., Phan, M. S., Pylvänäinen, J. W., Rigaud, S. U., Le Blanc, L., Charles-Orszag, A., et al. (2022). TrackMate 7: integrating state-of-the-art segmentation algorithms into tracking pipelines. *Nat. Methods* 19, 829–832. doi:10.1038/s41592-022-01507-1

Guo, C., Zhang, Z., Lau, A. K. H., Lin, C. Q., Chuang, Y. C., Chan, J., et al. (2018). Effect of long-term exposure to fine particulate matter on lung function decline and risk of chronic obstructive pulmonary disease in taiwan: a longitudinal, cohort study. *Lancet Planet. heal.* 2, e114–e125. doi:10.1016/S2542-5196(18)30028-7

Heisterkamp, A., Maxwell, I. Z., Mazur, E., Underwood, J. M., Nickerson, J. A., Kumar, S., et al. (2005). Pulse energy dependence of subcellular dissection by femtosecond laser pulses. *Opt. Express* 13, 3690–3696. doi:10.1364/opex.13.003690

Hogan, B. L. M., Barkauskas, C. E., Chapman, H. A., Epstein, J. A., Jain, R., Hsia, C. C. W., et al. (2014). Repair and regeneration of the respiratory system: complexity, plasticity, and mechanisms of lung stem cell function. *Cell Stem Cell* 15, 123–138. doi:10.1016/j.stem.2014.07.012

Hsu, H. S., Liu, C. C., Lin, J. H., Hsu, T. W., Su, K., and Hung, S. C. (2014). Repair of naphthalene-induced acute tracheal injury by basal cells depends on β-catenin. *J. Thorac. Cardiovasc. Surg.* 148, 322–332. doi:10.1016/j.jtcvs.2013.10.039

Ito, J., Harada, N., Nagashima, O., Makino, F., Usui, Y., Yagita, H., et al. (2011). Wound-induced TGF-β1 and TGF-β2 enhance airway epithelial repair via HB-EGF and TGF-α. *Biochem. Biophys. Res. Commun.* 412, 109–114. doi:10.1016/j.bbrc.2011.07.054

König, K., Riemann, I., Fischer, P., and Halbhuber, K. J. (1999). Intracellular nanosurgery with near infrared femtosecond laser pulses. *Cell. Mol. Biol. (Noisy-le-grand)* 45, 195–201.

Kotogány, E., Dudits, D., Horváth, G. V., and Ayaydin, F. (2010). A rapid and robust assay for detection of S-phase cell cycle progression in plant cells and tissues by using ethynyl deoxyuridine. *Plant Methods* 6, 5. doi:10.1186/1746-4811-6-5

Lanza, M., Marinari, B., Papoutsaki, M., Giustizieri, M. L., D'Alessandra, Y., Chimenti, S., et al. (2006). Cross-talks in the p53 family: deltaNp63 is an anti-apoptotic target for deltaNp73alpha and p53 gain-of-function mutants. *Cell Cycle* 5, 1996–2004. doi:10.4161/cc.5.17.3188

Liang, X.-X., and Vogel, A. (2022). Probing neuronal functions with precise and targeted laser ablation in the living cortex: comment. *Optica* 9, 868. doi:10.1364/OPTICA.454469

Mori, M., Mahoney, J. E., Stupnikov, M. R., Paez-Cortez, J. R., Szymaniak, A. D., Varelas, X., et al. (2015). Notch3-Jagged signaling controls the pool of undifferentiated airway progenitors. *Development* 142, 258–267. doi:10.1242/dev.116855

Müller, D., Hagenah, D., Biswanath, S., Coffee, M., Kampmann, A., Zweigerdt, R., et al. (2019). Femtosecond laser-based nanosurgery reveals the endogenous regeneration of single Z-discs including physiological consequences for cardiomyocytes. *Sci. Rep.* 9, 3625–3710. doi:10.1038/s41598-019-40308-z

Müller, D., Klamt, T., Gentemann, L., Heisterkamp, A., and Kalies, S. M. K. (2021). Evaluation of laser induced sarcomere microdamage: role of damage extent and location in cardiomyocytes. *PLoS One* 16, 02523466–e252417. doi:10.1371/journal.pone.0252346

Ochieng, J. K., Schilders, K., Kool, H., Boerema-De Munck, A., Buscop-Van Kempen, M., Gontan, C., et al. (2014). Sox2 regulates the emergence of lung basal cells by directly activating the transcription of Trp63. *Am. J. Respir. Cell Mol. Biol.* 51, 311–322. doi:10.1165/rcmb.2013-0419OC

Pardo-Saganta, A., Law, B. M., Tata, P. R., Villoria, J., Saez, B., Mou, H., et al. (2015). Injury induces direct lineage segregation of functionally distinct airway basal stem/progenitor cell subpopulations. *Cell Stem Cell* 16, 184–197. doi:10.1016/j.stem.2015.01.002

Puchelle, E., Zahm, J. M., Tournier, J. M., and Coraux, C. (2006). Airway epithelial repair, regeneration, and remodeling after injury in chronic obstructive pulmonary disease. *Proc. Am. Thorac. Soc.* 3, 726–733. doi:10.1513/pats.200605-126SF

Rabata, A., Hampl, A., and Koledova, Z. (2017). Lungosphere assay: 3D culture of lung epithelial stem/progenitor cells. *Methods Mol. Biol.* 1612, 149–165. doi:10.1007/978-1-4939-7021-6_11

Rao Tata, P., and Rajagopal, J. (2017). Plasticity in the lung: making and breaking cell identity. *Dev* 144, 755–766. doi:10.1242/dev.143784

Rawlins, E. L., Okubo, T., Xue, Y., Brass, D. M., Auten, R. L., Hasegawa, H., et al. (2009). The role of Scgb1a1+ clara cells in the long-term maintenance and repair of lung airway, but not alveolar, epithelium. *Cell Stem Cell* 4, 525–534. doi:10.1016/j.stem.2009.04.002

Rock, J., and Königshoff, M. (2012). Endogenous lung regeneration: potential and limitations. *Am. J. Respir. Crit. Care Med.* 186, 1213–1219. doi:10.1164/rccm.201207-1151PP

Rock, J. R., Gao, X., Xue, Y., Randell, S. H., Kong, Y. Y., and Hogan, B. L. M. (2011). Notch-dependent differentiation of adult airway basal stem cells. *Cell Stem Cell* 8, 639–648. doi:10.1016/j.stem.2011.04.003

Rock, J. R., Onaitis, M. W., Rawlins, E. L., Lu, Y., Clark, C. P., Xue, Y., et al. (2009). Basal cells as stem cells of the mouse trachea and human airway epithelium. *Proc. Natl. Acad. Sci. U. S. A.* 106, 12771–12775. doi:10.1073/pnas.0906850106

Rock, J. R., Randell, S. H., and Hogan, B. L. M. (2010). Airway basal stem cells: A perspective on their roles in epithelial homeostasis and remodeling. *DMM Dis. Model. Mech.* 3, 545–556. doi:10.1242/dmm.006031

Sachs, N., Papaspyropoulos, A., Zomer-van Ommen, D. D., Heo, I., Böttinger, L., Klay, D., et al. (2019). Long-term expanding human airway organoids for disease modeling. *EMBO J.* 38, 1–20. doi:10.15252/embj.2018100300

Schambach, A., Galla, M., Modlich, U., Will, E., Chandra, S., Reeves, L., et al. (2006). Lentiviral vectors pseudotyped with murine ecotropic envelope: increased biosafety and convenience in preclinical research. *Exp. Hematol.* 34, 588–592. doi:10.1016/j.exphem.2006.02.005

Schindelin, J., Arganda-Carreras, I., Frise, E., Kaynig, V., Longair, M., Pietzsch, T., et al. (2012). Fiji: an open-source platform for biological-image analysis. *Nat. Methods* 9, 676–682. doi:10.1038/nmeth.2019

Schmidt, U., Weigert, M., Broaddus, C., and Myers, G. (2018). "Cell detection with star-convex polygons," in *Medical image computing and computer assisted intervention – MICCAI 2018*. Editors A. F. Frangi, J. A. Schnabel, C. Davatzikos, C. Alberola-López, and G. Fichtinger (Cham: Springer International Publishing), 265–273.

Shannon, P., Markiel, A., Ozier, O., Baliga, N. S., Wang, J. T., Ramage, D., et al. (2003). Cytoscape: A software environment for integrated models of biomolecular interaction networks. *Genome Res.* 13, 2498–2504. doi:10.1101/gr.1239303

Tata, P. R., Mou, H., Pardo-Saganta, A., Zhao, R., Prabhu, M., Law, B. M., et al. (2013). Dedifferentiation of committed epithelial cells into stem cells *in vivo*. *Nature* 503, 218–223. doi:10.1038/nature12777

Thompson, H. G. R., Mih, J. D., Krasieva, T. B., Tromberg, B. J., and George, S. C. (2006). Epithelial-derived TGF-beta2 modulates basal and wound-healing subepithelial matrix homeostasis. *Am. J. Physiol. - Lung Cell. Mol. Physiol.* 291, 1277–1285. doi:10.1152/ajplung.00057.2006

Tsao, P., Vasconcelos, M., Izvolsky, K. I., Qian, J., Lu, J., and Cardoso, W. V. (2009). Notch signaling controls the balance of ciliated and secretory cell fates in developing airways. *Development* 136, 2297–2307. doi:10.1242/dev.034884

Van Lidth De Jeude, J. F., Vermeulen, J. L. M., Montenegro-Miranda, P. S., Van Den Brink, G. R., and Heijmans, J. (2015). A protocol for lentiviral transduction and downstream analysis of intestinal organoids. *J. Vis. Exp.* 2015, 52531. doi:10.3791/52531

Vernooy, J. H. J., Dentener, M. A., Van Suylen, R. J., Buurman, W. A., and Wouters, E. F. M. (2002). Long-term intratracheal lipopolysaccharide exposure in mice results in chronic lung inflammation and persistent pathology. *Am. J. Respir. Cell Mol. Biol.* 26, 152–159. doi:10.1165/ajrcmb.26.1.4652

Vogel, A., Noack, J., Hüttman, G., and Paltauf, G. (2005). Mechanisms of femtosecond laser nanosurgery of cells and tissues. *Appl. Phys. B* 81, 1015–1047. doi:10.1007/s00340-005-2036-6

Warner, S. M. B., Hackett, T. L., Shaheen, F., Hallstrand, T. S., Kicic, A., Stick, S. M., et al. (2013). Transcription factor p63 regulates key genes and wound repair in human airway epithelial Basal cells. *Am. J. Respir. Cell Mol. Biol.* 49, 978–988. doi:10.1165/rcmb.2012-0447OC

Wu, M., Zhang, X., Lin, Y., and Zeng, Y. (2022). Roles of airway basal stem cells in lung homeostasis and regenerative medicine. *Respir. Res.* 23, 122–212. doi:10.1186/s12931-022-02042-5

Xing, Y., Li, A., Borok, Z., Li, C., and Minoo, P. (2012). NOTCH1 is required for regeneration of clara cells during repair of airway injury. *Stem Cells* 30, 946–955. doi:10.1002/stem.1059

Zahm, J.-M., Kaplan, H., Hérard, A.-L., Doriot, F., Pierrot, D., Somelette, P., et al. (1997). Cell migration and proliferation during the *in vitro* wound repair of the respiratory epithelium. *Cell Motil. Cytoskelet.* 37, 33–43. doi:10.1002/(SICI)1097-0169(1997)37:1<33::AID-CM4>3.0.CO;2-I

Zhao, R., Fallon, T. R., Saladi, S. V., Pardo-Saganta, A., Villoria, J., Mou, H., et al. (2014). Yap tunes airway epithelial size and architecture by regulating the identity, maintenance, and self-renewal of stem cells. *Dev. Cell* 30, 151–165. doi:10.1016/j.devcel.2014.06.004

Zhao, Y., and Young, S. L. (1996). Requirement of transforming growth factor-β (TGF-β) type II receptor for TGF-β-induced proliferation and growth inhibition. *J. Biol. Chem.* 271, 2369–2372. doi:10.1074/jbc.271.5.2369

frontiers | Frontiers in Cell and Developmental Biology

TYPE Original Research
PUBLISHED 19 September 2023
DOI 10.3389/fcell.2023.1165581

Check for updates

OPEN ACCESS

EDITED BY
Xiao Xiao Tang,
First Affiliated Hospital of Guangzhou Medical University, China

REVIEWED BY
Huisheng Liu,
Guangzhou National Laboratory, China
Gavin Tjin,
University of Melbourne, Australia

*CORRESPONDENCE
P. P. S. J. Khedoe,
✉ p.p.s.j.khedoe@lumc.nl

RECEIVED 14 February 2023
ACCEPTED 28 August 2023
PUBLISHED 19 September 2023

CITATION
Khedoe PPSJ, van Schadewijk WAAM, Schwiening M, Ng-Blichtfeldt JP, Marciniak SJ, Stolk J, Gosens R and Hiemstra PS (2023), Cigarette smoke restricts the ability of mesenchymal cells to support lung epithelial organoid formation.
Front. Cell Dev. Biol. 11:1165581.
doi: 10.3389/fcell.2023.1165581

Cigarette smoke restricts the ability of mesenchymal cells to support lung epithelial organoid formation

P. P. S. J. Khedoe[1]*, W. A. A. M. van Schadewijk[1], M. Schwiening[2], J. P. Ng-Blichtfeldt[3,4], S. J. Marciniak[2], J. Stolk[1], R. Gosens[3] and P. S. Hiemstra[1]

[1]Department of Pulmonology, Leiden University Medical Centre, Leiden, Netherlands, [2]Department of Medicine, Cambridge Institute for Medical Research, University of Cambridge, Cambridge, United Kingdom, [3]Department of Molecular Pharmacology, Groningen Research Institute of Pharmacy, University of Groningen, Groningen, Netherlands, [4]MRC Laboratory of Molecular Biology, Cambridge Biomedical Campus, Cambridge, United Kingdom

Adequate lung epithelial repair relies on supportive interactions within the epithelial niche, including interactions with WNT-responsive fibroblasts. In fibroblasts from patients with chronic obstructive pulmonary disease (COPD) or upon *in vitro* cigarette smoke exposure, Wnt/β-catenin signalling is distorted, which may affect interactions between epithelial cells and fibroblasts resulting in inadequate lung repair. We hypothesized that cigarette smoke (CS), the main risk factor for COPD, interferes with Wnt/β-catenin signalling in fibroblasts through induction of cellular stress responses, including oxidative- and endoplasmic reticulum (ER) stress, and thereby alters epithelial repair support potential. Therefore, we assessed the effect of CS-exposure and the ER stress inducer Thapsigargin (Tg) on Wnt/β-catenin signalling activation in MRC-5 fibroblasts, and on their ability to support lung epithelial organoid formation. Exposure of MRC-5 cells for 15 min with 5 AU/mL CS extract (CSE), and subsequent 6 h incubation induced oxidative stress (*HMOX1*). Whereas stimulation with 100 nM Tg increased markers of both the integrated stress response (ISR - *GADD34/PPP1R15A*, *CHOP*) and the unfolded protein response (UPR - *XBP1spl*, *GADD34/PPP1R15A*, *CHOP* and *HSPA5/BIP*), CSE only induced *GADD34/PPP1R15A* expression. Strikingly, although treatment of MRC-5 cells with the Wnt activator CHIR99021 upregulated the Wnt/β-catenin target gene *AXIN2,* this response was diminished upon CSE or Tg pre-exposure, which was confirmed using a Wnt-reporter. Furthermore, pre-exposure of MRC-5 cells to CSE or Tg, restricted their ability to support organoid formation upon co-culture with murine pulmonary EpCam^{+} cells in Matrigel at day 14. This restriction was alleviated by pre-treatment with CHIR99021. We conclude that exposure of MRC-5 cells to CSE increases oxidative stress, *GADD34/PPP1R15A* expression and impairs their

---

Abbreviations: ACT, acetylated tubulin; AU/mL, arbitrary units/mL; BMP-4, bone morphogenic protein-4; COPD, chronic obstructive pulmonary disease; CS, cigarette smoke; CSE, CS extract; eIF2-a, eukaryotic initiation factor-a; EMT, epithelial-to-mesenchymal transition; ER, endoplasmic reticulum; FGF, fibroblast growth factors; HFL-1, human fetal lung fibroblasts; HGF, hepatocyte growth factor; ILD, interstitial lung diseases; ISR, integrated stress response; MACS, Magnetic-activated cell sorting; MEF, mouse embryonic fibroblasts; NAC, N-acetylcysteine; NEAAS, non-essential amino acids; SFTPC, pro-surfactant protein-C; Tg, Thapsigargin; UPR, unfolded protein response.

ability to support organoid formation. This inhibitory effect may be restored by activating the Wnt/β-catenin signalling pathway.

KEYWORDS

cigarette smoke extract, lung epithelial organoid, COPD, fibroblasts, oxidative stress, ER stress

Introduction

Lung injury and inadequate repair processes underlie a variety of chronic lung diseases, including chronic obstructive pulmonary disease (COPD) and interstitial lung diseases (ILD) (Kneidinger et al., 2011; Rock and Konigshoff, 2012; Baarsma et al., 2017). Adequate lung epithelial repair requires interactive cross-talk within the alveolar stem cell/progenitor niche between progenitor cells and their microenvironment, including structural cells such as fibroblasts (Baarsma et al., 2017; Skronska-Wasek et al., 2018). The mesenchymal niche orchestrates alveolar cell function and repair through secretion of fibroblast growth factors (FGFs), Wnt ligands, Wnt signalling activation and other growth factors (Frank et al., 2016; Zepp et al., 2017; Khedoe et al., 2021; Penkala et al., 2021). Dysfunctional signalling of repair pathways, including the Wnt/β-catenin pathway, has been implicated in aberrant lung epithelial repair in COPD (Rock and Konigshoff, 2012; Kneidinger et al., 2011). Importantly, Wnt-responsive mesenchymal cells dictate alveolar cell proliferation and differentiation, whereas myofibroblasts impair alveolar repair (Zepp et al., 2017). The Wnt/β-catenin signalling pathway is central to the interaction between epithelial cells and surrounding mesenchymal cells during repair processes. In lung diseases such as COPD, it has been hypothesized that this crosstalk is impaired, leading to inappropriate signalling between, for example, airway epithelial cells and fibroblasts. Wnt/β-catenin signalling is thus important for proper interaction between both lung epithelial cell and fibroblasts and its distortion may lead to disturbed cross-talk. In COPD, distorted Wnt/β-catenin signalling in fibroblasts may help to explain remodelling processes that together with tissue injury are a cause of impaired lung function (Baarsma et al., 2017).

One common cellular stress response, which is activated in smokers with and without COPD, is the unfolded protein response (UPR) to endoplasmic reticulum stress (ER stress) (Malhotra et al., 2009; Gan et al., 2011; Lawson et al., 2011; Marciniak, 2019). It has been demonstrated that ER stress may interfere with various repair pathways, which is relevant for COPD and ILD, since these pathways are overactivated in diseased lung tissue (Tanjore et al., 2012; Wei et al., 2013; Dickens et al., 2019). Whereas this cellular response is activated to restore homeostasis upon cellular or micro-environmental stress, prolonged activation can lead to cell dysfunction, inappropriate differentiation and cell death (Marciniak, 2019). Three transducers mediate sensing of ER stress and initiate activation of the UPR: ATF6, IRE1 and PERK. Autophosphorylation of the kinase domain of PERK results in attenuation of protein synthesis by phosphorylation of eukaryotic initiation factor (eIF2)-α, and this mechanism also contributes to the integrated stress response (ISR). However, in addition to PERK and ER stress, further eIF2α kinases can respond to a range of other cellular stresses to trigger the ISR resulting in similar downstream events (Emanuelli et al., 2020). Not only cigarette smoke, but also various endogenous and exogenous triggers are able to activate either the UPR or the ISR (Marciniak, 2019; Emanuelli et al., 2020; van 't Wout et al., 2015). Importantly, there is evidence for prolonged activation of the UPR and ISR in (epithelial) cells in cigarette smokers and COPD patients (Malhotra et al., 2009), and this has been implicated in dysfunction of both airway epithelial cells and pulmonary fibroblasts, leading to epithelial-to-mesenchymal transition (EMT) and myofibroblast differentiation (Delbrel et al., 2019; Song et al., 2019), respectively. Mutations in various genes, including *SFPTC* and *MUC5B* may induce ER stress in lung epithelial cells, contributing to EMT and fibrosis in IPF (Burman et al., 2018; Dickens et al., 2019). In addition to causing cellular dysfunction, prolonged activation of the UPR and ISR may interfere with mRNA processing and translation of proteins, leading to impairment of signalling pathways involved in repair.

In this study, we used an *in vitro* model of lung repair in which mesenchymal cells support epithelial organoid formation. Using this model, we have recently shown that TGF-β treatment of fibroblasts impairs their ability to support organoid formation (Ng-Blichfeldt et al., 2019). In the present study, our aim was to dissect the impact of cellular stress responses (e.g., oxidative stress and ER stress) on the supportive role of the lung fibroblast for lung epithelial cell repair. Therefore, we focused on the effect of cigarette smoke extract- and chemically-induced ER stress in MRC-5 fibroblasts, including Wnt/β-catenin signalling and their ability to support epithelial progenitor function.

Materials and methods

Mouse epithelial cell isolation

Lung epithelial cells were isolated from C57BL6/J mice (8–14 weeks) as described before (Ng-Blichfeldt et al., 2019; Wu et al., 2019). Mice were kept under a 12/12 h light/dark cycle and had *ad libitum* access to food and water. In short, after anesthesia (40 mg/kg ketamine and 0.5 mg/kg dexdomitor, i.p.) the pulmonary vasculature of C57BL/6N or C57BL6/J mice was flushed with PBS, after which the lungs were filled with Dispase (BD, Biosciences, Oxford, United Kingdom) in low-melting agarose (Sigma Aldrich, Poole, United Kingdom) for 45 min at room temperature (RT). Lung lobes were homogenized in DMEM containing DNase1 (Applichem, Germany), after which a single-cell suspension was prepared. Subsequently, using magnetic-activated cell sorting (MACS isolation), cell suspensions underwent a negative selection for CD45 (Miltenyi Biotec, Teterow, Germany) and CD31 (Miltenyi), after which EpCAM^{+} (CD326) epithelial cells were isolated (Miltenyi) as described before (Ng-Blichfeldt et al., 2019; Wu et al., 2019). Antibodies used for experimental procedures are listed in Table 1. EpCAM$^+$ cells were resuspended in DMEM with 10% fetal calf serum (FCS, Bodinco, Alkmaar, Netherlands). Experimental animal protocols were approved by the University of Groningen animal experimentation committee under CCD license AVD105002015303.

MRC-5 lung fibroblast and MEF culture and stimulation

MRC-5 lung fibroblasts (ATCC CCL 171, United States) were cultured in MEM (Gibco) containing 100 U/ml penicillin/streptomycin (Gibco), 25 mM HEPES (Invitrogen), non-essential amino acids (NEAAS, Gibco) and 10% heat-inactivated FCS at 37°C in 5% CO_2. For mRNA analyses, MRC-5 lung fibroblasts were grown to confluence and kept in serum-free medium overnight. MRC-5 were then stimulated for 15 min with 2 or 5 AU/mL freshly prepared cigarette smoke extract (CSE) generated as described in (23), washed with PBS and then further cultured for 6 h. To induce ER stress, MRC-5 fibroblasts were incubated for 6 h with 100 nM thapsigargin (Tg, Sigma). To examine the effect of Wnt/β-catenin activation on cellular stress responses (e.g., oxidative stress and ER stress), MRC-5 cells were treated with vehicle, 2 μM CHIR99021 or 10 mM N-acetylcysteine (NAC) during the 6 h exposure. After 6 h, MRC-5 cells were lysed for RNA isolation and gene expression analyses. Similar stimulation procedures were applied to mouse embryonic fibroblasts (MEFs), derived from WT, Gadd34$^{-/-}$, Chop$^{-/-}$ or EIF2a AA signalling deficient mice (Scheuner et al., 2001).

For organoid assays, MRC-5 fibroblasts were first mitotically inactivated using 10 μg/mL Mitomycin-C (Sigma-Aldrich) (Ng-Blichfeldt et al., 2019), followed by washing and a restoration period of 1 h. MRC-5 fibroblasts were then stimulated for 15 min with 5 AU/mL freshly prepared CSE (Luppi et al., 2005), washed with PBS and then incubated for 6 h, either in the presence or absence of 2 μM CHIR99021 or 10 mM NAC. ER stress was induced using 100 nM Tg for 6 h, either or not in presence of CHIR99021 or NAC. MRC-5 fibroblasts were trypsinized thereafter and immediately used for organoid assays. An overview of the experimental set-up is shown in Figure 1A.

Organoid assay

Organoid assays were performed as previously described (Ng-Blichfeldt et al., 2019). Pre-treated or pre-exposed MRC-5 fibroblasts were resuspended in a 1:1 ratio (20.000 cells each) with EpCAM$^+$ cells in 50 μL DMEM/10% FBS +50 μL growth-factor reduced Matrigel (Corning). Cell suspensions were seeded on 24-transwell inserts and subsequently incubated at 37°C for ~30 min to enable polymerization of the Matrigel. Organoid cultures were maintained in DMEM/F12 with 5% (vol/vol) FBS, 2 mM L-glutamine, p/s, 1x insulin-transferrin-selenium (Gibco), recombinant mouse EGF (0.025 μg/mL, Sigma), bovine pituitary extract (30 μg/mL, Sigma), and freshly added all-trans retinoic acid (0.01 μM, Sigma) at 37°C with 5% CO_2. Y-27632 (10 μM, Tocris, Oxford, United Kingdom) was added for the first 48 h of culture. To quantify colony-forming efficiency, the total number of organoids per well was counted manually 7 days after seeding using a light microscope at ×20 magnification. Organoid diameter was measured 14 days after seeding with a light microscope connected to NIS-Elements software (Nikon Europe, Netherlands). For immunofluorescence, organoid cultures were fixed with ice-cold acetone/methanol (1:1) for 12 min at −20°C, then non-specific binding sites were blocked in PBS with 5% bovine serum albumin (BSA; Sigma). Samples were stored at 4°C until immunofluorescence analysis.

Immunofluorescence staining

Immunofluorescence staining was performed as described before (Ng-Blichfeldt et al., 2019; Wu et al., 2019). Cultures were incubated with primary antibodies (alveolar cells: anti-proSP-C Millipore AB3786; ciliated cells: anti-Acetylated tubulin Sigma T6793) diluted in PBS with 0.1% (wt/vol) BSA and 0.1% (vol/vol) Triton X-100 at 4°C overnight, then washed three times in PBS (> 20 min between washes), after which cultures were incubated with secondary antibodies and DAPI at 4°C overnight. After 3x washing with PBS, transwell membranes were excised from inserts and mounted on glass slides with mounting media and glass coverslips. Immunofluorescence was visualized using a Leica SP8 confocal microscope (Wetzlar, Germany), and images were obtained with Leica Application Suite software. Per condition, > 150 organoids were analyzed at ×40 magnification, and the number of alveolar vs airway organoids was quantified (Ng-Blichfeldt et al., 2019; Hu et al., 2020).

TOP/FLASH reporter assay

The TOP/FOP flash assay was performed as described before (Baarsma et al., 2017; Wu et al., 2019). In short, MRC-5 fibroblasts were seeded in 96-well plates, and upon confluence, were transfected with 100 ng/well TOP luciferase reporter plasmid or negative control (FOP plasmid) using Lipofectamine™ LTX Reagent with PLUS™ Reagent (Invitrogen, Carlsbad, United States) in serum-free Opti-MEM® medium (Life Technologies, Carlsbad, United States) for 5 h. Thereafter, MRC-5 cells were stimulated for 6 h with vehicle, 2 or 5 AU/mL freshly prepared CSE (15 min exposure washed and incubated), 100 nM Tg without or with 2 μM CHIR99021 and/or 10 mM NAC in Opti-MEM® medium with 0.1% FBS. After incubation, MRC-5 fibroblasts were lysed using the Bright-Glo™ Luciferase Assay System (Promega) and luciferase activity was measured using a Spectramax Microplate Reader (Molecular Devices, San Jose, United States). SoftmaxPro (Molecular Devices) was used to collect and analyze data.

q-PCR analysis

RNA was isolated from MRC-5 fibroblasts according to the manufacturer's instruction using Maxwell RNA extraction kits (Promega, Madison, WI, United States). Quantitative RT-PCR

TABLE 1 Antibodies for experimental procedures.

Antibody	Technique	Supplier + Cat. No.
CD45	MACS sorting	Miltenyi Biotec, Germany 130-052-301
CD31	MACS sorting	Miltenyi Biotec, Germany 130-097-418
CD326	MACS sorting	Miltenyi Biotec, Germany 130-091-051
Pro-Surfactant protein-C	Immunofluorescence staining	Millipore AB3786
Acetylated tubulin	Immunofluorescence staining	Sigma T7451
Donkey anti-Mouse Secondary Antibody, Alexa Fluor™ 568	Immunofluorescence staining	Invitrogen/Life Technologies A10037
Goat anti-Rabbit Secondary Antibody, Alexa Fluor™ 488	Immunofluorescence staining	Invitrogen/Life Technologies A11008

TABLE 2 Primer pairs used for gene expression analysis.

Gene (human)	Forward primer sequence (5′ to 3′)	Reverse primer sequence (3′ to 5′)
ATP5B	TCACCCAGGCTGGTTCAGA	AGTGGCCAGGGTAGGCTGAT
RPL13A	AAGGTGGTGGTCGTACGCTGTG	CGGGAAGGGTTGGTGTTCATCC
AXIN2	CGGGAGCCACACCCTTCT	TGGACACCTGCCAGTTTCTTT
GADD34	ATGTATGGTGAGCGAGAGGC	GCAGTGTCCTTATCAGAAGGC
Bip	CGAGGAGGAGGACAAGAAGG	CACCTTGAACGGCAAGAACT
CHOP	GCACCTCCCAGAGCCCTCACTCTCC	GTCTACTCCAAGCCTTCCCCCTGCG
XBP1SPL	TGCTGAGTCCGCAGCAGGTG	GTCGGCAGGCTCTGGGGAAG
HGF	TCCAGAGGTACGCTACGAAGTCT	CCCATTGCAGGTCATGCAT
FGF2	AGAAGAGCGACCCTCACATCA	CGGTTAGCACACACTCCTTTG
FGF7	TCCTGCCAACTTTGCTCTACA	CAGGGCTGGAACAGTTCACAT
FGF10	CAGTAGAAATCGGAGTTGTTGCC	TGAGCCATAGAGTTTCCCCTTC
HMOX1	AAGACTGCGTTCCTGCTCAAC	AAAGCCCTACAGCAACTGTCG
Wnt5A	GGG TGG GAA CCA AGA AAA AT	TGG AAC CTA CCC ATC CCA TA
WNT5B	ACG CTG GAG ATC TCT GAG GA	CGA GGT TGA AGC TGA GTT CC
Gene (murine)	**Forward primer sequence (5′ to 3′)**	**Reverse primer sequence (3′ to 5′)**
Xbp1spl	CTGAGTCCGCAGCAGGTGCAG	GTCCATGGGAAGATGTTCTGG
Chop	GGAGCTGGAAGCCTGGTATGAG	GCAGGGTCAAGAGTAGTGAAGG
Gadd34	CCCGAGATTCCTCTAAAAGC	CCAGACAGCAAGGAAATGG
Axin2	CGCTTTGATAAGGTCCTGGC	AGTTCCTCTCAGCAATCGGC
Hmox1	GATAGAGCGCAACAAGCAGAA	CAGTGAGGCCCATACCAGAAG
Actb	GTGACGTTGACATCCGTAAAGA	GCCGGACTCATCGTACTCC

(q-PCR) was performed as described previously (Delbrel et al., 2019). q-PCR reactions were performed in triplicate. We included two reference genes, selected using the "Genorm method" (Genorm, Primer design, Southampton, United Kingdom), to calculate the normalized gene expression. Expression values were determined by the relative gene expression of a standard curve as determined by CFX manager software, and expressed as fold increase (Bio-Rad). Used primer pairs are listed in Table 2.

Statistical analyses

Data are presented as mean ± SEM. *N* refers to number of independent experiments using MRC-5 fibroblasts, and n refers to number of independent experiments upon EpCAM$^+$ isolation. Data were analyzed using One-way or Two-way ANOVA (as indicated in the legends) and Tukey *post hoc* test to compare differences amongst groups. All analyses were performed using Graphpad Prism 9.3.1. Differences at a value of $p < 0.05$ were considered statistically significant.

Results

CSE induces cellular stress responses in MRC-5 lung fibroblasts, whilst impairing CHIR99021-induced Wnt/β-catenin signalling

The experimental set-up is visualized in Figure 1A. MRC-5 lung fibroblast were exposed to 5 AU/mL CSE for 15 min and subsequently incubated for 6 h, and a CSE-induced expression of *HMOX1* (Figure 1B) was observed. Tg, a widely used nonspecific activator of the UPR, clearly increased expression of *GADD34/PPP1R15A*, *CHOP*, *XBP1spl* and *BiP* (Figures 1C, D, Supplementary Figure S1A), whereas CSE exposure only significantly increased *GADD34/PPP1R15A* expression (Figures 1C, D), and therefore we cannot conclude that CSE activates the UPR and/or ISR. As activation of the Wnt/β-catenin pathway is suggested to tip the balance towards a pro-repair and regenerative response in both epithelial cells and fibroblasts in COPD (Kneidinger et al., 2011; Hu et al., 2020), we treated MRC-5 lung fibroblasts with the Wnt/β-catenin activating compound, CHIR99021 (2 μM), during stimulation with CSE and Tg. Activation of the Wnt/β-catenin pathway did not modulate CSE-induced *GADD34/PPP1R15A* and *HMOX1* expression. However, CSE inhibited CHIR-induced activation of the Wnt/β-catenin target gene *AXIN2*, whereas the inhibitory effect of Tg on CHIR-induced *AXIN2* was less pronounced (Figure 2A). This inhibitory effect of CSE on CHIR99021-induced Wnt/β-catenin signalling activation was confirmed in a TOP/FLASH reporter assay (Figure 2B).

To determine whether the CSE-mediated reduction of CHIR99021-induced Wnt/β-activation was dependent on components of the UPR and/or ISR pathways, we used mouse embryonic fibroblasts (MEF) from wildtype, *Gadd34−/−*, *Chop−/−* or EIF*2a (AA)* signalling deficient mice (Supplementary Figure S1A).

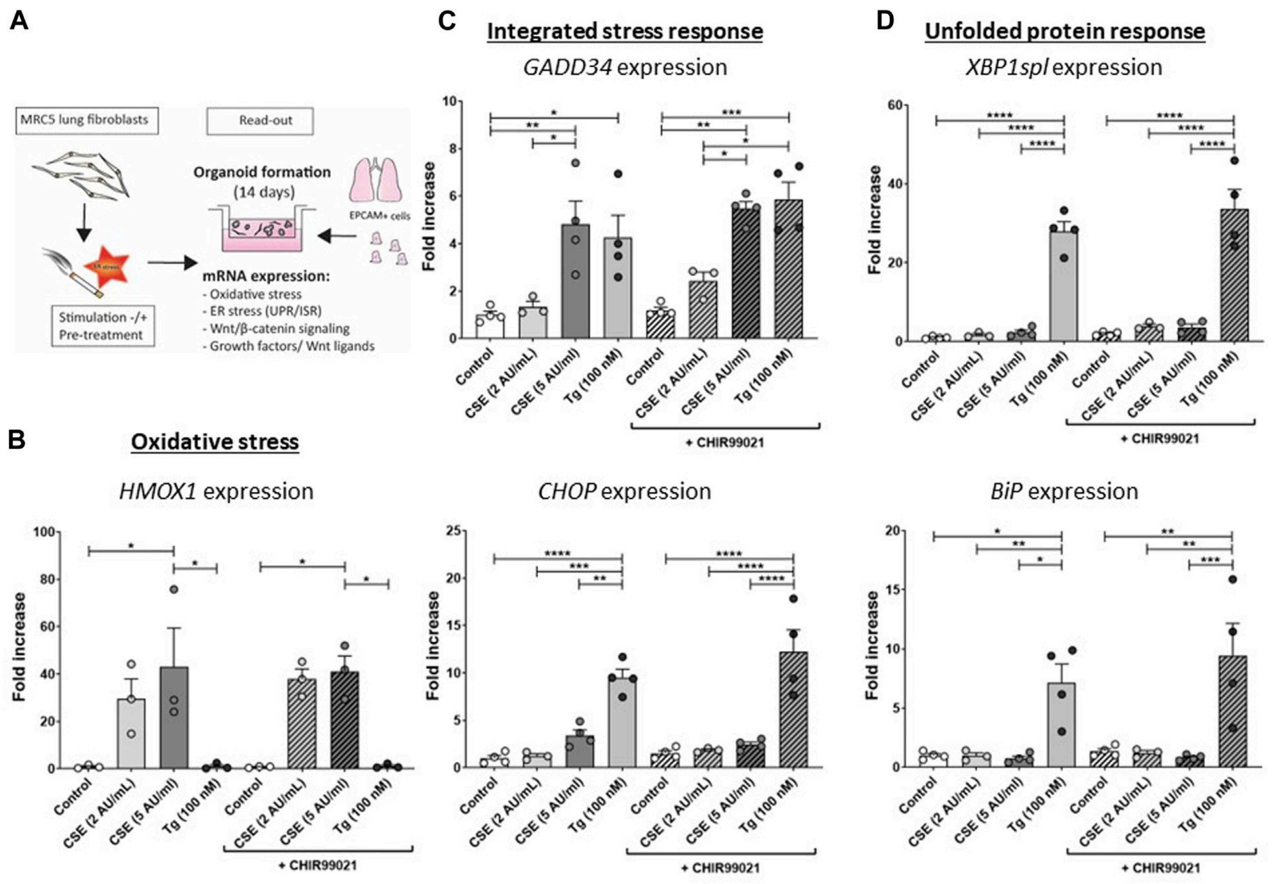

FIGURE 1
CSE induces stress responses in MRC-5 lung fibroblasts MRC-5 fibroblasts were cultured until confluency was reached, after which they were serum-starved for 24 h. Upon starvation, MRC-5 fibroblasts were exposed to vehicle (white dots/bars) freshly-prepared CSE (2 or 5 AU/mL, light and dark grey dots/bars resp.) for 15 min or Tg (dark grey dots/grey bars) and stimulated for 6 h. CHIR99021 or vehicle (2 μM, stripes bars) was added during stimulation with CSE or Tg (experimental set-up shown in **(A)**). Cells were then lysed for RNA isolation, cDNA synthesis and RT-qPCR. HMOX1 expression **(B)** was measured as marker for oxidative stress. GADD34 **(C)** and CHOP mRNA expression were determined as a read-out for activation of the ISR, whereas XBP1spl and BiP **(D)** were measured to determine UPR activation. Data are shown as mean ± SEM (with individual datapoints); N = 3–4 independent experiments; $^{*}p < 0.05$, $^{**}p < 0.01$, $^{***}p < 0.001$, $^{****}p < 0.0001$ Data were analyzed using One-way ANOVA statistical testing in Graphpad Prism 9.3.1. Abbreviations: AU/mL: arbitrary units/mL; CSE: cigarette smoke extract; ER stress: endoplasmic reticulum stress; ISR: integrated stress response; Tg: thapsigargin; UPR: unfolded protein response.

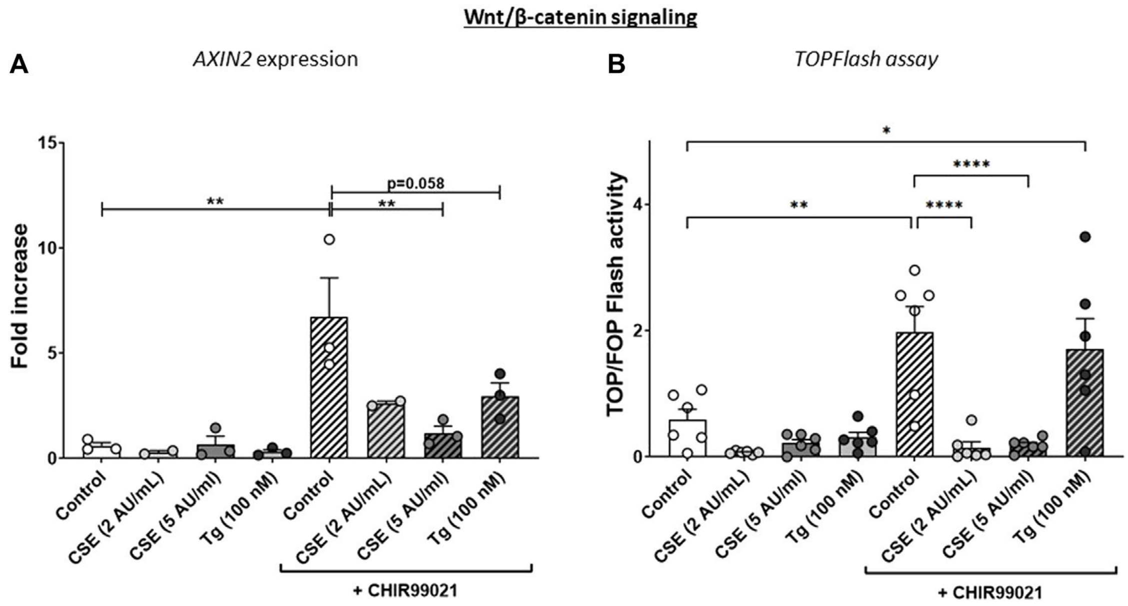

FIGURE 2
CSE lowers CHIR99021-induced Wnt/b-catenin signalling in MRC-5 lung fibroblasts. MRC-5 fibroblasts were cultured until confluency was reached, after which they were serum-starved for 24h. Upon starvation, MRC-5 fibroblasts were exposed to vehicle (white dots/bars) freshly-prepared CSE (2 or 5 AU/mL, light and dark grey dots/bars resp.) for 15 min or Tg (dark grey dots/grey bars) and stimulated for 6 h. CHIR99021 or vehicle (2 μM, stripes bars) was added during stimulation with CSE or Tg. Cells were then lysed for RNA isolation, cDNA synthesis and RT-qPCR. The effect on Wnt/β-catenin signalling was assessed by determining mRNA expression of AXIN2 **(A)** and using a TOP/FLASH reporter **(B)**. Data are shown as mean ± SEM; N = 3-4 independent experiments; *$p < 0.05$, **$p < 0.01$, ***$p < 0.001$, ****$p < 0.0001$. Data were analyzed using One-way ANOVA statistical testing in Graphpad Prism 9.3.1. Abbreviations: AU/mL: arbitrary units/mL; CSE: cigarette smoke extract; Tg: thapsigargin.

In line with our observations in human MRC-5 cells, *Gadd34* and *Hmox1* expression was increased upon CSE exposure in MEFs, whereas CSE did not increase *Xbp1spl* (data not shown). In contrast to MRC-5 fibroblasts, CSE did increase *Chop* expression in MEFs (data not shown). CHIR99021-induced activation of Wnt/β-catenin signalling appeared less pronounced in MEF. Importantly, absence of Gadd34 or Chop did not affect CSE- or Tg-induced impairment in CHIR-induced responses (Supplementary Figures S1B–E), whereas this impairment was less clear in MEFs unable to phosphorylate eIF2α. These data suggest that Gadd34 and CHOP may not be required for the suppressive effect of CSE on activation of CHIR99021-induced Wnt/β-catenin signalling, whereas oxidative stress may be involved in this effect.

CSE exposure impairs repair-related factors

To further understand the effects of CSE and Tg exposure on MRC-5 fibroblast and their suggested supportive function for epithelial cells, we measured expression of several growth factors and Wnt ligands related to (impaired) repair. Expression of *WNT5A* was induced upon treatment with CHIR99021 compared to control, and exposure to 5 AU/mL CSE, but not Tg, reduced CHIR99021-induced *WNT5A* expression (Figure 3A). *WNT5B* was increased significantly upon exposure to 2 AU/mL CSE and CHIR99021 treatment compared to control and exposure to 5 AU/mL and Tg. Interestingly, also CHIR99021 alone significantly reduced *FGF7* expression, which was not further reduced by CSE or Tg. These findings suggest that CSE and Tg both alter expression of repair-related mediators in MRC-5 cells, which could not all be restored by CHIR99021-induced Wnt/β-catenin activation.

Exposure to CSE and ER stress in MRC-5 fibroblasts impairs support of epithelial organoid formation, which is partly restored by treatment with the Wnt/β-catenin activator CHIR99021

As Wnt/β-catenin signalling as well as expression of repair related factors was altered upon CSE/Tg exposure in MRC-5 fibroblasts, we performed a lung epithelial organoid assay in order to assess the functional consequence on lung epithelial progenitor function. Therefore, mitomycin-treated MRC-5 fibroblasts were stimulated with 5 AU/mL CSE or Tg to induce ER stress, and subsequently seeded in Matrigel with murine lung EpCAM$^+$ epithelial cells (Figure 1A). Organoid formation was followed for 14 days. Pre-exposure of MRC-5 lung fibroblast to Tg resulted in a lower number of epithelial organoids both at day 7 and day 14, while CSE pre-exposure lowered epithelial organoid formation only at day 14 (Figure 4A); organoid size and composition was unaffected (Figures 4B, C). After showing that CSE and Tg impair CHIR-induced Wnt-signalling based on analysis of *AXIN2* expression (Figure 2), we next investigated whether residual Wnt signalling sufficed to increase organoid formation. To this end,

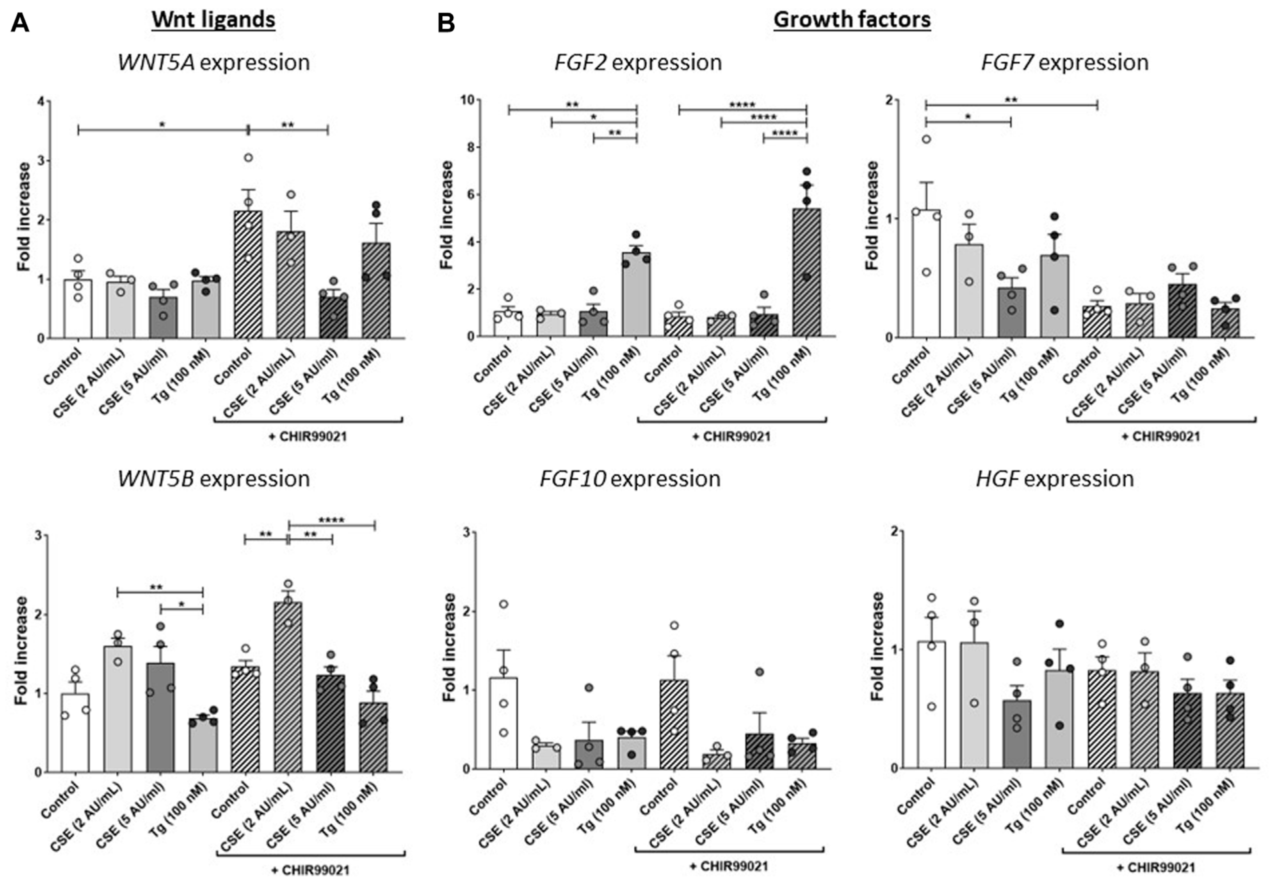

FIGURE 3
CSE impairs repair-related factors. MRC-5 fibroblasts were cultured until confluency was reached, after which they were serum-starved for 24 h. Upon starvation, MRC-5 fibroblasts were exposed to vehicle (white dots/bars) freshly-prepared CSE (2 or 5 AU/mL, light and dark grey dots/bars resp.) for 15 min or Tg (dark grey dots/grey bars) and stimulated for 6 h. Cells were then lysed for RNA isolation, cDNA synthesis and RT-qPCR. Expression of Wnt ligands (WNT5A and WNT5B) **(A)** and growth factors (FGF2, FGF7, FGF10 and HGF) **(B)** were determined as a read-out of repair-related factors. Data are shown as mean ± SEM; N = 3–4 independent experiments; $*p < 0.05$, $**p < 0.01$, $***p < 0.001$, $****p < 0.0001$. Data were analyzed using One-way ANOVA statistical testing in Graphpad Prism 9.3.1. Abbreviations: AU/mL: arbitrary units/mL; CSE: cigarette smoke extract; FGF: fibroblast growth factor; HFG: hepatocyte growth factor; Tg: thapsigargin.

MRC-5 lung fibroblasts were treated with 2 µM CHIR99021 during stimulation with CSE and Tg and effects on support of epithelial organoid formation were assessed. Remarkably, CHIR99021 pre-treatment of MRC-5 fibroblasts alone did not increase organoid numbers, but pre-treatment with CHIR99021 during CSE exposure restored support of epithelial organoid formation (Figure 4A), which was evident most clearly at 14 days. Also, CHIR99021-pre-treatment of MRC-5 cells appeared to induce a more mature organoid phenotype with higher numbers of SFTPC$^+$ cells compared to CHIR99021-untreated organoids, although this effect was not significant.

These findings suggest that Tg and CSE pre-exposure of MRC-5 lung fibroblasts impairs their ability to support epithelial organoid formation. CSE-induced impairment of support of epithelial organoid formation and maturation of organoids was partly restored upon pre-treatment with the Wnt/β-catenin activator CHIR99021, suggesting that activation of Wnt/β-catenin signalling during CSE exposure reverses some of the CSE-induced anti-repair effects.

Treatment with the oxidative stress inhibitor, N-acetylcysteine, partly restores effects of CSE exposure

To determine the role of oxidative stress in the observed effects on Wnt/β-catenin signalling activation and support of organoid formation, MRC-5 fibroblasts were treated with CHIR99021 (2 µM) and/or N-acetylcysteine (NAC, 10 mM) or vehicle during the 6 h stimulation with CSE (2 or 5 AU/mL, 15 min exposure) or 100 nM Tg. There were no differences in expression of *GADD34/PPP1R15A* upon NAC or NAC + CHIR99021 pre-treatment (Figure 5A) compared to vehicle control. In contrast, *XBP1spl* was upregulated upon NAC pre-treatment of CSE-exposed cells (Figure 5B). Although non-significant, NAC pre-treatment reduced CSE-induced expression of *HMOX1* (Figure 5C). mRNA expression of *AXIN2* (Figure 5D) was unaltered upon NAC pre-treatment, which was confirmed using a Wnt/β-catenin reporter (Figure 5E). Despite our observation that NAC prevented CSE-induced effects on *GADD34/PPP1R15A*, and *HMOX1*, pre-treatment of MRC-5

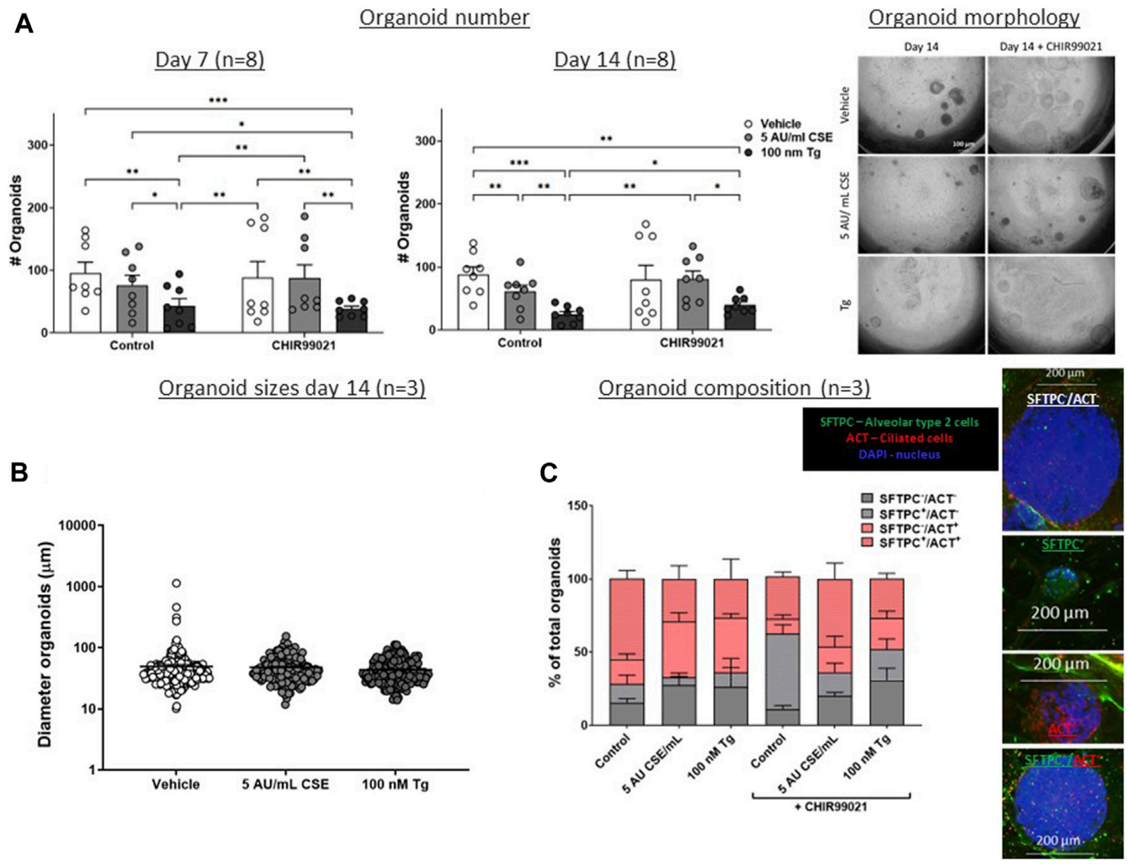

FIGURE 4
CSE and Tg pre-exposure of MRC-5 fibroblasts impairs mesenchymal support of epithelial organoid formation. MRC-5 fibroblasts were mitomycin-C inactivated for 2 h, followed by washing and a 1h recovery-period. Upon starvation, MRC-5 fibroblasts were exposed to vehicle (white dots/bars) freshly-prepared CSE (5 AU/mL, ldark grey dots/bars) for 15 min or Tg (dark grey dots/dark grey bars) and stimulated for 6 h. MRC-5 cells were then detached and seeded with freshly isolated mouse Epcam + lung epithelial cells in a 1:1 ratio in Matrigel, and organoid formation and growth was followed for 14 days. Organoid number (white arrows) was counted at day 7 and 14 **(A)**. Data are shown as mean ± SEM; N = 4 independent MRC-5 fibroblast experiments, EPCAM$^+$ cells: $n = 8$ mice; $*p < 0.05$, $**p < 0.01$, $***p < 0.001$. Organoid size was determined at day 14 **(B)** in, and organoid composition was determined using immunofluorescence staining of organoids fixed at day 14 organoids. Organoids were costained for proSFTPC (alveolar, green) and ACT (bronchial, red) and displayed as percentage of total organoids expressing one, both, or neither markers **(C)** (for both $n = 3$ mice). The nuclei were visualized using DAPI (blue). Data presented in 4B were analyzed using One-way ANOVA statistical testing in Graphpad Prism 9.3.1. Data presented in Figures 4A,C were analyzed using Two-way ANOVA statistical testing in Graphpad Prism 9.3.1. Abbreviations: ACT: acetylated tubulin; AU/mL: arbitrary units/mL; CSE: cigarette smoke extract; SFTPC: pro-surfactant protein-C; Tg: thapsigargin.

cells with NAC did not affect epithelial organoid formation (Figure 5F). These findings suggest that the observed CSE-mediated inhibition of support of epithelial organoid formation (Figure 2A) only partly results from oxidative stress.

Discussion

Crosstalk between fibroblasts and lung epithelial cells is crucial for both lung development and appropriate repair responses following lung injury, and this beneficial interaction has been suggested to be impaired in chronic lung diseases such as COPD. In this study, we show that exposure to cigarette smoke extract (CSE) of MRC-5 lung fibroblasts induced cellular stress responses, including oxidative stress and upregulation of *GADD34/PPP1R15A*. Furthermore, we showed that CSE caused an impairment of the ability of MRC-5 cells to support of epithelial progenitor function, as assessed by the organoid forming capacity of lung EpCAM$^+$ cells. This effect was partially restored upon activation of the Wnt/β-catenin signalling pathway in fibroblasts during CSE stimulation.

Previous studies showed that CSE exposure induces myofibroblast differentiation of MRC-5 fibroblasts as assessed by enhanced α-SMA expression (Baek et al., 2012; Song et al., 2019) and altered expression profiles of proteins related to stress responses, mitochondrial activity, and aging in human fetal lung fibroblasts (HFL-1) (D'Anna et al., 2015). Myofibroblast activation has been associated with impaired repair and remodelling, and may contribute to progression of COPD and ILD (Ng-Blichfeldt et al., 2019; Liu et al., 2021). We showed that exposure to CSE induced expression of *GADD34/PPP1R15A* in MRC-5 lung fibroblasts, whereas UPR markers were unaffected. These findings are in contrast to previously reported findings using MRC-5 fibroblasts, in which the UPR was found to be activated upon CSE stimulation (Song et al., 2019). This apparent discrepancy may result from differences in CSE preparation method, CSE dosage and CSE exposure duration. Exposure to the chemical ER stress inducer

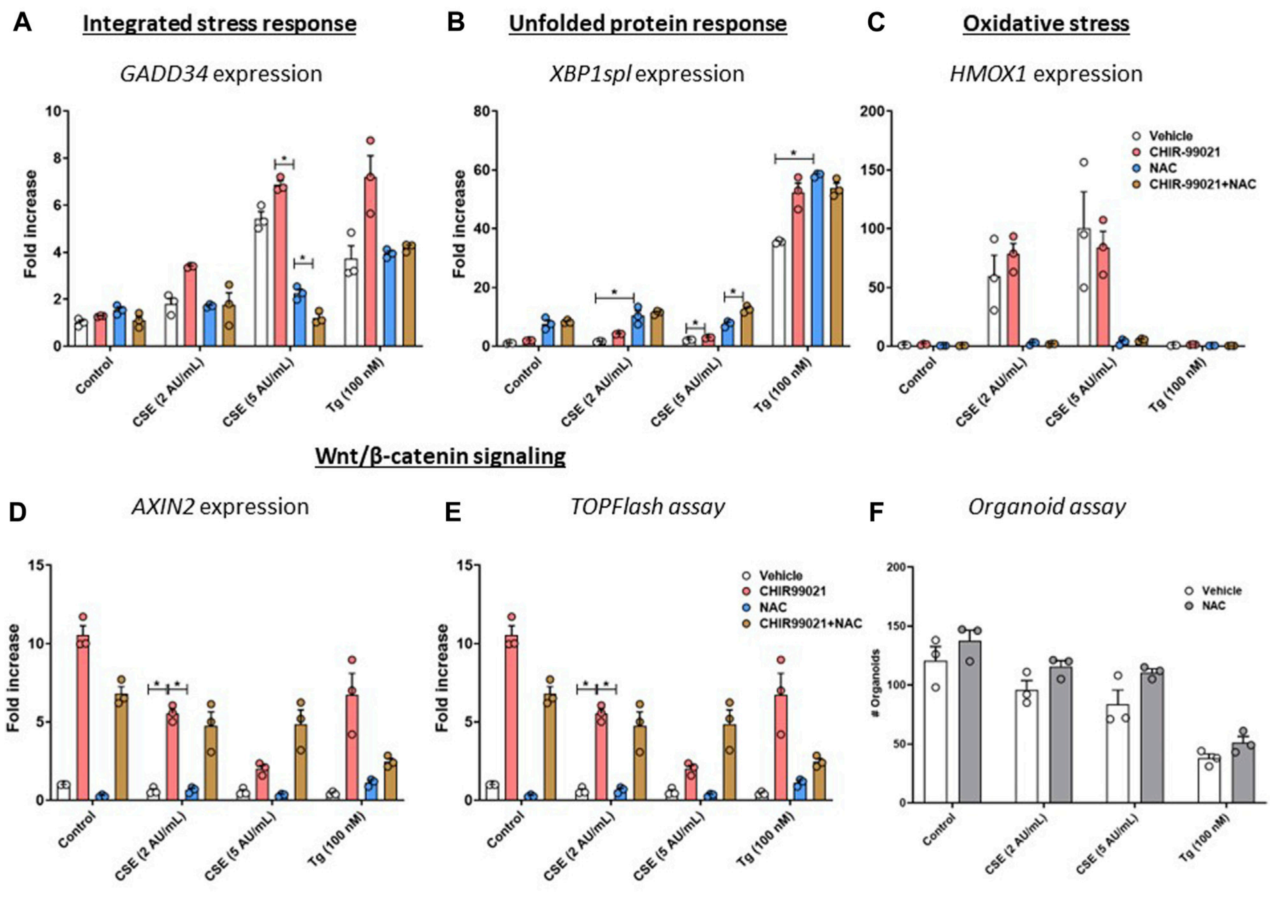

FIGURE 5
Pre-treatment with an anti-oxidant does not restore impaired Wnt/β-catenin signalling upon CSE exposure. MRC-5 fibroblasts were cultured until confluency was reached, after which they were serum-starved for 24h. Upon starvation, MRC-5 fibroblasts were exposed to freshly-prepared CSE (2 or 5 AU/mL) for 15 min or Tg and stimulated for 6h. CHIR-99021 (2 µM, pink dots and bars) or vehicle (white dots and bars) and (brown dots and bars)/or N-acetylcysteine (10 mM, blue dots and bars) was added during stimulation with CSE or Tg. Cells were then lysed for RNA isolation, cDNA synthesis and RT-qPCR. Gadd34 **(A)** mRNA expression were determined as a read-out for activation of the ISR, whereas XBP1spl **(B)** was measured to determine UPR activation. HMOX1 expression **(C)** was measured as marker for oxidative stress and the effect on Wnt/β-catenin signalling was assessed by determining mRNA expression of AXIN2 **(D)** and using a TOP/FLASH reporter **(E)**. MRC-5 fibroblasts were mitomycin-C inactivated for 2 h, followed by washing and a 1 h recovery-period. MRC-5 fibroblasts were subsequently exposed to freshly-prepared CSE (5 AU/mL) for 15 min, Tg or Tm and stimulated for 6 h. N-acetylcysteine (10 mM) or vehicle was added during stimulation with CSE, Tg or Tm. MRC-5 cells were then detached and seeded with freshly isolated mouse Epcam + lung epithelial cells in a 1:1 ratio in Matrigel, and organoid formation and growth was followed for 14 days; organoid number was counted at day 14 **(F)**. Data are shown as mean ± SEM; *n* = 3 mice; **p* < 0.05. Data presented in **(A–F)** were analyzed using Two-way ANOVA statistical testing in Graphpad Prism 9.3.1. Abbreviations: AU/mL: arbitrary units/mL; CSE: cigarette smoke extract; NAC: N-acetylcystein; Tg: thapsigargin.

Tg did activate markers of both the ISR and the UPR, which is in line with other studies. However, it needs to be noted that Tg may also activate other cellular processes unrelated to the UPR and ISR by its effect on intracellular calcium stores.

We showed that CSE and TG not only induced cellular stress responses in MRC-5 cells, but also decreased the capacity of the MRC-5 fibroblasts to support epithelial organoid formation. Furthermore, we showed that pre-exposure of MRC-5 cells to CSE resulted in (non-significantly) diminished expression of maturation markers in the organoids, as shown by an increase in $SFTPC^-/ACT^-$ organoids. Interestingly, CHIR99021 treatment was able to partially restore this inhibitory effect of CSE treatment, although CSE pre-treatment did lower ((but did not abolish) CHIR-99021-induced *AXIN2* expression as marker of Wnt/β-catenin signalling activation compared to control.

The reduced ability of MRC-5 fibroblasts to support organoid formation upon CSE or Tg exposure may result from a cascade of events, including impaired growth factor production and activation of cellular stress signals. TGF-β is increased in COPD lungs and contributes to myofibroblast formation (Konigshoff et al., 2009; Baarsma et al., 2011). Furthermore, we previously showed that fibroblast exposure to TGF-β decreases their capacity to support epithelial organoid formation (Ng-Blichfeldt et al., 2019), which results from altered expression of Wnt/β-catenin signalling components and target genes. Our results using Tg indicate that ER stress reduced CHIR99021-induced Wnt/β-catenin signalling activation. Whereas acute ER stress is important in maintaining cellular homeostasis (Marciniak, 2019), prolonged ER stress responses may result in cellular dysfunction and cell death and is closely linked to other cellular stress responses including oxidative stress, mitochondrial dysfunction and cellular senescence (Kanaji et al., 2014; Koloko Ngassie et al., 2021), processes that are increased in lungs from COPD patients. Fibroblasts from COPD patients show disorganized organelle organization and enhanced ER stress (Weidner et al., 2018), which may impact the niche-function of fibroblasts in lung epithelial repair. ER stress may interfere with Wnt/β-catenin signalling in various ways. Firstly, ER stress may interfere with Wnt ligand processing and secretion in Wnt-producing cells, leading to lower production or inactivity of secreted Wnt ligands (Verras et al., 2008). Secondly, ER stress leads to attenuation of protein translation resulting in a transient decrease in short-lived signalling molecules including bone morphogenic protein-4 (BMP-4) (Malzer et al., 2018) and potentially β-catenin. ER stress may also inhibit transcription of proteins downstream of β-catenin (van Lidth de Jeude et al., 2017), and finally ER stress responses may lead to proteosomal degradration of proteins (Fabre et al., 2019). There are thus several mechanisms by which ER stress may interfere in the Wnt/β-catenin signalling pathway, although the precise mechanism is unclear yet.

Although we did not find altered gene expression of β-catenin upon CSE- or Tg-induced ER stress (not shown), we did show that gene expression of various injury- and repair-related factors (*FGF7*, *WNT5A*) and CHIR99021-induced Wnt/β-catenin signalling activation was altered upon CSE exposure in MRC-5 cells. This is in line with previous findings showing that the mesenchymal niche secretes fibroblast growth factors (FGFs), Wnt ligands/signalling activation and other growth factors (Frank et al., 2016; Zepp et al., 2017; Khedoe et al., 2021; Penkala et al., 2021), and thereby orchestrates alveolar cell function. We did not measure protein levels of secreted growth factors, due to the short-lived nature of especially Wnt ligands, but do show a functional impairment in support of epithelial organoid formation. Various FGFs have been shown to enhance lung epithelial organoid formation (Rabata et al., 2020), and HGF and FGF7 were able to reverse diminished organoid growth upon co-culture with TGF-β-treated MRC-5 fibroblasts (Ng-Blichfeldt et al., 2019). Future studies are needed to define whether altered expression of these growth factors contributes to impaired repair in COPD. Furthermore, additional factors induced by CSE-exposure in MRC-5 cells, including pro-inflammatory factors, may have contributed to the impaired capacity to support lung epithelial progenitor function, which we did not study here.

Cigarette smoke induces oxidative stress and various studies suggest that oxidative stress may alter mitochondrial and ER function (Fabre et al., 2019) and Wnt/β-catenin signalling (Qu et al., 2019). Therefore, we investigated whether oxidative stress mediates the CSE-induced reduction in CHIR99021-induced *AXIN2* expression. Reducing oxidative stress by NAC treatment has been shown to restore diesel-induced impaired lung epithelial organoid formation (Wu et al., 2022). Whereas we show that NAC treatment did reduce the oxidative stress (e.g., *HMOX1* mRNA expression), NAC only partly restored *AXIN2* expression and did not improve organoid supporting capacity of CSE-exposed MRC-5 fibroblasts, suggesting that the observed effects may be (partly) independent from oxidative stress. It has to be noted, that NAC not only has anti-oxidant activities, but also breaks disulfide bridges (Aldini et al., 2018). Previous research showed that DTT, which also breaks disulfide bridges, induces ER stress (Sundaram et al., 2018), which is in line with our observation that NAC increased *XBP1spl* in CSE- and Tg-exposed cells. Furthermore, oxidative stress has been shown to alter Wnt/β-catenin signalling (directly) by various mechanisms, which is discussed in detail elsewhere (Qu et al., 2019), and the direct interaction between oxidative stress and Wnt/β-catenin signalling activation is beyond the scope of the current study. CSE exposure induces various cellular stress responses, and CHIR99021-induced Wnt/β-catenin signalling activation was lowered by CSE exposure. However the relative contribution of oxidative stress, ER stress and factors related to repair to the ability of CSE to impair WNT/β-catenin signalling and organoid growth is unclear.

Whereas we show a clear effect of CSE and ER stress on mesenchymal cellular responses and their ability to support of epithelial organoid formation, there are several limitations of our model. We used a single exposure of CSE in MRC-5 cells. Future studies using repeated exposures may better mimic COPD pathogenesis. Here, we used MEF to determine the role of CSE-mediated reduction of CHIR-induced Wnt/β-catenin activation, and showed that MEFs deficient in components of the UPR or ISR, did not respond differently to CSE exposure compared to WT MEFs. A limitation could be that we did not use lung fibroblasts from mice deficient in UPR/ISR components. However, as WT MEF exhibited similar responses as MRC-5 fibroblasts, we do not expect large differences in responses. Furthermore, mice deficient in some of the UPR/ISR components present a lethal phenotype, and therefore experiments with lung fibroblasts for those mice was not feasible. Furthermore, heightened ER stress has also been shown in lung epithelial cells (Malhotra et al., 2009; Wang et al., 2017) and may also affect lung epithelial progenitor function (Goldfarbmuren et al., 2020). Here, we specifically investigated the cross-talk between mesenchymal cells and epithelial cells, as ER stress is also increased in fibroblasts of COPD patients (Weidner et al., 2018). Finally, we used Tg as a well-established activator of the UPR, that causes ER stress by depletion of Ca^{2+} stores. We cannot formally exclude the possibility that activities of Tg independent of UPR activation have contributed to our observations.

Despite these limitations, the findings from our study point to potential targets for improving altered cross-talk and lung epithelial repair in COPD. Studies have shown that CS-induced effects on ER stress and the subsequent activation of the UPR may be targeted through treatment with Tauroursodeoxycholic acid (TUDCA) (Tong et al., 2021) or 4-phenylbutyric acid (4-PBA) (Wang et al., 2017); treatment with these compounds prevented EMT in experimental fibrosis and experimental emphysema in mice. There are several other compounds available that also target the ER stress pathway, that may be studied in the context of lung epithelial repair. Our results show that the responses to ER stress and the ISR may partly mediate cigarette smoke-induced alterations in the cross-talk between mesenchymal cells and lung epithelial cells. Targeting ER stress or the ISR in fibroblasts may therefore represent an attractive therapeutic target to restore altered cross-talk and lung epithelial repair in COPD.

In conclusion, our study showed that CSE and ER stress impair Wnt/β-catenin activation in MRC-5 fibroblasts and subsequent cross-talk between lung fibroblasts and lung epithelial cells, resulting in impaired lung organoid formation at day 14. Thereby, we provide further insight into the way disturbed mesenchymal cell function in COPD may contribute to the impairment of repair processes observed in COPD.

Data availability statement

The original contributions presented in the study are included in the article/Supplementary Material, further inquiries can be directed to the corresponding author.

Ethics statement

Ethical approval was not required for the studies on humans in accordance with the local legislation and institutional requirements because only commercially available established cell lines were used. The animal study was approved by University of Groningen animal experimentation committee under CCD license AVD105002015303. The study was conducted in accordance with the local legislation and institutional requirements.

Author contributions

PK designed and performed the experiments, processed the data and prepared the manuscript. WS and JN-B performed experiments and provided intellectual input for the manuscript. SM and MS provided MEF, RG provided the TOP/FLASH reporter. PH, JS, RG and SM supervised the project and contributed to writing of the manuscript. All authors contributed to the article and approved the submitted version.

Funding

This project was funded by the Lung Foundation Netherlands (#6.1.14.009).

Acknowledgments

The authors thank Sophie Bos, Xinhui Wu and Chiara Ciminieri (Dept. of Molecular Pharmacology, Groningen Research Institute of Pharmacy, University of Groningen, Groningen, the Netherlands) for their technical support during the experiments.

Conflict of interest

The authors declare that the research was conducted in the absence of any commercial or financial relationships that could be construed as a potential conflict of interest.

The reviewer GT declared a past co-authorship with the authors RG to the handling Editor

Publisher's note

Supplementary material

The Supplementary Material for this article can be found online at: https://www.frontiersin.org/articles/10.3389/fcell.2023.1165581/full#supplementary-material

References

Aldini, G., Altomare, A., Baron, G., Vistoli, G., Carini, M., Borsani, L., et al. (2018). N-acetylcysteine as an antioxidant and disulphide breaking agent: the reasons why. *Free Radic. Res.* 52 (7), 751–762. doi:10.1080/10715762.2018.1468564

Baarsma, H. A., Skronska-Wasek, W., Mutze, K., Ciolek, F., Wagner, D. E., John-Schuster, G., et al. (2017). Noncanonical WNT-5A signaling impairs endogenous lung repair in COPD. *J. Exp. Med.* 214 (1), 143–163. doi:10.1084/jem.20160675

Baarsma, H. A., Spanjer, A. I., Haitsma, G., Engelbertink, L. H., Meurs, H., Jonker, M. R., et al. (2011). Activation of WNT/β-catenin signaling in pulmonary fibroblasts by TGF-β_1 is increased in chronic obstructive pulmonary disease. *PLoS One* 6 (9), e25450. doi:10.1371/journal.pone.0025450

Baek, H. A., Kim, D. S., Park, H. S., Jang, K. Y., Kang, M. J., Lee, D. G., et al. (2012). Involvement of endoplasmic reticulum stress in myofibroblastic differentiation of lung fibroblasts. *Am. J. Respir. Cell Mol. Biol.* 46 (6), 731–739. doi:10.1165/rcmb.2011-0121OC

Burman, A., Tanjore, H., and Blackwell, T. S. (2018). Endoplasmic reticulum stress in pulmonary fibrosis. *Matrix Biol.* 68-69, 355–365. doi:10.1016/j.matbio.2018.03.015

D'Anna, C., Cigna, D., Costanzo, G., Bruno, A., Ferraro, M., Di Vincenzo, S., et al. (2015). Cigarette smoke alters the proteomic profile of lung fibroblasts. *Mol. Biosyst.* 11 (6), 1644–1652. doi:10.1039/c5mb00188a

Delbrel, E., Uzunhan, Y., Soumare, A., Gille, T., Marchant, D., Planes, C., et al. (2019). ER stress is involved in epithelial-to-mesenchymal transition of alveolar epithelial cells exposed to a hypoxic microenvironment. *Int. J. Mol. Sci.* 20 (6), 1299. doi:10.3390/ijms20061299

Dickens, J. A., Malzer, E., Chambers, J. E., and Marciniak, S. J. (2019). Pulmonary endoplasmic reticulum stress-scars, smoke, and suffocation. *FEBS J.* 286 (2), 322–341. doi:10.1111/febs.14381

Emanuelli, G., Nassehzadeh-Tabriz, N., Morrell, N. W., and Marciniak, S. J. (2020). The integrated stress response in pulmonary disease. *Eur. Respir. Rev.* 29 (157), 200184. doi:10.1183/16000617.0184-2020

Fabre, B., Livneh, I., Ziv, T., and Ciechanover, A. (2019). Identification of proteins regulated by the proteasome following induction of endoplasmic reticulum stress. *Biochem. Biophys. Res. Commun.* 517 (2), 188–192. doi:10.1016/j.bbrc.2019.07.040

Frank, D. B., Peng, T., Zepp, J. A., Snitow, M., Vincent, T. L., Penkala, I. J., et al. (2016). Emergence of a wave of Wnt signaling that regulates lung alveologenesis by controlling epithelial self-renewal and differentiation. *Cell Rep.* 17 (9), 2312–2325. doi:10.1016/j.celrep.2016.11.001

Gan, G., Hu, R., Dai, A., Tan, S., Ouyang, Q., Fu, D., et al. (2011). The role of endoplasmic reticulum stress in emphysema results from cigarette smoke exposure. *Cell Physiol. Biochem.* 28 (4), 725–732. doi:10.1159/000335766

Goldfarbmuren, K. C., Jackson, N. D., Sajuthi, S. P., Dyjack, N., Li, K. S., Rios, C. L., et al. (2020). Dissecting the cellular specificity of smoking effects and reconstructing lineages in the human airway epithelium. *Nat. Commun.* 11 (1), 2485. doi:10.1038/s41467-020-16239-z

Hu, Y., Ng-Blichfeldt, J. P., Ota, C., Ciminieri, C., Ren, W., Hiemstra, P. S., et al. (2020). Wnt/β-catenin signaling is critical for regenerative potential of distal lung epithelial progenitor cells in homeostasis and emphysema. *Stem Cells* 38, 1467–1478. doi:10.1002/stem.3241

Kanaji, N., Basma, H., Nelson, A., Farid, M., Sato, T., Nakanishi, M., et al. (2014). Fibroblasts that resist cigarette smoke-induced senescence acquire profibrotic phenotypes. *Am. J. Physiol. Lung Cell Mol. Physiol.* 307 (5), L364–L373. doi:10.1152/ajplung.00041.2014

Khedoe, P., Wu, X., Gosens, R., and Hiemstra, P. S. (2021). Repairing damaged lungs using regenerative therapy. *Curr. Opin. Pharmacol.* 59, 85–94. doi:10.1016/j.coph.2021.05.002

Kneidinger, N., Yildirim, A. O., Callegari, J., Takenaka, S., Stein, M. M., Dumitrascu, R., et al. (2011). Activation of the WNT/β-catenin pathway attenuates experimental emphysema. *Am. J. Respir. Crit. Care Med.* 183 (6), 723–733. doi:10.1164/rccm.200910-1560OC

Koloko Ngassie, M. L., Brandsma, C. A., Gosens, R., Prakash, Y. S., and Burgess, J. K. (2021). The stress of lung aging: endoplasmic reticulum and senescence tete-a-tete. *Physiol. (Bethesda)* 36 (3), 150–159. doi:10.1152/physiol.00039.2020

Konigshoff, M., Kneidinger, N., and Eickelberg, O. (2009). TGF-Beta signaling in COPD: deciphering genetic and cellular susceptibilities for future therapeutic regimen. *Swiss Med. Wkly.* 139 (39-40), 554–563. doi:10.4414/smw.2009.12528

Lawson, W. E., Cheng, D. S., Degryse, A. L., Tanjore, H., Polosukhin, V. V., Xu, X. C., et al. (2011). Endoplasmic reticulum stress enhances fibrotic remodeling in the lungs. *Proc. Natl. Acad. Sci. U. S. A.* 108 (26), 10562–10567. doi:10.1073/pnas.1107559108

Liu, G., Philp, A. M., Corte, T., Travis, M. A., Schilter, H., Hansbro, N. G., et al. (2021). Therapeutic targets in lung tissue remodelling and fibrosis. *Pharmacol. Ther.* 225, 107839. doi:10.1016/j.pharmthera.2021.107839

Luppi, F., Aarbiou, J., van Wetering, S., Rahman, I., de Boer, W. I., Rabe, K. F., et al. (2005). Effects of cigarette smoke condensate on proliferation and wound closure of bronchial epithelial cells *in vitro*: role of glutathione. *Respir. Res.* 6, 140. doi:10.1186/1465-9921-6-140

Malhotra, D., Thimmulappa, R., Vij, N., Navas-Acien, A., Sussan, T., Merali, S., et al. (2009). Heightened endoplasmic reticulum stress in the lungs of patients with chronic obstructive pulmonary disease: the role of nrf2-regulated proteasomal activity. *Am. J. Respir. Crit. Care Med.* 180 (12), 1196–1207. doi:10.1164/rccm.200903-0324OC

Malzer, E., Dominicus, C. S., Chambers, J. E., Dickens, J. A., Mookerjee, S., and Marciniak, S. J. (2018). The integrated stress response regulates BMP signalling through effects on translation. *BMC Biol.* 16 (1), 34. doi:10.1186/s12915-018-0503-x

Marciniak, S. J. (2019). Endoplasmic reticulum stress: a key player in human disease. *FEBS J.* 286 (2), 228–231. doi:10.1111/febs.14740

Ng-Blichfeldt, J. P., de Jong, T., Kortekaas, R. K., Wu, X., Lindner, M., Guryev, V., et al. (2019). TGF-beta activation impairs fibroblast ability to support adult lung epithelial progenitor cell organoid formation. *Am. J. Physiol. Lung Cell Mol. Physiol.* 317 (1), L14–L28. doi:10.1152/ajplung.00400.2018

Penkala, I. J., Liberti, D. C., Pankin, J., Sivakumar, A., Kremp, M. M., Jayachandran, S., et al. (2021). Age-dependent alveolar epithelial plasticity orchestrates lung homeostasis and regeneration. *Cell stem Cell* 28 (10), 1775–1789.e5. doi:10.1016/j.stem.2021.04.026

Qu, J., Yue, L., Gao, J., and Yao, H. (2019). Perspectives on Wnt signal pathway in the pathogenesis and therapeutics of chronic obstructive pulmonary disease. *J. Pharmacol. Exp. Ther.* 369 (3), 473–480. doi:10.1124/jpet.118.256222

Rabata, A., Fedr, R., Soucek, K., Hampl, A., and Koledova, Z. (2020). 3D cell culture models demonstrate a role for FGF and WNT signaling in regulation of lung epithelial cell fate and morphogenesis. *Front. Cell Dev. Biol.* 8, 574. doi:10.3389/fcell.2020.00574

Rock, J., and Konigshoff, M. (2012). Endogenous lung regeneration: potential and limitations. *Am. J. Respir. Crit. Care Med.* 186 (12), 1213–1219. doi:10.1164/rccm.201207-1151PP

Scheuner, D., Song, B., McEwen, E., Liu, C., Laybutt, R., Gillespie, P., et al. (2001). Translational control is required for the unfolded protein response and *in vivo* glucose homeostasis. *Mol. Cell* 7 (6), 1165–1176. doi:10.1016/s1097-2765(01)00265-9

Skronska-Wasek, W., Gosens, R., Konigshoff, M., and Baarsma, H. A. (2018). WNT receptor signalling in lung physiology and pathology. *Pharmacol. Ther.* 187, 150–166. doi:10.1016/j.pharmthera.2018.02.009

Song, M., Peng, H., Guo, W., Luo, M., Duan, W., Chen, P., et al. (2019). Cigarette smoke extract promotes human lung myofibroblast differentiation by the induction of endoplasmic reticulum stress. *Respiration* 98 (4), 347–356. doi:10.1159/000502099

Sundaram, A., Appathurai, S., Plumb, R., and Mariappan, M. (2018). Dynamic changes in complexes of IRE1α, PERK, and ATF6α during endoplasmic reticulum stress. *Mol. Biol. Cell* 29 (11), 1376–1388. doi:10.1091/mbc.E17-10-0594

Tanjore, H., Blackwell, T. S., and Lawson, W. E. (2012). Emerging evidence for endoplasmic reticulum stress in the pathogenesis of idiopathic pulmonary fibrosis. *Am. J. Physiol. Lung Cell Mol. Physiol.* 302 (8), L721–L729. doi:10.1152/ajplung.00410.2011

Tong, B., Fu, L., Hu, B., Zhang, Z. C., Tan, Z. X., Li, S. R., et al. (2021). Tauroursodeoxycholic acid alleviates pulmonary endoplasmic reticulum stress and epithelial-mesenchymal transition in bleomycin-induced lung fibrosis. *BMC Pulm. Med.* 21 (1), 149. doi:10.1186/s12890-021-01514-6

van 't Wout, E. F., van Schadewijk, A., van Boxtel, R., Dalton, L. E., Clarke, H. J., Tommassen, J., et al. (2015). Virulence factors of *Pseudomonas aeruginosa* induce both the unfolded protein and integrated stress responses in airway epithelial cells. *PLoS Pathog.* 11 (6), e1004946. doi:10.1371/journal.ppat.1004946

van Lidth de Jeude, J. F., Meijer, B. J., Wielenga, M. C. B., Spaan, C. N., Baan, B., Rosekrans, S. L., et al. (2017). Induction of endoplasmic reticulum stress by deletion of Grp78 depletes Apc mutant intestinal epithelial stem cells. *Oncogene* 36 (24), 3397–3405. doi:10.1038/onc.2016.326

Verras, M., Papandreou, I., Lim, A. L., and Denko, N. C. (2008). Tumor hypoxia blocks Wnt processing and secretion through the induction of endoplasmic reticulum stress. *Mol. Cell Biol.* 28 (23), 7212–7224. doi:10.1128/MCB.00947-08

Wang, Y., Wu, Z. Z., and Wang, W. (2017). Inhibition of endoplasmic reticulum stress alleviates cigarette smoke-induced airway inflammation and emphysema. *Oncotarget* 8 (44), 77685–77695. doi:10.18632/oncotarget.20768

Wei, J., Rahman, S., Ayaub, E. A., Dickhout, J. G., and Ask, K. (2013). Protein misfolding and endoplasmic reticulum stress in chronic lung disease. *Chest* 143 (4), 1098–1105. doi:10.1378/chest.12-2133

Weidner, J., Jarenback, L., Aberg, I., Westergren-Thorsson, G., Ankerst, J., Bjermer, L., et al. (2018). Endoplasmic reticulum, Golgi, and lysosomes are disorganized in lung fibroblasts from chronic obstructive pulmonary disease patients. *Physiol. Rep.* 6 (5), e13584. doi:10.14814/phy2.13584

Wu, X., Ciminieri, C., Bos, I. S. T., Woest, M. E., D'Ambrosi, A., Wardenaar, R., et al. (2022). Diesel exhaust particles distort lung epithelial progenitors and their fibroblast niche. *Environ. Pollut.* 305, 119292. doi:10.1016/j.envpol.2022.119292

Wu, X., van Dijk, E. M., Ng-Blichfeldt, J. P., Bos, I. S. T., Ciminieri, C., Konigshoff, M., et al. (2019). Mesenchymal WNT-5A/5B signaling represses lung alveolar epithelial progenitors. *Cells* 8 (10), 1147. doi:10.3390/cells8101147

Zepp, J. A., Zacharias, W. J., Frank, D. B., Cavanaugh, C. A., Zhou, S., Morley, M. P., et al. (2017). Distinct mesenchymal lineages and niches promote epithelial self-renewal and myofibrogenesis in the lung. *Cell* 170 (6), 1134–1148. doi:10.1016/j.cell.2017.07.034

frontiers | Frontiers in Cell and Developmental Biology

TYPE Mini Review
PUBLISHED 02 October 2023
DOI 10.3389/fcell.2023.1254904

Check for updates

OPEN ACCESS

EDITED BY
Chunheng Mo,
Sichuan University, China

REVIEWED BY
Mark Mellett,
University Hospital Zürich, Switzerland
Sarang Tartey,
IGM Biosciences, United States

*CORRESPONDENCE
Changwan Ryu,
✉ changwan.ryu@yale.edu

RECEIVED 07 July 2023
ACCEPTED 19 September 2023
PUBLISHED 02 October 2023

CITATION
Woo S, Gandhi S, Ghincea A, Saber T, Lee CJ and Ryu C (2023), Targeting the NLRP3 inflammasome and associated cytokines in scleroderma associated interstitial lung disease.
Front. Cell Dev. Biol. 11:1254904.
doi: 10.3389/fcell.2023.1254904

Targeting the NLRP3 inflammasome and associated cytokines in scleroderma associated interstitial lung disease

Samuel Woo, Shifa Gandhi, Alexander Ghincea, Tina Saber, Chris J. Lee and Changwan Ryu*

Department of Internal Medicine, Yale School of Medicine, Section of Pulmonary, Critical Care and Sleep Medicine, New Haven, CT, United States

SSc-ILD (scleroderma associated interstitial lung disease) is a complex rheumatic disease characterized in part by immune dysregulation leading to the progressive fibrotic replacement of normal lung architecture. Because improved treatment options are sorely needed, additional study of the fibroproliferative mechanisms mediating this disease has the potential to accelerate development of novel therapies. The contribution of innate immunity is an emerging area of investigation in SSc-ILD as recent work has demonstrated the mechanistic and clinical significance of the NLRP3 inflammasome and its associated cytokines of TNFα (tumor necrosis factor alpha), IL-1β (interleukin-1 beta), and IL-18 in this disease. In this review, we will highlight novel pathophysiologic insights afforded by these studies and the potential of leveraging this complex biology for clinical benefit.

KEYWORDS

scleroderma associated interstitial lung disease, NLRP3, tumor necrosis factor, alpha, IL-1 beta, IL-18

Introduction

SSc (scleroderma) is a complex rheumatic disease characterized by diffuse microvascular injury and immune dysregulation leading to the progressive fibrotic replacement of normal tissue architecture (Denton and Khanna, 2017). One of the leading causes of morbidity and mortality of this condition is the development of ILD (interstitial lung disease) (Volkmann and Fischer, 2021), where current therapeutic strategies include non-specific immunosuppressive drugs (Denton and Khanna, 2017) and anti-fibrotic agents (Distler et al., 2019) that are associated with heterogenous efficacy, high costs, and at times, intolerable side-effects (Rahaghi et al., 2023). Because better treatment options are sorely needed, additional study of the fibroproliferative mechanisms mediating this disease has the potential to accelerate development of novel therapies.

While the mechanisms by which autoimmunity engenders pathologic remodeling of the SSc lung remains poorly understood, aberrant adaptive immune responses and fibroblast activation are heavily implicated (Herzog et al., 2014). Although the contribution of innate immunity is less known in this context, its role in fibrogenesis has been an emerging area of investigation (Taroni et al., 2017). Innate immunity is activated by PRRs (pattern recognition receptors), which senses epitopes broadly conserved across pathogenic microbes, known as PAMPs (pathogen-associated molecular patterns), and endogenous ligands, known as DAMPs (danger-associated molecular patterns), that are released by stressed or activated cells and tissues (Ellson et al., 2014). When sensing excessive amounts of PAMPs or DAMPs, PRRs mediate activation of downstream inflammatory pathways (Li and Wu, 2021), including assembly of multimeric protein complexes known as inflammasomes, a caspase-1 activating platform (Franchi et al., 2009). While several PRRs are known to trigger inflammasome formation (Franchi et al., 2009; Kelley et al., 2019), the fibroproliferative role of the NLRP3 (NOD [nucleotide-binding oligomerization domain], LRR [leucine-rich repeat] containing proteins, and PYD-3 [pyrin domain-containing protein-3]) inflammasome has been of significant interest in SSc-ILD. Thus, the purpose of our review is to highlight recent work characterizing the mechanistic and clinical relevance of the NLRP3 inflammasome and its associated cytokines in this disease.

NLRP3 inflammasome

Initially described in 2002, NLRP3 is a sensor protein that along with the adaptor protein ASC (apoptosis-related spot-like protein containing CARD [carboxy-terminal caspase recruitment domain]) and the effector protein caspase-1 comprises the NLRP3 inflammasome (Swanson et al., 2019; Yang et al., 2019). Its activation first requires a priming step mediated by NF-κB (nuclear factor kappa light chain enhancer of activated B cells) signaling, which occurs via PAMP or DAMP activation of TLRs (Toll-like receptors) or NOD2 (nucleotide binding oligomerization domain containing 2), or through soluble mediators such as TNFα (tumor necrosis factor alpha) and IL-1β (interleukin-1 beta) (Swanson et al., 2019; Gritsenko et al., 2020). Priming serves to (1) upregulate transcription of inflammasome components of NLRP3, pro-IL-18, and pro-IL-1β, and (2) induce post-translational modifications of NLRP3 to stabilize its function (Swanson et al., 2019; Gritsenko et al., 2020). Following this step, NLRP3 forms oligomers through homotypic interactions via NACHT domains (NAIP [neuronal apoptosis inhibitor protein], CIITA [MHC class II transcription activator], HET-E [incompatibility locus protein from *Podospora anserina*] and TP1 [telomerase-associated protein]) (Damiano et al., 2004), which recruits ASC proteins via homotypic PYD–PYD interactions to nucleate helical ASC filament formation (Swanson et al., 2019). Multiple ASC filaments coalesce into a single macromolecule, known as an ASC speck, to recruit caspase-1 through CARD–CARD interactions to facilitate caspase-1 self-cleavage and activation (Swanson et al., 2019; Yang et al., 2019). Caspase-1 cleaves and activates IL-1β, IL-18 (Swanson et al., 2019; Li et al., 2020), and the membrane pore-forming protein GSDMD (gasdermin-D), where its N-terminal domain ($\mathrm{GSDMD^{Nterm}}$) oligomerizes to create a cell membrane pore (Shi et al., 2015; Swanson et al., 2019). Though the exact mechanism of NLRP3 inflammasome activation remains elusive, many sources suggest that common second-messenger pathways link the multiple upstream signals to inflammasome activation, including potassium efflux, decrease in intracellular calcium, lysosomal disruption, mitochondrial dysfunction, and reactive oxygen species (Artlett and Thacker, 2015; Elliott and Sutterwala, 2015; Man and Kanneganti, 2015; He et al., 2016). Given the inflammatory properties inherent with NLRP3 inflammasome activation, this pathway has been interrogated in autoimmune conditions such as SSc-ILD.

Aberrant activation of the NLRP3 inflammasome has garnered significant interest for its potential pathogenic role in inflammatory conditions such as SSc-ILD. Genome-wide association studies have shown polymorphisms in the NLRP3 gene to be linked with the development of ILDs such as asbestosis (rs35829419) (Franko et al., 2020), coal workers pneumoconiosis (rs1539019) (Ji et al., 2012), and silicosis (rs1539019 and rs34298354) (Weng et al., 2015); while specific NLRP3 polymorphisms have yet to be identified in SSc-ILD, further study in this arena could identify convergent molecular mechanisms linking divergent disease states. However, translational work completed by Artlett and colleagues demonstrated the connection between NLRP3 inflammasome activation and SSc by showing that dermal fibroblasts from SSc patients exhibit increased expression of inflammasome components, and that experimentally induced caspase-1 inhibition of both dermal and lung SSc fibroblasts ameliorated collagen deposition, reduced IL-1β and IL-18 secretion, and decreased αSMA (alpha smooth muscle actin) expression (Artlett et al., 2011). Additionally, studies investigating the pathogenic contribution of chronic parvovirus B19 (B19V) infection in SSc revealed that monocytes derived from SSc patients express significantly elevated mRNA levels of *NLRP3* than monocytes derived from healthy control subjects in the presence of B19V infection (Zakrzewska et al., 2019). Furthermore, mice deficient in NLRP3 (−/−) and ASC (−/−) were shown to be resistant to BLM (bleomycin) induced skin and lung fibrosis (Artlett et al., 2011). Additional work validated the finding of NLRP3 overexpression in SSc, including the association between skin thickness and NLRP3 expression (Martinez-Godinez et al., 2015). More recently, it was shown that miR-155 (microRNA-155) expression is indispensable for NLRP3 inflammasome mediated collagen production in SSc dermal and lung fibroblasts (Artlett et al., 2017; Henderson and O'Reilly, 2017). $\mathrm{NLRP3^{-/-}}$ fibroblasts and those treated with caspase-1 inhibition had significantly decreased miR-155 expression and collagen synthesis, leading the authors to conclude that the NLRP3 inflammasome is required for miR-155 expression (Artlett et al., 2017; Henderson and O'Reilly, 2017). These discoveries not only advance our understanding of the pathophysiologic importance of the NLRP3 inflammasome in SSc, but also lend scientific rationale for targeting its inhibition.

Early preclinical studies targeting the NLRP3 inflammasome identified the sulfonylurea glyburide as a potential inhibiting agent as *in vitro* studies showed a reduction in caspase-1 activation and IL-1β and IL-18 secretion in ATP-treated, lipopolysaccharide-sensitized macrophages (Lamkanfi et al., 2009). MCC950 (also known as CRID-3 or CP-456,773) is a disulfonylurea compound similar to glyburide that has been shown to specifically bind to NLRP3 and prevent inflammasome activation, interrupting IL-1β, IL-1α, and IL-18 secretion in a myriad of preclinical work (Coll et al., 2015; Primiano et al., 2016; van der Heijden et al., 2017; van Hout et al., 2017; Perera et al., 2018; Coll et al., 2019; Tapia-Abellan et al., 2019; Vande Walle et al., 2019; Corcoran et al., 2021). While clinical evaluation of MCC950 led to its discontinuation due to hepatotoxicity (Chen et al., 2021), these early efforts provided the scientific premise for other small-molecule NLRP3 inhibitors that are in various phases of clinical trials, including dapansutrile, a specific NLRP3 inhibitor (Marchetti et al., 2018; Sanchez-Fernandez et al., 2019) that has been shown to be safe in heart failure (Wohlford et al., 2020) and gout (Kluck et al., 2020). Other small molecule NLRP3 inhibitors under investigation include IFM2427, inzomelid, somalix, IZD334, and NT-0167 (El-Sharkawy et al., 2020; Chen et al., 2021); their relevance and benefit to SSc-ILD will require additional translational and clinical evaluation.

Along with direct antagonism of the NLRP3 inflammasome, targeting soluble mediators related to this pathway has also been an area of active study. As stated above, TNFα and IL-1β mediate priming of the inflammasome, and its activation result in the production of IL-1β and IL-18. Moreover, integrative analysis of RNA sequencing studies of peripheral blood and lungs from SSc patients has further demonstrated the pathophysiologic significance of these cytokines (Kobayashi et al., 2021). Single cell RNA sequencing of lung tissue from SSc-ILD subjects revealed a subpopulation of monocytes (termed FCN1^{hi}) that highly expressed, among others, genes related to *TNF, IL1B,* and *IL1R2* (Valenzi et al., 2019; Kobayashi et al., 2021). Thus, in the next section of this review, we will discuss the fibroproliferative contribution of TNFα, IL-1β, and IL-18 in SSc-ILD.

Tumor necrosis factor alpha

TNFα is a pleiotropic pro-inflammatory cytokine produced by various stromal and immune cells that is initially expressed as a transmembrane precursor protein and undergoes cleavage by TACE (TNFα-converting enzyme) to release soluble TNFα (Black et al., 1997; Moha et al., 2002). Both transmembrane and soluble TNFα binds to TNFR1 (TNF receptor 1), while only its transmembrane form is able to recognize TNFR2 (TNF receptor 2) (Vandenabeele et al., 1995). TNFR1 is ubiquitously expressed and contains a conserved death domain that facilitates recruitment of the adaptor protein TRADD (TNFR1-associated death domain), triggering activation of four potential signaling complexes (Hsu et al., 1995). Complex I forms when TNF binds to TNFR1, leading to a conformation change in its cytoplasmic domain, leading to recruitment of key mediators that include TRADD, RIPK1 (receptor-interacting serine/threonine-protein kinase 1), TRAF2 (TNFR-associated factor 2), cIAP1/2 (cellular inhibitor of apoptosis protein 1 or 2), and LUBAC (linear ubiquitin chain assembly complex); these interactions mediate downstream events critical for canonical NF-κB and MAPK (mitogen-activated protein kinases) signaling that promote tissue and cell inflammation, survival, and proliferation (Baud and Karin, 2001; Micheau and Tschopp, 2003; Brenner et al., 2015). The formation of complexes IIa and IIb (known as apoptosomes) also involve TNF-TNFR1-TRADD-RIPK1 interactions, but also include recruitment of FADD (Fas-associated protein with death domain) and pro-caspase 8 to induce cytoplasmic apoptotic signaling; complex IIb also requires activation of RIPK3 (Cain et al., 1999; Wang et al., 2008; Brenner et al., 2015). Complex IIc (known as a necrosome) requires TNF-TNFR1-TRADD-RIPK1-RIPK3 interactions that mediate activation of MLKL (mixed lineage kinase domain-like protein) to initiate cellular necroptosis (Cho et al., 2009; Brenner et al., 2015). Meanwhile, TNFR2, expressed exclusively by immune and endothelial cells, lacks the death domain present in TNFR1, and alternatively recruits TRAF1 and TRAF2 to form Complex 1, leading to activation of NF-κB and MAPK pathways (Faustman and Davis, 2010; Brenner et al., 2015). Not surprisingly, TNFα signaling has been extensively evaluated in inflammatory conditions such as SSc-ILD.

Early translational studies with this cytokine demonstrated its critical role in experimental models of pulmonary fibrosis as TNFα was shown to modulate expression of TGFβ in various cells in the lungs (Warshamana et al., 2001; Sullivan et al., 2005; Sullivan et al., 2009). In elegant work completed by Sullivan and colleagues, they showed that both transcriptional and post-transcriptional modifications in TGFβ expression in mouse lung fibroblasts are induced by TNFα (Sullivan et al., 2005; Sullivan et al., 2009). In rodent models of lung fibrosis, mice exposed to BLM displayed increased expression of TNFα that was associated with TGFβ levels (Ortiz et al., 1998; Brass et al., 1999; Hou et al., 2018); moreover, adenoviral mediated TNFα overexpression in otherwise normal rat lungs resulted in upregulation of TGFβ1 and accumulation of αSMA expressing myofibroblasts (Sime et al., 1998). Additionally, in various murine models, genetic (Liu et al., 1998) and pharmacologic (Phan and Kunkel, 1992; Piguet et al., 1993) knockdown of TNFα and its receptor ameliorated chemically-induced lung fibrosis in a TGFβ dependent manner, suggesting a synergistic association between TNFα and TGFβ-mediated fibrosis. In a direct connection to the SSc disease state, high levels of TNFα have been detected in the BAL (bronchoalveolar lavage) (Bolster et al., 1997; Pantelidis et al., 2001) of SSc-ILD patients. Moreover, relative to alveolar macrophages (AMs) derived from SSc patients without pulmonary fibrosis, AMs from fibrotic SSc lungs displayed enhanced secretion of this cytokine (Pantelidis et al., 2001). However, other reports implicate an antagonistic relationship as chronic overexpression of TNFα not only protected mice from BLM-induced lung fibrosis (Fujita et al., 2003), but also accelerated resolution of this pathology through a reduction in profibrotic lung macrophages (Redente et al., 2014). This constellation of findings demonstrates a paradigm wherein TNFα exerts pathogenic or protective roles in pulmonary fibrosis that depends on cell-specific and temporal cues that would benefit from further evaluation.

Despite these findings, TNFα antagonism has been clinically therapeutic in inflammatory diseases such as RA (rheumatoid arthritis), ankylosing spondylitis, inflammatory bowel disease, and psoriasis, as well as various off-label indications (Haraoui, 2005; Jang et al., 2021). Not unexpectedly, this treatment strategy has been associated with exacerbating underlying ILD or resulting in *de novo* pneumonitis (Tengstrand et al., 2005; Andrew et al., 2006; Perez-Alvarez et al., 2011; Tamao et al., 2014), which has tempered enthusiasm for this agent in SSc-ILD. However, given that the blood of SSc patients is enriched for this cytokine (Pehlivan et al., 2012), particularly among those with lung disease (Murdaca et al., 2014), as well as the availability of several FDA-approved TNFα inhibitors, the indication for these agents in SSc-ILD have been explored. In an open-label pilot trial for diffuse cutaneous SSc, infliximab, a recombinant chimeric mouse/human monoclonal antibody, showed no significant improvement in MRSS (modified Rodnan skin scores); while there was potential for stabilization of skin

TABLE 1 Antagonists and their mechanism of action.

Antagonist	Mechanism of action
Adalimumab	● Recombinant human IgG1 anti-TNFα monoclonal antibody
	● Inhibits binding of both soluble and transmembrane TNFα to TNFα receptors
Anakinra	● Recombinant non-glycosylated human IL-1 receptor antagonist
	● Competitively inhibits IL-1 binding to the interleukin-1 type I receptor
Canakinumab	● Recombinant human IgGκ anti-IL-1β monoclonal antibody
	● Binds to IL-1β to inhibit IL-1 receptor activation
Dapansutrile	● β-sulfonyl nitrile compound
	● Binds to the NLRP3 protein to prevent NLRP3 ATPase activity and NLRP3-ASC interactions
Etanercept	● Soluble TNF receptor
	● Binds to both TNFα and TNFβ to inhibit TNF receptor activation
Golimumab	● Human IgG1κ anti-TNFα monoclonal antibody
	● Binds to soluble and transmembrane TNFα to inhibit TNFα receptor activation
Glyburide	● Sulfonylurea compound
	● Unknown mechanism of action, believed to inhibit potassium efflux needed for NLRP3 inflammasome activation
GSK1070806	● Human IgG anti-IL-18 monoclonal antibody
	● Binds to IL-18 to inhibit IL-18 receptor activation
Infliximab	● Chimeric IgG1 anti- TNFα monoclonal antibody
	● Binds to soluble and transmembrane TNFα to inhibit TNFα receptor activation
Rilonacept	● Soluble IL-1β receptor
	● Binds to IL-1β to inhibit IL-1 receptor activation
Tadekinig alpha	● Recombinant IL-18 binding protein
	● Binds to free IL-18 to inhibit IL-18 receptor activation

disease, a high number of transfusion reactions limited use of this agent in this population (Denton et al., 2009). The role of infliximab remains unknown in SSc-ILD as there were no reports of its effect on lung function (Bosello et al., 2005; Denton et al., 2009); however, studies in sarcoidosis, another multi-system ILD, suggest that it has the potential to improve lung function (Baughman et al., 2006) and ameliorate multi-organ disease (Russell et al., 2013). Etanercept, a human TNF-receptor p75 Fc fusion protein that binds TNFα, showed promise in decreasing SSc associated inflammatory synovitis and was safely tolerated (Gordon et al., 2007). Although its role in SSc-ILD is largely unknown, in the same study, there was a no significant change in lung function (Gordon et al., 2007), and studies with this agent in sarcoidosis also demonstrated no change in lung function (Utz et al., 2003). Other FDA approved TNFα monoclonal antibodies include adalimumab and golimumab (Haraoui, 2005; Jang et al., 2021). While these agents have yet to be studied in SSc, they have been evaluated in sarcoidosis, where adalimumab has shown promise in improving lung function (Kamphuis et al., 2011; Milman et al., 2012; Sweiss et al., 2014), while golimumab demonstrated no benefit (Judson et al., 2014). Thus, despite the inflammatory nature of SSc-ILD, antagonism of TNFα signaling has demonstrated mixed results.

Interleukin-1 beta

IL-1β is a cytokine mainly produced by myeloid cells in its inactive form, pro-IL-1β (Dinarello, 2011). It is cleaved intracellularly by caspase 1, and extracellularly by serine proteases that result in its activation (Lamkanfi, 2011; Bode et al., 2012). IL-1β binds to its receptor, IL-1R1, which heterodimerizes with the accessory protein IL-1RAcP (IL-1 receptor accessory protein) to transmit signaling via intracellular activation of adaptor proteins such as MyD88 (myeloid differentiation primary response gene-88), leading to the production of NF-κB and MAPK (Dinarello, 2009; Van Gorp et al., 2019; Chauhan et al., 2020). IL-1β signaling results in the production of additional pro-inflammatory cytokines and chemokines such as TNFα, IL-6, IL-8, MCP1 (monocyte chemoattractant protein 1), CXCL1 (chemokine ligand 1), and MIP2 (macrophage inflammatory protein 2) (Chauhan et al., 2020). IL-1β signaling also drives amplification and polarization of CD4$^+$ T-cells toward a Th1 and Th17 phenotype and promotes differentiation of antigen-specific CD8$^+$ T-cells (Ben-Sasson et al., 2009; Santarlasci et al., 2013; Chauhan et al., 2020). As an effector of both innate and adaptive immune responses, the study of IL-1β can lend novel immunopathogenic insight into inflammatory conditions such as SSc-ILD.

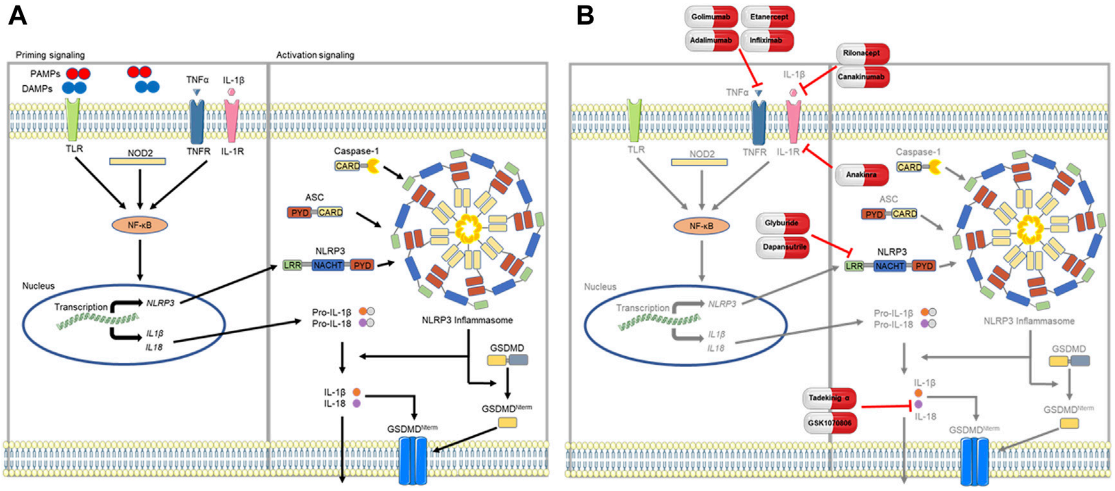

FIGURE 1
Proposed model of NLRP3 inflammasome signaling. **(A)** Assembly of the NLRP3 inflammasome first requires a priming step that is mediated by NF-κB (nuclear factor kappa light chain enhancer of activated B cells) signaling, which occurs via PAMP (pathogen associated molecular pattern) or DAMP (damage associated molecular pattern) activation of TLRs (toll-like receptors) or NOD2 (nucleotide binding oligomerization domain containing 2), or through soluble mediators such as TNFα (tumor necrosis factor alpha) and IL-1β (interleukin-1 beta). Priming upregulates transcription of inflammasome components of NLRP3, pro-IL-18, and pro-IL-1β. Following this step, components of the NLRP3 inflammasome coalesce to form the ASC speck and subsequently the inflammasome, activating caspase-1 to cleave pro-IL-1β and pro-IL-18 into their respective products, IL-1β and IL-18. **(B)** Antagonism of the NLRP3 inflammasome or mediating cytokines (TNFα, IL-1β, and IL-18) have shown potential as novel therapeutic targets in SSc-ILD. Parts of the figure were drawn by using pictures from Servier Medical Art. Servier Medical Art by Servier is licensed under a Creative Commons Attribution 3.0 Unported License (https://creativecommons.org/licenses/by/3.0/).

Somewhat surprisingly, studies of IL-1β signaling have led to conflicting findings. Initial translational efforts found that excessive concentrations of IL-1β were present in the lungs, blood, and skin of SSc patients (Hussein et al., 2005). In experimental models of lung fibrosis, mice treated with BLM displayed increased IL-1β production, inflammation, remodeling, and fibrosis in a manner dependent on IL-1R1/MyD88 signaling (Gasse et al., 2007). These findings were significantly reduced in IL-1R1-and MyD88-deficient mice, suggesting the indispensable nature of endogenous IL-1β in pulmonary inflammation and fibrosis (Gasse et al., 2007). However, these findings are tempered by recent reports showing that IL-1 receptor inhibition can exacerbate pulmonary fibrosis; employing a murine model of SSc through the overexpression of Fra-2 (fos-related antigen-2), mice treated with an IL-1 inhibitor demonstrated worse lung function, enhanced Th2 inflammation, and greater numbers of pro-fibrotic, alternatively activated macrophages (Birnhuber et al., 2019). Similar to that of TNFα, these data demonstrate the context-dependent nature of IL-1β that warrants additional investigation.

Nonetheless, re-purposing FDA-approved IL-1β antagonists has been considered for this and other autoimmune diseases. Anakinra is a recombinant human IL-1Ra that competitively inhibits IL-1α and IL-1β interaction with IL-1R1 and is currently indicated for the treatment of refractory RA and for CAPS (Cryopyrin Associated Periodic Syndrome) (Cavalli and Dinarello, 2015). Its safety and efficacy have yet to be explored in SSc. Canakinumab is a human monoclonal anti-IL-1β antibody that has demonstrated efficacy in treating multiple autoimmune conditions (De Benedetti et al., 2018) as well atherosclerotic diseases in the CANTOS Trial (Ridker et al., 2012; Ridker et al., 2017a). Interestingly, additional analysis of the CANTOS cohort revealed a significant reduction in incident lung cancer and lung cancer mortality (Ridker et al., 2017b); these findings suggest that this agent is able to modulate processes in the lung, making it a promising candidate for treating SSc-ILD. Lastly, rilonacept is a soluble IL-1 trap that binds IL-1α and IL-1β; it has been approved for the treatment of CAPS (Hoffman et al., 2012) and has demonstrated safety and efficacy in other inflammatory disorders (Krause et al., 2012). Moreover, in a small cohort of SSc patients ($n = 19$), this drug, while demonstrating an acceptable safety and tolerability profile, did not demonstrate biologic (based on gene expression) or clinical (based on MRSS) efficacy (Manter et al., 2018). Ultimately, further work is required to determine the clinical benefit of IL-1β inhibition in SSc-ILD.

Interleukin-18

Along with IL-1β, NLRP3 inflammasome activation mediates production of IL-18, formerly known as IFN-γ (interferon-gamma) inducing factor. This cytokine is produced as pro-IL-18 by a number of cells, including macrophages and dendritic cells, and as with IL-1β, requires cleavage by caspase-1 to become biologically active (Arend et al., 2008; Dinarello et al., 2013). The IL-18 receptor, comprised of IL-18Rα and IL-18Rβ subunits, forms a high-affinity heterodimer expressed on various immune, endothelial, and smooth muscle cells, and is modulated by various other cytokines (Arend et al., 2008). Similar to the IL-1 receptor, IL-18 signal transduction proceeds via several intracellular adaptor molecules, including MyD88, IRAK1 (interleukin 1 receptor associated kinase 1), and TRAF6 to activate MAPK, NF-κB, and JNK (c-Jun N-terminal kinase) (Arend et al., 2008; Dinarello et al., 2013; Xu et al., 2019; Yasuda et al., 2019). IL-18 stimulates production of GM-CSF (granulocyte-monocyte colony-stimulating factor), TNFα, and IL-1β, and mediates both innate and adaptive immune responses (Arend et al., 2008). In the presence of IL-12 and IL-15, IL-18 can induce IFN-γ production by various T-cells and favors Th1 differentiation, a pro-inflammatory state; in the absence of IL-12 and IL-15, IL-18 signaling favors Th2 differentiation and promotes fibrosis (Dinarello et al., 2013; Kaplanski, 2018). Much like IL-1β, IL-18 has pleotropic effects in immune activation, suggesting a potential contribution in inflammatory conditions such as SSc-ILD.

Similar to work done with TNFα and IL-1β, studies of IL-18 have also led to contradictory results in SSc-ILD. In the serum of patients with SSc, increased concentrations of IL-18 were identified, and these levels negatively correlated with lung function, suggesting a role in mediating lung disease (Lin et al., 2019). However, both profibrotic and anti-fibrotic properties of IL-18 have been illustrated. In experimentally-induced pulmonary fibrosis, mice subjected to BLM administration exhibited increased concentrations of IL-18 in the lung (Oku et al., 2008). Additionally, novel work investigating the myeloid-specific contribution of autophagy in lung injury showed that mice deficient in the key autophagy gene *Atg7* develop spontaneous lung inflammation that was predominantly mediated by IL-18 from constitutive inflammasome activation (Abdel Fattah et al., 2015). Here, the authors showed that IL-18 antagonism inhibited the recruitment of lymphocytes and neutrophils in the lungs of these mice, suggesting a critical role for myeloid-specific IL-18 (Abdel Fattah et al., 2015). However, another study showed that mice deficient in IL-18 exhibited greater lung injury and weight loss in response to BLM administration (Nakatani-Okuda et al., 2005). In that same study, while therapeutic administration of IL-18 had no effect on BLM-induced lung injury, prophylactic IL-18 treatment prior to BLM administration ameliorated findings of lung injury (Nakatani-Okuda et al., 2005). The pleotropic effects of IL-18 altering the balance between Th1 and Th2 responses is likely contributing to this conundrum (Kim et al., 2010), and further study is sorely needed to unravel this complex biology.

Despite these conflicting *in vivo* data, IL-18 inhibition is currently under investigation for therapeutic benefit. Tadekinig alfa, a recombinant human IL-18 binding protein, was shown to be effective in treating adult onset Still's disease (Gabay et al., 2018; Kiltz et al., 2020) and NLRC4 associated macrophage activation syndrome (Canna et al., 2017). GSK1070806, a monoclonal IL-18 antibody, was shown to be safely tolerated (Mistry et al., 2014) and is currently being evaluated in a phase 1b clinical trial for atopic dermatitis (NCT04975438) and phase 2 clinical trial for moderate to severe Crohn's disease (NCT03681067). Additional work will be needed to determine whether IL-18 is promoting disease or protecting the lung in SSc-ILD.

Conclusion

This concludes our review of NLRP3 inflammasome signaling and associated cytokines of TNFα, IL-1β, and IL-18 as novel therapeutic targets in SSc-ILD; these findings are summarized in Table 1 and depicted in Figure 1. Study of this complex biology requires further investigation to fully characterize the context-dependent roles of this signaling pathway and soluble mediators in protecting against or promoting pulmonary fibrosis in SSc-ILD. Addressing such knowledge gaps require improved modeling systems that better recapitulate human disease; rodent models exhibit relatively swift progression of lung fibrosis, fail to reproduce lung histopathology, and resolve fibrosis with discontinuation of the pro-fibrotic agent (Herzog et al., 2014). Thus, while animal modeling is viewed as a useful tool for the *in vivo* study of lung disease that would be unethical and impractical in humans, their value is limited. Work complemented by studies of primary human cells and tissues, as well as functional studies of explanted cells and organs, have been instrumental in replicating the salient features of the healthy and diseased adult mammalian lung (Herzog et al., 2014). Translational studies integrating traditional *in vivo* models with state-of-the-art *ex vivo* mimetics will have more direct relevance to the human disease state. Such work has the potential to yield insight into novel pathophysiologic mechanisms while catalyzing new treatment approaches, including repurposing old and developing new drugs, in this intractable condition.

Author contributions

SW: Writing–original draft, Writing–review and editing. SG: Writing–review and editing, Conceptualization, Supervision. AG: Writing–original draft, Writing–review and editing. TS: Conceptualization, Supervision, Writing–review and editing. CL: Writing–review and editing, Writing–original draft. CR: Conceptualization, Supervision, Writing–review and editing, Funding acquisition, Visualization, Writing–original draft.

Funding

The author(s) declare financial support was received for the research, authorship, and/or publication of this article. SG was supported by T32HL007778-21. AG was supported by T32HL007778-21. CR was supported by K08HL151970-01 and the Cystic Fibrosis Foundation.

Conflict of interest

The authors declare that the research was conducted in the absence of any commercial or financial relationships that could be construed as a potential conflict of interest.

Publisher's note

References

Abdel Fattah, E., Bhattacharya, A., Herron, A., Safdar, Z., and Eissa, N. T. (2015). Critical role for IL-18 in spontaneous lung inflammation caused by autophagy deficiency. *J. Immunol.* 194 (11), 5407–5416. doi:10.4049/jimmunol.1402277

Andrew, J. K. O., Chilvers, E. R., Somerville, M. F., Lim, A. Y. N., Lane, S. E., Crisp, A. J., et al. (2006). Pulmonary complications of infliximab therapy in patients with rheumatoid arthritis. *J. Rheumatology* 33 (3), 622–628.

Arend, W. P., Palmer, G., and Gabay, C. (2008). IL-1, IL-18, and IL-33 families of cytokines. *Immunol. Rev.* 223, 20–38. doi:10.1111/j.1600-065X.2008.00624.x

Artlett, C. M., Sassi-Gaha, S., Hope, J. L., Feghali-Bostwick, C. A., and Katsikis, P. D. (2017). Mir-155 is overexpressed in systemic sclerosis fibroblasts and is required for NLRP3 inflammasome-mediated collagen synthesis during fibrosis. *Arthritis Res. Ther.* 19 (1), 144. doi:10.1186/s13075-017-1331-z

Artlett, C. M., Sassi-Gaha, S., Rieger, J. L., Boesteanu, A. C., Feghali-Bostwick, C. A., and Katsikis, P. D. (2011). The inflammasome activating caspase 1 mediates fibrosis and myofibroblast differentiation in systemic sclerosis. *Arthritis Rheum.* 63 (11), 3563–3574. doi:10.1002/art.30568

Artlett, C. M., and Thacker, J. D. (2015). Molecular activation of the NLRP3 inflammasome in fibrosis: common threads linking divergent fibrogenic diseases. *Antioxid. Redox Signal* 22 (13), 1162–1175. doi:10.1089/ars.2014.6148

Baud, V., and Karin, M. (2001). Signal transduction by tumor necrosis factor and its relatives. *Trends Cell Biol.* 11 (9), 372–377. doi:10.1016/s0962-8924(01)02064-5

Baughman, R. P., Drent, M., Kavuru, M., Judson, M. A., Costabel, U., du Bois, R., et al. (2006). Infliximab therapy in patients with chronic sarcoidosis and pulmonary involvement. *Am. J. Respir. Crit. Care Med.* 174 (7), 795–802. doi:10.1164/rccm.200603-402OC

Ben-Sasson, S. Z., Hu-Li, J., Quiel, J., Cauchetaux, S., Ratner, M., Shapira, I., et al. (2009). IL-1 acts directly on CD4 T cells to enhance their antigen-driven expansion and differentiation. *Proc. Natl. Acad. Sci. U. S. A.* 106 (17), 7119–7124. doi:10.1073/pnas.0902745106

Birnhuber, A., Crnkovic, S., Biasin, V., Marsh, L. M., Odler, B., Sahu-Osen, A., et al. (2019). IL-1 receptor blockade skews inflammation towards Th2 in a mouse model of systemic sclerosis. *Eur. Respir. J.* 54 (3), 1900154. doi:10.1183/13993003.00154-2019

Black, R. A., Rauch, C. T., Kozlosky, C. J., Peschon, J. J., Slack, J. L., Wolfson, M. F., et al. (1997). A metalloproteinase disintegrin that releases tumour-necrosis factor-alpha from cells. *Nature* 385 (6618), 729–733. doi:10.1038/385729a0

Bode, J. G., Albrecht, U., Häussinger, D., Heinrich, P. C., and Schaper, F. (2012). Hepatic acute phase proteins-regulation by IL-6- and IL-1-type cytokines involving STAT3 and its crosstalk with NF-κB-dependent signaling. *Eur. J. Cell Biol.* 91 (6-7), 496–505. doi:10.1016/j.ejcb.2011.09.008

Bolster, M. B., Ludwicka, A., Sutherland, S. E., Strange, C., and Silver, R. M. (1997). Cytokine concentrations in bronchoalveolar lavage fluid of patients with systemic sclerosis. *Arthritis & Rheumatism* 40 (4), 743–751. doi:10.1002/art.1780400422

Bosello, S., De Santis, M., Tolusso, B., Zoli, A., and Ferraccioli, G. (2005). Tumor necrosis factor-alpha inhibitor therapy in erosive polyarthritis secondary to systemic sclerosis. *Ann. Intern. Med.* 143 (12), 918–920. doi:10.7326/0003-4819-143-12-200512200-00019

Brass, D. M., Hoyle, G. W., Poovey, H. G., Liu, J. Y., and Brody, A. R. (1999). Reduced tumor necrosis factor-alpha and transforming growth factor-beta1 expression in the lungs of inbred mice that fail to develop fibroproliferative lesions consequent to asbestos exposure. *Am. J. Pathol.* 154 (3), 853–862. doi:10.1016/s0002-9440(10)65332-1

Brenner, D., Blaser, H., and Mak, T. W. (2015). Regulation of tumour necrosis factor signalling: live or let die. *Nat. Rev. Immunol.* 15 (6), 362–374. doi:10.1038/nri3834

Cain, K., Brown, D. G., Langlais, C., and Cohen, G. M. (1999). Caspase activation involves the formation of the aposome, a large (approximately 700 kDa) caspase-activating complex. *J. Biol. Chem.* 274 (32), 22686–22692. doi:10.1074/jbc.274.32.22686

Canna, S. W., Girard, C., Malle, L., de Jesus, A., Romberg, N., Kelsen, J., et al. (2017). Life-threatening NLRC4-associated hyperinflammation successfully treated with IL-18 inhibition. *J. Allergy Clin. Immunol.* 139 (5), 1698–1701. doi:10.1016/j.jaci.2016.10.022

Cavalli, G., and Dinarello, C. A. (2015). Treating rheumatological diseases and co-morbidities with interleukin-1 blocking therapies. *Rheumatol. Oxf.* 54 (12), 2134–2144. doi:10.1093/rheumatology/kev269

Chauhan, D., Vande Walle, L., and Lamkanfi, M. (2020). Therapeutic modulation of inflammasome pathways. *Immunol. Rev.* 297 (1), 123–138. doi:10.1111/imr.12908

Chen, Q. L., Yin, H. R., He, Q. Y., and Wang, Y. (2021). Targeting the NLRP3 inflammasome as new therapeutic avenue for inflammatory bowel disease. *Biomed. Pharmacother.* 138, 111442. doi:10.1016/j.biopha.2021.111442

Cho, Y. S., Challa, S., Moquin, D., Genga, R., Ray, T. D., Guildford, M., et al. (2009). Phosphorylation-driven assembly of the RIP1-RIP3 complex regulates programmed necrosis and virus-induced inflammation. *Cell* 137 (6), 1112–1123. doi:10.1016/j.cell.2009.05.037

Coll, R. C., Hill, J. R., Day, C. J., Zamoshnikova, A., Boucher, D., Massey, N. L., et al. (2019). MCC950 directly targets the NLRP3 ATP-hydrolysis motif for inflammasome inhibition. *Nat. Chem. Biol.* 15 (6), 556–559. doi:10.1038/s41589-019-0277-7

Coll, R. C., Robertson, A. A. B., Chae, J. J., Higgins, S. C., Muñoz-Planillo, R., Inserra, M. C., et al. (2015). A small-molecule inhibitor of the NLRP3 inflammasome for the treatment of inflammatory diseases. *Nat. Med.* 21 (3), 248–255. doi:10.1038/nm.3806

Corcoran, S. E., Halai, R., and Cooper, M. A. (2021). Pharmacological inhibition of the nod-like receptor family pyrin domain containing 3 inflammasome with MCC950. *Pharmacol. Rev.* 73 (3), 968–1000. doi:10.1124/pharmrev.120.000171

Damiano, J. S., Oliveira, V., Welsh, K., and Reed, J. C. (2004). Heterotypic interactions among NACHT domains: implications for regulation of innate immune responses. *Biochem. J.* 381 (1), 213–219. doi:10.1042/BJ20031506

De Benedetti, F., Gattorno, M., Anton, J., Ben-Chetrit, E., Frenkel, J., Hoffman, H. M., et al. (2018). Canakinumab for the treatment of autoinflammatory recurrent fever syndromes. *N. Engl. J. Med.* 378 (20), 1908–1919. doi:10.1056/NEJMoa1706314

Denton, C. P., Engelhart, M., Tvede, N., Wilson, H., Khan, K., Shiwen, X., et al. (2009). An open-label pilot study of infliximab therapy in diffuse cutaneous systemic sclerosis. *Ann. Rheumatic Dis.* 68 (9), 1433–1439. doi:10.1136/ard.2008.096123

Denton, C. P., and Khanna, D. (2017). Systemic sclerosis. *Lancet* 390 (10103), 1685–1699. doi:10.1016/S0140-6736(17)30933-9

Dinarello, C. A. (2011). A clinical perspective of IL-1β as the gatekeeper of inflammation. *Eur. J. Immunol.* 41 (5), 1203–1217. doi:10.1002/eji.201141550

Dinarello, C. A. (2009). Immunological and inflammatory functions of the interleukin-1 family. *Annu. Rev. Immunol.* 27, 519–550. doi:10.1146/annurev.immunol.021908.132612

Dinarello, C. A., Novick, D., Kim, S., and Kaplanski, G. (2013). Interleukin-18 and IL-18 binding protein. *Front. Immunol.* 4, 289. doi:10.3389/fimmu.2013.00289

Distler, O., Highland, K. B., Gahlemann, M., Azuma, A., Fischer, A., Mayes, M. D., et al. (2019). Nintedanib for systemic sclerosis-associated interstitial lung disease. *N. Engl. J. Med.* 380 (26), 2518–2528. doi:10.1056/NEJMoa1903076

El-Sharkawy, L. Y., Brough, D., and Freeman, S. (2020). Inhibiting the NLRP3 inflammasome. *Molecules* 25 (23), 5533. doi:10.3390/molecules25235533

Elliott, E. I., and Sutterwala, F. S. (2015). Initiation and perpetuation of NLRP3 inflammasome activation and assembly. *Immunol. Rev.* 265 (1), 35–52. doi:10.1111/imr.12286

Ellson, C. D., Dunmore, R., Hogaboam, C. M., Sleeman, M. A., and Murray, L. A. (2014). Danger-associated molecular patterns and danger signals in idiopathic pulmonary fibrosis. *Am. J. Respir. Cell Mol. Biol.* 51 (2), 163–168. doi:10.1165/rcmb.2013-0366TR

Faustman, D., and Davis, M. (2010). TNF receptor 2 pathway: drug target for autoimmune diseases. *Nat. Rev. Drug Discov.* 9 (6), 482–493. doi:10.1038/nrd3030

Franchi, L., Eigenbrod, T., Muñoz-Planillo, R., and Nuñez, G. (2009). The inflammasome: A caspase-1-activation platform that regulates immune responses and disease pathogenesis. *Nat. Immunol.* 10 (3), 241–247. doi:10.1038/ni.1703

Franko, A., Goricar, K., Kovac, V., Dodic-Fikfak, M., and Dolzan, V. (2020). NLRP3 and CARD8 polymorphisms influence risk for asbestos-related diseases. *J. Med. Biochem.* 39 (1), 91–99. doi:10.2478/jomb-2019-0025

Fujita, M., Shannon, J. M., Morikawa, O., Gauldie, J., Hara, N., and Mason, R. J. (2003). Overexpression of tumor necrosis factor-alpha diminishes pulmonary fibrosis induced by bleomycin or transforming growth factor-beta. *Am. J. Respir. Cell Mol. Biol.* 29 (6), 669–676. doi:10.1165/rcmb.2002-0046OC

Gabay, C., Fautrel, B., Rech, J., Spertini, F., Feist, E., Kötter, I., et al. (2018). Open-label, multicentre, dose-escalating phase II clinical trial on the safety and efficacy of tadekinig alfa (IL-18BP) in adult-onset Still's disease. *Ann. Rheum. Dis.* 77 (6), 840–847. doi:10.1136/annrheumdis-2017-212608

Gasse, P., Mary, C., Guenon, I., Noulin, N., Charron, S., Schnyder-Candrian, S., et al. (2007). IL-1R1/MyD88 signaling and the inflammasome are essential in pulmonary inflammation and fibrosis in mice. *J. Clin. investigation* 117 (12), 3786–3799. doi:10.1172/JCI32285

Gordon, K. L., Hummers, L. K., Woods, A., and Wigley, F. M. (2007). Efficacy and safety of etanercept in the treatment of scleroderma-associated joint disease. *J. Rheumatology* 34 (7), 1636–1637.

Gritsenko, A., Green, J. P., Brough, D., and Lopez-Castejon, G. (2020). Mechanisms of NLRP3 priming in inflammaging and age related diseases. *Cytokine & Growth Factor Rev.* 55, 15–25. doi:10.1016/j.cytogfr.2020.08.003

Haraoui, B., Differentiating the efficacy of the tumor necrosis factor inhibitors. *Seminars Arthritis Rheumatism*, 2005. 34(5): p. 7–11. doi:10.1016/j.semarthrit.2005.01.003

He, Y., Hara, H., and Nunez, G. (2016). Mechanism and regulation of NLRP3 inflammasome activation. *Trends Biochem. Sci.* 41 (12), 1012–1021. doi:10.1016/j.tibs.2016.09.002

Henderson, J., and O'Reilly, S. (2017). Inflammasome lights up in systemic sclerosis. *Arthritis Res. Ther.* 19 (1), 205. doi:10.1186/s13075-017-1420-z

Herzog, E. L., Mathur, A., Tager, A. M., Feghali-Bostwick, C., Schneider, F., and Varga, J. (2014). Review: interstitial lung disease associated with systemic sclerosis and idiopathic pulmonary fibrosis: how similar and distinct? *Arthritis Rheumatol.* 66 (8), 1967–1978. doi:10.1002/art.38702

Hoffman, H. M., Throne, M. L., Amar, N. J., Cartwright, R. C., Kivitz, A. J., Soo, Y., et al. (2012). Long-term efficacy and safety profile of rilonacept in the treatment of cryopryin-associated periodic syndromes: results of a 72-week open-label extension study. *Clin. Ther.* 34 (10), 2091–2103. doi:10.1016/j.clinthera.2012.09.009

Hou, J., Ma, T., Cao, H., Chen, Y., Wang, C., Chen, X., et al. (2018). TNF-α-induced NF-κB activation promotes myofibroblast differentiation of LR-MSCs and exacerbates bleomycin-induced pulmonary fibrosis. *J. Cell Physiol.* 233 (3), 2409–2419. doi:10.1002/jcp.26112

Hsu, H., Xiong, J., and Goeddel, D. V. (1995). The TNF receptor 1-associated protein TRADD signals cell death and NF-κB activation. *Cell* 81 (4), 495–504. doi:10.1016/0092-8674(95)90070-5

Hussein, M. R., Hassan, H. I., Hofny, E. R. M., Elkholy, M., Fatehy, N. A., Abd Elmoniem, A. E. A., et al. (2005). Alterations of mononuclear inflammatory cells, CD4/CD8+ T cells, interleukin 1beta, and tumour necrosis factor alpha in the bronchoalveolar lavage fluid, peripheral blood, and skin of patients with systemic sclerosis. *J. Clin. pathology* 58 (2), 178–184. doi:10.1136/jcp.2004.019224

Jang, D.-i., Lee, A. H., Shin, H. Y., Song, H. R., Park, J. H., Kang, T. B., et al. (2021). The role of tumor necrosis factor alpha (TNF-α) in autoimmune disease and current TNF-α inhibitors in therapeutics. *Int. J. Mol. Sci.* 22, 2719. doi:10.3390/ijms22052719

Ji, X., Hou, Z., Wang, T., Jin, K., Fan, J., Luo, C., et al. (2012). Polymorphisms in inflammasome genes and risk of coal workers' pneumoconiosis in a Chinese population. *PLoS One* 7 (10), e47949. doi:10.1371/journal.pone.0047949

Judson, M. A., Baughman, R. P., Costabel, U., Drent, M., Gibson, K. F., Raghu, G., et al. (2014). Safety and efficacy of ustekinumab or golimumab in patients with chronic sarcoidosis. *Eur. Respir. J.* 44 (5), 1296–1307. doi:10.1183/09031936.00000914

Kamphuis, L. S., Lam-Tse, W. K., Dik, W. A., van Daele, P. L., van Biezen, P., Kwekkeboom, D. J., et al. (2011). Efficacy of adalimumab in chronically active and symptomatic patients with sarcoidosis. *Am. J. Respir. Crit. Care Med.* 184 (10), 1214–1216. doi:10.1164/ajrccm.184.10.1214

Kaplanski, G. (2018). Interleukin-18: biological properties and role in disease pathogenesis. *Immunol. Rev.* 281 (1), 138–153. doi:10.1111/imr.12616

Kelley, N., Jeltema, D., Duan, Y., and He, Y. (2019). The NLRP3 inflammasome: an overview of mechanisms of activation and regulation. *Int. J. Mol. Sci.* 20 (13), 3328. doi:10.3390/ijms20133328

Kiltz, U., Kiefer, D., Braun, J., Schiffrin, E. J., Girard-Guyonvarc'h, C., and Gabay, C. (2020). Prolonged treatment with Tadekinig alfa in adult-onset Still's disease. *Ann. Rheum. Dis.* 79 (1), e10. doi:10.1136/annrheumdis-2018-214496

Kim, H. J., Song, S. B., Choi, J. M., Kim, K. M., Cho, B. K., Cho, D. H., et al. (2010). IL-18 downregulates collagen production in human dermal fibroblasts via the ERK pathway. *J. Investigative Dermatology* 130 (3), 706–715. doi:10.1038/jid.2009.302

Kluck, V., Jansen, T. L. T. A., Janssen, M., Comarniceanu, A., Efdé, M., Tengesdal, I. W., et al. (2020). Dapansutrile, an oral selective NLRP3 inflammasome inhibitor, for treatment of gout flares: an open-label, dose-adaptive, proof-of-concept, phase 2a trial. *Lancet Rheumatol.* 2 (5), e270–e280. doi:10.1016/s2665-9913(20)30065-5

Kobayashi, S., Nagafuchi, Y., Okubo, M., Sugimori, Y., Shirai, H., Hatano, H., et al. (2021). Integrated bulk and single-cell RNA-sequencing identified disease-relevant monocytes and a gene network module underlying systemic sclerosis. *J. Autoimmun.* 116, 102547. doi:10.1016/j.jaut.2020.102547

Krause, K., Weller, K., Stefaniak, R., Wittkowski, H., Altrichter, S., Siebenhaar, F., et al. (2012). Efficacy and safety of the interleukin-1 antagonist rilonacept in schnitzler syndrome: an open-label study. *Allergy* 67 (7), 943–950. doi:10.1111/j.1398-9995.2012.02843.x

Lamkanfi, M. (2011). Emerging inflammasome effector mechanisms. *Nat. Rev. Immunol.* 11 (3), 213–220. doi:10.1038/nri2936

Lamkanfi, M., Mueller, J. L., Vitari, A. C., Misaghi, S., Fedorova, A., Deshayes, K., et al. (2009). Glyburide inhibits the Cryopyrin/Nalp3 inflammasome. *J. Cell Biol.* 187 (1), 61–70. doi:10.1083/jcb.200903124

Li, D., and Wu, M. (2021). Pattern recognition receptors in health and diseases. *Signal Transduct. Target. Ther.* 6 (1), 291. doi:10.1038/s41392-021-00687-0

Li, Z., Guo, J., and Bi, L. (2020). Role of the NLRP3 inflammasome in autoimmune diseases. *Biomed. Pharmacother.* 130, 110542. doi:10.1016/j.biopha.2020.110542

Lin, E., Vincent, F. B., Sahhar, J., Ngian, G. S., Kandane-Rathnayake, R., Mende, R., et al. (2019). Analysis of serum interleukin(IL)-1α, IL-1β and IL-18 in patients with systemic sclerosis. *Clin. Transl. Immunol.* 8 (4), e1045. doi:10.1002/cti2.1045

Liu, J. Y., Brass, D. M., Hoyle, G. W., and Brody, A. R. (1998). TNF-alpha receptor knockout mice are protected from the fibroproliferative effects of inhaled asbestos fibers. *Am. J. Pathol.* 153 (6), 1839–1847. doi:10.1016/s0002-9440(10)65698-2

Man, S. M., and Kanneganti, T. D. (2015). Regulation of inflammasome activation. *Immunol. Rev.* 265 (1), 6–21. doi:10.1111/imr.12296

Mantero, J. C., Kishore, N., Ziemek, J., Stifano, G., Zammitti, C., Khanna, D., et al. (2018). Randomised, double-blind, placebo-controlled trial of IL1-trap, rilonacept, in systemic sclerosis. A phase I/II biomarker trial. *Clin. Exp. Rheumatol.* 36 (4): p. 146–149.

Marchetti, C., Swartzwelter, B., Gamboni, F., Neff, C. P., Richter, K., Azam, T., et al. (2018). OLT1177, a beta-sulfonyl nitrile compound, safe in humans, inhibits the NLRP3 inflammasome and reverses the metabolic cost of inflammation. *Proc. Natl. Acad. Sci. U. S. A.* 115 (7), E1530–E1539. doi:10.1073/pnas.1716095115

Martinez-Godinez, M. A., Cruz-Domínguez, M. P., Jara, L. J., Domínguez-López, A., Jarillo-Luna, R. A., Vera-Lastra, O., et al. (2015). Expression of NLRP3 inflammasome, cytokines and vascular mediators in the skin of systemic sclerosis patients. *Isr. Med. Assoc. J.* 17 (1), 5–10.

Micheau, O., and Tschopp, J. (2003). Induction of TNF receptor I-mediated apoptosis via two sequential signaling complexes. *Cell* 114 (2), 181–190. doi:10.1016/s0092-8674(03)00521-x

Milman, N., Graudal, N., Loft, A., Mortensen, J., Larsen, J., and Baslund, B. (2012). Effect of the TNF-alpha inhibitor adalimumab in patients with recalcitrant sarcoidosis: A prospective observational study using FDG-PET. *Clin. Respir. J.* 6 (4), 238–247. doi:10.1111/j.1752-699X.2011.00276.x

Mistry, P., Reid, J., Pouliquen, I., McHugh, S., Abberley, L., DeWall, S., et al. (2014). Safety, tolerability, pharmacokinetics, and pharmacodynamics of single-dose antiinterleukin- 18 mAb GSK1070806 in healthy and obese subjects. *Int. J. Clin. Pharmacol. Ther.* 52 (10), 867–879. doi:10.5414/CP202087

Mohan, M. J., Seaton, T., Mitchell, J., Howe, A., Blackburn, K., Burkhart, W., et al. (2002). The tumor necrosis factor-alpha converting enzyme (TACE): A unique metalloproteinase with highly defined substrate selectivity. *Biochemistry* 41 (30), 9462–9469. doi:10.1021/bi0260132

Murdaca, G., Spanò, F., Contatore, M., Guastalla, A., and Puppo, F. (2014). Potential use of TNF-α inhibitors in systemic sclerosis. *Immunotherapy* 6 (3), 283–289. doi:10.2217/imt.13.173

Nakatani-Okuda, A., Ueda, H., Kashiwamura, S. I., Sekiyama, A., Kubota, A., Fujita, Y., et al. (2005). Protection against bleomycin-induced lung injury by IL-18 in mice. *Am. J. Physiology-Lung Cell. Mol. Physiology* 289 (2), L280–L287. doi:10.1152/ajplung.00380.2004

Oku, H., Shimizu, T., Kawabata, T., Nagira, M., Hikita, I., Ueyama, A., et al. (2008). Antifibrotic action of pirfenidone and prednisolone: different effects on pulmonary cytokines and growth factors in bleomycin-induced murine pulmonary fibrosis. *Eur. J. Pharmacol.* 590 (1), 400–408. doi:10.1016/j.ejphar.2008.06.046

Ortiz, L. A., Lasky, J., Hamilton, R. F., Jr, Holian, A., Hoyle, G. W., Banks, W., et al. (1998). Expression of TNF and the necessity of TNF receptors in bleomycin-induced lung injury in mice. *Exp. Lung Res.* 24 (6), 721–743. doi:10.3109/01902149809099592

Pantelidis, P., McGrath, D. S., Southcott, A. M., Black, C. M., and du Bois, R. M. (2001). Tumour necrosis factor-alpha production in fibrosing alveolitis is macrophage subset specific. *Respir. Res.* 2 (6), 365–372. doi:10.1186/rr87

Pehlivan, Y., Onat, A. M., Ceylan, N., Turkbeyler, I. H., Buyukhatipoglu, H., Comez, G., et al. (2012). Serum leptin, resistin and TNF-α levels in patients with systemic sclerosis: the role of adipokines in scleroderma. *Int. J. Rheumatic Dis.* 15 (4), 374–379. doi:10.1111/j.1756-185X.2012.01755.x

Perera, A. P., Fernando, R., Shinde, T., Gundamaraju, R., Southam, B., Sohal, S. S., et al. (2018). MCC950, a specific small molecule inhibitor of NLRP3 inflammasome attenuates colonic inflammation in spontaneous colitis mice. *Sci. Rep.* 8 (1), 8618. doi:10.1038/s41598-018-26775-w

Perez-Alvarez, R., Perez-de-Lis, M., Diaz-Lagares, C., Pego-Reigosa, J. M., Retamozo, S., Bove, A., et al. (2011). Interstitial lung disease induced or exacerbated by TNF-targeted therapies: analysis of 122 cases. *Semin. Arthritis Rheum.* 41 (2), 256–264. doi:10.1016/j.semarthrit.2010.11.002

Phan, S. H., and Kunkel, S. L. (1992). Lung cytokine production in bleomycin-induced pulmonary fibrosis. *Exp. Lung Res.* 18 (1), 29–43. doi:10.3109/01902149209020649

Piguet, P. F., Ribaux, C., Karpuz, V., Grau, G. E., and Kapanci, Y. (1993). Expression and localization of tumor necrosis factor-alpha and its mRNA in idiopathic pulmonary fibrosis. *Am. J. Pathol.* 143 (3), 651–655.

Primiano, M. J., Lefker, B. A., Bowman, M. R., Bree, A. G., Hubeau, C., Bonin, P. D., et al. (2016). Efficacy and pharmacology of the NLRP3 inflammasome inhibitor CP-456,773 (CRID3) in murine models of dermal and pulmonary inflammation. *J. Immunol.* 197 (6), 2421–2433. doi:10.4049/jimmunol.1600035

Rahaghi, F. F., Hsu, V. M., Kaner, R. J., Mayes, M. D., Rosas, I. O., Saggar, R., et al. (2023). Expert consensus on the management of systemic sclerosis-associated interstitial lung disease. *Respir. Res.* 24 (1), 6. doi:10.1186/s12931-022-02292-3

Redente, E. F., Keith, R. C., Janssen, W., Henson, P. M., Ortiz, L. A., Downey, G. P., et al. (2014). Tumor necrosis factor-alpha accelerates the resolution of established pulmonary fibrosis in mice by targeting profibrotic lung macrophages. *Am. J. Respir. Cell Mol. Biol.* 50 (4), 825–837. doi:10.1165/rcmb.2013-0386OC

Ridker, P. M., Everett, B. M., Thuren, T., MacFadyen, J. G., Chang, W. H., Ballantyne, C., et al. (2017a). Antiinflammatory therapy with canakinumab for atherosclerotic disease. *N. Engl. J. Med.* 377 (12), 1119–1131. doi:10.1056/nejmoa1707914

Ridker, P. M., Howard, C. P., Walter, V., Everett, B., Libby, P., Hensen, J., et al. (2012). Effects of interleukin-1β inhibition with canakinumab on hemoglobin A1c, lipids, C-reactive protein, interleukin-6, and fibrinogen: A phase IIb randomized, placebo-controlled trial. *Circulation* 126 (23), 2739–2748. doi:10.1161/CIRCULATIONAHA.112.122556

Ridker, P. M., MacFadyen, J. G., Thuren, T., Everett, B. M., Libby, P., Glynn, R. J., et al. (2017b). Effect of interleukin-1β inhibition with canakinumab on incident lung cancer in patients with atherosclerosis: exploratory results from a randomised, double-blind, placebo-controlled trial. *Lancet* 390 (10105), 1833–1842. doi:10.1016/S0140-6736(17)32247-X

Russell, E., Luk, F., Manocha, S., Ho, T., O'Connor, C., and Hussain, H. (2013). Long term follow-up of infliximab efficacy in pulmonary and extra-pulmonary sarcoidosis refractory to conventional therapy. *Semin. Arthritis Rheum.* 43 (1), 119–124. doi:10.1016/j.semarthrit.2012.10.008

Sanchez-Fernandez, A., Skouras, D. B., Dinarello, C. A., and López-Vales, R. (2019). OLT1177 (dapansutrile), a selective NLRP3 inflammasome inhibitor, ameliorates experimental autoimmune encephalomyelitis pathogenesis. *Front. Immunol.* 10, 2578. doi:10.3389/fimmu.2019.02578

Santarlasci, V., Cosmi, L., Maggi, L., Liotta, F., and Annunziato, F. (2013). IL-1 and T Helper immune responses. *Front. Immunol.* 4, 182. doi:10.3389/fimmu.2013.00182

Shi, J., Zhao, Y., Wang, K., Shi, X., Wang, Y., Huang, H., et al. (2015). Cleavage of GSDMD by inflammatory caspases determines pyroptotic cell death. *Nature* 526 (7575), 660–665. doi:10.1038/nature15514

Sime, P. J., Marr, R. A., Gauldie, D., Xing, Z., Hewlett, B. R., Graham, F. L., et al. (1998). Transfer of tumor necrosis factor-alpha to rat lung induces severe pulmonary inflammation and patchy interstitial fibrogenesis with induction of transforming growth factor-beta1 and myofibroblasts. *Am. J. Pathol.* 153 (3), 825–832. doi:10.1016/s0002-9440(10)65624-6

Sullivan, D. E., Ferris, M., Nguyen, H., Abboud, E., and Brody, A. R. (2009). TNF-alpha induces TGF-beta1 expression in lung fibroblasts at the transcriptional level via AP-1 activation. *J. Cell Mol. Med.* 13 (8), 1866–1876. doi:10.1111/j.1582-4934.2009.00647.x

Sullivan, D. E., Ferris, M., Pociask, D., and Brody, A. R. (2005). Tumor necrosis factor-alpha induces transforming growth factor-beta1 expression in lung fibroblasts through the extracellular signal-regulated kinase pathway. *Am. J. Respir. Cell Mol. Biol.* 32 (4), 342–349. doi:10.1165/rcmb.2004-0288OC

Swanson, K. V., Deng, M., and Ting, J. P. (2019). The NLRP3 inflammasome: molecular activation and regulation to therapeutics. *Nat. Rev. Immunol.* 19 (8), 477–489. doi:10.1038/s41577-019-0165-0

Sweiss, N. J., Noth, I., Mirsaeidi, M., Zhang, W., Naureckas, E. T., Hogarth, D. K., et al. (2014). Efficacy results of a 52-week trial of adalimumab in the treatment of refractory sarcoidosis. *Sarcoidosis Vasc. Diffuse Lung Dis.* 31 (1), 46–54.

Tamao, N., Ando, K., Kaneko, N., Takahashi, K., and Motojima, S. (2014). Potential risk of TNF inhibitors on the progression of interstitial lung disease in patients with rheumatoid arthritis. *BMJ Open* 4 (8), e005615. doi:10.1136/bmjopen-2014-005615

Tapia-Abellan, A., Angosto-Bazarra, D., Martínez-Banaclocha, H., de Torre-Minguela, C., Cerón-Carrasco, J. P., Pérez-Sánchez, H., et al. (2019). MCC950 closes the active conformation of NLRP3 to an inactive state. *Nat. Chem. Biol.* 15 (6), 560–564. doi:10.1038/s41589-019-0278-6

Taroni, J. N., Greene, C. S., Martyanov, V., Wood, T. A., Christmann, R. B., Farber, H. W., et al. (2017). A novel multi-network approach reveals tissue-specific cellular modulators of fibrosis in systemic sclerosis. *Genome Med.* 9 (1), 27. doi:10.1186/s13073-017-0417-1

Tengstrand, B., Ernestam, S., Engvall, I. L., Rydvald, Y., and Hafström, I. (2005). TNF blockade in rheumatoid arthritis can cause severe fibrosing alveolitis. Six case reports. *Lakartidningen.* 102(49): p. 3788–3790.

Utz, J. P., Limper, A. H., Kalra, S., Specks, U., Scott, J. P., Vuk-Pavlovic, Z., et al. (2003). Etanercept for the treatment of stage II and III progressive pulmonary sarcoidosis. *Chest* 124 (1), 177–185. doi:10.1378/chest.124.1.177

Valenzi, E., Bulik, M., Tabib, T., Morse, C., Sembrat, J., Trejo Bittar, H., et al. (2019). Single-cell analysis reveals fibroblast heterogeneity and myofibroblasts in systemic sclerosis-associated interstitial lung disease. *Ann. Rheum. Dis.* 78 (10), 1379–1387. doi:10.1136/annrheumdis-2018-214865

van der Heijden, T., Kritikou, E., Venema, W., van Duijn, J., van Santbrink, P. J., Slütter, B., et al. (2017). NLRP3 inflammasome inhibition by MCC950 reduces atherosclerotic lesion development in apolipoprotein E-deficient mice-brief report. *Arterioscler. Thromb. Vasc. Biol.* 37 (8), 1457–1461. doi:10.1161/ATVBAHA.117.309575

Van Gorp, H., Van Opdenbosch, N., and Lamkanfi, M. (2019). Inflammasome-dependent cytokines at the crossroads of health and autoinflammatory disease. *Cold Spring Harb. Perspect. Biol.* 11 (1), a028563. doi:10.1101/cshperspect.a028563

van Hout, G. P., Bosch, L., Ellenbroek, G. H. J. M., de Haan, J. J., van Solinge, W. W., Cooper, M. A., et al. (2017). The selective NLRP3-inflammasome inhibitor MCC950 reduces infarct size and preserves cardiac function in a pig model of myocardial infarction. *Eur. Heart J.* 38 (11), 828–836. doi:10.1093/eurheartj/ehw247

Vande Walle, L., Stowe, I. B., Šácha, P., Lee, B. L., Demon, D., Fossoul, A., et al. (2019). MCC950/CRID3 potently targets the NACHT domain of wild-type NLRP3 but not disease-associated mutants for inflammasome inhibition. *PLoS Biol.* 17 (9), e3000354. doi:10.1371/journal.pbio.3000354

Vandenabeele, P., Declercq, W., Vanhaesebroeck, B., Grooten, J., and Fiers, W. (1995). Both TNF receptors are required for TNF-mediated induction of apoptosis in PC60 cells. *J. Immunol.* 154 (6), 2904–2913. doi:10.4049/jimmunol.154.6.2904

Volkmann, E. R., and Fischer, A. (2021). Update on morbidity and mortality in systemic sclerosis-related interstitial lung disease. *J. Scleroderma Relat. Disord.* 6 (1), 11–20. doi:10.1177/2397198320915042

Wang, L., Du, F., and Wang, X. (2008). TNF-alpha induces two distinct caspase-8 activation pathways. *Cell* 133 (4), 693–703. doi:10.1016/j.cell.2008.03.036

Warshamana, G. S., Corti, M., and Brody, A. R. (2001). TNF-Alpha, PDGF, and TGF-beta(1) expression by primary mouse bronchiolar-alveolar epithelial and mesenchymal cells: tnf-alpha induces TGF-beta(1). *Exp. Mol. Pathology* 71 (1), 13–33. doi:10.1006/exmp.2001.2376

Weng, S., Wang, L., Rong, Y., Liu, Y., Wang, X., Guan, H., et al. (2015). Effects of the interactions between dust exposure and genetic polymorphisms in Nalp3, caspase-1, and IL-1β on the risk of silicosis: A case-control study. *PLOS ONE* 10 (10), e0140952. doi:10.1371/journal.pone.0140952

Wohlford, G. F., Van Tassell, B. W., Billingsley, H. E., Kadariya, D., Canada, J. M., Carbone, S., et al. (2020). Phase 1B, randomized, double-blinded, dose escalation, single-center, repeat dose safety and pharmacodynamics study of the oral NLRP3 inhibitor dapansutrile in subjects with NYHA II-III systolic heart failure. *J. Cardiovasc Pharmacol.* 77 (1), 49–60. doi:10.1097/FJC.0000000000000931

Xu, D., Mu, R., and Wei, X. (2019). The roles of IL-1 family cytokines in the pathogenesis of systemic sclerosis. *Front. Immunol.* 10, 2025. doi:10.3389/fimmu.2019.02025

Yang, Y., Wang, H., Kouadir, M., Song, H., and Shi, F. (2019). Recent advances in the mechanisms of NLRP3 inflammasome activation and its inhibitors. *Cell Death Dis.* 10 (2), 128. doi:10.1038/s41419-019-1413-8

Yasuda, K., Nakanishi, K., and Tsutsui, H. (2019). Interleukin-18 in health and disease. *Int. J. Mol. Sci.* 20 (3), 649. doi:10.3390/ijms20030649

Zakrzewska, K., Arvia, R., Torcia, M. G., Clemente, A. M., Tanturli, M., Castronovo, G., et al. (2019). Effects of parvovirus B19 *in vitro* infection on monocytes from patients with systemic sclerosis: enhanced inflammatory pathways by caspase-1 activation and cytokine production. *J. Investigative Dermatology* 139 (10), 2125–2133. doi:10.1016/j.jid.2019.03.1144

frontiers | Frontiers in Genetics

TYPE Original Research
PUBLISHED 24 November 2023
DOI 10.3389/fgene.2023.1246983

Machine learning identified MDK score has prognostic value for idiopathic pulmonary fibrosis based on integrated bulk and single cell expression data

Shichen Zhang[1†], Lanlan Zhang[2†], Lu Wang[1], Hongqiu Wang[3], Jiaxin Wu[1], Haoyang Cai[1], Chunheng Mo[4*] and Jian Yang[1*]

[1]Center of Growth, Metabolism, and Aging, Key Laboratory of Bio-Resources and Eco-Environment, College of Life Sciences, Sichuan University, Chengdu, China, [2]State Key Laboratory of Respiratory Health and Multimorbidity, Department of Respiratory and Critical Care Medicine, West China Hospital, Sichuan University, Chengdu, China, [3]Systems Hub, The Hong Kong University of Science and Technology (Guangzhou), Guangzhou, China, [4]Key Laboratory of Birth Defects and Related Diseases of Women and Children of MOE, State Key Laboratory of Biotherapy, West China Second University Hospital, Sichuan University, Chengdu, China

OPEN ACCESS

EDITED BY
Ramani Ramchandran,
Medical College of Wisconsin,
United States

REVIEWED BY
Shanze Chen,
Jinan University, China
Jia-Hua Qu,
University of California, United States
Fengyan Meng,
Sichuan Agricultural University, China

*CORRESPONDENCE
Chunheng Mo,
✉ chunhengmo@gmail.com
Jian Yang,
✉ stardustcx@163.com

†These authors have contributed equally to this work

RECEIVED 25 June 2023
ACCEPTED 10 November 2023
PUBLISHED 24 November 2023

CITATION
Zhang S, Zhang L, Wang L, Wang H, Wu J, Cai H, Mo C and Yang J (2023), Machine learning identified MDK score has prognostic value for idiopathic pulmonary fibrosis based on integrated bulk and single cell expression data.
Front. Genet. 14:1246983.
doi: 10.3389/fgene.2023.1246983

Idiopathic pulmonary fibrosis (IPF) is a progressive and fatal lung disease that poses a significant challenge to medical professionals due to its increasing incidence and prevalence coupled with the limited understanding of its underlying molecular mechanisms. In this study, we employed a novel approach by integrating five expression datasets from bulk tissue with single-cell datasets; they underwent pseudotime trajectory analysis, switch gene selection, and cell communication analysis. Utilizing the prognostic information derived from the GSE47460 dataset, we identified 22 differentially expressed switch genes that were correlated with clinical indicators as important genes. Among these genes, we found that the midkine (MDK) gene has the potential to serve as a marker of Idiopathic pulmonary fibrosis because its cellular communicating genes are differentially expressed in the epithelial cells. We then utilized midkine and its cellular communication-related genes to calculate the midkine score. Machine learning models were further constructed through midkine and related genes to predict Idiopathic pulmonary fibrosis disease through the bulk gene expression datasets. The midkine score demonstrated a correlation with clinical indexes, and the machine learning model achieved an AUC of 0.94 and 0.86 in the Idiopathic pulmonary fibrosis classification task based on lung tissue samples and peripheral blood mononuclear cell samples, respectively. Our findings offer valuable insights into the pathogenesis of Idiopathic pulmonary fibrosis, providing new therapeutic directions and target genes for further investigation.

KEYWORDS

idiopathic pulmonary fibrosis, machine learning, midkine, single cell sequencing, integrated analysis

1 Introduction

Idiopathic pulmonary fibrosis (IPF) is a chronic and progressive lung disease characterized by the accumulation of scar tissue in the lungs, leading to difficulty breathing and chronic respiratory failure (Martinez et al., 2017; Chanda et al., 2019). The disease primarily affects older adults and is associated with high mortality rates, with a median survival of 3–5 years if untreated. The exact cause of IPF is not yet fully understood, though it is believed to be a result of a combination of genetic susceptibility and environmental exposures such as smoking, air pollution, and viral infections (Martinez et al., 2017). Currently, treatment options for IPF are limited, and there is still much to discover about its underlying mechanisms and potential therapeutic targets.

Some studies have focused on several key pathways involved in IPF pathogenesis, including epithelial-mesenchymal transition (EMT) and extracellular matrix (ECM) dysregulation (Chanda et al., 2019; Peng et al., 2020). In response to environmental triggers, immune cells such as macrophages and T cells are activated, leading to the release of pro-inflammatory cytokines and chemokines (Lee et al., 2021; Tanner et al., 2023). This activation results in the recruitment and activation of fibroblasts, which contribute to excessive ECM deposition and scarring in the lungs. EMT is a process in which epithelial cells lose their characteristic properties and acquire mesenchymal characteristics, enabling them to migrate and differentiate into other cell types. In IPF, EMT contributes to the accumulation of activated fibroblasts and myofibroblasts, which play a major role in ECM remodeling and fibrosis. ECM dysregulation is a hallmark of IPF and is characterized by excessive deposition and remodeling of ECM proteins such as collagen, fibronectin, and elastin. Understanding the complex interactions between these pathways and identifying potential therapeutic targets are major areas of focus in current IPF research (Martinez et al., 2017; Chanda et al., 2019).

The single-cell technique is a high-throughput analytical technique that enables gene expression profiling of individual cells, allowing for the detection of subtypes and functional differences between different cells, identification of rare cell types, and discovery of disease-related key genes and pathways at the cellular level (Sklavenitis-Pistofidis et al., 2021). Moreover, single-cell studies have also made significant contributions to the understanding of the pathogenesis of IPF. For instance, Morse et al. revealed an increase in fibroblasts, basal cells, ciliated cells, and club cells in IPF. They also identified macrophages expressing high levels of SPP1 and MERTK, which contribute significantly to lung fibrosis (Morse et al., 2019). Adams et al. discovered a unique basal cell population in IPF that expresses markers associated with basal cells, epithelial cells, mesenchymal cells, aging, and development. These findings suggest that the appearance of this cell population may be related to EMT in IPF patients (Peng et al., 2020). Additionally, Kobayashi et al. focused on the pre-alveolar type-1 transitional cell state (PATS) and found that markers of stratifin (*SFN*), tumor protein p63 (*TP63*), keratin 17 (*KRT17*), and *TP63* are co-expressed with collagen type I alpha 1 chain (*COL1A1*) in highly fibrotic cells, resulting in an aberrant elongated shape of the PATS cells (Kobayashi et al., 2020). Despite the progress made in understanding IPF through these studies, the specific pathogenesis of IPF, as well as the underlying causes of EMT and ECM formation in IPF, remain unclear and require further investigation.

In this study, we integrated five bulk gene expressing datasets and performed a comprehensive analysis with single-cell RNA sequencing (scRNA-seq) data results. We identified several differentially expressed genes that have clinical relevance and provided new insights into pathogenic factors, such as ECM and EMT, that are involved in IPF. Specifically, we constructed an SVM classifier for the MDK gene and related communication genes, achieving high accuracy in both lung tissue and peripheral blood sequencing datasets. These findings offer new directions for future research into the pathogenesis of IPF.

2 Results

2.1 Integrated bulk gene expression datasets identified consistently differentially expressed genes

Following acquisition of the bulk gene expression datasets, we conducted an analysis and identified a total of 1215 differentially expressed genes (DEGs). Among these DEGs, 745 were upregulated in more than two datasets, and 23 genes were consistently upregulated in all five datasets (Figure 1A, Supplementary Figure S1). Notably, the upregulated genes, such as *MDK*, tetraspanin 1 (*TSPAN1*), *COL1A1*, and collagen type I alpha 2 chain (*COL1A2*), were found to be enriched in extracellular matrix-related pathways, cytokines and cytokine receptor pathways, and collagen binding pathways (Supplementary Figures S1A, S1B). On the other hand, the downregulated genes were primarily enriched in G protein-coupled receptor (GPCR) signaling and cytokine binding (Supplementary Figures S1C, S1D).

To elucidate the interplay among the DEGs and provide insight into their biological functions in IPF, we conducted protein–protein interaction (PPI) network analysis using the STRING database, which enabled identification of subnetworks. Notably, we identified a subnet consisting of the *COL1A1* and *COL1A2* genes, which showed significant enrichment in extracellular matrix (ECM)-related pathways (Figure 1B), predominantly comprising upregulated genes. This finding corroborated previous research, highlighting the pivotal role of ECM in IPF pathogenesis (Figure 1C).

2.2 Single-cell atlas of IPF lung tissues reveals the roles of different cell types in IPF

During the single-cell RNA sequencing (scRNA-seq) process, we initially selected IPF and normal samples from the GSE135893 dataset, specifically targeting IPF and normal control samples. We excluded samples diagnosed with interstitial lung disease (ILD) from the dataset (Habermann et al., 2020a). After discarding empty droplets, doublet cells, and dead cells, we ultimately identified a total of 54,151 cells from 12 IPF samples and 29,601 cells from 10 normal samples. We annotated these cells as belonging to four primary groups based on the marker genes and unsupervised clustering: fibroblasts, endothelial cells, epithelial cells, and immune cells (Figure 2A). Subsequently, each primary group

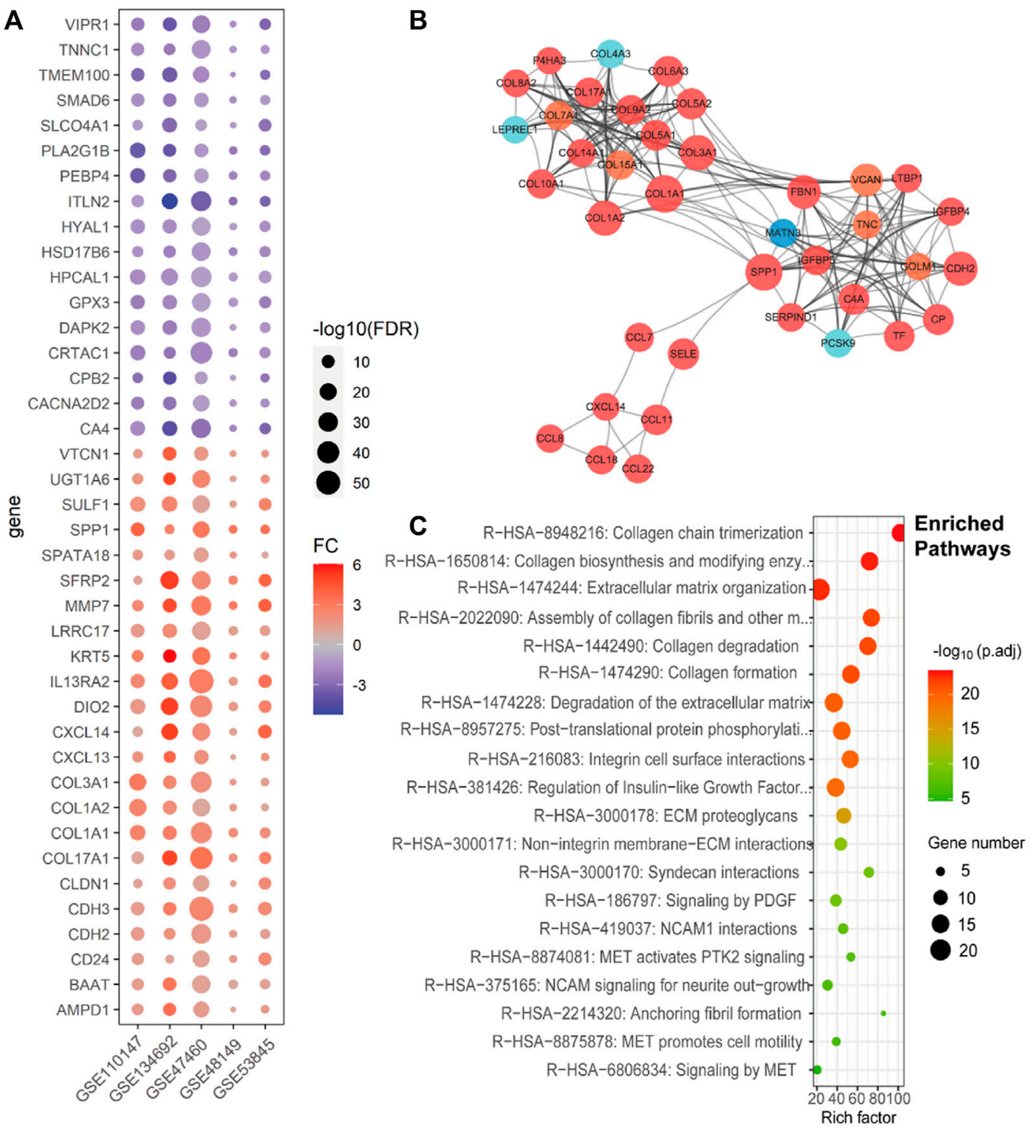

FIGURE 1
Consistent differentially expressed genes from bulk gene expression datasets, their subnetwork, and enriched pathways of IPF. **(A)**. Dot plot shows the fold change and *p*-values of consistent DEGs in all five lung tissue bulk gene expression datasets (GSE110147, GSE134692, GSE47460, GSE48149, and GSE53845). **(B)**. The sub-network from the protein−protein interactions network (PPI network), which includes the genes related to ECM of the IPF, with the red ones representing high expression in IPF, orange ones representing both high expression and being clinically related in IPF, light blue ones representing low expression in IPF, and deep blue one representing both low expression and being clinically related in IPF. **(C)**. The Reactomes enrich pathways related to the subnet of Figure 1B.

was further divided into specific cell types, including 16 types of immune cells, 4 types of endothelial cells, 7 types of epithelial cells, and 7 types of fibroblasts (Figures 2B, C).

We further performed cell proportion analysis, pseudotime analysis, switch gene selection, and cell communication analysis on the primary cell types. For immune cells, we identified 124 downregulated and 182 upregulated DEGs (Supplementary Table S2), with a subset of 8 downregulated and 12 upregulated DEGs observed in the bulk gene expression data. Similarly, for endothelial cells, we detected 327 downregulated and 270 upregulated DEGs (Supplementary Table S2), among which 79 downregulated and 14 upregulated DEGs were also identified in the bulk gene expression data.

Within fibroblasts, we identified 334 downregulated DEGs and 569 upregulated DEGs (Supplementary Table S2), with 24 downregulated and 68 upregulated DEGs overlapping with the DEGs from bulk gene expression data. The proportion of fibroblasts has increased from 2% in the control group to 5% in the IPF group (Figure 2D). Notably, a subgroup of fibroblast exhibiting high expression of gene markers for both myofibroblasts [*COL1A1*, actin alpha 2, smooth muscle (*ACTA2*)] and lipofibroblasts [*COL1A1*, perilipin 2 (*PLIN2*)] was identified and classified as *PLIN2*$^{+}$ myofibroblasts (Figures 2B,C; Figure 3A). Most of the myofibroblasts and lipofibroblasts were derived from IPF patients (Figure 3B, Supplementary Figure S5F). We analyzed the pseudotime trajectory from the lipofibroblasts to myofibroblasts in IPF (Figures 3C,D), and

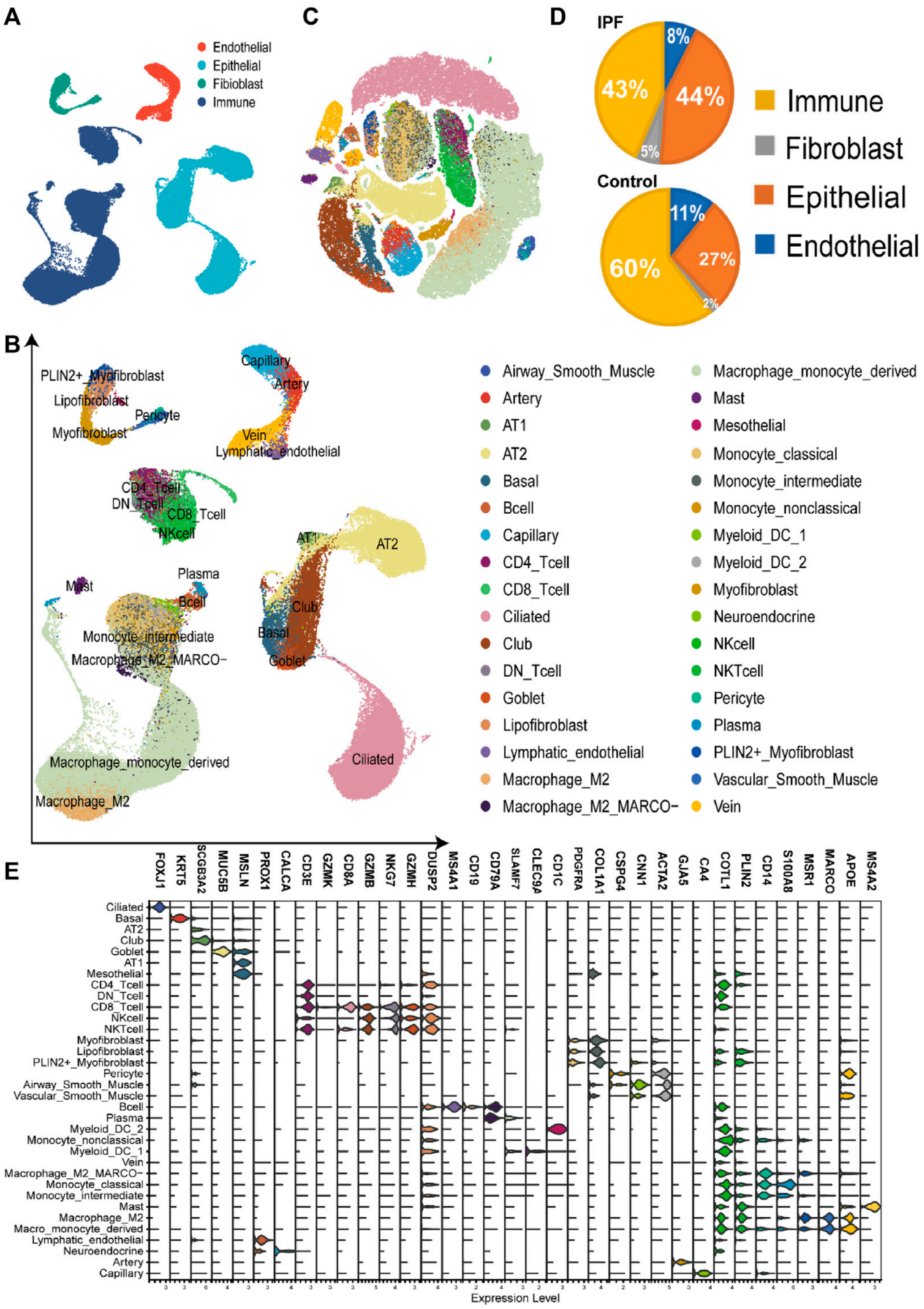

FIGURE 2
Construction of single-cell RNA-seq atlas of the lung tissue from IPF **(A)**. The UMAP plot of four main cell types in single-cell sequencing data, including endothelial cells, immune cells, epithelial cells, and fibroblasts. **(B)**. The UMAP plot of the single-cell sequencing data, including 83752 cells of 34 cell types from the lung tissue. **(C)**. The TSNE plot with the label of different cell types, which have the same label as Figure 2B. **(D)**. The cell proportion of four main types in different groups, revealing the high proportion of fibroblasts and epithelial cells in the IPF group. **(E)**. The volcano plot of the cell markers in different types of cells in the single-cell sequencing data.

identified 17 transcription factors and 34 surface proteins, many of which were related to ECM pathways (Supplementary Figure S3, Figure 3E). Additionally, cell communication analysis revealed strong communication in ECM-related pathways, particularly in collagen signaling (Figure 3F), which are critical components of ECM, and has been implicated in IPF (Chanda et al., 2019; Hamanaka et al., 2019).

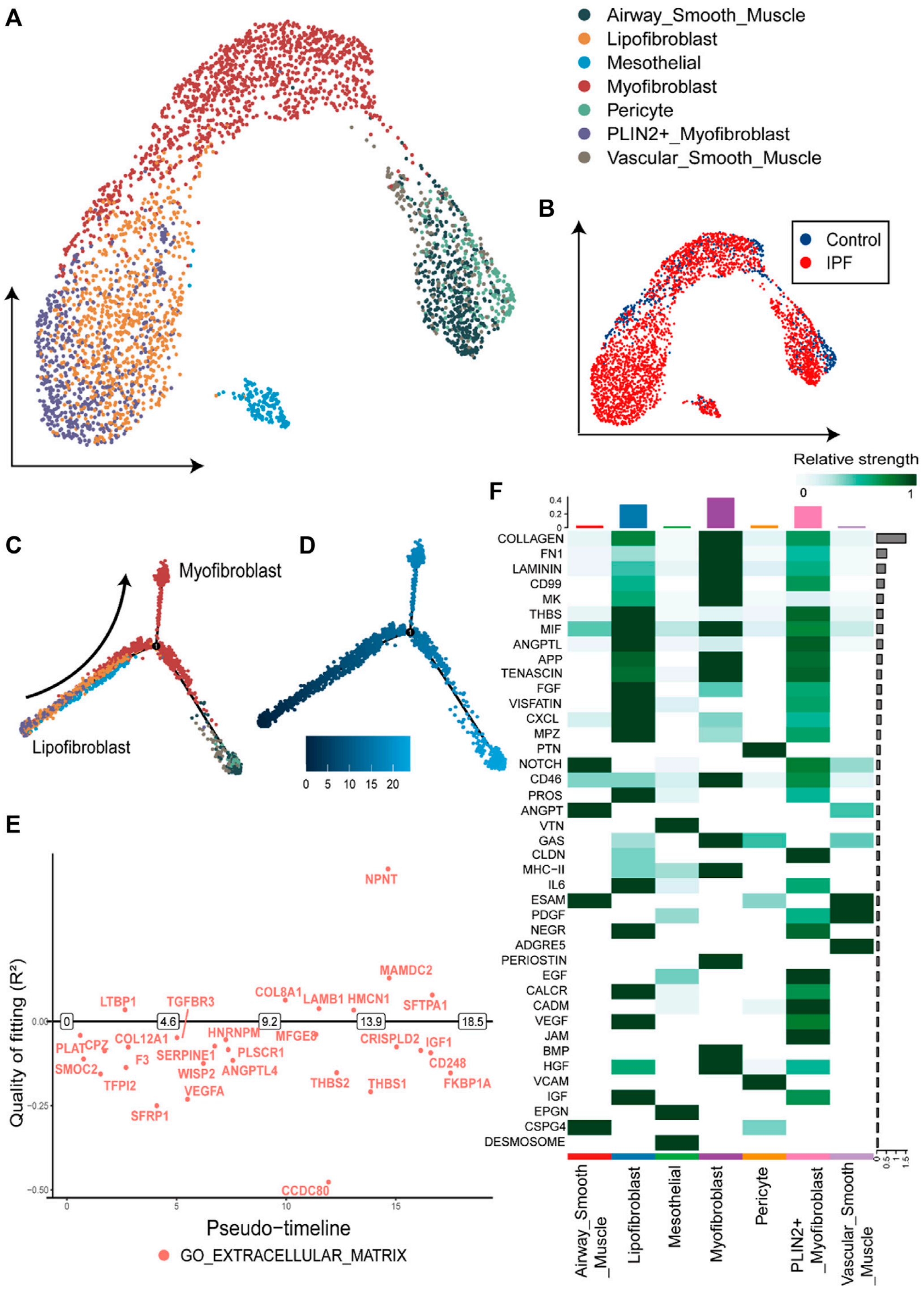

FIGURE 3
Overview and pseudotime results of fibroblasts from single-cell RNA-seq dataset **(A)**. The UMAP plot of the fibroblasts in single cell sequencing data, containing seven subtypes of fibroblasts. **(B)**. The UMAP plot with the labels of different groups, with the blue representing the control group and red the IPF group. **(C)**. Pseudotime trajectory plot of fibroblast calculated by monocle2. The trace from left to right reveals the trace from lipofibroblasts to myofibroblasts. **(D)**. The pseudotime of the cell development trajectory plot in Figure 3C. **(E)**. The switch DEGs of the GO: extracellular matrix pathway in the trace from lipofibroblasts to myofibroblasts. **(F)**. The strength of the cell-to-cell communication pathways in fibroblasts from the IPF group. The collagen-related communication shows the strongest communication.

The most significant difference between IPF and control groups was found in the epithelial cells. There were 107 downregulated DEGs and 163 upregulated DEGs identified in both the single-cell dataset and bulk gene expression (Supplementary Table S1 and Supplementary Table S2). The proportion of the epithelial cells in IPF patients was higher (44%) compared to the control group (27%)

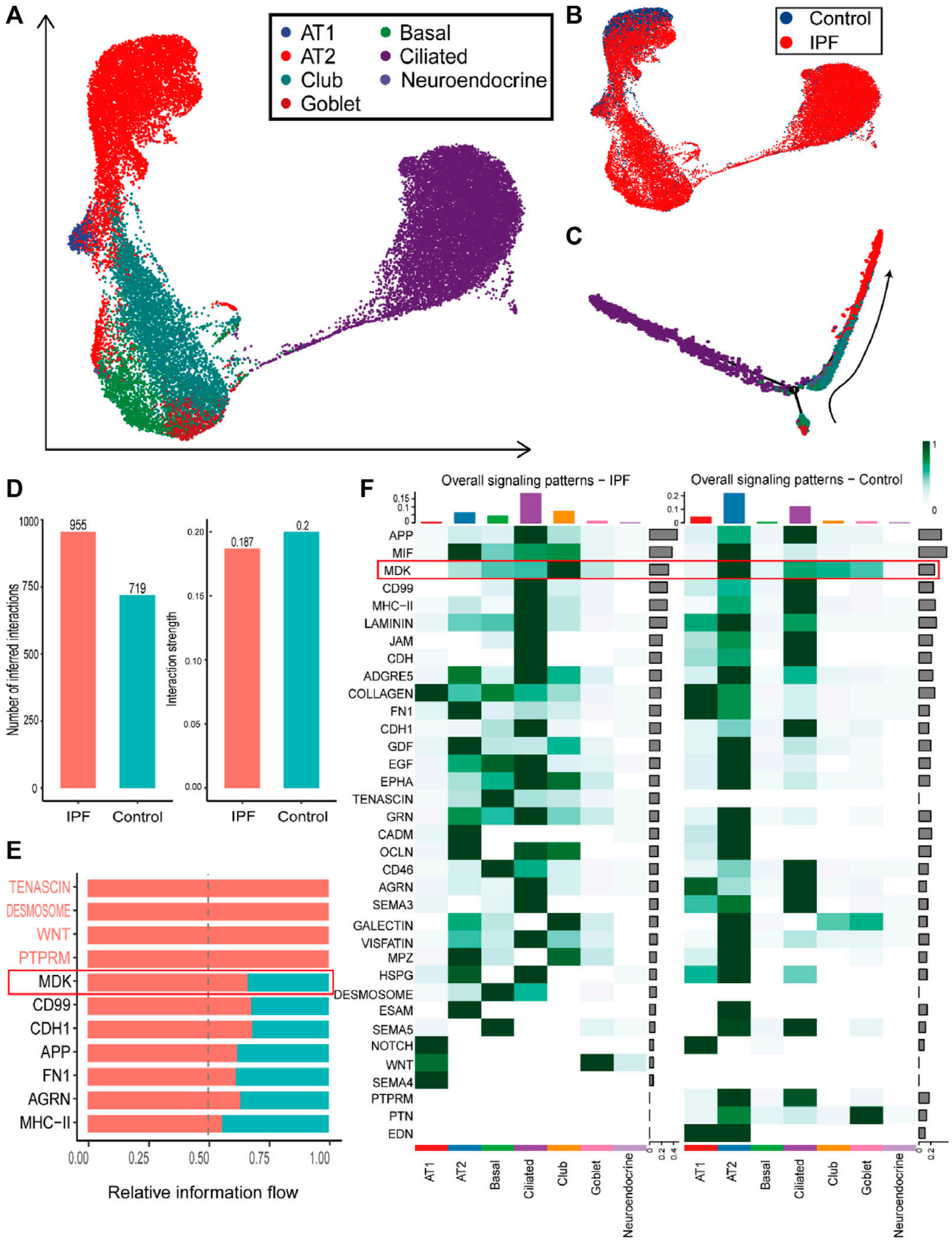

FIGURE 4
Overview and communication results of epithelial cells from single-cell RNA-seq dataset **(A)**. UMAP plot of the epithelial cells in single-cell sequencing data containing seven subtypes of epithelial cells. **(B)**. UMAP plot with the labels of different groups of epithelial cells, with blue representing the control group and red the IPF group. **(C)**. Pseudotime trajectory plot of epithelial cells calculated by monocle2. The trace from beneath to right up reveals the trace from basal cells to AT2 and AT1 cells. **(D)**. The number of inferred cell-to-cell interactions (left) and the interaction strength (right) in epithelial cells. **(E)**. The upregulated pathways in the communication of epithelial cells from the IPF group. **(F)**. The comparison of overall signaling patterns in the IPF and control groups of epithelial cells.

(Figure 2D, Supplementary Figure S5G). Specifically, epithelial cells from IPF samples were predominantly ciliated and club cells, while normal epithelial cells were primarily composed of alveolar type 2 progenitor (AT2) cells (Figures 4A, B). To gain a better understanding of the transition of epithelial cells, we analyzed the pseudotime trajectory from basal cells to AT2 cells and identified switch genes in this trace from control and IPF groups (Figure 4C). In the IPF group, a total of 1241 genes were identified as switch genes. Among these genes, there were 83 differentially expressed genes with absolute log2 fold change (|log2FC|) > 0.58. Additionally, we found 87 surface proteins, including MDK, *TSPAN1*, and serpin family F member 1 (*SERPINF1*), as well as

37 transcription factors, such as nuclear receptor 4A 1 (*NR4A1*) (Supplementary Table S3). In the control group, 1198 genes were identified as switch genes, including 74 differentially expressed genes, 79 surface proteins (including *MDK*, TIMP metallopeptidase inhibitor 1 (*TIMP1*), and *TSPAN1*), and 39 transcription factors (including *NR4A1*) (Supplementary Table S3). Among these genes, 28 were identified as distinct switch genes between IPF and control groups, with 8 exhibiting differential expression. For the common switch genes, by intersecting with DEGs in bulk gene expression datasets and single cell datasets, specific genes such as *MDK* and *TSPAN1* are highlighted.

Furthermore, cell communication analysis revealed more interactions and similar strengths in the IPF group compared to the control group (Figure 4D). In particular, cell communication that was more expressed in IPF epithelial cells was mainly concentrated in MDK, CD99, and other pathways (Figure 4E). Besides, ECM-related cell communication was found to be increased in basal cells and ciliated cells but decreased in AT2 and AT1 cells (Figure 4F). Notably, we identified a potentially important gene, *MDK*, based on multiple lines of evidence. Firstly, the expression of the *MDK* gene was found to be upregulated in both bulk datasets and epithelial cells. Secondly, MDK was identified as a switch gene in both the IPF and Control groups. Thirdly, MDK-related communication pathway genes showed differential expression between the IPF and Control group. The related midkine pathway also exhibited significant differences between the IPF and control groups (Figure 4F), suggesting that MDK plays a major role in the progression of IPF. These findings provide novel insights into the underlying mechanisms of IPF pathogenesis and offer potential targets for therapeutic intervention.

2.3 Clinical indexes correlation analysis in GSE47460 identified the clinically related genes of IPF

To evaluate the clinical relevance of the differentially expressed genes and switch genes, we analyzed the dataset GSE47460. We calculated the Pearson's correlation coefficient (PCC) between gene expression data and various clinical indicators, such as pre- and post-bronchodilator Forced Expiratory Volume (FEV1), pre- and post-bronchodilator Forced Vital Capacity (FVC), and diffusing capacity of the lungs for carbon monoxide (DLCO). Among the differentially expressed genes identified from five lung tissue gene expression datasets, we found 143 genes that showed moderate correlation with clinical indicators, including 79 upregulated genes and 64 downregulated genes ($|PCC| > 0.4$). Specifically, upregulated genes were negatively correlated with clinical indicators, whereas downregulated genes showed the opposite trend (Supplementary Figure S4). Additionally, enriched pathway analysis revealed that the upregulated genes associated with clinical relevance were primarily involved in ECM and GPCR binding-related pathways (Supplementary Table S2). These findings provide valuable insights into the link between gene expression and clinical indicators in IPF patients.

In order to further screen the related genes of IPF disease, we defined the genes satisfying the following conditions as important genes: 1. DEGs obtained from bulk gene expression datasets, 2. DEGs of different cell types from single-cell sequencing, 3. switch genes in main cell types, and 4. genes related to clinical indicators. This led to the identification of 22 genes (Supplementary Table S5). Among these genes, caveolin 1 (*CAV1*), insulin-like growth factor (*IGF1*), and *TSPAN1* have previously been reported as potential markers of IPF (Lin et al., 2019; Liu et al., 2019; Hernandez et al., 2020). For other genes, glutathione peroxidase 3 (*GPX3*) was identified as a switch gene in both endothelial and immune cells and as a DEG in all five gene expression datasets. Furthermore, the *MDK* gene, as previously mentioned, may play an important role in the development of IPF in epithelial cells through the MDK-related pathway and the MDK-TSPAN1 ligand-receptor pair.

2.4 Regulation of *MDK* genes in epithelial and endothelial cells of IPF

Through integrative analysis of bulk gene expression and single-cell RNA sequencing data, we identified MDK as an important gene in IPF. MDK was upregulated in three gene expression datasets, similar to TSPAN1 expression, which is another important gene and composed ligand-receptor pair with MDK. Both MDK and TSPAN1 were significantly correlated with clinical indicators. Specifically, MDK expression showed a negative correlation with FEV indices and DLCO index (post-bronchodilator FEV: coefficient = −0.47; pre-bronchodilator FEV: coefficient = −0.4; DLCO: coefficient = −0.32), while TSPAN1 was negatively correlated with the DLCO index (coefficient = −0.45) (Figure 5A). Moreover, MDK was highly expressed in both endothelial and epithelial cells in the single-cell RNA sequencing data, whereas TSPAN1 exhibited high expression specifically in epithelial cells (Figure 5B). Furthermore, MDK was identified as a switch gene in the cell trajectory analysis from basal cells to AT2 cells in both IPF and control groups together with TSPAN1 (Supplementary Table S3).

Through cell communication analysis, we observed that the MDK gene exhibited a high degree of communication with club cells and ciliated cells in IPF group. In contrast, AT2 cells showed increased communication in the control group (Figure 5C, Supplementary Figure S3A). Specifically, in the IPF group, club cells were identified as the senders in the MDK communication pathway, with ciliated cells and club cells acting as the main receivers. Other cells, including AT2 cells and basal cells, acted as mediators and influencers in the communication process (Figure 5D). In contrast, in addition to club cells, the senders in the control group were also comprised of ciliated cells and goblet cells, with only AT2 cells serving as the receivers (Figure 5D). Other cells, such as basal cells, club cells, and ciliated cells, were relatively reduced in the MDK signaling pathway network. These findings highlight the complex interactions involved in MDK-mediated cell communication in the context of IPF.

To elucidate the mechanisms underlying the transition of ciliated cells from senders to receivers in the IPF group, we conducted an analysis of the ligand-receptor pairs in the IPF and control groups. The results revealed that MDK-nucleolin (NCL), MDK- syndecan 1 (SDC1), MDK-SDC2, and MDK-SDC4 were involved in signaling from ciliated cells to AT2 cells in the control group, while no such signal was detected in the IPF group. Moreover, the ligand-receptor pairs MDK-NCL and MDK-SDC4 were involved in signaling from

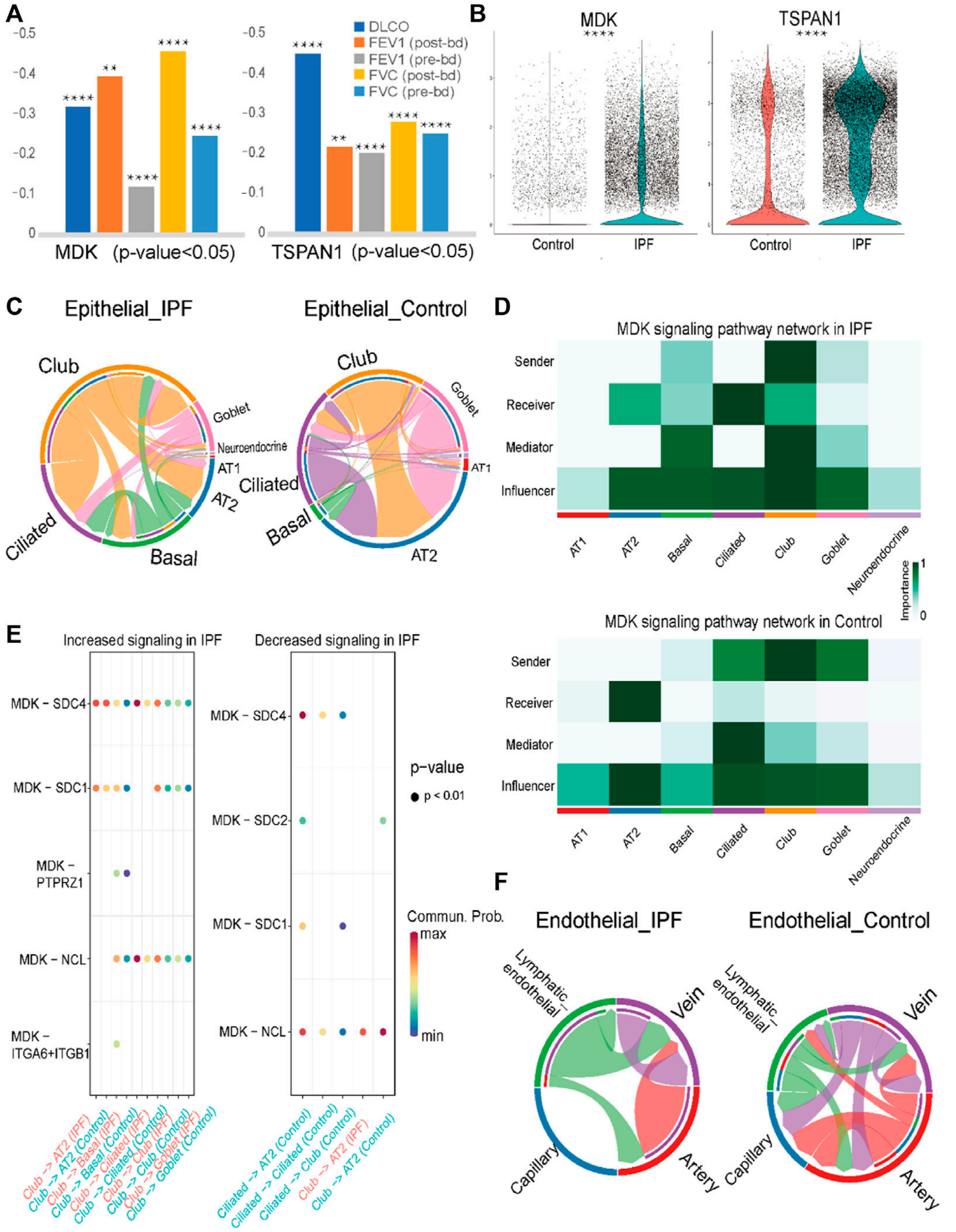

FIGURE 5
Analysis results of MK signaling pathway and prediction result of lung tissue datasets **(A)**. Pearson coefficient of MDK and TSPAN1 gene in five clinical indexes in GSE47460. **(B)**. Violin plot of MDK and TSPAN1 in the epithelial cells, with the red representing the control group and the blue representing the IPF group. **(C)**. Chord chart of cell-to-cell communication of the MK signaling pathway in epithelial cells, with the left one being IPF and the right one the control group. **(D)**. The MK signaling pathway network in the epithelial cells, with the upper one being the IPF group and the lower one being the control group. **(E)**. The bubble plot of increasing and decreasing signaling ligand–receptor pairs in IPF, with high communication of club cells being seen in IPF and low communication in AT2 cells in IPF. **(F)**. Chord chart of MK signaling pathway network in endothelial cells. Statistical analysis was performed to verify the Pearson correlation, or the two-sample *t*-test was used for comparisons between two groups. $^{*}p < 0.05$, $^{**}p < 0.01$, $^{***}p < 0.001$, $^{****}p < 0.0001$.

ciliated cells to ciliated cells or club cells in the control group, whereas in the IPF group, MDK-SDC4 and MDK-NCL exhibited higher expression in basal cells, club cells, and goblet cells compared to ciliated cells. These findings may be related to the abnormal expression patterns observed in the epithelial cells of IPF. Additionally, other differences in cell communication were mainly observed between club and AT2 cells (Figure 5E).

In addition to its role in epithelial cells, MDK has also been identified as a DEG in endothelial cells, prompting us to conduct an analysis of its cellular communication. The results revealed that in IPF,

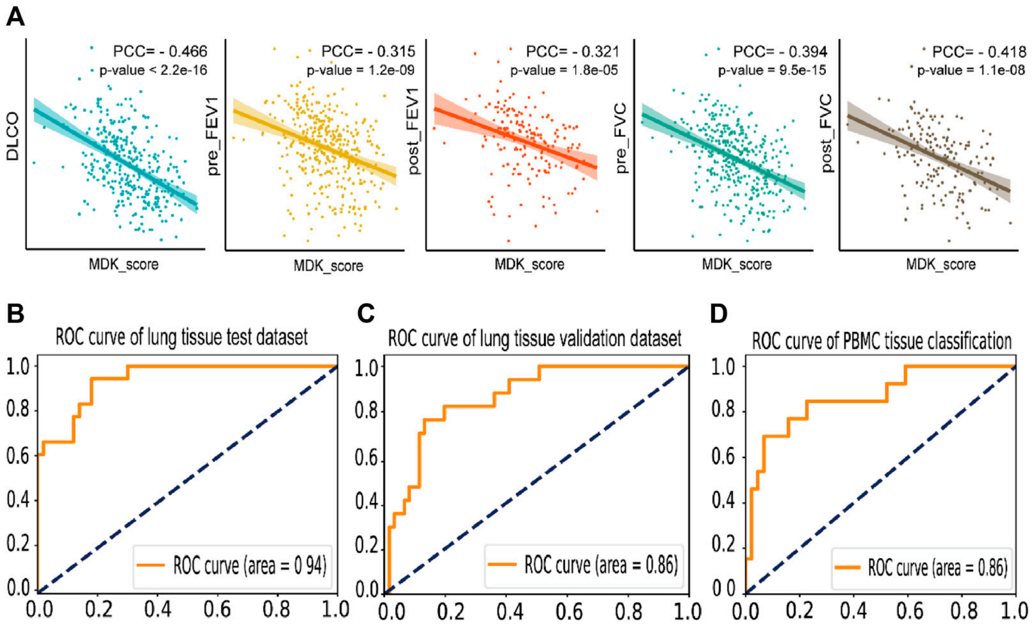

FIGURE 6
Prediction and correlation analysis result of MK score and MDK related genes **(A)**. Dot plot of the Pearson coefficient of MK score in five clinical indexes in GSE47460, labeling the value of the Pearson coefficient and the *p*-value of the result. **(B)**. The ROC curve of the IPF disease classification test dataset by SVM model based on the expression of MDK and related genes in lung tissue bulk gene expression data, with an AUC = 0.94. **(C)**. The ROC curve of the individual validation dataset of lung tissue by SVM based on the expression of MDK and related genes. **(D)**. The ROC curve of the IPF disease classification by SVM model based on the expression of MDK and related genes in PBMC bulk gene expression data, with an AUC = 0.86.

lymphatic endothelial cells and vein cells primarily functioned as senders, with vein cells acting as the main receivers. In contrast, in the control group, the role of lymphatic endothelial cells was diminished, and the communication was predominantly observed in the artery and capillary endothelial cells (Figure 5F, Supplementary Figure S3B, C). The ligand-receptor pairs involved in the MDK signaling pathway in endothelial cells are mainly comprised of MDK-NCL and MDK-[integrin subunit alpha 6 (ITGA6) + integrin subunit beta 1 (ITGB1)] (Supplementary Figure S3D). Taken together with the findings from our analysis of epithelial cells, these results highlight the differential expression pattern and cellular communication mechanisms of MDK and their potential implications for disease pathogenesis.

2.5 SVM models accurately classify the IPF using MDK and its communication genes in both lung tissue and PBMC datasets

In the previous section, we identified MDK as a crucial gene involved in the pathogenesis of IPF. The regulation of MDK is primarily mediated by two potential pathways: the MDK-TSPAN1 ligand–receptor pair and the MK signaling pathway in epithelial cells. We hypothesized that differences in the MK signaling pathway network in ciliated cells, club cells, and AT2 cells may play a critical role in the development of IPF. To investigate whether MDK and related receptors can serve as markers for IPF, we constructed a machine learning model utilizing gene expression data from both lung tissue and PBMC samples. Our aim is to examine the diagnostic potential of MDK and its associated genes in identifying patients with IPF.

In this analysis, we employed an approach to calculate the MDK score (referred to as MK score) in lung tissue by determining the mean expression levels of MDK-related genes. The set of MDK-related genes included MDK, TSPAN1, SDC1, SDC2, SDC4, protein tyrosine phosphatase receptor type Z1 (PTPRZ1), ITGA4, ITGA6, ITGB1, low-density lipoprotein receptor-related protein-1 (LRP1), NCL, and anaplastic lymphoma kinase (ALK). To explore the relationship between the MK score and clinical indicators, we utilized the GSE47460 dataset. Pearman's correlation analysis revealed a moderate correlation between the MK score and clinical indicators, which included −0.466 for DLCO, −0.315 and −0.321 for pre- and post-FEV1, and -0.394 and −0.418 for pre- and post-FVC (Figure 6A). These findings support the feasibility of employing MDK-related genes as potential markers of IPF.

Moreover, we employed machine learning techniques to develop predictive models for the identification of IPF using three lung tissue bulk gene expression datasets and three PBMC bulk gene expression datasets. Prior to model development, we conducted rigorous quality checks and performed necessary data preprocessing on the lung tissue datasets. We utilized 316 samples for training and testing purposes, with an 8:2 ratio, and selected 78 independent validation samples. Among the various models (support vector machine, Adaboost, and random forest) after five-fold cross-validation and grid search, the support vector machine (SVM) model exhibited the highest accuracy of 0.838 in the test dataset. Importantly, the independent validation dataset demonstrated an accuracy of 0.821. The AUC of 0.94 and 0.86 for test and validate datasets (Figures 6B, C). Regarding the PBMC datasets, we performed a random split of the samples into training (227 samples) and testing datasets (56 samples) with an 8:2 ratio. The SVM model yielded an AUC of 0.86, with precision rates of 0.857 for IPF patients and 0.6 for the control group (Figure 6D). These findings suggest that MDK may serve as a potential marker gene for IPF diagnosis, highlighting its significant role in the context of IPF.

3 Methods

3.1 Data acquisition

The datasets utilized in this study were obtained from the Gene Expression Omnibus (GEO, https://www.ncbi.nlm.nih.gov/geo/). The datasets included the GSE47460, GSE110147, GSE134692, GSE48149, and GSE53845 gene expression datasets from lung samples (DePianto et al., 2015; Anathy et al., 2018; Cecchini et al., 2018; Sivakumar et al., 2019; Renaud et al., 2020), GSE135893 single-cell RNA sequencing dataset from lung samples (Habermann et al., 2020b), and GSE132607, GSE28042, as well as GSE38958 (Herazo-Maya et al., 2013; Huang et al., 2014; 2021) gene expression datasets from PBMC samples. A total of 365 IPF lung samples and 155 normal lung tissue bulk gene expression data, 184 IPF and 99 normal PBMC bulk gene expression data, as well as 12 IPF lung and 10 normal lung single-cell RNA sequencing data, were analyzed. Further details regarding the dataset can be found in Supplementary Table S6.

3.2 The process of bulk gene expression datasets

For each bulk dataset of lung samples, we first checked the quality of samples by measuring the distribution of relative log expression (RLE). Assuming the majority of expressed genes are not differentially expressed, the RLE values should generally be centered around 0 and spread within a limited range (Gregory Alvord et al., 2007). As shown in Supplementary Figure S4, most of the samples have RLE centered around 0 and spread within a small range (Supplementary Figure S4A, S4B). Then we performed differential analysis using the limma package for expression chips or EdgeR package for bulk gene expression data by selecting genes with absolute log2 fold change (|log2FC|) >1 and adjusted $p < 0.05$ as the differentially expressed genes in each dataset (Ritchie et al., 2015; Zhu et al., 2021). We subsequently selected genes with consistently up- or downregulated in at least two datasets and no opposite differential expression in other datasets like DEGs. Using the clusterProfiler package (Yu et al., 2012), we conducted pathway enrichment analysis of GO (Carbon et al., 2021), KEGG (Kanehisa et al., 2021), and Reactome (Gillespie et al., 2022) for the differentially expressed genes, using adjusted *p*-value <0.05 as the screening criteria to obtain relevant gene pathways. Additionally, we carried out PPI analysis of the selected differentially expressed genes through the protein network interaction database STRING (https://string-db.org/), which was then imported into the cytoscape 3.7.2 software (Shannon et al., 2003) and identified key gene modules using the MCODE plug-in. We used the haircut method with a node score of 0.2 and selected nodes with a degree of more than 2, maximum depth of 100, and k-core of 2 to discover relevant gene clusters.

3.3 The process of single-cell RNA sequencing

3.3.1 Quality check

In this study, we utilized single-cell RNA sequencing analysis by R (version 3.6.0) and Seurat (version 4.0.1) (Stuart et al., 2019; Qiu et al., 2023). We first used emptyDrops method from Seurat to calculate and select FDR less than 0.1 as threshold to replace the empty droplets. After that, we used the PercentageFeatureSet function to calculate the proportion of mitochondrial genes in the cells and replaced the dead cells deciding by a mitochondrial genes proportion more than 25% combined with identifying RNA values of less than 1000 (Supplementary Figure S4C). For each sample, the top 2000 variable feature genes were selected by using the FindVariableFeatures function from 27674 genes in each cell. The repeatedly present variable genes were selected by using the SelectIntegrationFeatures function. Then, the samples were integrated using the FindIntegrationAnchors and IntegrateData functions. These integration steps can align cell populations from different batches to correct for technical differences between datasets. Then the integrated data for all cells were further processed using the ScaleData, RunPCA, and RunUMAP functions. Cells were finally clustered with the FindNeighbors and FindClusters functions. The cells are generally clustered by cell types and not by sample or disease status (Supplementary Figures S5A–D).

3.3.2 Cell annotation, double droplets removal, and DEG calling

To classify cells with high accuracy, we divided the cell annotation process into two steps. Firstly, cells are divided into four major kinds: immune cells (PTPRC+), stroma cells (PTPRC-, EPCAM-, PECAM1-), epithelial cells (EPCAM+), and endothelial cells (PECAM1+, CLDN5+, VWF+, CDH5+, NRP1+) (Supplementary Figure S5E). Then, for each major subtype cluster, we conducted the same preprocess steps as described above and extracted marker genes from the CellMarker2.0 database (Hu et al., 2023) and the classical published paper (Travaglini et al., 2020), which is constructing the cell atlas of human lungs to classify the specific cell clusters with affiliated verification from the SingleR package (Aran et al., 2019). Furthermore, to remove the cells expressing markers of different cell types, which is caused by the doublet cells, we used the DoubletFinder R package to calculate the possible multi-droplet and removed the doublet cells identified by the pk > 0.25 (McGinnis et al., 2019). For each cell type, we identified differentially expressed genes (DEGs) using the FindAllMarkers function from the Seurat package with the following settings: logfc.threshold = 0.25, min.pct = 0.1, only.pos = True and test.use = "wilcox".

3.3.3 Trajectory analysis and switch gene analysis

The R package monocle2 was used to perform pseudo-time-based cell trajectory analysis (Qiu et al., 2017) of four main types, separately. With the result of the cell trajectory analysis, switch genes were identified using R package GeneSwitches (Cao et al., 2020). The switch genes, which may influence cell differentiation and transformation, were further enriched by the GO and KEGG pathways by way of the find_switch_pathway function with default parameters to reflect the pathway expression in the pseudo-time.

3.3.4 Cell communication analysis

To analyze the cell-to-cell interactions in different major types, we used R package CellChat (Jin et al., 2021). The computeCommunProb function was used to identify related ligand-receptor pairs in the cell communication, while the computeCommunProbPathway function was used to calculate the expression of the pathways related to the cells. Besides, we used the compareInteractions function to find the disparity communication pathways and ligand-receptor pair in the IPF and control groups.

3.4 Filter DEGs related to clinical indexes

To investigate the genetic basis of clinical data in lung fibrosis, we obtained the GSE47460 dataset with clinical data and removed samples unrelated to lung fibrosis (Anathy et al., 2018). Using the prognostic data within this dataset, we selected DLCO, FEV1 pre/post, and FVC pre/post as prognostic indicators. We then conducted a Pearson's correlation analysis between genes (which includes MDK and TSPAN1) and clinical data. Differentially expressed genes of moderate correlation (>0.4) with at least one clinical criterion were treated as clinically relevant.

Additionally, we selected genes related to intercellular communication with MDK expression (MDK, SDC1, SDC2, SDC4, PTPRZ1, ITGA4, ITGA6, ITGB1, LRP1, NCL, ALK, TSPAN1) and calculated their average expression levels, resulting in a score named MK score. The MK score was also subjected to Pearson's correlation analysis with the prognostic indicators.

3.5 Machine learning model building to classify IPF with MDK-related genes

To evaluate the function of MDK-related communication genes in the IPF, we used bulk gene expression datasets GSE47460, GSE110147, and GSE48149 as the lung tissue group and bulk gene expression datasets GSE132607, GSE28042, and GSE38958 as the PBMC group to construct machine learning models separately. For GSE132607, we selected samples with the source name of "COMET-IPF_Baseline" to represent IPF patients. Quality control and preprocessing are performed for each dataset, and batch effects between different datasets are eliminated by the SVA package's Combat function (Leek et al., 2012). The scikit-learn python package is used in the model construction, cross-validation, and result visualization in this section.

To be specific, the GSE47460 has two sub-datasets sequenced by different platforms. The sub-dataset sequenced by GPL 14550 was selected as the validation dataset. We integrated the sub-dataset sequenced by GPL6480 and two other datasets (GSE110147 and GSE48149) to construct the training and test datasets by correcting the batch effect using the SVA package's Combat function (Leek et al., 2012). To train and testing the model, we randomly split the integrated datasets into a training part and test part with a ratio of 8:2. On the other hand, for the PBMC samples, we first integrated GSE132607, GSE28042, and GSE38958 datasets by correcting the batch effect using the SVA package's Combat function. Then the integrated dataset was randomly split into a training part and testing part with a ratio of 8:2. We selected random forest (RF), support vector machine (SVM), and AdaBoost algorithms as our testing models. We used the GridSearchCV function to select the best parameters of the model and set the 5-fold cross-validation during the training process.

4 Discussion

IPF is a chronic and progressive lung disease that predominantly affects the elderly population and is characterized by thickening and scarring of lung tissue, leading to difficulty breathing. Despite being associated with high mortality rates, its etiology remains unclear. However, recent advances in sequencing technology and single-cell sequencing provide new possibilities for comprehensively analyzing IPF pathogenesis. In light of these developments, this study endeavors to execute a multi-dimensional interrogation of assorted sequencing data modalities with the objective of pinpointing key genes implicated in IPF pathogenesis that exhibit a strong correlation with established clinical indices of pulmonary function.

To investigate IPF pathogenesis, we utilized five datasets of bulk gene expression data as well as one single-cell RNA-sequencing dataset for comprehensive analysis. Analysis of the bulk gene expression dataset revealed that upregulated genes were primarily enriched in the ECM and cytokine-cytokine related pathways, whereas downregulated genes were enriched in the regulation of G protein-coupled receptors. These pathways have been previously reported to be associated with IPF pathogenesis (Chanda et al., 2019). To further excavate the function behind the genes, we calculated the correlation coefficient of clinical indexes and process gene switch analysis. Among the final selected 22 important genes, we identified that the MDK gene has the potential to regulate certain physiological processes in the epithelial cell of IPF.

The MDK gene encodes the midkine protein associated with cell growth, migration, and angiogenesis, and it has been identified as a key regulator of epithelial and endothelial cells (Filippou et al., 2020). In endothelial cells, the MDK signaling pathway occurs separately in IPF for lymphoid endothelial cells as ligand cells and vein cells as receptors. The main differences were concentrated in epithelial cells, club cells, and ciliated cells in IPF, which accounted for the majority of MK signaling, while AT2 cells are major components of the control group. Coincidentally, the expression strength of the MDK signaling pathway matched the proportion of epithelial cells in both the IPF and control group. Additionally, switch gene analysis on the trajectory of AT2 cells indicated that MDK may be involved in the development of AT2 cells. Further research and analysis found that the pathway focused on communication with MDK as a ligand, with NCL, SDC1, and SDC4 acting as receptors. These genes have been shown to be involved in the EMT process.

EMT is critical factor considered to be involved in the pathogenesis of pulmonary fibrosis, leading to changes in the balance and communication between lung cell groups, and contributing to the development of IPF (Liu et al., 2019). Although there are some works that reveal the role of MDK in the EMT process, most of them are associated with physiological processes involved in organ formation during embryogenesis. In our study, by screening differentially expressed genes and analyzing their relation to prognostic indicators, we found that MDK regulates EMT processes by communicating with SDC1, SDC2, SDC4, NCL, and TSPAN1 in IPF patients. Notably, it was previously reported that the MDK gene has a certain effect on the TGFβ signaling pathway, which has the ability to induce the development of EMT, enabling epithelial cells to acquire a mesenchymal phenotype. In addition to MDK, genes related to cell communication have also been shown to affect the development of the TGFβ signaling pathway. Our results potentially suggested that extrabronchial secretory cells known as club cells may elicit TGFβ signaling by secreting MDK protein and binding to the ligand gene on AT2 cell surfaces. This stimulation leads to induce of EMT processes (Ichihashi et al., 2016; Liu et al., 2019; 2020; Thatikonda et al., 2023), thereby facilitating transformation of epithelial cells in IPF patients and contributing to the progression of pulmonary fibrosis.

In a noteworthy development, validation of the hypothesis was accomplished by demonstrating a correlation between MDK gene expression, the MK score computed utilizing these genes, and numerous clinical indicators. Furthermore, the IPF machine learning classification model exhibited high accuracy in both lung tissue samples (AUC = 0.94 for test dataset and AUC = 0.86 for validate dataset) and PBMC samples (AUC = 0.86). For comparative purposes, White employed logistic regression to uncover biomarkers in the blood of IPF patients, utilizing the OPN, SP-D, and MMP-7 genes for IPF patient prediction and achieving an AUC of 0.709 (White et al., 2016). Ley et al. reported an AUC of 0.76 using cCK18 to differentiate IPF from HP/NSIP (Ley et al., 2014). The elevated accuracy of the classification model in this investigation serves to bolster the evidence, supporting the substantial influence of MDK and its related communication in the pathogenesis of IPF.

Studies have shown that administration of bleomycin in mice has been shown to increase the expression of MDK in lung tissue, while the lung tissue of MDK gene knockout mice exhibited decreased expression of fibrosis markers such as collagen, α-SMA, TNF-α, and TGF-β. This suggests the importance of MDK in the inflammatory response and fibrosis process (Misa et al., 2017). Furthermore, studies by Horiba et al. (Horiba et al., 2000) have demonstrated that MDK can enhance the recruitment of inflammatory cells, which may be involved in promoting lung fibrosis. Zhang et al. (Zhang et al., 2015) have found that MDK plays a critical role in the mechanical stress-induced EMT spectrum in human lung epithelial cells. The absence of MDK weakened these EMT features. This indicates that MDK may promote lung fibrosis by interacting with Notch2 and activating angiotensin-converting enzyme (ACE) expression. Additionally, the research by Xu et al. (Xu et al., 2021) has revealed that inhibiting MDK can improve lung injury induced by sepsis through the ACE/Ang II pathway and the involvement of Notch 2. This further emphasizes the role of MDK and provides potential therapeutic value for MDK as a target. In summary, these studies suggest that MDK plays an important regulatory role in the pathogenesis of lung fibrosis, including promoting inflammation and extracellular matrix deposition, participating in epithelial-mesenchymal transition, and modulating ACE expression. Further research will help to elucidate the exact role and mechanisms of MDK in the development of IPF, providing new directions for future therapeutic strategies.

In addition, we noticed the myofibroblasts and lipofibroblasts mostly occur in the IPF group (Supplementary Figure S5F), where communication are related to the collagen of ECM. Previous studies have shown that the peptides and glycoproteins in the ECM stimulate fibroblast growth and activation, exacerbating the degree of lung fibrosis (Tian et al., 2019). In our study, fibroblasts increased ECM synthesis by raising collagen-related communication in myofibroblasts and lipofibroblasts by way of switch DEGs such as IGF1 and SFRP1 (Blackstock et al., 2014; Wang, 2020).

Despite the interesting and noteworthy findings, several limitations should be noticed. Firstly, although the machine learning model achieved notable improvement in identifying IPF samples, the model may be further improved with larger and more balanced datasets. Secondly, in our analysis, MDK and its receptors are important for IPF development. However, further functional experiments and mechanical studies would better resolve the relationship between MDK signaling and IPF. Additionally, it is worth noting that our original data lacked comprehensive information of factors such as gender, age, comorbidities, and clinical manifestations. Therefore, conducting further analysis that incorporates these variables would yield a more nuanced understanding of the association between MDK and IPF, particularly in different clinical contexts and human characteristics.

In summary, we employed a comprehensive analysis utilizing single-cell datasets and multiple bulk gene expression datasets to identify clinically relevant DEGs associated with IPF pathogenesis. We also incorporated a detailed examination of MDK gene regulation mechanisms and constructed a machine learning model to identify IPF patients based on both lung tissue and PBMC samples. Our study provides valuable insights for future investigations into the regulatory processes underlying IPF.

Data availability statement

The datasets presented in this study can be found in online repositories. The names of the repository/repositories and accession number(s) can be found in the article/Supplementary Material.

Author contributions

JY and CM conceived and designed this project. SZ, LZ, JY, and CM collected datasets and designed a bioinformatics analysis process. SZ, LW, JW, and JY analyzed the bulk and single-cell expression data. HW and SZ designed and constructed the machine learning model. JY, HC, and CM conceived and supervised the project. SZ, JY, HC, LZ, and CM wrote and revised the manuscript with input from all the authors. All authors contributed to the article and approved the submitted version.

Funding

This work was supported by the National Natural Science Foundation of China (32100441 and 82200084), Natural Science Foundation of Sichuan Province (2023NSFSC1456), Postdoctoral Science Foundation funded project of Sichuan Province (TB2023047), International Science and Technology Cooperation Project of Chengdu (2023-GH02-00092-HZ), the Fundamental Research Funds for the Central Universities, and Sichuan University postdoctoral interdisciplinary Innovation Fund (0020404153020).

Conflict of interest

The authors declare that the research was conducted in the absence of any commercial or financial relationships that could be construed as a potential conflict of interest.

Publisher's note

Supplementary material

The Supplementary Material for this article can be found online at: https://www.frontiersin.org/articles/10.3389/fgene.2023.1246983/full#supplementary-material

References

Anathy, V., Lahue, K. G., Chapman, D. G., Chia, S. B., Casey, D. T., Aboushousha, R., et al. (2018). Reducing protein oxidation reverses lung fibrosis. *Nat. Med.* 24, 1128–1135. doi:10.1038/s41591-018-0090-y

Aran, D., Looney, A. P., Liu, L., Wu, E., Fong, V., Hsu, A., et al. (2019). Reference-based analysis of lung single-cell sequencing reveals a transitional profibrotic macrophage. *Nat. Immunol.* 20, 163–172. doi:10.1038/s41590-018-0276-y

Blackstock, C. D., Higashi, Y., Sukhanov, S., Shai, S. Y., Stefanovic, B., Tabony, A. M., et al. (2014). Insulin-like growth factor-1 increases synthesis of collagen type I via induction of the mRNA-binding protein LARP6 expression and binding to the 5′ stem-loop of COL1a1 and COL1a2 mRNA. *J. Biol. Chem.* 289, 7264–7274. doi:10.1074/jbc.M113.518951

Cao, E. Y., Ouyang, J. F., and Rackham, O. J. L. (2020). GeneSwitches: ordering gene expression and functional events in single-cell experiments. *Bioinformatics* 36, 3273–3275. doi:10.1093/bioinformatics/btaa099

Carbon, S., Douglass, E., Good, B. M., Unni, D. R., Harris, N. L., Mungall, C. J., et al. (2021). The gene ontology resource: enriching a GOld mine. *Nucleic Acids Res.* 49, D325–D334. doi:10.1093/nar/gkaa1113

Cecchini, M. J., Hosein, K., Howlett, C. J., Joseph, M., and Mura, M. (2018). Comprehensive gene expression profiling identifies distinct and overlapping transcriptional profiles in non-specific interstitial pneumonia and idiopathic pulmonary fibrosis. *Respir. Res.* 19, 153. doi:10.1186/s12931-018-0857-1

Chanda, D., Otoupalova, E., Smith, S. R., Volckaert, T., De Langhe, S. P., and Thannickal, V. J. (2019). Developmental pathways in the pathogenesis of lung fibrosis. *Mol. Asp. Med.* 65, 56–69. doi:10.1016/j.mam.2018.08.004

DePianto, D. J., Chandriani, S., Abbas, A. R., Jia, G., N'Diaye, E. N., Caplazi, P., et al. (2015). Heterogeneous gene expression signatures correspond to distinct lung pathologies and biomarkers of disease severity in idiopathic pulmonary fibrosis. *Thorax* 70, 48–56. doi:10.1136/thoraxjnl-2013-204596

Filippou, P. S., Karagiannis, G. S., and Constantinidou, A. (2020). Midkine (MDK) growth factor: a key player in cancer progression and a promising therapeutic target. *Oncogene* 39, 2040–2054. doi:10.1038/s41388-019-1124-8

Gillespie, M., Jassal, B., Stephan, R., Milacic, M., Rothfels, K., Senff-Ribeiro, A., et al. (2022). The reactome pathway knowledgebase 2022. *Nucleic Acids Res.* 50, D687–D692. doi:10.1093/nar/gkab1028

Gregory Alvord, W., Roayaei, J. A., Quiñones, O. A., and Schneider, K. T. (2007). A microarray analysis for differential gene expression in the soybean genome using Bioconductor and R. *Brief. Bioinform* 8, 415–431. doi:10.1093/bib/bbm043

Habermann, A. C., Gutierrez, A. J., Bui, L. T., Yahn, S. L., Winters, N. I., Calvi, C. L., et al. (2020a). *Single-cell RNA sequencing reveals profibrotic roles of distinct epithelial and mesenchymal lineages in pulmonary fibrosis.*

Habermann, A. C., Gutierrez, A. J., Bui, L. T., Yahn, S. L., Winters, N. I., Calvi, C. L., et al. (2020b). Single-cell RNA sequencing reveals profibrotic roles of distinct epithelial and mesenchymal lineages in pulmonary fibrosis. Available at: https://www.science.org.

Hamanaka, R. B., O'Leary, E. M., Witt, L. J., Tian, Y., Gökalp, G. A., Meliton, A. Y., et al. (2019). Glutamine metabolism is required for collagen protein synthesis in lung fibroblasts. *Am. J. Respir. Cell Mol. Biol.* 61, 597–606. doi:10.1165/rcmb.2019-0008OC

Herazo-Maya, J. D., Noth, I., Duncan, S. R., Kim, S. H., Ma, S. F., Tseng, G. C., et al. (2013). Peripheral blood mononuclear cell gene expression profiles predict poor outcome in idiopathic pulmonary fibrosis. *Sci. Transl. Med.* 5, 205ra136. doi:10.1126/scitranslmed.3005964

Hernandez, D. M., Kang, J. H., Choudhury, M., Andrianifahanana, M., Yin, X., Limper, A. H., et al. (2020). IPF pathogenesis is dependent upon TGFβ induction of IGF-1. *FASEB J.* 34, 5363–5388. doi:10.1096/fj.201901719RR

Horiba, M., Kadomatsu, K., Nakamura, E., Muramatsu, H., Ikematsu, S., Sakuma, S., et al. (2000). Neointima formation in a restenosis model is suppressed in midkine-deficient mice. *J. Clin. Investigation* 105, 489–495. doi:10.1172/JCI7208

Hu, C., Li, T., Xu, Y., Zhang, X., Li, F., Bai, J., et al. (2023). CellMarker 2.0: an updated database of manually curated cell markers in human/mouse and web tools based on scRNA-seq data. *Nucleic Acids Res.* 51, D870–D876. doi:10.1093/nar/gkac947

Huang, L. S., Mathew, B., Li, H., Zhao, Y., Ma, S. F., Noth, I., et al. (2014). The mitochondrial cardiolipin remodeling enzyme lysocardiolipin acyltransferase is a novel target in pulmonary fibrosis. *Am. J. Respir. Crit. Care Med.* 189, 1402–1415. doi:10.1164/rccm.201310-1917OC

Huang, Y., Oldham, J. M., Ma, S. F., Unterman, A., Liao, S. Y., Barros, A. J., et al. (2021). Blood transcriptomics predicts progression of pulmonary fibrosis and associated natural killer cells. *Am. J. Respir. Crit. Care Med.* 204, 197–208. doi:10.1164/rccm.202008-3093OC

Ichihashi, Y. T., Yamaoka, T., Ohmori, T., and Ohba, M. (2016). Up-regulation of Syndecan-4 contributes to TGF-β1-induced epithelial to mesenchymal transition in lung adenocarcinoma A549 cells. *Biochem. Biophys. Rep.* 5, 1–7. doi:10.1016/j.bbrep.2015.11.021

Jin, S., Guerrero-Juarez, C. F., Zhang, L., Chang, I., Ramos, R., Kuan, C. H., et al. (2021). Inference and analysis of cell-cell communication using CellChat. *Nat. Commun.* 12, 1088. doi:10.1038/s41467-021-21246-9

Kanehisa, M., Furumichi, M., Sato, Y., Ishiguro-Watanabe, M., and Tanabe, M. (2021). KEGG: integrating viruses and cellular organisms. *Nucleic Acids Res.* 49, D545–D551. doi:10.1093/nar/gkaa970

Kobayashi, Y., Tata, A., Konkimalla, A., Katsura, H., Lee, R. F., Ou, J., et al. (2020). Persistence of a regeneration-associated, transitional alveolar epithelial cell state in pulmonary fibrosis. *Nat. Cell Biol.* 22, 934–946. doi:10.1038/s41556-020-0542-8

Lee, J. W., Chun, W., Lee, H. J., Min, J. H., Kim, S. M., Seo, J. Y., et al. (2021). The role of macrophages in the development of acute and chronic inflammatory lung diseases. *Cells* 10, 897. doi:10.3390/cells10040897

Leek, J. T., Johnson, W. E., Parker, H. S., Jaffe, A. E., and Storey, J. D. (2012). The SVA package for removing batch effects and other unwanted variation in high-throughput experiments. *Bioinformatics* 28, 882–883. doi:10.1093/bioinformatics/bts034

Ley, B., Brown, K. K., and Collard, H. R. (2014). Molecular biomarkers in idiopathic pulmonary fibrosis. *Am. J. Physiol. Lung Cell Mol. Physiol.* 307, 681–691. doi:10.1152/ajplung.00014.2014

Lin, X., Barravecchia, M., Matthew Kottmann, R., Sime, P., and Dean, D. A. (2019). Caveolin-1 gene therapy inhibits inflammasome activation to protect from bleomycin-induced pulmonary fibrosis. *Sci. Rep.* 9, 19643. doi:10.1038/s41598-019-55819-y

Liu, G., Wang, Y., Yang, L., Zou, B., Gao, S., Song, Z., et al. (2019). Tetraspanin 1 as a mediator of fibrosis inhibits EMT process and Smad2/3 and beta-catenin pathway in human pulmonary fibrosis. *J. Cell Mol. Med.* 23, 3583–3596. doi:10.1111/jcmm.14258

Liu, Z., Jin, H., Yang, S., Cao, H., Zhang, Z., Wen, B., et al. (2020). SDC1 knockdown induces epithelial–mesenchymal transition and invasion of gallbladder cancer cells via the ERK/Snail pathway. *J. Int. Med. Res.* 48, 300060520947883. doi:10.1177/0300060520947883

Martinez, F. J., Collard, H. R., Pardo, A., Raghu, G., Richeldi, L., Selman, M., et al. (2017). Idiopathic pulmonary fibrosis. *Nat. Rev. Dis. Prim.* 3, 17074. doi:10.1038/nrdp.2017.74

McGinnis, C. S., Murrow, L. M., and Gartner, Z. J. (2019). DoubletFinder: doublet detection in single-cell RNA sequencing data using artificial nearest neighbors. *Cell Syst.* 8, 329–337. doi:10.1016/j.cels.2019.03.003

Misa, K., Tanino, Y., Wang, X., Nikaido, T., Kikuchi, M., Sato, Y., et al. (2017). Involvement of midkine in the development of pulmonary fibrosis. *Physiol. Rep.* 5, e13383. doi:10.14814/phy2.13383

Morse, C., Tabib, T., Sembrat, J., Buschur, K. L., Bittar, H. T., Valenzi, E., et al. (2019). Proliferating SPP1/MERTK-expressing macrophages in idiopathic pulmonary fibrosis. *Eur. Respir. J.* 54, 1802441. doi:10.1183/13993003.02441-2018

Peng, L., Wen, L., Shi, Q. F., Gao, F., Huang, B., Meng, J., et al. (2020). Scutellarin ameliorates pulmonary fibrosis through inhibiting NF-κB/NLRP3-mediated epithelial–mesenchymal transition and inflammation. *Cell Death Dis.* 11, 978. doi:10.1038/s41419-020-03178-2

Qiu, X., Mao, Q., Tang, Y., Wang, L., Chawla, R., Pliner, H. A., et al. (2017). Reversed graph embedding resolves complex single-cell trajectories. *Nat. Methods* 14, 979–982. doi:10.1038/nmeth.4402

Qiu, Y., Mo, C., Xu, S., Chen, L., Ye, W., Kang, Y., et al. (2023). Research progress on perioperative blood-brain barrier damage and its potential mechanism. *Front. Cell Dev. Biol.* 11, 1174043. doi:10.3389/fcell.2023.1174043

Renaud, L., da Silveira, W. A., Takamura, N., Hardiman, G., and Feghali-Bostwick, C. (2020). Prominence of IL6, IGF, TLR, and bioenergetics pathway perturbation in lung tissues of scleroderma patients with pulmonary fibrosis. *Front. Immunol.* 11, 383. doi:10.3389/fimmu.2020.00383

Ritchie, M. E., Phipson, B., Wu, D., Hu, Y., Law, C. W., Shi, W., et al. (2015). Limma powers differential expression analyses for RNA-sequencing and microarray studies. *Nucleic Acids Res.* 43, e47. doi:10.1093/nar/gkv007

Shannon, P., Markiel, A., Ozier, O., Baliga, N. S., Wang, J. T., Ramage, D., et al. (2003). Cytoscape: a software Environment for integrated models of biomolecular interaction networks. *Genome Res.* 13, 2498–2504. doi:10.1101/gr.1239303

Sivakumar, P., Thompson, J. R., Ammar, R., Porteous, M., McCoubrey, C., Cantu, E., et al. (2019). RNA sequencing of transplant-stage idiopathic pulmonary fibrosis lung reveals unique pathway regulation. *ERJ Open Res.* 5, 00117-2019. doi:10.1183/23120541.00117-2019

Stuart, T., Butler, A., Hoffman, P., Hafemeister, C., Papalexi, E., Mauck, W. M., et al. (2019). Comprehensive integration of single-cell data. *Cell* 177, 1888–1902. doi:10.1016/j.cell.2019.05.031

Tanner, L., Single, A. B., Bhongir, R. K. V., Heusel, M., Mohanty, T., Karlsson, C. A. Q., et al. (2023). Small-molecule-mediated OGG1 inhibition attenuates pulmonary inflammation and lung fibrosis in a murine lung fibrosis model. *Nat. Commun.* 14, 643. doi:10.1038/s41467-023-36314-5

Thatikonda, S., Pooladanda, V., Tokala, R., Nagula, S., and Godugu, C. (2023). Niclosamide inhibits epithelial-mesenchymal transition with apoptosis induction in BRAF/NRAS mutated metastatic melanoma cells. *Toxicol. Vitro* 89, 105579. doi:10.1016/j.tiv.2023.105579

Tian, Y., Li, H., Gao, Y., Liu, C., Qiu, T., Wu, H., et al. (2019). Quantitative proteomic characterization of lung tissue in idiopathic pulmonary fibrosis. *Clin. Proteomics* 16, 6–11. doi:10.1186/s12014-019-9226-4

Travaglini, K. J., Nabhan, A. N., Penland, L., Sinha, R., Gillich, A., Sit, R. V., et al. (2020). A molecular cell atlas of the human lung from single-cell RNA sequencing. *Nature* 587, 619–625. doi:10.1038/s41586-020-2922-4

Wang, H., Liu, Y., Liang, X., Yang, G., Liu, Y., Li, F., et al. (2020). Effects of Secreted frizzled-related protein 1 on inhibiting cardiac remodeling. *Eur. Rev. Med. Pharmacol. Sci.* 24, 6270–6278. doi:10.26355/eurrev_202006_21525

White, E. S., Xia, M., Murray, S., Dyal, R., Flaherty, C. M., Flaherty, K. R., et al. (2016). Plasma surfactant protein-D, matrix metalloproteinase-7, and osteopontin index distinguishes idiopathic pulmonary fibrosis from other idiopathic interstitial pneumonias. *Am. J. Respir. Crit. Care Med.* 194, 1242–1251. doi:10.1164/rccm.201505-0862OC

Xu, J. Y., Chang, W., Sun, Q., Peng, F., and Yang, Y. (2021). Pulmonary midkine inhibition ameliorates sepsis induced lung injury. *J. Transl. Med.* 19, 91. doi:10.1186/s12967-021-02755-z

Yu, G., Wang, L. G., Han, Y., and He, Q. Y. (2012). ClusterProfiler: an R package for comparing biological themes among gene clusters. *OMICS* 16, 284–287. doi:10.1089/omi.2011.0118

Zhang, R., Pan, Y., Fanelli, V., Wu, S., Luo, A. A., Islam, D., et al. (2015). Mechanical stress and the induction of lung fibrosis via the midkine signaling pathway. *Am. J. Respir. Crit. Care Med.* 192, 315–323. doi:10.1164/rccm.201412-2326OC

Zhu, G., Fang, C., Mo, C., Wang, Y., Huang, Y., and Li, J. (2021). Transcriptomic analysis of granulosa cell populations proximal and distal to the germinal disc of chicken preovulatory follicles. *Sci. Rep.* 11, 4683. doi:10.1038/s41598-021-84140-w

Frontiers in Endocrinology

TYPE Original Research
PUBLISHED 08 December 2023
DOI 10.3389/fendo.2023.1258646

OPEN ACCESS

EDITED BY
Gianluca Bagnato,
University of Messina, Italy

REVIEWED BY
Ebrahim Abbasi,
Hamadan University of Medical Sciences,
Iran
Fahd Qadir,
Tulane University, United States

*CORRESPONDENCE
Lanlan Zhang
zhanglanlan@wchscu.edu.cn
Chunheng Mo
chunhengmo@gmail.com

[†]These authors have contributed equally to this work

RECEIVED 14 July 2023
ACCEPTED 15 November 2023
PUBLISHED 08 December 2023

CITATION
Zhang X, Deng X, Zhang L, Wang P, Tong X, Mo Y, Zhang Y, Zhang Y, Mo C and Zhang L (2023) Single-cell RNA sequencing analysis of lung cells in COVID-19 patients with diabetes, hypertension, and comorbid diabetes-hypertension.
Front. Endocrinol. 14:1258646.
doi: 10.3389/fendo.2023.1258646

Single-cell RNA sequencing analysis of lung cells in COVID-19 patients with diabetes, hypertension, and comorbid diabetes-hypertension

Xin Zhang[1,2†], Xiaoqian Deng[3†], Liangliang Zhang[1†], Pengbo Wang[4], Xia Tong[2], Yan Mo[5], Yuansheng Zhang[1], Yan Zhang[6], Chunheng Mo[7,8*] and Lanlan Zhang[1*]

[1]Department of Pulmonary and Critical Care Medicine, State Key Laboratory of Respiratory Health and Multimorbidity, West China Hospital, Sichuan University, Chengdu, China, [2]Department of Gastroenterology, West China (Airport) Hospital of Sichuan University (The First People's Hospital of Shuangliu District, Chengdu), Chengdu, China, [3]Department of Anesthesiology, West China Hospital, Sichuan University, Chengdu, China, [4]School of Professional Studies, Columbia University, New York, NY, United States, [5]Department of Neurology Medicine, The Aviation Industry Corporation of China (AVIC) 363 Hospital, Chengdu, China, [6]Department of Gastroenterology, West China Hospital, Sichuan University, Chengdu, China, [7]Key Laboratory of Birth Defects and Related Diseases of Women and Children of MOE, West China Second University Hospital, Sichuan University, Chengdu, China, [8]State Key Laboratory of Biotherapy, West China Second University Hospital, Sichuan University, Chengdu, China

Background: There is growing evidence that the lung is a target organ for injury in diabetes and hypertension. There are no studies on the status of the lungs, especially cellular subpopulations, and related functions in patients with diabetes, hypertension, and hypertension-diabetes after combined SARS-CoV-2 infection.

Method: Using single-cell meta-analysis in combination with bulk-RNA analysis, we identified three drug targets and potential receptors for SARS-CoV-2 infection in lung tissues from patients with diabetes, hypertension, and hypertension-diabetes, referred to as "co-morbid" patients. Using single-cell meta-analysis analysis in combination with bulk-RNA, we identified drug targets and potential receptors for SARS-CoV-2 infection in the three co-morbidities.

Results: The single-cell meta-analysis of lung samples from SARS-CoV-2-infected individuals with diabetes, hypertension, and hypertension-diabetes comorbidity revealed an upregulation of fibroblast subpopulations in these disease conditions associated with a predictive decrease in lung function. To further investigate the response of fibroblasts to therapeutic targets in hypertension and diabetes, we analyzed 35 upregulated targets in both diabetes and hypertension. Interestingly, among these targets, five specific genes were upregulated in fibroblasts, suggesting their potential association with enhanced activation of endothelial cells. Furthermore, our investigation into the underlying mechanisms driving fibroblast upregulation indicated that KREMEN1, rather than ACE2, could be the receptor responsible for fibroblast activation. This finding adds novel insights into the molecular processes involved in fibroblast modulation in the context of SARS-CoV-2 infection within these comorbid conditions. Lastly, we compared the efficacy of Pirfenidone and Nintedanib as therapeutic interventions targeting fibroblasts prone to pulmonary fibrosis. Our findings suggest that Nintedanib may be a more suitable treatment option for COVID-19 patients with diabetes and hypertension who exhibit fibrotic lung lesions.

Conclusion: In the context of SARS-CoV-2 infections, diabetes, hypertension, and their coexistence predominantly lead to myofibroblast proliferation. This phenomenon could be attributed to the upregulation of activated endothelial cells. Moreover, it is noteworthy that therapeutic interventions targeting hypertension-diabetes demonstrate superior efficacy. Regarding treating fibrotic lung conditions, Nintedanib is a more compelling therapeutic option.

KEYWORDS

SARS-CoV-2, diabetes, hypertension, endothelial cells, fibroblasts

1 Introduction

Diabetes and hypertension are common microvascular and macrovascular diseases that affect multiple organs. The alveolar-capillary network in the lungs is a large microvascular unit that may be affected by microvascular pathology (1–7). Considering the microvascular effects of diabetes and hypertension in the retina and glomeruli, the microvasculature in the lungs may also be affected by them (8). However, because the lungs have a large reserve capacity, much of the loss from microvascular damage can be tolerated without the need for symptoms of dyspnea. Therefore, microvascular pathology due to diabetes in the lungs may be underestimated, especially when accompanied by reduced lung function. Loss of posterior elasticity produced by collagen glycosylation in lung tissue has been suggested as a possible mechanism leading to this condition (9). There is a correlation between insulin resistance and hypoxia-induced by low birth weight with insulin resistance and impaired lung function, which may be related to collagen glycosylation in lung tissue. Several epidemiologic and clinical studies have found that adults with diabetes have an increased risk of decreased lung function compared to adults without diabetes (10, 11). However, studies on the exact relationship between decreased lung function and diabetic hypertension, as well as the pathophysiologic mechanisms, have not reached a consensus conclusion.

Current efforts following coronavirus disease 2019 (COVID-19) infection focus on new crown sequelae (12–14). COVID-19 exhibits similar physiological responses and clinical features in patients with diabetes and hypertension. However, each individual is involved in a different molecular pathway before or during SARS-CoV-2 infection. Several potential pathways have been proposed, including increased inflammatory storms (15), immunocompromised state, dysfunctional glucose homeostasis, hypercoagulability, alveolar hyperpermeability and vascular endothelial damage (9). Activation of these molecular pathways determines whether new-onset diabetic symptoms and complications are temporary or persist after viral clearance. However, to date, no study has given a definitive answer as to the effect of the superimposition of these three diseases on the sequelae of lung tissue, such as fibrosis.

On the medication of COVID-19 in diabetes combined with hypertension, GLP-1R agonists, DPP-4 inhibitors, or pioglitazone were associated with significant reductions in hospital admissions, respiratory complications, and mortality, and may improve COVID-19 outcomes in patients with T2DM (16). Hypertensive patients treated with long-term ACE inhibitors or ARBs have a lower risk of COVID-19 compared with CCBs. These results, if confirmed, often contradict previous hypotheses and suggest new ones (17). However, a fibrotic complication such as pulmonary fibrosis caused by COVID-19 patients, which is a serious prognostic threat, also deserves our attention (18–23). Direct evidence that SARS-CoV-2 causes pulmonary fibrosis: pulmonary fibrosis was found in autopsy and lung puncture pathology. Indirect evidence: transforming growth factor TGF-β, tumor necrosis factor TNF-α, and interleukin IL-6 were elevated in lung tissues, and the therapeutic value of two drugs (Pirfenidone and Nintedanib) for idiopathic pulmonary fibrosis in COVID-19-induced pulmonary fibrosis. However, it has not been analyzed from a molecular point of view whether fibrosis caused by patients with “co-morbidities” is effective in the treatment with Pirfenidone and Nintedanib.

The process of lung tissue subpopulation change cannot be adequately captured by clinical or molecular assays alone, and thus a comprehensive systems biology strategy is needed to address the complexity of this multiple cellular state change in order to unravel the mechanisms involved in new-onset diabetes. Single-cell sequencing is a technological approach to assessing cellular function in lung tissue, and by performing single-cell analyses in COVID-19 patients with comorbid diabetes mellitus, hypertension, and hypertension-diabetes, we sought to answer the following questions:1. which cellular subpopulations undergo the greatest changes after comorbid co-morbidities? 2. what are the underlying mechanisms of these changes? 3. which cellular subpopulations are predictive of lower lung function? 4. which diabetes and hypertension medications are more effective? 5. Pirfenidone and Nintedanib, which are more effective in comorbidity-induced pulmonary fibrosis? To answer the above questions, we performed single cell RNA sequencing combined bulk-RNA analysis aimed at supporting clinical diagnosis and treatment from a single-cell perspective.

2 Methods

2.1 Data collection

2.1.1 Single cell RNA sequencing datasets

We downloaded the available COVID-19 and IPF-related scRNA-seq datasets from Gene Expression Omnibus (GEO) and collected the datasets as follows:

1) COVID-19: The characteristics of the included studies in our article were as follows: 1) Patients with confirmed diagnoses of COVID-19. 2) Human lung tissue samples. 3) All lung cell types. 4) Availability of clinical information regarding comorbidities such as hypertension and diabetes. The datasets included in our analysis were GSE171524, GSE171668, GSE149878, GSE161382, and GSE163919. These datasets encompassed a total of 131,887 cells from 45 healthy controls, 45,473 cells from 10 patients with COVID-19, 6,948 cells from 1 patient with COVID-19 combined with diabetes, 106,618 cells from 22 patients with COVID-19 combined with hypertension, and 81,810 cells from 22 patients with COVID-19 combined with both hypertension and diabetes (Table S1).

2) Idiopathic pulmonary fibrosis (IPF): GSE132771, GSE135893, GSE122960, GSE128033, GSE128169, GSE136831, GSE159354.These 7 datasets included 77 Control, 87 IPF, 15 systemic sclerosis (SSc), 4 chronic hypersensitivity pneumonitis (cHP), 1 Myositis, 4 non-specific interstitial pneumonia (NSIP), 3 Sarcoidosis. (Table S2).

2.1.2 Bulk RNA datasets

GSE47460, 254 frozen tissue samples from interstitial lung diseases (ILD) patients were collected from GEO.

2.2 Flow of single-cell sequencing data analysis

2.2.1 scRNA/snRNA data processing

We used Seurat package (v4.0) to analyze scRNA/snRNA sequencing data. The specific steps are as follows: 1) Data quality control: remove low-quality cells with gene number less than 200 or more than 5000 and remove cells with more than 20% of mitochondrial genes. 2) Data normalization: execute LogNormalize, FindVariableFeatures, ScaleData functions, respectively. 3) Use Harmony Perform sample integration and batch effect removal. 4) Downscaling and visualization: use RunPCA function for principal component analysis, FindNeighbors for clustering, FindClusters for cell subpopulation analysis, and UMAP for dimensional reduction. 5) **Cell type identification:**cell types were determined mainly by " FindAllMarkers", classical cell marker genes, and prediction using R packages (clustermole, singscore) is done jointly.

2.2.2 Identification and functional analysis of differentially expressed genes

(1) **Identification of DEGs**: the FindMarkers function was used to find DEGs between different cell subpopulations or between different diseases of the same cell subpopulation. Here, we defined that a P-value less than 0.05 and avg_log$_2$FC>0.25 were statistically significant DEGs.

(2) **Functional analysis of gene clusters**: Use the "clusterProfiler" package in R to analyze the GO/KEGG enrichment of DEGs of cell subpopulations, and further determine their contribution to biological functions.

(3) **Gene set scoring**: AUCell was used to score the enriched relevant signaling pathways on individual cells, the scores were differentiated by different color scales, where yellow scored high and black scored low. As well as using the Seurat toolkit AddModuleScore function to calculate the scores of genes and gene sets on individual cells, the scores are differentiated by different color scales, with purple scoring high and gray scoring low in the Addmodule.

2.3 Integration of scRNA/snRNA dataset and dataset to identify features associated with low lung function in patients with pulmonary fibrosis

Expression matrices of bulk-RNA GSE47460 data and clinical phenotypes of lung function were used. single-cell expression matrices of COVID-19 patient lung tissue fibroblasts and endothelial cells were used, respectively. The expression matrix of GSE47460 data and the clinical phenotype lung function were integrated with the cellular dataset using the Scissor algorithm to identify cellular subpopulations or disease subtypes associated with the clinical phenotype lung function. Cell subpopulations of Scissor+, Scissor- were identified. Differential genes for Scissor+ and Scissor- cellular subpopulations were obtained using the FindMarkers function (p-values less than 0.05 and avg_log$_2$FC > 0.25 were statistically significant DEGs).

2.4 Selection of drug target genes and gene-positive cell extraction

Hypertensive drug, diabetic drug, Nintedanib and Pirfenidone target genes were selected based on literature reports. Among the hypertensive drug target genes were Calcium channel blockers

(CCBs):KCNMB1, CACNA1C, CACNB2, CACNA1D, CYP3A5, CYP3A4, ABCB1; Angiotensin-II Receptor Blockers (ARB) and Angiotensin-Converting Enzyme Inhibitors (ACEi): NPHS1, NOS3, CAMK1D, SCNN1G, GPR83, PRKCA, BDKRB2; Polymorphisms in Genes Affecting the Adrenergic Receptor Blocker Response : ADRB1, GRK4, FGD5, SLC25A31, ACY3; Polymorphisms in Genes Affecting Diuretic Response: ACE, ADD1, GNB3. ALDH1A2, LYZ, YEATS4, FRS2, NEDD4L. Diabetes drug target genes include: Glucagon-like peptide-1 (GLP-1): GLP1R; Novel glucose-sodium co-transport protein 2 (SGLT2). SLC5A2; Dipeptidyl peptidase IV (DPP-IV): DPP4; Peroxisome proliferator-activated receptor (PPAR): PPARG, PPARA, PPARB; Protein tyrosine phosphatase-1B (PTP-1B): PTPN1; Glucokinase agonists (GKA): GCK; 11β-hydroxysteroid dehydrogenase type1 (11β-HSDl) inhibitors, including HSD11B1. Nintedanib target genes are: PDGFRB, PDGFRA, KDR, FLT4, FLT1, FGFR3, FGFR2, FGFR1. Pirfenidone target genes were TGFB1, TGFB2,TGFB3,TGFBR1,TGFBR2; FGF2; MMP2, TIMP1, SERPINH1.

The above target gene-positive cells were extracted, and the proportion of target gene-positive cells in each cell subpopulation of different types of patients was calculated for further Meta analyses and functional analyses.

2.5 Meta analyses

Meta-analysis was done separately using the continuous variable metacount function of the meta data package of R software. The overall difference in means between different patients and healthy controls was quantified by pooling the differences provided by the original studies using a random effects model, and the results are presented as forest plots. Results for the proportion of gene-positive cells are given as mean difference MD (95% CI). Statistical heterogeneity between studies was assessed using I^2. For results from more than 2 studies, publication bias was assessed using Egger regression.

2.6 Analysis of intercellular communication

Cell communication analysis between activated endothelial cells and myofibroblasts was performed using the NicheNet toolkit to predict ligand-receptor connections between the two cells.

Communication analysis between myofibroblasts and the rest of the cells was performed using CellChat, which uses network analysis and pattern recognition methods to predict the major signaling inputs and outputs of the cells, as well as the probability of communication of ligand-receptor pairs between these cells.

2.7 Statistical methods

All data are expressed as mean ± standard error. Comparisons between groups were performed using t-tests, and comparisons between multiple groups were performed using one-way ANOVA. All calculations or analyses were performed using the Prism 9 software package (GraphPad) or R language. DEGs in each cluster were analyzed using the Wilcoxon rank sum statistical test. *Correlations* between two variables were analyzed using Pearson correlation analysis, and $P<0.05$ was considered statistically significant.

3 Results

3.1 Fibroblasts have worse lung function in all three disease

Single-cell sequencing data were obtained from public databases, encompassing pulmonary SARS-CoV-2 infection cases in 10 COVID-19 patients (abbreviated as Covid). In addition, data from 1 COVID-19 patient with concurrent diabetes mellitus (abbreviated as DM), 22 COVID-19 patients with concurrent hypertension (abbreviated as HTN), and 22 COVID-19 patients with combined hypertension and diabetes mellitus (abbreviated as HD), 54 Healthy patients (Control) were included. To analyze the bulk RNA (bulk-RNA) data and identify the disease associated with lower lung function, we employed single-cell subpopulation analysis and incorporated indicators of lung function (Figure 1A, sFigure 1A). Through the application of cellular subpopulation clustering, we identified a total of 16 distinct subpopulations (Figure 1B). By extracting the subpopulation ratios for each sample, we conducted statistical analysis, which revealed notable alterations in the fibroblast subpopulations. Compared to the healthy control group, myofibroblasts were significantly increased in the Covid, DM, HD, and HTN groups. Relative to the Covid group, myofibroblasts showed significant upregulation in both the DM, HD, and HTN groups (Figure 1C). Conversely, no significant changes were observed in the subpopulations of immune cells, blood vessels, or other cell types (Figures 1D–F).

In another study, we used data from 45 healthy controls, 58 Covid-19 patients, and 64 Idiopathic Pulmonary Fibrosis (IPF) patients. Our findings revealed that compared to the healthy control group, Covid-19 patients were more prone to undergo endothelial-to-mesenchymal transition and epithelial-to-mesenchymal transition. Additionally, there was a significant increase in the proportion of myofibroblasts, which is considered a key factor in Covid-19-induced pulmonary fibrosis (24). Furthermore, this article focuses on the analysis of the pulmonary conditions in COVID-19 patients with diabetes, hypertension.

We further examined the differential expression of genes in the fibroblast group compared to the Covid group, which revealed decreased activity of DEGs specifically associated with myofibroblasts (Figure 1G, sFigures 1B–F). To gain more insight into the lung function within the fibroblast subpopulation, we applied a scoring method using scissor analysis (Figures 1H, I), which identifies cell subpopulations highly associated with a specific clinical phenotype based on bulk clinical data in scRNA-seq analysis (25). This analysis showed that the proportion of cells associated with poor lung function was significantly increased in the DM, HTN, and HD groups compared with the Covid group

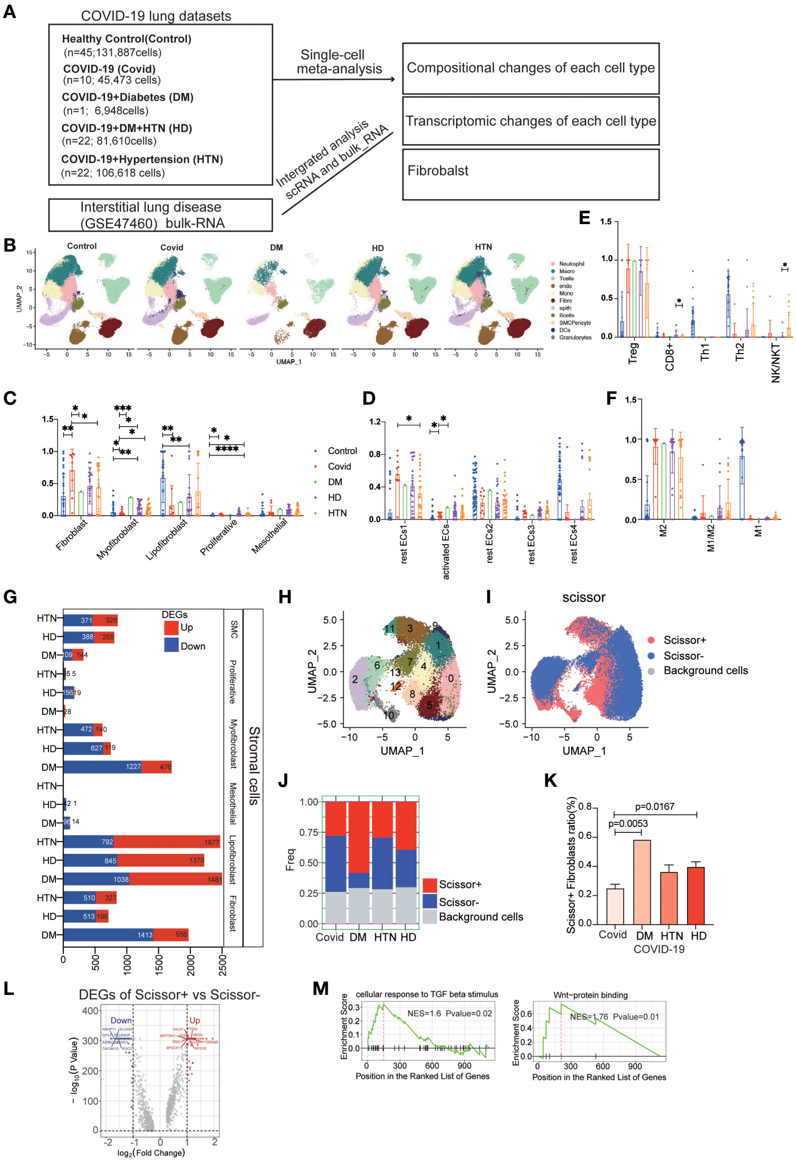

FIGURE 1

COVID-19 patients with combined diabetes/hypertension showed large differences in the number and transcriptome levels of lung cell subpopulations and were more prone to pulmonary fibrosis. **(A)** The lung scRNA-seq and bulk-RNA datasets used in the meta-analysis consisted of 131,887 cells from 45 healthy controls, 44,316 cells from 10 COVID-19 patients, 6,717 cells from 1 COVID-19 patient with diabetes, 79,290 cells from 22 COVID-19 patients with hypertension, and 103,911 cells from 22 COVID-19 patients with both hypertension and diabetes. Additionally, bulk RNA data from 254 frozen tissue samples from ILD patients were obtained from the GSE47460 dataset. **(B)** UMAP visualization of all cell types (Fibroblasts, T cells, Macrophages, Endothelials, Epithelials, Neutrophils, Plasma, Monocytes, Ciliated, SMC, Granulocytes, B cells, Mast, DCs) in the Control, DM, HTN, and HD groups, with cell types color-coded. C-F. Bar graphs displaying significant differences in the proportions of cell subtypes in the Covid, DM, HTN, and HD groups compared to the Control group in fibroblast **(C)**, endothelial **(D)**, T cell **(E)**, and macrophage **(F)** samples from lung tissues. The proportions of fibroblast cells were significantly higher in the DM, HTN, and HD groups compared to the Control group, as shown in Figure **(C)** Compared to the healthy control group, myofibroblasts were increased in the Covid, DM, HD, and HTN groups, with a statistically significant difference in the Covid group. Relative to the Covid group, myofibroblasts showed significant upregulation in both the DM, HD, and HTN groups, as illustrated in Figure **(C)** Regarding endothelial cells, the proportion of activated endothelial cells (activated ECs) was higher in the Covid, DM, HTN, and HD groups, with a statistically significant difference in the Covid group. Relative to the Covid group, activated ECs showed upregulation in both the DM, HD, and HTN groups, as illustrated in Figure **(D)**. **(G)** Bar graph exhibiting the number of differentially expressed genes (DEGs) in fibroblasts from COVID-19 patients, comparing the DM, HTN, HD, and Covid groups, categorized by cell type (FDR < 0.05). **(H)** UMAP visualization of fibroblasts in the four groups, with clusters color-coded. **(I)** Scissor analysis relating phenotypic data of lung function from bulk-RNA data of IPF (idiopathic pulmonary fibrosis) patients from the GEO dataset with scRNA-seq data of COVID-19 patients. UMAP plots depict the position of cells associated with normal lung function (blue) or low lung function (red). **(J, K)** Bar graph displaying the proportion of Scissor+ fibroblast cells in the four disease groups. The proportion of Scissor+ fibroblast cells was significantly higher in the DM, HTN, and HD groups compared to the Control group, with statistically significant differences observed in the DM and HD groups. **(L)** Volcano plot exhibiting the differentially expressed genes (DEGs) between Scissor+ and Scissor- cells. It shows the number of upregulated and downregulated genes. **(M)** GSEA enrichment analysis of DEGs in Scissor+ and Scissor- cells, indicating that the upregulated DEGs were significantly enriched in TGF-beta and Wnt-related signaling pathways. The NES (normalized enrichment score) represents the statistical score of the enriched pathway, with positive scores signifying enrichment at the front of the sorted sequence, and negative scores indicating enrichment at the back. The P value indicates the statistical significance of the enrichment score for a pathway gene set, where smaller values indicate better enrichment.

(Figures 1J, K). Subsequently, we isolated cells associated with poor lung function and performed differential expression analysis by comparing them with cells associated with good lung function (Figure 1L). This analysis revealed DEGs, and further gene set enrichment analysis (GSEA) demonstrated greater enrichment of fibrosis-related signaling pathways, such as TGF-β and WNT signaling (Figure 1M, sFigures 2A–D).

3.2 Fibroblasts are the major cellular subpopulation responsible for the upregulation of diabetic hypertensive drugs after SARS-CoV-2 infection

In our analysis, we investigated the expression of common targets of diabetic and hypertensive drugs in the lungs of patients following SARS-CoV-2 infection (Figure 2A). The red color in the figure represents genes that were statistically upregulated, indicating that the targets of diabetic and hypertensive drugs were among the most altered in fibroblasts. Specifically, we observed that the diabetic target gene SLC5A2 was upregulated in fibroblasts, while hypertensive target genes CACNA1C, PRKCA, CACNB2, and FRS2 were also upregulated in fibroblasts (Figure 2B). Additionally, we categorized and identified genes that were both classified as drug targets in diabetes and hypertension and upregulated in our analysis (Figure 2B, sFigures 3A). Upon further analysis of the expression levels of these genes across all lung cell subtypes, we found that they were indeed highest in myofibroblasts (Figure 2C). Furthermore, we compared the expression of upregulated target genes specifically in diabetic myofibroblasts (Figures 2D, E). This analysis indicated that these target genes were indeed expressed at higher levels in diabetic myofibroblast cells. Finally, we identified the genes that showed a positive association with myofibroblast cells (Figure 2F). These findings suggest that the expression of some targets of diabetic hypertensive drugs may be dysregulated in the lungs of patients after SARS-CoV-2 infection and that myofibroblasts are the major cellular subpopulation responsible for the upregulation of diabetic hypertensive drugs after SARS-CoV-2 infection. This may promote the occurrence of pulmonary fibrosis in patients with COVID-19 combined with hypertension and diabetes.

3.3 Association of entry factors with fibroblast alterations and correlation with myofibroblasts and upregulated drug targets

In our investigation of the effects of entry factors on the lungs in patients with the combined presence of diabetes, hypertension, and SARS-CoV-2 infection, we focused on 17 genes related to receptors, coreceptors, and cofactors (Figure 3A). By comparing the expression levels of the entry factors across all cell subpopulations in the three diseases with the Covid group, we observed that fibroblasts exhibited the most significant alterations (Figure 3B, sFigures 4A–D).We further evaluated the impact of the entry factors in two ways. Firstly, we extracted the proportions of cells expressing these factors, indicating an increase in diabetic and hypertensive fibroblasts (Figures 3C, D). Additionally, we performed scoring of several entry factors using the "Addmodule Score" method, suggesting varying degrees of upregulation in the three diseases (Figure 3E). Subsequently, we conducted correlation analysis between the last five entry factors and other variables. Interestingly, we found that the receptor gene KREMEN1 exhibited a positive correlation with myofibroblasts (Figure 3F). Furthermore, KREMEN1 showed a positive correlation with the upregulated drug targets (Figure 3G, sFigures 4E–G). These findings suggest that KREMEN1 displayed a positive correlation with myofibroblasts. This suggests a potential role of KREMEN1 in the fibrotic process. Additionally, KREMEN1 showed a positive correlation with upregulated drug targets, highlighting its involvement in disease-related pathways and potential therapeutic implications.

3.4 Activated endothelial cells may cause aggregation of fibroblasts

It is well-known that the pulmonary vasculature is a common target in hypertension and diabetes, particularly affecting vascular endothelial cells (26). In our study, we identified two subpopulations of endothelial cells: rest endothelial cells and activated endothelial cells (Figure 4A). Activated endothelial cells exhibited high expression levels of the atypical chemokine receptor 1 (ACKR1) and adhesion molecules SELE (E-selectin) and SELP (P-selectin) (Figure 4B) (27, 28). Notably, activated endothelial cells exhibited significant upregulation in both diabetes and hypertension (Figures 4C, D). To further characterize activated endothelial cells, we examined the expression of cytokines and fibrogenic factors. We found that cytokines were significantly upregulated in activated endothelial cells (Figure 4E), suggesting an increased inflammatory response. Fibrogenic factors were also significantly upregulated in activated endothelial cells (Figure 4F), implying their involvement in fibrosis development. Utilizing a ligand-receptor approach, we identified several myofibroblast-inducing factors, such as TGF-beta and VEGFC, that are highly expressed in activated endothelial cells (Figure 4G). Additionally, activated endothelial cells showed a positive correlation with myofibroblasts (Figure 4H, sFigure 5). We further explored the correlation between activated endothelial cells and entry factors, indicating that most of the entry factors were indeed correlated (Figure 4I). Moreover, there was a correlation with hypertension-diabetes targets (Figure 4J). Lastly, investigating changes in lung function, we found that activated endothelial cells was associated with worse lung function (Figures 4K–M). After calculating the differential expression of scissor + and scissor -, signaling pathways such as IL1, PDGFR, and collagen were suggested to be up-regulated after analysis by GSEA clustering (Figures 4N, O). These findings suggest that the activated endothelial cells play a role in the exacerbation of lung effects in patients with hypertension and diabetes following SARS-CoV-2 infection.

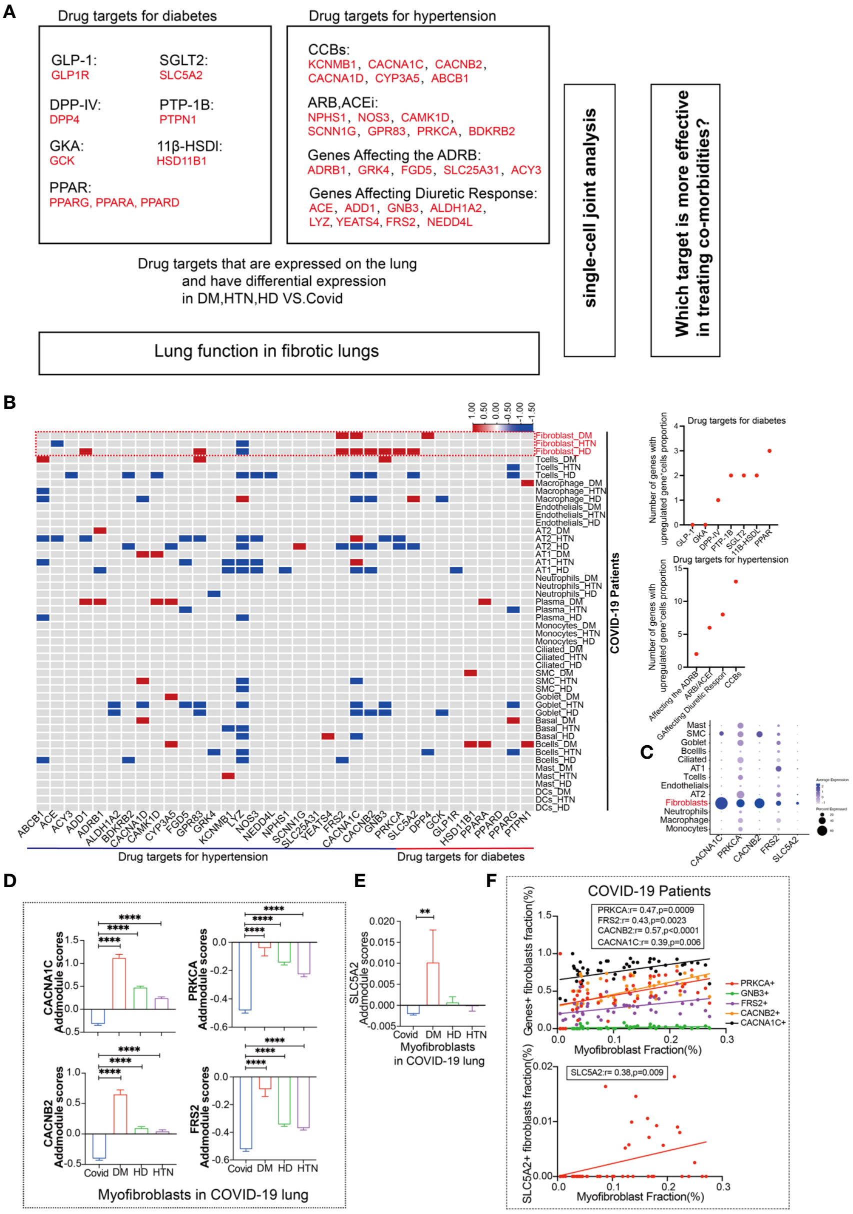

FIGURE 2

Fibroblasts have more targets for hypertension, diabetes drug response. **(A)** Schematic diagram showing the workflow for the analysis of common targets of common diabetes and hypertension drugs expressed in the lungs. Among the hypertensive drug target genes include Calcium channel blockers (CCBs): KCNMB1, CACNA1C, CACNB2, CACNA1D, CYP3A5, CYP3A4, ABCB1; Angiotensin-II Receptor Blockers (ARB) and Angiotensin-Converting Enzyme Inhibitors (ACEi): NPHS1, NOS3, CAMK1D, SCNN1G, GPR83, PRKCA, BDKRB2; Polymorphisms in Genes Affecting the Adrenergic Receptor Blocker Response : ADRB1, GRK4, FGD5, SLC25A31, ACY3; Polymorphisms in Genes Affecting Diuretic Response: ACE, ADD1, GNB3. ALDH1A2, LYZ, YEATS4, FRS2, NEDD4L. Diabetes drug target genes include: Glucagon-like peptide-1 (GLP-1): GLP1R; Novel glucose-sodium co-transport protein 2 (SGLT2). SLC5A2; Dipeptidyl peptidase IV (DPP-IV): DPP4; Peroxisome proliferator-activated receptor (PPAR): PPARG, PPARA, PPARB; Protein tyrosine phosphatase-1B (PTP-1B): PTPN1; Glucokinase agonists (GKA): GCK; 11β-hydroxysteroid dehydrogenase type 1 (11β-HSDI) inhibitors, including HSD11B1. **(B)** The heatmap presents the results of a meta-analysis showing the differences in the percentage of positive cells for hypertension and diabetes drug target genes in various cell subpopulations (Fibroblasts, T cells, Macrophages, Endothelial cells, AT2, AT1, Neutrophils, Plasma, Monocytes, Ciliated, SMC, Goblet, Basal, B cells, Mast, DCs) in lung tissues of the four patient groups (DM, HTN, HD) compared to the Control group. The dot plots display the number of upregulated positive cells in the percentage of drug-targeted genes across different cell types within hypertension and diabetes groups. **(C)** The DOT plot shows the expression of hypertension target genes (CACNA1C, CACNB2, PRKCA, FRS2) and diabetes target gene SLC5A2 in all lung cell subtypes. **(D)** The bar graph represents the Addmodule Scores of hypertension target genes (CACNA1C, CACNB2, PRKCA, FRS2) in myofibroblasts of patients in the Control, DM, HTN, and HD groups. The scores were significantly higher in the DM, HTN, and HD groups compared to the Control group. **(E)** The bar graph shows the Addmodule Scores of the diabetes target gene SLC5A2 in myofibroblasts of patients in the Control, DM, HTN, and HD groups. The scores were elevated in the DM, HTN, and HD groups compared to the Control group. **(F)** The correlation analysis demonstrates the positive correlation between the myofibroblast ratio and hypertension and diabetes target genes using the Pearson test. Four hypertension drug-related target genes and one diabetes target gene showed positive correlations with myofibroblasts. **P < 0.01, ****P < 0.0001.

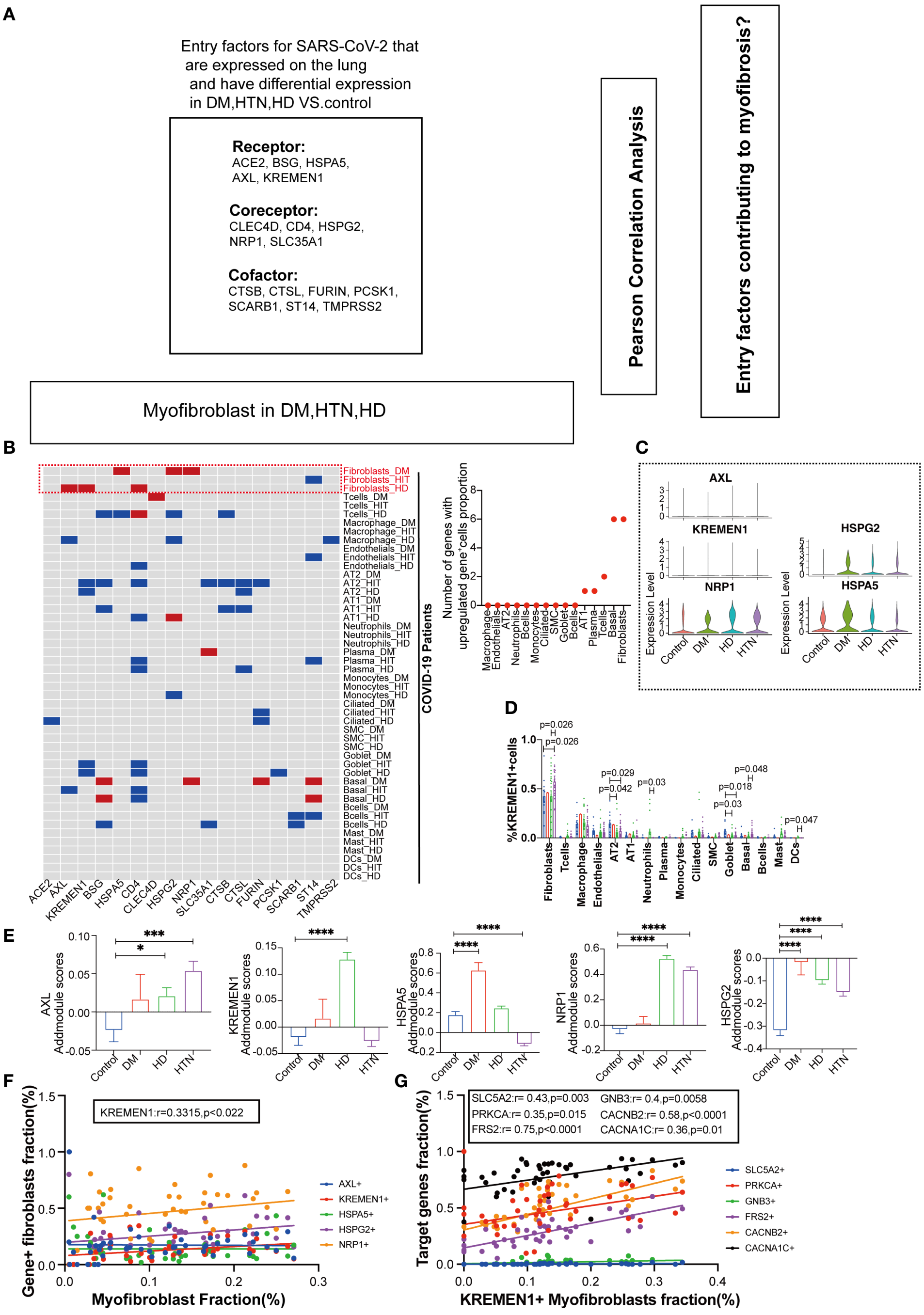

FIGURE 3

Association of Entry Factors with Fibroblast Alterations and Correlation with Myofibroblasts and Upregulated Drug Targets. **(A)** Schematic diagram showing the workflow for the analysis of entry factors expressed in the lung. Among the entry factors Receptor: ACE2, BSG, HSPA5, AXL, KREMEN1; Cofactor: CTSB, CTSL, FURIN, PCSK1, SCARB1, ST14, TMPRSS2; Coreceptor: CLEC4D, CD4, HSPG2, NRP1, SLC35A1. **(B)** Heatmap showing the meta-analysis of the differences in the percentage of entry factors positive cells in each cell subpopulation (Fibroblasts, T cells, Macrophages, Endothelials, AT2, AT1, Neutrophils, Plasma, Monocytes, Ciliated, SMC, Goblet, Basal, Bcells, Mast, DCs) in the lung tissues of the four groups of patients (DM, HTN, HD) vs. the Control group. Meta-analysis of differences in the percentage of cells positive for the entry factors in Ciliated, SMC, Goblet, Basal, Bcells, Mast, DCs. (Red indicates up-regulation, blue indicates down-regulation, and gray indicates no significant change). Dot plots show the number of up-regulated invasion target gene positive cell percentage in different cell subpopulations, respectively. **(C)** Violin plots showing the expression levels of invasion-associated genes (AXL, KREMEN1, HSPA5, NRP1, HSPG2) in four groups of diseases. **(D)** The bars show the percentage of KREMEN1-positive cells in each cell subpopulation, which was found to be significantly elevated in fibroblasts. **(E)** The bar graphs show the addmodule scores of invasion-associated genes (AXL, KREMEN1, HSPA5, NRP1, HSPG2) in myofibroblasts of patients with four diseases Control group (blue), DM group (red), HTN group (green), and HD group (purple). Scores were elevated in the DM, HTN, and HD groups relative to the Control group. (*P < 0.05, ***P < 0.001,****P < 0.0001). **(F)** Correlation analysis of myofibroblast fraction with new crown entry factors (Pearson test), showing KREMEN1 is positively correlated with myofibroblasts. **(G)** Correlation analysis of hypertension-targeted genes (CACNA1C, CACNB2, PRKCA, FRS2) and diabetes-targeted gene (SLC5A2) with entry factors KREMEN1 (Pearson test), showing KREMEN1 is positively correlated with drug target genes.

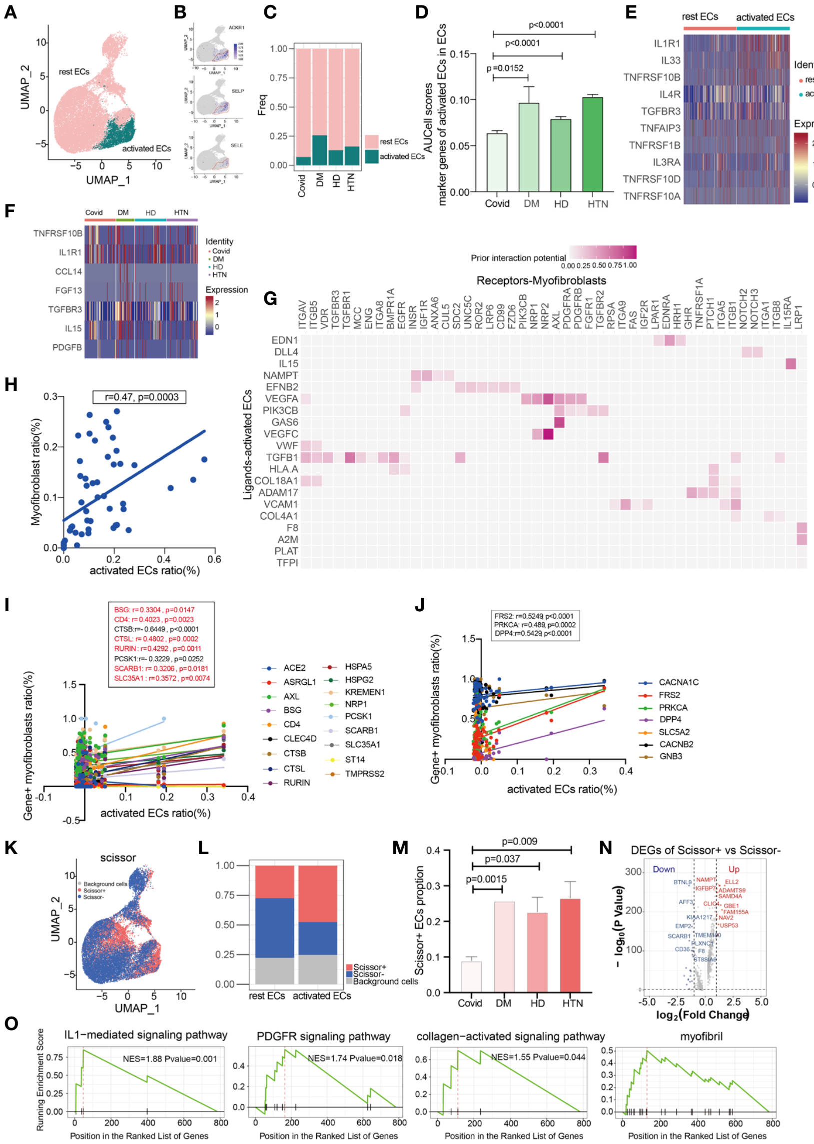

FIGURE 4

Activated endothelial cells may cause aggregation of fibroblasts. **(A)** UMAP visualization of endothelial cells, colored by celltype compartment. **(B)** UMAP shows the marker of activated ECs, mainly focusing on ACKR1, SELP, SELE. **(C, D)** Bar graphs demonstrate the proportion of endothelial cell subsets in the four disease groups; the DM, HTN and HD groups had significantly higher proportions of activated endothelial cells than the Control group. **(E)** Heatmap showing a comparison of major cytokine expression in endothelial cell subpopulations, indicating that activated endothelial cells are enriched in more cytokines (IL1R1, IL33, TNFRSF10B, IL4R, TGFBR3, TNFAIP3, TNFRSF1B, IL3RA, TNFRSF10D, TNFRSF10A) compared to other groups. **(F)** Heatmap showing the cytokines that were significantly elevated in the activated endothelial cells in the DM, HTN, and HD groups relative to the Control group: CCL14, FGF13, TGFBR3, IL15, and PDGFB in the DM group; TNFRSF10B in the HTN group; and TNFRSF10B and IL1R1 in the HD group. **(G)** NicheNet analysis showing ligand maps of activated endothelial cells with myofibroblast bodies. Darker colors in the matrix represent greater ligand-receptor interaction capacity. **(H)** Correlation analysis of myofibroblast with activated endothelial cells (Pearson test), showing activated endothelial cells is positively correlated with myofibroblasts. **(I)** Correlation analysis of SARS-CoV-2 entry factors with activated endothelial cells (Pearson test), showing that activated endothelial cells is positively correlated with the entry factors (BSG, CD4, CTSL, RURIN, SCARB1, SLC35A1). **(J)** Correlation analysis of hypertension/diabetes drug target genes with activated endothelial cells (Pearson test), showing activated endothelial cells is positively correlated with hypertension/diabetes drug target genes (FRS2, PRKCA, DPP4). **(K)** Scissor analysis relating lung function phenotypic information from bulk-RNA data of IPF patients from GEO with endothelial cells of COVID-19. UMAP plots indicate the position of cells normal lung function (blue) or low lung function (red) associated with lung function. **(L)** Bar graph showing the proportion of Scissor+, Scissor-, and background cells in rest ECs versus activated ECs. **(M)** Bar graph showing the cell proportion of Scissor+ endothelial cells in the four disease groups, the cell proportion of Scissor+ fibroblasts was significantly higher in the DM, HTN and HD groups relative to the Control group and the difference was statistically significant. **(N)** Volcano plot showing Scissor+ cell vs. Scissor- cell DGEs. the number of differentially up-regulated genes is 413 and the number of down-regulated genes is 252. **(O)** The GSEA enrichment analysis of differential genes has revealed that the IL1-mediated signaling pathway, PDGFR signaling pathway, collagen-activated signaling pathway, and myofibril were significantly enriched in the Scissor+ endothelial cells when compared to scissor- endothelial cells. The NES statistic of the enriched pathway score is positive and indicates that the pathway gene set is enriched and is in front of the sorting sequence. Conversely, if the NES statistic is negative, it means that a certain functional gene set is enriched behind the sorting sequence. When the Pvalue is less than 0.05, it indicates that the results are statistically significant.

3.5 Nintedanib but not Pirfenidone is more useful in patients with underlying fibrotic lungs with three disease

Based on the Cell Chat analysis, we observed that there are numerous receptor-ligand interactions between the targets of Pirfenidone and Nintedanib, specifically in the context of hypertension and diabetes (Figures 5A–D). Furthermore, the levels of these receptor-ligand interactions were progressively elevated during the onset of diabetes (Figure 5E). This led us to hypothesize that Pirfenidone and Nintedanib may have a therapeutic role in treating fibrosis sequelae caused by COVID-19, particularly in individuals with hypertension and diabetes. To identify the targets that are upregulated in fibroblasts, we incorporated five different fibrotic targets. Our analysis revealed that the main targets upregulated by Nintedanib were Fgfr1 and Fgfr2 (Figures 5F, G, sFigures 6A–C). After Addmodule Score analysis, Fgfr1 and Fgfr2 were increased in hypertension as well as hypertension-diabetes (Figures 5H, I), respectively, but no significant changes were seen in TGF-b1, TGF-b2, and TGF-b3, the targets of Pirfenidone (Figures 5J–L). We set scissor+ as poor lung function and scissor- as normal lung function, and a comparison of the two suggests that scissor+ ratios are upregulated in hypertension and diabetes. Also, scissor+ cell proportion was upregulated in hypertension, diabetes, and hypertension-diabetes groups versus Covid group (Figures 5M, N, sFigure 6D). Finally, we identified that the targets of Nintedanib, specifically Fgfr1 and Fgfr2, are indeed upregulated in individuals with hypertension and diabetes. This suggests that Nintedanib may have potential therapeutic benefits for targeting fibrosis in the lungs of patients with COVID-19 who also have comorbid hypertension and diabetes.

4 Discussion

We are the first single-cell meta-analysis of SARS-CoV-2 infection lungs of diabetes, hypertension, and hypertension-diabetes patients. We identify that lung function is worse in fibroblasts in all three diseases. We identified that lung function was worse in fibroblasts in all three diseases condition and identified that myofibroblast expression was elevated in diabetes, hypertension, and hypertension-diabetes patients, and identified five targets in diabetes, hypertension where myofibroblast was elevated, suggesting a better therapeutic regimen. For the entry factor of SARS-CoV-2, it was KREMEN1 rather than ACE2 that dominated its myofibroblast elevation, while finally identifying the antifibrotic agent, Nintedanib, as a possible target for diabetes, hypertension, and hypertension-diabetes in SARS-CoV-2 infection-induced fibrotic lungs.

The specific subtype of cell that is damaged by diabetes or hypertension is myofibroblast, and using fibrotic lung function, mapped to fibroblasts, we can see that patients with diabetes, hypertension, or diabetes-hypertension have worse lung function. Digging further into what causes the increased myofibroblast, we find that the target organ that is damaged by both diabetes and hypertension, the endothelial cells, has significantly higher activated endothelial cells. The major marker gene for endothelial cells, ACKR1, is now thought to be a gene associated with fibrosis (29), is also a marker gene for activated endothelial cells, and our current results suggest that in addition to increased myofibroblast, the expression of activated endothelial cells is also significantly increased, while becoming positively correlated with myofibroblast expression. This is because more and more studies are beginning to consider the lung as a “target organ” for diabetes or hypertension (30). This is not surprising, as pulmonary circulation is a major source of diabetes and hypertension (25). This is not surprising since the pulmonary circulation has the largest capillary network in the body and can accommodate the entire cardiac output (31). This is not surprising since the pulmonary circulation has the largest capillary network in the body and accommodates the entire cardiac output. Microvascular lesions in the lungs have been identified and have been described in autopsy studies and include thickening of the alveolar epithelium and capillary basement membranes (32). This structural abnormality is similar to those observed in the diabetic kidney and retina. Therefore, we suggest that activated endothelial cells may be a potential “bridge” leading to increased myofibroblast. By targeting endothelial cells, we may be able to slow down the increase in myofibroblast, thereby achieving the goal of slowing down lung function.

Interestingly, in our study we did not observe an increase in therapeutic targets in patients with hypertension alone, but in patients with comorbid hypertension-diabetesor diabetes mellitus, we observed an increase in targets in relation to each other. Positively associated with the increased targets was increased myofibroblast, suggesting that patients with combined hypertension-diabetes may be more impaired after SARS-CoV-2 infection. This may be related to more severe cumulative damage to blood vessels and stromal cells in hypertension-diabetesor diabetes mellitus (33, 34). Further study of these findings will allow us to better understand the effects of COVID-19 in patients with comorbid hypertension-diabetes and to search for more effective treatments. In this study, an inhibitor of the antidiabetic drug SGLT2 (sodium-glucose cotransporter-2/SLC5A2), which reduces renal reabsorption of glucose to lower blood glucose, could indirectly reduce lung infection in diabetic mice (35). However, a new clinical study was initiated in April 2020 to understand the substantial cardiorenal protective effects of SLGT2 inhibitors in reducing disease progression, complications, and all-cause mortality in hospitalized adult patients with a focus on those with COVID-19 (36, 37). Our study suggests that SLC5A2 is elevated in fibroblasts and positively correlates with myofibroblast, predicting that SLC5A2 is target of COVID-19 related-fibrosis.

According to the literature, host cell receptors play a key role in determining viral tropism and pathogenesis (38). However, little is known about the host receptors for SARS-CoV-2 other than ACE2 (39, 40). In our study, we did not observe upregulation of classical entry factors such as ACE2; instead, we found that the upregulation of KREMEN1 correlated with an increase in myofibroblast. This suggests that ACE2 alone cannot explain the multiorgan invasiveness of SARS-CoV-2 or the fact that ACE2 expression is

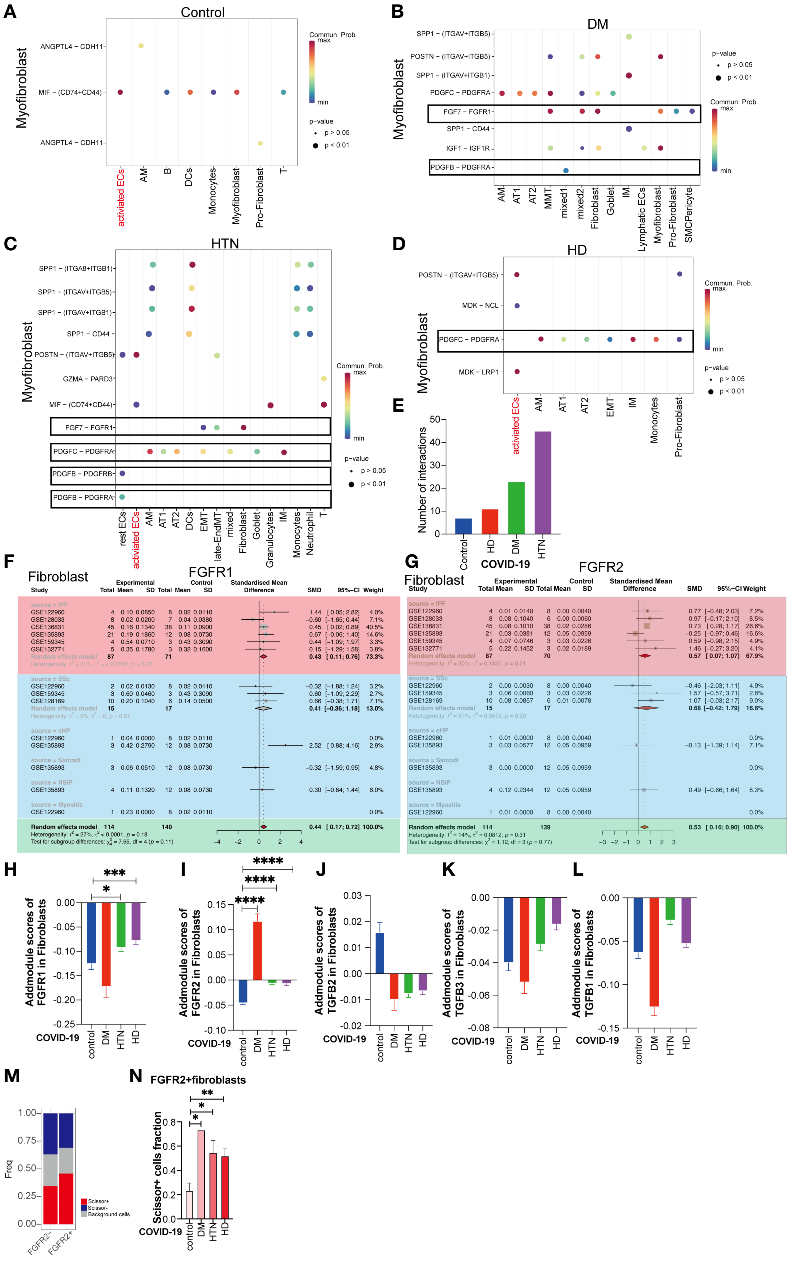

FIGURE 5

Nintedanib but not Pirfenidone is more useful in patients with underlying fibrotic lungs with three disease. **(A–D)** Dot plot demonstrating that in Control group, DM group, HTN group and HD group, the remaining cell subpopulations act as signal senders and can have cellular conversations with myofibroblasts via ligand-receptors. Among them, the gene pairs in Control group are ANGPTL4-CDH11, ANGPTL4-CDH11, MIF-(CD74+CD44); DM group: SPP1-(ITGAV+ITGB5), SPP1- (ITGAV+ITGB1), SPP1-CD44, POSTN- (ITGAV+ITGB5), IGF1-IGF1R, PDGFC- PDGFRA, PDGFB-PDGFRA, FGF7-FGFR1; HTN group: SPP1-(ITGA8+ITGB1), SPP1-(ITGAV+ITGB5), SPP1 -(ITGAV+ITGB1), SPP1-CD44, POSTN-(ITGAV+ITGB5), GZMA-PARD3, MIF-(CD74+CD44), FGF7 - FGFR1, PDGFC-PDGFRA, PDGFB - PDGFRA, PDGFB - PDGFRB; HD group: POSTN-(ITGAV+ITGB5), the MDK-NCL, PDGFC - PDGFRA, MDK-LRP1. **(E)** The bar graphs show the number of pairs of handheld ligands that produce cellular interactions with myofibroblasts in the four diseases and were found to be significantly higher in the disease groups. **(F, G)** Subgroup analysis of the difference in the proportion of Nintedanib -targeted gene-positive fibroblasts in pulmonary fibrosis versus healthy controls. Subgroup analysis of the difference in the proportion of Nintedanib -targeted gene-positive fibroblasts in pulmonary fibrosis versus healthy controls. the proportion of FGFR1, and FGFR2 gene-positive fibroblasts was significantly higher in ILD. **(H)** The bar graph illustrates the addmodule score of FGFR1 in fibroblasts of patients with four diseases: Control group (blue), DM group (red), HTN group (green), and HD group (purple). The scores of HTN group and HD group show an increase compared to the Control group (*P value<0.05, ***P value<0.001). **(I)** The bar graph displays the addmodule score of FGFR2 in fibroblasts of patients with four diseases: Control group (blue), DM group (red), HTN group (green), and HD group (purple). The scores of DM group, HTN group, and HD group show an increase compared to the Control group (****P value<0.0001). **(J–L)** The bar graph demonstrates the addmodule scores of TGFB1, TGFB2, and TGFB3 in fibroblasts of patients with four diseases: Control group (blue), DM group (red), HTN group (green), and HD group (purple). **(M)** The bar graph shows the proportion of Scissor+, Scissor-, and background cells in FGFR2- and FGFR2+ groups. The proportion of Scissor+ fibroblast cells increase in the FGFR2+ group relative to the FGFR2- group. **(N)** The bar graph indicates that among the FGFR2+ fibroblasts, the proportion of Scissor+ cells in the four disease groups is significantly higher than that in the Control group, DM group, HTN group, and HD group, and the difference is statistically significant. (*P < 0.05, **P < 0.01) not significantly altered after SARS-CoV-2 infection. Indeed, KREMEN1 plays a sufficiently important role in SARS-CoV-2 entry (41, 42), and we therefore suggest that KREMEN1 may act as an alternative functional receptor that plays an important role in ACE2-independent viral invasion. This also provides the explanation that diabetic and hypertensive patients may still be associated with increased myofibroblast in the absence of significant ACE2 elevation. In addition, our study shows that KREMEN1-positive cells have poorer lung function, providing us with a relevant basis. Taken together, our study reveals that KREMEN1 may be an important alternative receptor in SARS-CoV-2 infection, playing an important role in lung fibrosis and deterioration of lung function (41). Finally, by examining patients with the three diseases combined diabetes, hypertension, and hypertension-diabetes after SARS-CoV-2 infection, we propose that activated endothelial cells may be a potential bridge to fibrosis, as well as suggesting that the preference of anti-hypertensive drug targets and the influence of entry factors on the combined three diseases is not a traditional ACE2, while proposing that Nintedanib is a superior choice for late fibrotic sequelae.

Nintedanib as add-on therapy for pulmonary fibrosis after COVID-19 did not improve oxygenation or mortality, but improved the SpO2/FiO2 ratio in patients (43). The use of Nintedanib alongside treatment of COVID-19 pulmonary fibrosis showed a more pronounced improvement in lung CT severity score compared with Pirfenidone (44). Consistent with our findings of receptor upregulation of Nintedanib in fibroblasts. Noth et al. found that the incidence of major adverse cardiovascular events was similar between the nintedanib and placebo groups, both in patients with high and low cardiovascular risk (45). However, it should be noted that the most frequent adverse events associated with nintedanib use are diarrhea, decreased appetite, and vomiting (46). These adverse events may have an impact on the blood glucose and blood pressure of patients with diabetes. Therefore, close monitoring of blood glucose and blood pressure is recommended when using nintedanib.

It is important to acknowledge the limitations of our study. Firstly, we were unable to conduct *in vitro* or *in vivo* animal experiments to directly evaluate the preferential target receptor for SARS-CoV-2 infection. Secondly, we did not perform *in vitro* experiments to validate the impact of Nintedanib. Thirdly, the sample size in our study was limited, which prevented us from conducting a more detailed analysis of the impact of gender within our subgroup.

5 Conclusion

In conclusion, the analysis of single-cell data from the lungs of COVID-19 patients with comorbid diabetes and hypertension allowed us to assess their biological characteristics comprehensively and systematically. In this study, we found that vascular-related cells, especially activated endothelial cells, play an important role in the co-morbid process of diabetes, hypertension, and COVID-19. At the same time, we suggest that fibroblasts may be the ultimate "effector cells" that contribute to the deterioration of lung function. Based on these findings, we propose that activated endothelial cells may be a potential "bridge" to fibrosis and suggest preferred drug targets for treatment. In addition, we found that in the combination of these three diseases, the entry factor used by SARS-CoV-2 is not the traditional ACE2, but possibly KREMEN1, and finally, we suggest that Nintedanib may be a preferred therapeutic option for the late fibrotic sequelae. These findings provide important academic and clinical implications for better understanding and treating pulmonary complications due to combined diabetes and hypertension in patients with COVID-19.

Data availability statement

The datasets presented in this study can be found in online repositories. The names of the repository/repositories and accession number(s) can be found in the article/Supplementary Material.

Author contributions

XZ: Formal Analysis, Funding acquisition, Methodology, Project administration, Supervision, Visualization, Writing – original draft, Writing – review & editing. XD: Data curation, Project administration, Writing – review & editing. LiZ: Writing – review & editing. PW: Data curation, Formal Analysis, Software, Writing – review & editing. XT: Data curation, Formal Analysis, Investigation, Resources, Writing – original draft. YM: Data curation, Formal Analysis, Software, Writing – original draft. YSZ: Data curation, Formal Analysis, Software, Writing – original draft. YZ: Writing – review & editing. CM: Writing – review & editing. LaZ: Conceptualization, Funding acquisition, Project administration, Supervision, Writing – original draft, Writing – review & editing.

Funding

The author(s) declare financial support was received for the research, authorship, and/or publication of this article. The study was supported by National Science Foundation for Young Scientists of China (81900065, 82200084), International Science and Technology Cooperation Project of Chengdu (2023-GH02-00092-HZ), the Youth Innovation Project of Sichuan Medical Association (Q21018), Chengdu Medical Research Projects (2022516), Postdoctoral Science Foundation funded project of Sichuan Province (TB2023047), and Natural Science Foundation of Sichuan Province (2022NSFSC1394, 2023NSFSC1456).

Acknowledgments

The authors thank Dr Jianming Zeng (University of Macau), and all the members of his bioinformatics team, biotrainee, for generously sharing their experience and codes.

Conflict of interest

The authors declare that the research was conducted in the absence of any commercial or financial relationships that could be construed as a potential conflict of interest.

Publisher's note

Supplementary material

The Supplementary Material for this article can be found online at: https://www.frontiersin.org/articles/10.3389/fendo.2023.1258646/full#supplementary-material

References

1. Tiengo A, Fadini GP, Avogaro A. The metabolic syndrome, diabetes and lung dysfunction. *Diabetes Metab* (2008) 34(5):447–54. doi: 10.1016/j.diabet.2008.08.001

2. Kang Z, Luo S, Gui Y, Zhou H, Zhang Z, Tian C, et al. Obesity is a potential risk factor contributing to clinical manifestations of covid-19. *Int J Obes (Lond)* (2020) 44 (12):2479–85. doi: 10.1038/s41366-020-00677-2

3. Jiang T, Liu T, Deng X, Ding W, Yue Z, Yang W, et al. Adiponectin ameliorates lung ischemia-reperfusion injury through sirt1-pink1 signaling-mediated mitophagy in type 2 diabetic rats. *Respir Res* (2021) 22(1):258. doi: 10.1186/s12931-021-01855-0

4. Price LC, McAuley DF, Marino PS, Finney SJ, Griffiths MJ, Wort SJ. Pathophysiology of pulmonary hypertension in acute lung injury. *Am J Physiol Lung Cell Mol Physiol* (2012) 302(9):L803–15. doi: 10.1152/ajplung.00355.2011

5. Suresh K, Shimoda LA. Lung circulation. *Compr Physiol* (2016) 6(2):897–943. doi: 10.1002/cphy.c140049

6. Shlobin OA, Brown AW, Nathan SD. Pulmonary hypertension in diffuse parenchymal lung diseases. *Chest* (2017) 151(1):204–14. doi: 10.1016/j.chest.2016.08.002

7. Waxman AB, Elia D, Adir Y, Humbert M, Harari S. Recent advances in the management of pulmonary hypertension with interstitial lung disease. *Eur Respir Rev* (2022) 31(165):210220. doi: 10.1183/16000617.0220-2021

8. Roberts TJ, Burns AT, MacIsaac RJ, MacIsaac AI, Prior DL, La Gerche A. Diagnosis and significance of pulmonary microvascular disease in diabetes. *Diabetes Care* (2018) 41(4):854–61. doi: 10.2337/dc17-1904

9. Zhang L, Jiang F, Xie Y, Mo Y, Zhang X, Liu C. Diabetic endothelial microangiopathy and pulmonary dysfunction. *Front Endocrinol (Lausanne)* (2023) 14:1073878. doi: 10.3389/fendo.2023.1073878

10. Khateeb J, Fuchs E, Khamaisi M. Diabetes and lung disease: A neglected relationship. *Rev Diabetes Stud* (2019) 15:1–15. doi: 10.1900/rds.2019.15.1

11. Ehrlich SF, Quesenberry CP Jr., Van Den Eeden SK, Shan J, Ferrara A. Patients Diagnosed with Diabetes Are at Increased Risk for Asthma, Chronic Obstructive Pulmonary Disease, Pulmonary Fibrosis, and Pneumonia but Not Lung Cancer. *Diabetes Care* (2010) 33(1):55–60. doi: 10.2337/dc09-0880

12. Merad M, Blish CA, Sallusto F, Iwasaki A. The immunology and immunopathology of covid-19. *Science* (2022) 375(6585):1122–7. doi: 10.1126/science.abm8108

13. Raman B, Bluemke DA, Lüscher TF, Neubauer S. Long covid: post-acute sequelae of covid-19 with a cardiovascular focus. *Eur Heart J* (2022) 43(11):1157–72. doi: 10.1093/eurheartj/ehac031

14. Davis HE, McCorkell L, Vogel JM, Topol EJ. Long covid: major findings, mechanisms and recommendations. *Nat Rev Microbiol* (2023) 21(3):133–46. doi: 10.1038/s41579-022-00846-2

15. Trougakos IP, Stamatelopoulos K, Terpos E, Tsitsilonis OE, Aivalioti E, Paraskevis D, et al. Insights to sars-cov-2 life cycle, pathophysiology, and rationalized treatments that target covid-19 clinical complications. *J BioMed Sci* (2021) 28(1):9. doi: 10.1186/s12929-020-00703-5

16. Nyland JE, Raja-Khan NT, Bettermann K, Haouzi PA, Leslie DL, Kraschnewski JL, et al. Diabetes, drug treatment, and mortality in covid-19: A multinational retrospective cohort study. *Diabetes* (2021) 70(12):2903–16. doi: 10.2337/db21-0385

17. Semenzato L, Botton J, Drouin J, Baricault B, Vabre C, Cuenot F, et al. Antihypertensive drugs and covid-19 risk: A cohort study of 2 million hypertensive patients. *Hypertension* (2021) 77(3):833–42. doi: 10.1161/hypertensionaha.120.16314

18. George PM, Wells AU, Jenkins RG. Pulmonary fibrosis and covid-19: the potential role for antifibrotic therapy. *Lancet Respir Med* (2020) 8(8):807–15. doi: 10.1016/s2213-2600(20)30225-3

19. John AE, Joseph C, Jenkins G, Tatler AL. Covid-19 and pulmonary fibrosis: A potential role for lung epithelial cells and fibroblasts. *Immunol Rev* (2021) 302(1):228–40. doi: 10.1111/imr.12977

20. McDonald LT. Healing after Covid-19: Are Survivors at Risk for Pulmonary Fibrosis? *Am J Physiol Lung Cell Mol Physiol* (2021) 320(2):L257–l65. doi: 10.1152/ajplung.00238.2020

21. Wendisch D, Dietrich O, Mari T, von Stillfried S, Ibarra IL, Mittermaier M, et al. Sars-cov-2 infection triggers profibrotic macrophage responses and lung fibrosis. *Cell* (2021) 184(26):6243–61.e27. doi: 10.1016/j.cell.2021.11.033

22. King CS, Mannem H, Kukreja J, Aryal S, Tang D, Singer JP, et al. Lung transplantation for patients with covid-19. *Chest* (2022) 161(1):169–78. doi: 10.1016/j.chest.2021.08.041

23. Hirawat R, Jain N, Aslam Saifi M, Rachamalla M, Godugu C. Lung fibrosis: post-covid-19 complications and evidences. *Int Immunopharmacol* (2023) 116:109418. doi: 10.1016/j.intimp.2022.109418

24. Zhang L, Tang C, Zhang M, Tong X, Xie Y, Yan R, et al. Single cell meta-analysis of endmt and emt state in covid-19. *Front Immunol* (2022) 13:976512. doi: 10.3389/fimmu.2022.976512

25. Sun D, Guan X, Moran AE, Wu L-Y, Qian DZ, Schedin P, et al. Identifying phenotype-associated subpopulations by integrating bulk and single-cell sequencing data. *Nat Biotechnol* (2022) 40(4):527–38. doi: 10.1038/s41587-021-01091-3

26. Petrie JR, Guzik TJ, Touyz RM. Diabetes, hypertension, and cardiovascular disease: clinical insights and vascular mechanisms. *Can J Cardiol* (2018) 34(5):575–84. doi: 10.1016/j.cjca.2017.12.005

27. Aird WC. Phenotypic heterogeneity of the endothelium: ii. *Representative Vasc Beds Circ Res* (2007) 100(2):174–90. doi: 10.1161/01.RES.0000255690.03436.ae

28. Martin JC, Chang C, Boschetti G, Ungaro R, Giri M, Grout JA, et al. Single-cell analysis of crohn's disease lesions identifies a pathogenic cellular module associated with resistance to anti-tnf therapy. *Cell* (2019) 178(6):1493–508.e20. doi: 10.1016/j.cell.2019.08.008

29. Raslan AA, Pham TX, Lee J, Hong J, Schmottlach J, Nicolas K, et al. Single cell transcriptomics of fibrotic lungs unveils aging-associated alterations in endothelial and epithelial cell regeneration. *bioRxiv [Preprint]* 20:2023.01.17.523179 (2023). doi: 10.1101/2023.01.17.523179

30. Pitocco D, Fuso L, Conte EG, Zaccardi F, Condoluci C, Scavone G, et al. The diabetic lung–a new target organ? *Rev Diabetes Stud* (2012) 9(1):23–35. doi: 10.1900/rds.2012.9.23

31. Veerakumar A, Yung AR, Liu Y, Krasnow MA. Molecularly defined circuits for cardiovascular and cardiopulmonary control. *Nature* (2022) 606(7915):739–46. doi: 10.1038/s41586-022-04760-8

32. Foster DJ, Ravikumar P, Bellotto DJ, Unger RH, Hsia CC. Fatty diabetic lung: altered alveolar structure and surfactant protein expression. *Am J Physiol Lung Cell Mol Physiol* (2010) 298(3):L392–403. doi: 10.1152/ajplung.00041.2009

33. Rask-Madsen C, King GL. Vascular complications of diabetes: mechanisms of injury and protective factors. *Cell Metab* (2013) 17(1):20–33. doi: 10.1016/j.cmet.2012.11.012

34. Jenkins AJ, Joglekar MV, Hardikar AA, Keech AC, O'Neal DN, Januszewski AS. Biomarkers in diabetic retinopathy. *Rev Diabetes Stud* (2015) 12(1-2):159–95. doi: 10.1900/rds.2015.12.159

35. Åstrand A, Wingren C, Benjamin A, Tregoning JS, Garnett JP, Groves H, et al. Dapagliflozin-lowered blood glucose reduces respiratory pseudomonas aeruginosa infection in diabetic mice. *Br J Pharmacol* (2017) 174(9):836–47. doi: 10.1111/bph.13741

36. Heerspink HJL, Furtado RHM, Berwanger O, Koch GG, Martinez F, Mukhtar O, et al. Dapagliflozin and kidney outcomes in hospitalized patients with covid-19 infection: an analysis of the dare-19 randomized controlled trial. *Clin J Am Soc Nephrol* (2022) 17(5):643–54. doi: 10.2215/cjn.14231021

37. Kosiborod M, Berwanger O, Koch GG, Martinez F, Mukhtar O, Verma S, et al. Effects of dapagliflozin on prevention of major clinical events and recovery in patients with respiratory failure because of covid-19: design and rationale for the dare-19 study. *Diabetes Obes Metab* (2021) 23(4):886–96. doi: 10.1111/dom.14296

38. Maginnis MS. Virus-receptor interactions: the key to cellular invasion. *J Mol Biol* (2018) 430(17):2590–611. doi: 10.1016/j.jmb.2018.06.024

39. Bourgonje AR, Abdulle AE, Timens W, Hillebrands JL, Navis GJ, Gordijn SJ, et al. Angiotensin-converting enzyme 2 (Ace2), sars-cov-2 and the pathophysiology of coronavirus disease 2019 (Covid-19). *J Pathol* (2020) 251(3):228–48. doi: 10.1002/path.5471

40. Gawish R, Starkl P, Pimenov L, Hladik A, Lakovits K, Oberndorfer F, et al. Ace2 is the critical in vivo receptor for sars-cov-2 in a novel covid-19 mouse model with tnf- and ifnγ-driven immunopathology. *Elife* (2022) 11:e74623. doi: 10.7554/eLife.74623

41. Gu Y, Cao J, Zhang X, Gao H, Wang Y, Wang J, et al. Receptome profiling identifies kremen1 and asgr1 as alternative functional receptors of sars-cov-2. *Cell Res* (2022) 32(1):24–37. doi: 10.1038/s41422-021-00595-6

42. Hoffmann M, Pöhlmann S. Novel sars-cov-2 receptors: asgr1 and kremen1. *Cell Res* (2022) 32(1):1–2. doi: 10.1038/s41422-021-00603-9

43. Saiphoklang N, Patanayindee P, Ruchiwit P. The effect of nintedanib in post-covid-19 lung fibrosis: an observational study. *Crit Care Res Pract* (2022) 2022:9972846. doi: 10.1155/2022/9972846

44. Singh P, Behera D, Gupta S, Deep A, Priyadarshini S, Padhan P. Nintedanib vs pirfenidone in the management of covid-19 lung fibrosis: A single-centre study. *J R Coll Physicians Edinb* (2022) 52(2):100–4. doi: 10.1177/14782715221103402

45. Noth I, Wijsenbeek M, Kolb M, Bonella F, Moros L, Wachtlin D, et al. Cardiovascular Safety of Nintedanib in Subgroups by Cardiovascular Risk at Baseline in the Tomorrow and Inpulsis trials. *Eur Respir J* (2019) 54(3):1801797. doi: 10.1183/13993003.01797-2018

46. Crestani B, Huggins JT, Kaye M, Costabel U, Glaspole I, Ogura T, et al. Long-term safety and tolerability of nintedanib in patients with idiopathic pulmonary fibrosis: results from the open-label extension study, inpulsis-on. *Lancet Respir Med* (2019) 7(1):60–8. doi: 10.1016/s2213-2600(18)30339-4

Frontiers in
Cell and Developmental Biology

Explores the fundamental biological processes of life, covering intracellular and extracellular dynamics.

The world's most cited developmental biology journal, advancing our understanding of the fundamental processes of life. It explores a wide spectrum of cell and developmental biology, covering intracellular and extracellular dynamics.

Discover the latest Research Topics

See more →

frontiers

Frontiers in
Cell and Developmental Biology

Frontiers

Avenue du Tribunal-Fédéral 34
1005 Lausanne, Switzerland
frontiersin.org

Contact us

+41 (0)21 510 17 00
frontiersin.org/about/contact